

**A Penetration-Based Finite Element Method for Hyperelastic  
Three-Dimensional Biphase Tissues in Contact**

by

**Kerem Ün**

A Thesis Submitted to the Graduate

Faculty of Rensselaer Polytechnic Institute

in Partial Fulfillment of the

Requirements for the Degree of

DOCTOR OF PHILOSOPHY

Major Subject: Biomedical Engineering

Approved by the  
Examining Committee:

---

Robert L. Spilker, Thesis Advisor

---

John B. Brunski, Member

---

Mark H. Holmes, Member

---

Mark S. Shephard, Member

Rensselaer Polytechnic Institute  
Troy, New York

April 2002  
(For Graduation May 2002)



# Table of Contents

	page
<b>Table of Contents .....</b>	<b>iii</b>
<b>List of Tables .....</b>	<b>vi</b>
<b>List of Figures.....</b>	<b>vii</b>
<b>Acknowledgements .....</b>	<b>xiii</b>
<b>Abstract.....</b>	<b>xv</b>
<b>Chapter1: Introduction .....</b>	<b>1</b>
1.1 Prologue .....	1
1.2 Articular Cartilage .....	1
1.3 Cartilage Studies .....	4
1.4 Finite Element Formulations .....	7
1.5 Objective and Thesis Layout .....	9
<b>Chapter 2: Biphasic Theory of Articular Cartilage.....</b>	<b>11</b>
2.1 Introduction.....	11
2.2 Constitutive Equations for Biphasic Mixture .....	11
2.3 Cartilage Material Properties .....	13
<b>Chapter 3: Nonlinear Elasticity.....</b>	<b>15</b>
3.1 Introduction.....	15
3.2 Nonlinear Elasticity .....	15
3.3 Constitutive Modeling and Hyperelasticity .....	19
<b>Chapter 4: Finite Element Formulation .....</b>	<b>25</b>
4.1 Introduction.....	25
4.2 Velocity-Pressure Formulation .....	25
4.3 Weak Form .....	25
4.4 Linear Formulation .....	28

4.5 Computer Implementation .....	32
4.5.1 Object Oriented Programming.....	32
4.5.2 Implementation of the Linear Analysis.....	33
4.6 Nonlinear Formulation.....	36
4.6.1 Linearization .....	38
4.6.2 Partial Linearization.....	43
4.6.3 Solution of the Nonlinear System .....	45
4.6.4 Line Search .....	49
4.7 Computer Implementation of the Nonlinear Analysis.....	50
<b>Chapter 5: Penetration Method.....</b>	<b>54</b>
5.1 Introduction.....	54
5.2 Experimental Kinematics Data .....	55
5.2.1 Visualization Techniques.....	55
5.2.2 Interpolation through Discrete Kinematics Data .....	56
5.3 Biphasic Contact Boundary Conditions and Load Sharing .....	57
5.4 Derivation of the Approximate Boundary Conditions.....	59
5.5 Extension to Hyperelastic Solid Phase .....	65
5.5.1 Application and Computer Implementation.....	68
<b>Chapter 6: Linear Examples.....</b>	<b>70</b>
6.1 Introduction.....	70
6.2 Canonical Examples .....	70
6.2.1 Results for Case CT .....	72
6.2.2 Results for Case VT .....	86
6.2.3 Evaluation of the Penetration Analysis Results .....	87
6.3 Glenohumeral Analysis.....	95
6.3.1 Approximate Contact Boundary Conditions.....	97
6.3.2 Humerus Results .....	100

6.3.3 The Glenoid Results.....	105
6.3.4 Evaluation of the Glenohumeral Analysis Results .....	105
<b>Chapter 7: Nonlinear Examples .....</b>	<b>109</b>
7.1 Introduction.....	109
7.2 Confined Compression Examples.....	109
7.2.1 Creep .....	109
7.2.2 Stress Relaxation.....	112
7.2.3 Evaluation of the Confined Compression Analysis Results .....	114
7.3 Glenohumeral Analysis.....	115
7.3.1 Approximate Contact Boundary Conditions.....	115
7.3.2 Humerus Results .....	118
7.3.3 Glenoid Results .....	118
7.3.4 Evaluation of the Glenohumeral Analysis Results .....	123
<b>Chapter 8: Summary, Conclusions and Future Research .....</b>	<b>127</b>
8.1 Summary.....	127
8.2 Future Research .....	131
<b>Bibliography .....</b>	<b>133</b>
<b>Appendix A: Derivation of the Tangent Stiffness for the Hyperelastic Material Law</b> .....	<b>142</b>
<b>Appendix B: Element Matrices of Nonlinear <math>v</math>-<math>p</math> Formulation .....</b>	<b>145</b>
<b>Appendix C: Justification for Disregarding the Tissue Curvature Effect in</b> <b>Penetration Analysis .....</b>	<b>146</b>

# List of Tables

	page
Table 1: The numerical procedure for the nonlinear problem .....	48
Table 2: The values of geometrical parameters defined in Figure 2 for cases CT and VT. .....	71

## List of Figures

	page
Figure 1: Organization of articular cartilage into different zones (adopted from [70]). .....	2
Figure 2: Microstructure of articular cartilage (adopted from [70]). .....	3
Figure 3: Architecture of collagen fibers in articular cartilage (from[58]). .....	4
Figure 4. Sketches of common experiments applied to articular cartilage. From top to bottom: Confined compression (cross-sectional), unconfined compression and indentation. ....	6
Figure 5: Symbols used in object oriented diagrams. ....	33
Figure 6: Analysis hierarchy of the implemented finite element code.....	34
Figure 8: Time integrator and system assembler hierarchy of the implemented finite element code. ....	35
Figure 9: Material hierarchy of the implemented finite element code. ....	36
Figure 10: Nonlinear analysis object in the analysis hierarchy.....	51
Figure 11: Nonlinear biphasic stiffness object in the stiffness contributor hierarchy.....	51
Figure 12: Nonlinear assembler object in the assembler hierarchy.....	52
Figure 13: Nonlinear biphasic stiffness object in the stiffness contributor hierarchy.....	53
Figure 14: Graphical depiction of the idea behind penetration method.....	54
Figure 15: Picture of overlapping cartilage models as obtained from the solid modeler (top). Definitions of geometric parameters in overlapped models(bottom). ....	60
Figure 16: Problem definition and geometry for the 2-D biphasic contact and 3-D penetration-based analyses. Cartilage layers (dark gray) are attached to rigid bone (light gray). A force is applied along the axis of symmetry. The centerline thickness of layer A and layer B, and radii of curvature are defined. ....	71
Figure 17: Case CT-CP, comparison of pressure and normal elastic traction distribution on layers A and B, $t = 1$ sec. ....	75

Figure 18: Case CT-VP, comparison of pressure and normal elastic traction distribution on layers A and B, $t = 1$ sec.....	75
Figure 19: Case CT-CP, the axial displacement at the contact interface of layers A and B, $t = 1$ sec.....	76
Figure 20: Case CT-VP, the axial displacement at the contact interface of layers A and B, $t = 1$ sec.....	76
Figure 21: Case CT-CP, the normal velocity at the contact interface of layers A and B, $t = 1$ sec.....	77
Figure 22: Case CT-VP, the normal velocity at the contact interface of layers A and B, $t = 1$ sec.....	77
Figure 23: Case CT-CP, tissue A, comparison of the normal elastic traction with the shear stress components in the planes along the normal direction, $t = 1$ sec.....	78
Figure 24: Case CT-VP, tissue B, comparison of the normal elastic traction with the shear stress components in the planes along the normal direction, $t = 1$ sec.....	78
Figure 25: Case CT-CP, tissue A, total normal traction distribution from 3D penetration compared with 2D contact finite element analysis result, $t = 1$ sec. ....	79
Figure 26: Case CT-VP, tissue B, total normal traction distribution from 3D penetration compared with 2D contact finite element analysis result, $t = 1$ sec. ....	79
Figure 27: Case CT-CP, tissue B, pressure distribution from 3D penetration compared with 2D contact finite element analysis result, $t = 1$ sec. ....	80
Figure 28: Case CT-VP, tissue B, pressure distribution from 3D penetration compared with 2D contact finite element analysis result, $t = 1$ sec. ....	80
Figure 29: Case CT-CP, tissue A, normal elastic traction distribution from 3D penetration compared with 2D contact finite element analysis result, $t = 1$ sec. ....	82
Figure 30: CT-CP, tissue B, normal elastic traction distribution from 3D penetration compared with 2D contact finite element analysis result, $t = 1$ sec. ....	82
Figure 31: Case CT-VP, tissue A, normal elastic traction distribution from 3D penetration compared with 2D contact finite element analysis result, $t = 1$ sec. ....	83
Figure 32: Case CT-VP, tissue B, normal elastic traction distribution from 3D penetration compared with 2D contact finite element analysis result, $t = 1$ sec. ....	83

Figure 33: Case CT-CP, tissue A, axial displacement from 3D penetration compared with 2D contact finite element analysis result, t = 1 sec. ....	84
Figure 34: Case CT-CP, tissue B, axial displacement from 3D penetration compared with 2D contact finite element analysis result, t = 1 sec. ....	84
Figure 35: Case CT-VP, tissue A, axial displacement from 3D penetration compared with 2D contact finite element analysis result, t = 1 sec. ....	85
Figure 36: Case CT-VP, tissue B, axial displacement from 3D penetration compared with 2D contact finite element analysis result, t = 1 sec. ....	85
Figure 37: Case CT-CP, normal velocity from 3D penetration compared with 2D contact finite element analysis result, t = 1 sec. ....	86
Figure 38: Case VT-CP, comparison of pressure and normal elastic traction distribution on layers A and B, t = 1 sec. ....	88
Figure 39: Case VT-VP, comparison of pressure and normal elastic traction distribution on layers A and B, t = 1 sec. ....	88
Figure 40: Case VT-CP, tissue A, total normal traction distribution from 3D penetration compared with 2D contact finite element analysis result, t = 1 sec. ....	89
Figure 41: Case VT-VP, tissue B, total normal traction distribution from 3D penetration compared with 2D contact finite element analysis result, t = 1 sec. ....	89
Figure 42: Case VT-CP, tissue B, pressure distribution from 3D penetration compared with 2D contact finite element analysis result, t = 1 sec. ....	90
Figure 43: Case VT-VP, tissue A, pressure distribution from 3D penetration compared with 2D contact finite element analysis result, t = 1 sec. ....	90
Figure 44: Case VT-CP, tissue A, normal elastic traction distribution from 3D penetration compared with 2D contact finite element analysis result, t = 1 sec. ....	91
Figure 45: Case VT-CP, tissue B, normal elastic traction distribution from 3D penetration compared with 2D contact finite element analysis result, t = 1 sec. ....	91
Figure 46: Case VT-VP, tissue A, normal elastic traction distribution from 3D penetration compared with 2D contact finite element analysis result, t = 1 sec. ....	92
Figure 47: Case VT-VP, tissue B, normal elastic traction distribution from 3D penetration compared with 2D contact finite element analysis result, t = 1 sec. ....	92

Figure 48: Case VT-CP, tissue A, axial displacement from 3D penetration compared with 2D contact finite element analysis result, t = 1 sec. ....	93
Figure 49: Case VT-CP, tissue B, axial displacement from 3D penetration compared with 2D contact finite element analysis result, t = 1 sec. ....	93
Figure 50: Case VT-VP, tissue A, axial displacement from 3D penetration compared with 2D contact finite element analysis result, t = 1 sec. ....	94
Figure 51: Case VT-VP, tissue B, axial displacement from 3D penetration compared with 2D contact finite element analysis result, t = 1 sec. ....	94
Figure 52: Shoulder geometry with glenoid and humerus cartilages.....	96
Figure 53: Comparison of magnitude of the total traction (upper) and pressure (lower) on the contact faces of humeral head (left) and glenoid (right) cartilages at an arm elevation angle of 40° .....	98
Figure 54: Comparison of magnitude of the total traction (upper) and pressure(lower) on the contact faces of humeral head (left) and glenoid (right) cartilages at an arm elevation angle of 60° .....	99
Figure 55: Maximum tensile stress distribution on the contacting face of the humerus at arm elevations of 40° (top left), 50° (top right) and 60° (bottom). ....	101
Figure 56: Maximum tensile stress distribution on the bone interface of the humerus at arm elevations of 40° (top left), 50° (top right) and 60° (bottom). ....	102
Figure 57: Maximum compressive stress distribution on the bone interface of the humerus at arm elevations of 40° (top left), 50° (top right) and 60° (bottom). ....	103
Figure 58: Maximum shear stress distribution on the bone interface of the humerus at arm elevations of 40° (top left), 50° (top right) and 60° (bottom). ....	104
Figure 59: Maximum tensile stress distribution on the contacting face of the glenoid at arm elevations of 40° (left), 50° (center) and 60° (right). ....	106
Figure 60: Maximum tensile stress distribution on the bone interface of the glenoid at arm elevations of 40° (left), 50° (center) and 60° (right). ....	106
Figure 61: Maximum compressive stress distribution on the bone interface of the glenoid at arm elevations of 40° (left), 50° (center) and 60° (right). ....	107
Figure 62: Maximum shear stress distribution on the bone interface of the glenoid at arm elevations of 40° (left), 50° (center) and 60° (right). ....	107

Figure 63: The finite element mesh used in confined compression problems ..... 110

Figure 64: Pressure as function of depth at various time point in CC-CR. Solid lines indicate converged FD results while symbols are FE results. .... 111

Figure 65: Axial displacement as function of depth at various time point in CC-CR. Solid lines indicate converged FD results while symbols are FE results. .... 111

Figure 66: Axial stress as function of depth at various time point in CC-CR. Solid lines indicate converged FD results while symbols are FE results. .... 112

Figure 67: Pressure as function of depth at various time point in CC-SR. Solid lines indicate converged FD results while symbols are FE results. .... 113

Figure 68: Axial displacement as function of depth at various time point in CC-SR. Solid lines indicate converged FD results while symbols are FE results. .... 113

Figure 69: Axial stress as function of depth at various time point in CC-SR. Solid lines indicate converged FD results while symbols are FE results. .... 114

Figure 70: Comparison of magnitude of the total traction (upper) and pressure(lower) on the contact faces of humeral head (left) and glenoid (right) cartilages at an arm elevation angle of 40° originating from nonlinear penetration procedure..... 116

Figure 71: Comparison of magnitude of the total traction (upper) and pressure(lower) on the contact faces of humeral head (left) and glenoid (right) cartilages at an arm elevation angle of 60° originating from nonlinear penetration procedure..... 117

Figure 72: Maximum tensile stress distribution on the contacting face of the humerus at arm elevations of 40° (top left), 50° (top right) and 60° (bottom) degrees..... 119

Figure 73: Maximum tensile stress distribution on the bone interface of the humerus at arm elevations of 40° (top left), 50° (top right) and 60° (bottom) degrees..... 120

Figure 74: Maximum compressive stress distribution on the bone interface of the humerus at arm elevations of 40° (top left), 50° (top right) and 60° (bottom) degrees. .... 121

Figure 75: Maximum shear stress distribution on the bone interface of the humerus at arm elevations of 40° (top left), 50° (top right) and 60° (bottom) degrees. .... 122

Figure 76: Maximum tensile stress distribution on the contacting face of the glenoid at arm elevations of 40° (left) and 50° (right)..... 124

Figure 77: Maximum tensile stress distribution on the bone interface of the glenoid at arm elevations of 40° (left) and 50°(right)..... 124

Figure 78: Maximum compressive stress distribution on the bone interface of the glenoid at arm elevations of 40° (left) and 50° (right)..... 125

Figure 79: Maximum shear stress distribution on the bone interface of the glenoid at arm elevations of 40° (left) and 50° (right)..... 125

Figure C.1: The penetration distribution assigned to a curved surface where  $g$  denotes the varying penetration field and  $R$  is the radius of curvature. Line segment of length  $d$  takes the length  $d'$  after penetration is applied. .... 146

## Acknowledgements

Every doctoral thesis, I believe, has a personal component that is not evident in its scientific content. I always enjoyed reading the acknowledgements part of theses independent of subject to get a feel for the personal story behind them. It is like a dream coming true that I am writing that very special part of my own thesis now. And I am happy to have the opportunity to express my gratitude to those who made this thesis more than a scientific document with eight chapters.

I believe that every doctoral student sooner or later realizes that by far the most important factor for a successful doctoral work is a good advisor. I have been lucky to have such an advisor: Prof. Robert L. Spilker was a good advisor and the nicest person to work with. I am grateful to him for his guidance, support and for making a 'doctor' out of me. I would also like to thank Prof. John B. Brunski, Prof. Mark H. Holmes and Prof. Mark S. Shephard, my committee members, for their valuable input. It saddens me as much that I cannot express my gratitude to Dr. Peter S. Donzelli personally, as his unfortunate and untimely death in August, 2000. He was a great colleague and friend; I will always remember him.

Nobody has given me as much encouragement in various aspects of my life, including my doctoral study, as my mother, Ayla Ün. Although she was away from her son for more than 8 years she never complained. I am grateful to her for her loving care, patience and encouragement.

My brother Kerim was a great friend and supporter. He always understood me and supported me in stressful times. I greatly appreciate his love, care and friendship.

When spending a long time far away from home it is inevitable that one day the telephone rings and you hear some sad news from your beloved ones. I lost both of my grandparents while I was studying hard for my doctoral degree. I am sure that they would have been delighted to see my graduation day.

I guess, nobody could have been happier than my father, Dr. Resat Ün, to see me complete my degree to become, in his words, "the second Dr. Ün". Unfortunately, 11<sup>th</sup> April, 1998 was one of those days when my office phone rang and I was told that we had lost him. My father was a paragon of honesty in his scientific and personal life, and I will try to follow his footsteps to the best of my ability. I dedicate this work to his beloved memory.

I am fortunate that during my graduate years I had much more fun moments than sad ones. As valuable to me as this degree are the friends that I made during this time. While every scientific work eventually becomes outdated, true friends never do. Arnold Oyola, Mehmet Baran and Dean Nieuwma have been truly like brothers to me. They were always around at good times and bad times. I have greatly enjoyed the friendship of Mike Nathanson, Bülent Yegenoglu, Elena Martinova and Martin Martinov, Tasso Anagnostopoulos, Lale Ergene, and Bouchra Bouqata. Their presence made my life very colorful and I sincerely hope that I have had a similar impact on theirs.

Taiseung Yang and Echo Miller made my stay in the Computational Biomechanics Laboratory a lot of fun. I enjoyed our tea breaks and talking with them about a wide variety of scientific and non-scientific topics.

Last, but certainly not the least, I am grateful to Marella for her love, encouragement and support. She is the nourishment of my life; life is simply beautiful with her!

I am thankful to the Ministry of National Education of Turkey for making my study abroad possible through their scholarships. The financial support of NIH, NSF and Surdna Foundation is also gratefully acknowledged.

## Abstract

Advancements in theoretical, computational and experimental methods have enabled researchers to develop more refined and realistic models for articular cartilage. A realistic numerical simulation of cartilage mechanics under *in vivo* conditions requires the tissue layers to be modeled in contact, undergoing large deformation.

The objective of the current research is to develop an efficient finite element procedure for numerical simulation of three-dimensional (3-D) biphasic cartilage layers in contact. To achieve that objective, the penetration method is developed as a preprocessing technique that makes use of experimentally measured joint kinematic data to derive approximate contact boundary conditions. This process eliminates the nonlinearity associated with contact mechanics, and enables independent analyses of the contacting tissues. The derived boundary conditions provide the input to a finite element procedure where the material and geometric nonlinearities, as well as the strain-dependent permeability, of the tissue layers are taken into account through a biphasic continuum model.

The linear and nonlinear versions of penetration-based biphasic finite element analyses are critically evaluated using canonical problems, then applied to a physiological example, namely the glenohumeral joint of the shoulder. This work represents the first attempt to analyze contacting biphasic articular cartilage layers on physiological geometries under finite deformation. This is a numerically challenging problem and requires that conventional nonlinear solution procedures be improved. The research therefore included an examination of alternate linearizations of the nonlinear problem and line search techniques to stabilize the iterative solution scheme.

Both linear and nonlinear versions of this formulation have been implemented into the object-oriented analysis framework, *Trellis*, of the Scientific Computation Research Center at Rensselaer Polytechnic Institute using the C++ programming language.

# Chapter 1

## Introduction

### 1.1 Prologue

The interest of humankind in the mechanism of the human system is a centuries-old obsession that has attracted some of the brightest scientific minds of history, including Aristotle, Leonardo da Vinci, Galileo Galilei and Helmholtz. Today this interest is shared by an ever-growing number of scientists with an aim of thoroughly understanding the mechanisms involved in function of the human body in order to improve human life.

Biomedical engineering involves the application of engineering fundamentals to biological sciences. Although fundamentally interdisciplinary, it is rapidly emerging as a separate discipline. The existence of such a discipline is well justified by the fact that today health sciences utilize more high technology than ever before. In fact, many medical breakthroughs such as magnetic resonance imaging (MRI), artificial heart, dialysis and orthopedic implants are a product of this interdisciplinary engineering work.

Biomechanics, an important branch of biomedical engineering, involves the application of engineering mechanics in biological sciences. Within the diverse spectrum of biomechanics, the mechanical behavior of various tissues is an important topic.

Soft tissues constitute an important component of mammalian physiology and fulfill various mechanical functions. The flow of blood in the arteries, elasticity of veins, arteries and articular cartilage are just a few examples of properties that are of vital importance. In other cases, soft tissue mechanical properties are not of direct relevance for normal function; however, they can be important to the reaction of tissue to external effects. Brain trauma caused by impact, and the formation of pressure ulcers are examples of such situations. As a result of the significance of mechanical function, particularly in the cardiovascular and musculoskeletal systems, understanding and characterizing the mechanical behavior of soft tissue has emerged as a critical component of biomechanics.

### 1.2 Articular Cartilage

Diarthrodial joints such as the shoulder or the knee joint are characterized by the presence of articular cartilage and a strong fibrous capsule lined with a metabolically

active synovium. Articular cartilage is the thin layer of soft tissue that covers the contacting surfaces of bones in diarthrodial joints. Daily activities impose high contact forces on diarthrodial joints [3] that are transmitted from one bone to the other through these thin cartilage layers.

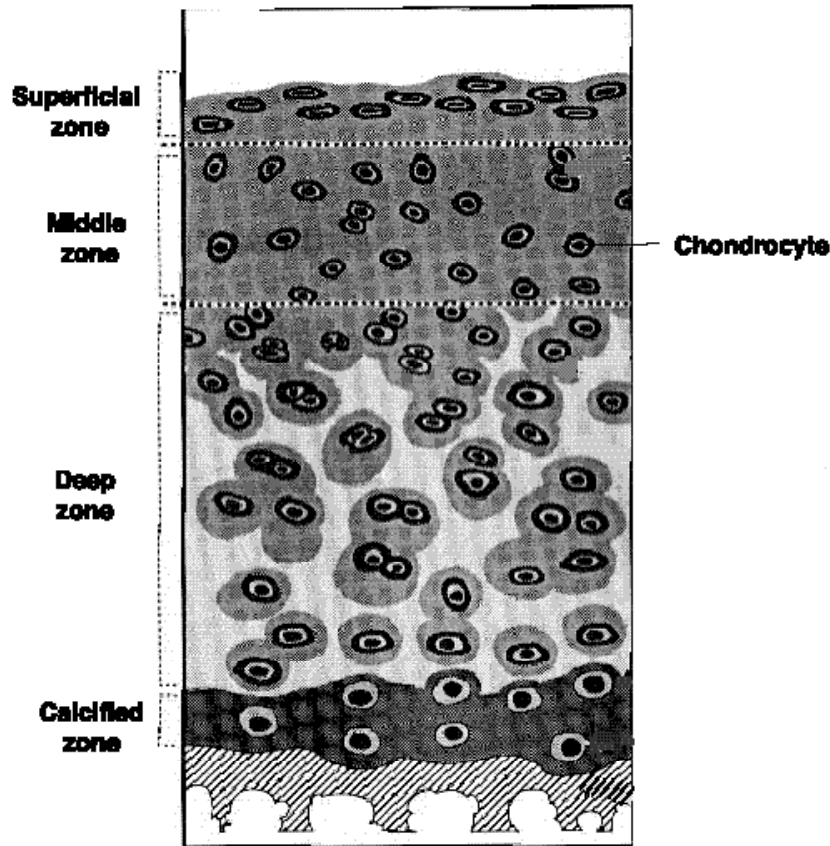
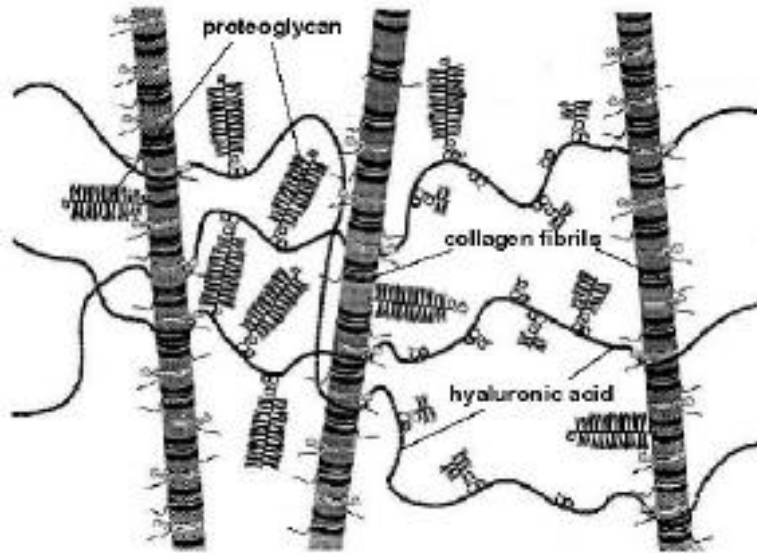


Figure 1: Organization of articular cartilage into different zones (adopted from [70]).

The macroscopic mechanical properties of articular cartilage are related to its microstructure. The structure and composition of articular cartilage vary through the depth [39], from the articular surface to the subchondral bone such that different zones are distinguished through the thickness (Fig. 1). Cartilage consists primarily of an extracellular matrix (ECM), which is the basic functional substance, with a sparse population of highly specialized cells, called *chondrocytes*, distributed through the tissue. The formation and maintenance of the cartilage depends on the chondrocytes. Because the chondrocytes occupy only a small proportion of the total tissue volume, tissue composition is determined primarily by the ECM. The main component of the ECM is

water. Negatively charged molecules called proteoglycans and structural molecules called collagen are held together by hyaluronic acid to form the solid part of the ECM (Fig. 2). Other proteins and glycoproteins are also present but in much lower concentrations [58].

Collagen is the main structural macromolecule in the human body and structural rigidity of the cartilage is provided by the collagen fibrils. The diameter and orientation of the collagen fibrils (together with proteoglycan concentration and water content) is different in each zone (Fig. 3) giving the cartilage its nonuniform mechanical properties.



*Figure 2: Microstructure of articular cartilage (adopted from [70]).*

Cartilage has remarkable durability. Under normal physiologic conditions, visual inspection of cartilage may show relatively pristine tissue even after 8 or 9 decades of use, with few signs of wear. In other cases, the tissue may experience damage due to trauma or inflammatory disease processes or it may undergo progressive degeneration causing the clinical syndrome of osteoarthritis (OA). Although cartilage is metabolically active, it has limited capacity for repair. As a result, damaged articular cartilage is not naturally restored to a normal condition. Damage can accumulate, leading to a complete loss of the articular surface, and exposing the underlying bone. Concomitant with these changes, joint shape and congruency are also altered. These changes are almost always associated with severely impaired joint function, at which point prosthetic joint replacement offers the best option for restoring pain-free mobility. These procedures are appropriate for the treatment of end-stage degenerative joint disease, often after prolonged suffering by the patient. Also, in a small percentage of cases these total joint

replacements lack the durability of the normal joint. Biological and biomechanical studies aimed at understanding the etiology of OA offer hope for the development of alternatives to prosthetic joint replacements.

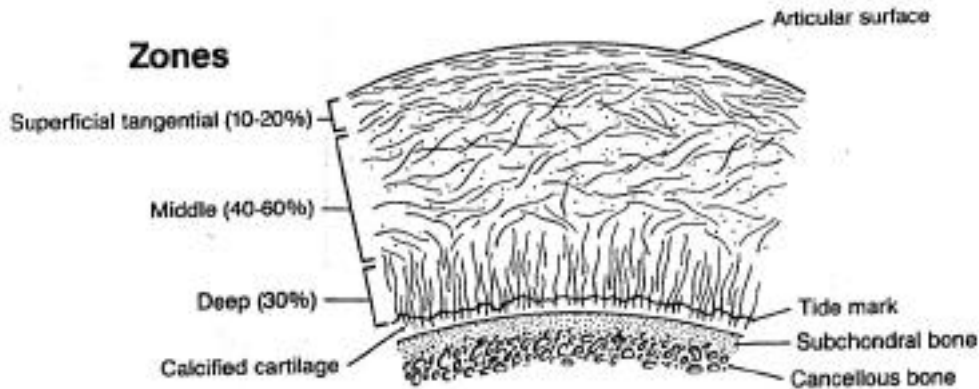


Figure 3: Architecture of collagen fibers in articular cartilage (from[58]).

### 1.3 Cartilage Studies

Characterizing the mechanical behavior of soft tissues is a critical step to gain insight into human functional physiology. For cartilage, mechanical properties should be related to occurrences and mechanisms of degenerative joint diseases. Knowledge accumulated through integrated experimental, theoretical and computational research is essential if biomechanics is to lead to improvement in diagnosis, treatment and rehabilitation.

One of the main challenges in cartilage studies is to predict the deformation behavior of cartilage. And the first ingredient to accomplish this is to determine a constitutive law for cartilage. Constitutive laws describe mathematically the relation between the loading and deformation of a material. A variety of constitutive laws have been proposed for cartilage. Elastic models of cartilage have been used extensively, particularly in early biomechanical studies. Viscoelastic models of different complexity have also been proposed to account for the time-dependent deformation behavior. (See [62] for a review.) Both of these approaches fail to account for the structure of cartilage although they can provide good agreement with experimental deformation data in some cases. Researchers recognized the importance of the interstitial fluid for some time, but it was not until 1980 that the fluid phase was incorporated into the constitutive model of cartilage. Mow *et al.* [63] proposed the superposition of a fluid continuum with a solid

continuum and used mixture laws [94] to derive the constitutive equations. This so-called *biphasic theory* was consistent with respect to the load-bearing mechanism in cartilage and the analytical results, based on an elastic solid phase and an inviscid fluid phase, agreed well with experimental data for cartilage under small strains. In subsequent studies, intrinsic viscoelasticity of the solid phase was also incorporated into the biphasic theory [56]. The continuum representation of cartilage has been improved by considering the stiffening caused by the Donnan effect of the charged particles in the cartilage matrix, leading to the triphasic theory, where the third phase is the ions [52].

Material testing to determine the coefficients in a proposed constitutive law of cartilage is usually through *confined compression*, *unconfined compression* and *indentation* tests (see Fig. 4). To evaluate the coefficients, a solution of the biphasic equations and constitutive law is required for the experimental configuration. In addition to determining the material coefficients, combinations of these tests can provide cross-validations of the constitutive law and biphasic model. Once a constitutive law is confirmed, it is theoretically possible to predict cartilage deformation behavior without the need for additional experiments.

Analytical solutions of the linear or nonlinear biphasic equations can only be derived for a specialized geometry and loading conditions. Analytical solutions for short and long-time response of biphasic cartilage have been derived for unconfined compression [4] and indentation [57] experiments, both with displacement control (stress relaxation) and force control (creep). However, these solutions are valid only for a perfectly lubricated interface between the cartilage and the loading platen. The analytical solution for confined compression has long been known from uniaxial consolidation in soil mechanics [24]. Perturbation and integral transform solutions have been derived for confined compression with strain-dependent permeability [41], for the canonical contact of two biphasic layers [6, 50, 101, 102] and for rolling contact [8].

The limited number of cases amenable to analytical solution underscore the value of numerical methods and the corresponding simulation tools in cartilage studies, as described in the next section.

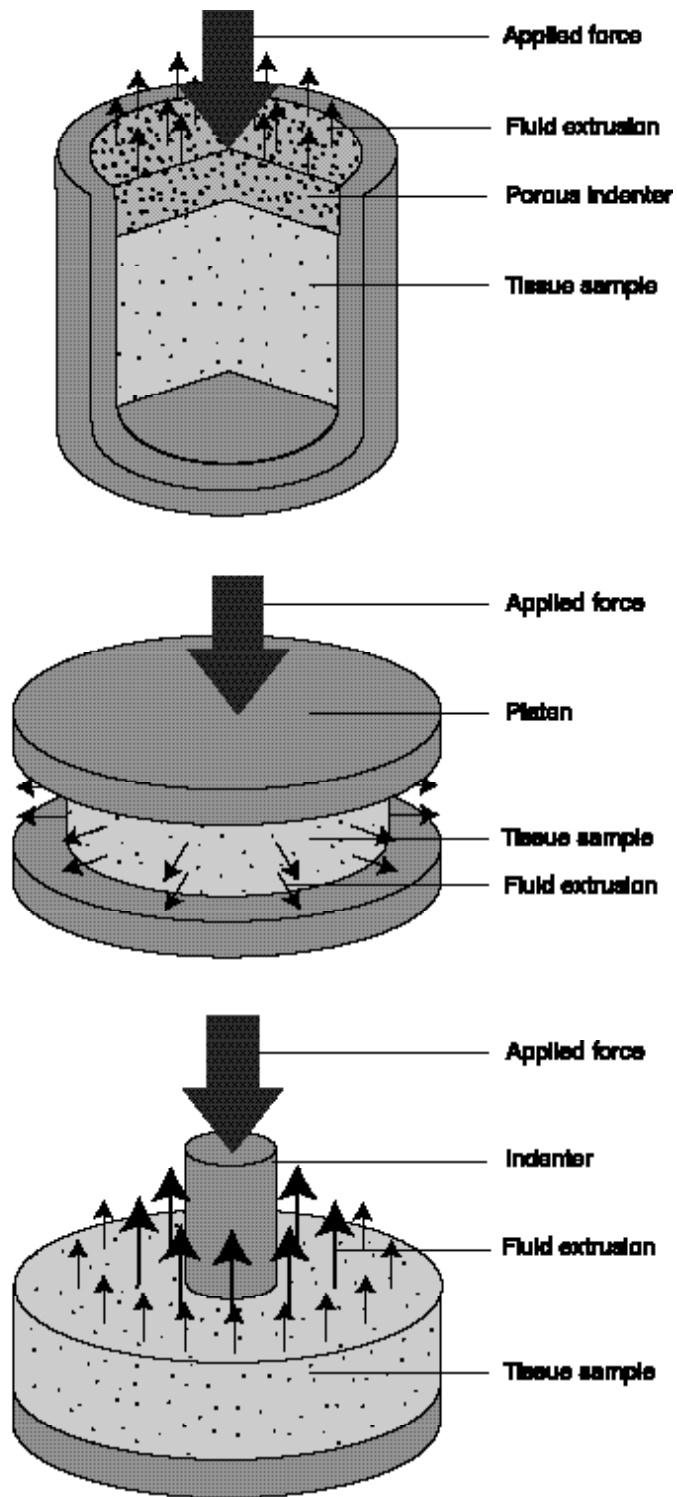


Figure 4. Sketches of common experiments applied to articular cartilage. From top to bottom: Confined compression (cross-sectional), unconfined compression and indentation.

## 1.4 Finite Element Formulations

Physiological soft tissue geometries represent complicated 3-D problem domains. The general inhomogeneity and anisotropy of the tissue complicates the situation even further. Analytical solution of such problems is not possible, and thus robust numerical methods, such as the finite element method, are required to study tissues under realistic physiological conditions.

Although the origin of the finite element method goes back to the 1940`s, it gained wide popularity only after high performance computers became available as research tools. The method has been increasingly employed in biological problems in the last two decades where continuum models and their underlying partial differential equations have been found applicable, and has been used extensively in soft tissue mechanics.

The physiological situation in a diarthrodial joint involves two contacting layers of articular cartilage, and in some cases three or more contacting bodies (e.g., the contact between tibial plateau, femur and interposed meniscus). An ideal numerical simulation therefore calls for a contact finite element analysis performed on the contacting cartilage layer geometries, possibly incorporating inhomogeneity, anisotropy and finite deformation. Although several attempts have been made to model cartilage layers in contact through finite element methods, those analyses have either used the (less realistic) elastic material law or been limited to certain experimental or canonical geometries [38, 73, 90, 91, 103]. One obvious reason for this is the high computational resources required by a realistic 3-D biphasic contact analysis of the type mentioned above.

Different finite element formulations have been proposed based on the biphasic model articular cartilage to study, mostly, canonical configurations too complex for analytic solution. The alternate finite element formulations arise from the choices of those governing equations to be satisfied exactly and those that are satisfied approximately (i.e., in a weak sense). In the biphasic soft tissue problem, alternate formulations originate additionally from options for treating the continuity constraint, and options for eliminating one of the variables from the governing equations (such as pressure or fluid velocity). Some formulations based on biphasic theory are comparable to formulations from consolidation theory of soil mechanics, although the definition of some parameters and their physical interpretation are different.

In the penalty method, the continuity equation is expressed in penalty form, and continuity is enforced as the penalty parameter approaches infinity. Numerically, (since

we can not have an infinitely large number) the penalty parameter should be large enough to enforce continuity but not so large that the system becomes ill-conditioned. Pressure is then eliminated from the governing equations using the penalty form of continuity. Suh *et al.* [83, 84] derived both linear and nonlinear axisymmetric versions of this formulation, and used that formulation to study articular cartilage in experimental configurations.

In the mixed-penalty formulation, the penalty form of the continuity is added to the weighted residual statement rather than used to eliminate the pressure from the governing equations. Unlike the penalty formulation, pressure is a primary variable in this approach and needs to be interpolated. Linear [82, 97] and nonlinear [2] versions of this formulation have been applied to study cartilage deformation. An axisymmetric contact formulation using this approach also has been implemented to study contact of articular cartilage layers [26]. A mesh-free multiquadratic method based on the penalty formulation has been proposed as an alternative to the classical finite element method [44]. Recently, Suh *et al.* incorporated a viscoelastic solid phase with a mixed-penalty based finite element formulation to model cartilage in confined [85] and unconfined compression [86].

Another formulation that is used in cartilage mechanics is the hybrid formulation which is similar to assumed stress methods proposed by Pian for elasticity problems [69]. In this method, the momentum equation of the mixture is exactly satisfied *a priori* by choosing the shape functions for elastic stress and pressure properly. The continuity equation, fluid momentum equation and the strain-displacement law, along with the natural boundary conditions, are introduced into a weighted residual statement [96].

Levenston *et al.* [55] derived three nonlinear formulations of the poroelastic theory based on three variational principles that make use of alternate penalized forms of the internal energy. Two of the forms lead to alternate 3-field formulations where the unknowns are solid phase velocity, pressure and relative velocity. The other form gives a 2-field formulation with solid phase velocity and relative velocity as unknowns.

Theories involving the additional (e.g. ion) phases, namely triphasic and quadriphasic theories have also been incorporated into finite element methods [33, 43, 78, 87]. They have been generally limited to either small deformation cases or to canonical geometries. It should be noted that without some simplifying assumptions, theories involving an ion phase lead to a set of nonlinear governing equations even in the absence of large deformations.

The velocity-pressure formulation [1] has been shown to be successful for 3-D biphasic problems discretized using tetrahedral elements, and is the method of choice in this thesis. A closely related formulation, namely displacement-pressure formulation is also evaluated for the nonlinear analysis. Both formulations are covered in detail in Chapter 4.

## 1.5 Objective and Thesis Layout

The on-going research, and advancements in the computer and experimental technology have enabled researchers to develop more refined and realistic models for articular cartilage. However, cartilage has still not been modeled under physiological conditions, which require not only a proper constitutive law and physiological geometric data, but also simulation of the *in vivo* mechanical environment. The objective of this thesis research is to improve the existing work by modeling cartilage under *in vivo* contact conditions. Here, we present a procedure where 3-D, biphasic, cartilage tissue layers in contact are modeled using finite element methods and experimental kinematics data. It is an interesting demonstration that what numerical or experimental studies alone cannot accomplish can be achieved by combining the two. A simplified numerical simulation of the biphasic contact is achieved by deriving approximate time-dependent contact boundary conditions from experimental data and applying those within a finite element scheme. The material and geometric nonlinearities, as well as the strain-dependent permeability associated with the tissue layers are also taken into account. Hence, the significance of the current work is that it constitutes the very first attempt for the nonlinear 3-D numerical simulation of biphasic tissue layers under contact conditions. Both the penetration method and the finite element procedures are implemented with an object-oriented framework. Additional numerical precautions are taken to handle the nonlinear contact simulation since it is a particularly challenging problem.

The thesis is organized as follows:

The biphasic theory of cartilage is outlined in Chapter 2 along with a description of cartilage material properties.

Chapter 3 provides the background for the nonlinear analysis of cartilage. Following an introduction to nonlinear elasticity, the basic principles for deriving constitutive rules are briefly mentioned and the hyperelastic law used in the nonlinear analysis of cartilage is described.

The linear and nonlinear finite element formulations are derived in detail in Chapter 4. The computer implementation of these formulations within the object-oriented finite element framework of the Scientific Computation Research Center at Rensselaer Polytechnic Institute is also described.

Chapter 5 presents the penetration method, which makes use of experimental data for approximate numerical simulation of tissue contact for both small and large deformation.

The method is validated and small deformation examples on physiological geometries are given in Chapter 6. The validation of the nonlinear finite element formulation is given in Chapter 7 where large deformation examples on physiological geometries are also presented.

Chapter 8 summarizes and evaluates the current work, and proposes directions for future research.

## Chapter 2

### Biphasic Theory of Articular Cartilage

#### 2.1 Introduction

The physics of continua is governed by conservation laws and restrictions imposed by the second law of thermodynamics. In this chapter, after covering briefly the conservation laws and the second law of thermodynamics, we will list the governing equations of biphasic soft tissue and discuss their physical meanings. The chapter concludes with the methods to determine the cartilage material properties.

#### 2.2 Constitutive Equations for Biphasic Mixture

As described briefly in the previous chapter, articular cartilage can be represented as a continuum solid matrix filled with an interstitial fluid. This biphasic structure plays an important role in cartilage function; thus, when modeling cartilage as an engineering material it is crucial to take its biphasic morphology into account.

Generally, two approaches are used to model a porous medium with filling liquid. One approach is to average the governing continuum equations. This is an elaborate process and has been done by Whitaker for porous media [99]. The averaging approach appears to be more appropriate for soil mechanics problems where the solid phase consists of relatively large particles compared to articular cartilage matrix. In soil mechanics, the shape of the solid particles affect the averaging process whereas in cartilage it is hard to define a “shape” for the collagen and proteoglycan molecules. The characteristic lengths involved would not allow the fluid phase to be considered as a uniform medium.

An alternative is to use continuum theories where each medium is treated as a continuum, independent of the particle shape. While the shape of the particles making up the solid matrix will have an effect on the solid phase constitutive equations, it will not affect the general conservation equations.

Deformation of saturated porous media was first presented by Terzaghi [89] in a one dimensional problem, and then extended to 3-D by Biot [12]. Their derivation was based on empirical evidence that the fluid flow in porous media obeys a conduction-type law (Darcy’s law), where the flow is proportional to the pressure gradient. Although in

practice identical to biphasic approach, consolidation theory takes the solid skeleton as the problem domain and does not explicitly mention of the fluid phase as a second phase.

The interstitial fluid, the second phase of the soft tissue, makes up 70-80% of the cartilage volume, and is known to be an important factor in the load bearing mechanism of this tissue. Mow *et al.* [63] first took the fluid phase of cartilage into account when deriving its constitutive equations to form the biphasic theory of soft tissue. They looked at the problem from a continuum mechanics view point and used mixture theory [15, 16, 94] to derive the governing equations and constitutive law. In this approach, the solid and fluid phases are considered separate overlapping continua. The individual phases, and the mixture as a whole, have separate balance equations that, according to principle of mixtures, should all have similar forms. In general mixture theory, mass, momentum, angular momentum and energy transfer from one phase to the other is possible. Specific to soft tissue, the phases are assumed to be immiscible, which simplifies mass balance. The temperatures of each phase are assumed to be the same, so there is no heat exchange between phases, a fact that simplifies energy balance.

Physically, the drag created by the movement of the fluid through the solid matrix gives the tissue its viscoelastic properties. The following equations describe the biphasic theory of soft tissue with the superscripts  $s$  and  $f$  referring to the solid and fluid phases, respectively. The crucial assumption is that both phases of hydrated soft tissue are incompressible, which results in a divergence-free, phase-averaged velocity. This serves as the continuity equation for the biphasic tissue and given as,

$$\cdot (\phi^f \mathbf{v}^f + \phi^s \mathbf{v}^s) = 0, \quad (1)$$

where  $\phi^\alpha$  are the phase volume fractions of the tissue and  $\mathbf{v}^\alpha$  denote the phase velocities. Substituting Eq. (1) into the Clausius-Duhem inequality, and assuming an elastic solid phase and inviscid fluid phase [1], provides the expressions for the solid and fluid phase stresses:

$$\sigma^s = -\phi^s p \mathbf{I} + \sigma^E, \quad (2)$$

$$\sigma^f = -\phi^f p \mathbf{I}, \quad (3)$$

where  $p$  is pressure and  $\sigma^E$  is the elastic stress tensor corresponding to the deformation of the solid phase. Momentum equations for each phase are expressed as,

$$\cdot \sigma^\alpha + \Pi^\alpha = \mathbf{0}, \quad \alpha = s, f, \quad (4)$$

where  $\sigma^\alpha$  is the Cauchy stress tensor and  $\Pi^\alpha$  is the momentum exchange between phases. given by

$$\Pi^s = -\Pi^f = p \phi^s + K(\mathbf{v}^f - \mathbf{v}^s). \quad (5)$$

In the above equation,  $K$  is the diffusive drag coefficient, related to the tissue permeability  $\kappa$  through [53].

$$K = \frac{(\phi^f)^2}{\kappa}. \quad (6)$$

Equation (5) originates directly from the Clausius-Duhem inequality. Note that according to Eq. (5), a momentum transfer from one phase to the other occurs only if the phases have a relative velocity with respect to each other, and/or if the solid phase fraction has a gradient in the tissue. Total stress is defined by adding the solid phase and fluid phase stresses, Eq. (2) and Eq. (3) respectively

$$\sigma^{Tot} = \sigma^s + \sigma^f = -p\mathbf{I} + \sigma^E \quad (7)$$

As seen in Eqs. (2) and (3), the superposed continua approach leads to the rather “unintuitive” result that pressure is shared between the phases. Physically, what the solid phase experiences is the sum of the elastic stress and the pressure, i.e. the total stress. Since hydrostatic pressure does not contribute to the failure of an elastic material, elastic stress stands out as the most important quantity in cartilage mechanics. In fact, elastic stress is attributed a special importance also in soil mechanics where it is called *effective stress* [66].

In the finite element method, depending on the formulation chosen, the above equations need to be satisfied either exactly or in integral sense.

### 2.3 Cartilage Material Properties

The determination of cartilage material properties has been a main focus in cartilage research, and remains an active research area. For a mechanical analysis, the material properties of interest are the elastic material properties and the tissue permeability. For electromechanical models of cartilage [52] it is also necessary to determine its electrochemical properties. The solid phase of the cartilage is usually modeled as an elastic material, although some investigators are assessing the need to include the intrinsic viscoelastic behavior of the solid phase to better capture the short term behavior [46, 86]. Under large deformation, cartilage, soft tissues such as cartilage are often modeled as hyperelastic, as discussed in detail in Chapter 3.

Early attempts mostly aimed at determining the Young's modulus of the cartilage at equilibrium. These involve usually an indentation experiment where the Young's modulus is calculated from the equilibrium deformation using the force, displacement and available analytical solutions to the experimental configuration (See [62] for a review). Similar analyses are still performed with more sophisticated experimentation techniques [92].

Once the elastic properties of the tissue are known the permeability can be determined using optimization techniques. Tabolt [88] describes a methodology where the analytical solutions for confined and unconfined compression tests are used to determine material properties as functions (polynomials of first or second order) of measurable experimental quantities such as the surface stress. This response-surface method less effective if the polynomial coefficients for both the elastic properties and permeability are determined simultaneously.

A simultaneous estimation of Young's modulus, Poisson's ratio and permeability is more complex because it constitutes an inverse problem. Mow *et al.* determine these three parameters by inverting numerically the semi-analytical solution of the biphasic indentation problem with a similarity principle. Other researchers have used this approach since the indentation test is relatively easy to apply [9, 35].

The above methods assume the tissue to be homogeneous and return one numerical value for each material parameter. If there is a variation in the material properties the inverse problem is solved numerically. In this approach a finite element or finite difference scheme is adapted and the material properties are determined at each node. Inverse problems, by their nature, are ill-conditioned, nevertheless examples of numerical methods to solve inverse problems with elastic [61] and biphasic [68, 75] laws exist in the biomechanics literature.

Depth-dependent inhomogeneous elastic properties can be determined through microscopy-based experimentation, too. This is usually accomplished by tracking the chondrocytes through labeling their nuclei fluorescently [72] or using confocal microscopy [36]. The locations of sparsely distributed chondrocytes before and after deformation provide information about the strain levels at different depths.

In this work, uniform material properties (whether linear or nonlinear) are taken from the literature, although the analysis program has the capability of handling spatially varying material properties.

## Chapter 3

### Nonlinear Elasticity

#### 3.1 Introduction

This chapter provides some background knowledge on nonlinear elasticity that will be necessary to understand the nonlinear finite element formulation presented in the next chapter. General constitutive axioms and hyperelasticity of the solid phase are also presented.

#### 3.2 Nonlinear Elasticity

Elasticity has a firm mathematical basis. It can be approached from a mathematical point of view involving functional analysis and geometry as well as from an engineering point of view. Both approaches eventually lead to the same outcome; however, in this thesis, the engineering point of view will be used.

Consider a material point having a position vector  $\mathbf{X}$  with respect to a chosen coordinate system, that as of finite displacement moves to a new location. Denoting the new coordinate of the material point as  $\mathbf{x}$ , the motion can be expressed as a mapping,  $\chi$ , of the initial (material) coordinates  $\mathbf{X}$  to the current (spatial) coordinates  $\mathbf{x}$ :

$$\mathbf{x} = \chi(\mathbf{X}, t). \quad (8)$$

In finite deformation analysis, the choice of a coordinate system is crucial. In general, any quantity can be described either in terms of the initial configuration (i.e. with respect to  $\mathbf{X}$ ) or in a deformed state (i.e. with respect to  $\mathbf{x}$ ). The former is called a *material* or *Lagrangian* description while the latter is termed a *spatial* or *Eulerian* description.

The displacement that material point  $\mathbf{X}$  undergoes during the motion is given as

$$\mathbf{u} = \mathbf{x} - \mathbf{X}. \quad (9)$$

The displacement itself does not give any information about the deformation of the material. Insight can be gained, however, by taking a line segment  $d\mathbf{X}$  in the material and observing it deform to become  $d\mathbf{x}$  after the motion. This information is provided by the deformation gradient  $\mathbf{F}$ , which is the key quantity in nonlinear elasticity, and is defined mathematically as follows:

$$\mathbf{F} = \frac{\partial \mathbf{x}}{\partial \mathbf{X}} \quad (10)$$

The subscript ‘ $o$ ’ on the gradient operator implies that the operation is performed with respect to the initial coordinates. The right hand side of the equation expresses the change in the relative position of two neighboring particles before and after deformation. Consequently, this quantity is central to the description of deformation. Note that a singular  $\mathbf{F}$  would indicate a finite length line segment  $d\mathbf{X}$  deforming to zero length, which is not possible physically. Hence  $\mathbf{F}$  is always nonsingular.

The well-known polar decomposition theorem says that a nonsingular tensor, such as  $\mathbf{F}$  can be multiplicatively decomposed into two second order tensors, one proper orthogonal and the other symmetric and positive definite:

$$\mathbf{F} = \mathbf{R}\mathbf{U} = \mathbf{V}\mathbf{R}. \quad (11)$$

In this equation  $\mathbf{R}$  is the orthogonal matrix and,  $\mathbf{U}$  and  $\mathbf{V}$  denote the symmetric matrices. From a mechanics point of view, equation implies that a motion can be decomposed into a rigid body motion and a pure stretch. Some tensor quantities are referred to as either material, spatial or mixed depending on which coordinates they operate.  $\mathbf{U}$  and  $\mathbf{V}$  are called *right (material)* and *left (spatial) stretch tensors*, respectively. Note that  $\mathbf{U}$  applies a pure stretch in the material configuration. Geometrically,  $\mathbf{U}$  retains the tangent space of the body and hence operates in the same coordinate system. Then  $\mathbf{R}$  rigidly rotates the configuration to current coordinates changing the tangent space. The order of the operations is reversed for the right hand side equality of Eq. (11).

Suppose one wants to calculate the change in length in  $d\mathbf{X}$  after deformation. Using (10)

$$d\mathbf{x} \cdot d\mathbf{x} = d\mathbf{X} \cdot \mathbf{F}^T \mathbf{F} d\mathbf{X}. \quad (12)$$

At this point, let us define the *right Cauchy-Green deformation tensor*:

$$\mathbf{C} = \mathbf{F}^T \mathbf{F}. \quad (13)$$

From Eq. (12) we see that  $\mathbf{C}$  operates on material element  $d\mathbf{X}$  and hence is a material (or Lagrangian) tensor. Similarly,

$$d\mathbf{x} \cdot \mathbf{b}^{-1} d\mathbf{x} = d\mathbf{X} \cdot d\mathbf{X}, \quad (14)$$

where  $\mathbf{b}$  is the *left Cauchy-Green* (or *Finger*) deformation tensor defined as

$$\mathbf{b} = \mathbf{F} \mathbf{F}^T. \quad (15)$$

Since it operates on the spatial element  $dx$ ,  $\mathbf{b}$  is a spatial tensor. Material tensors are mainly used in this work because they have the useful property of being invariant with respect to orthogonal transformation. This is easily observed in case of  $\mathbf{C}$  if Eq. (11) is substituted into Eq. (12):

$$dx \, dx = dX \, (\mathbf{R}\mathbf{U})^T (\mathbf{R}\mathbf{U}) dX = dX \, \mathbf{U}^T \mathbf{R}^T \mathbf{R} \mathbf{U} dX = dX \, \mathbf{U}^T \mathbf{U} dX, \quad (16)$$

since  $\mathbf{R}^T \mathbf{R} = \mathbf{I}$  for an orthogonal tensor. This shows that  $\mathbf{C}$  is independent of the rigid body motion component,  $\mathbf{R}$ , of  $\mathbf{F}$ .

The *Green* (or *Lagrangian*) *strain tensor*, defined as

$$\mathbf{E} = \frac{1}{2}(\mathbf{C} - \mathbf{I}), \quad (17)$$

is convenient to use since it is also a material tensor. Note that it can be written as

$$\mathbf{E} = \frac{1}{2}(\mathbf{U}^T \mathbf{U} - \mathbf{I}). \quad (18)$$

The corresponding spatial strain tensor, called *Eulerian* (or *Almansi*), is defined as

$$\mathbf{e} = \frac{1}{2}(\mathbf{I} - \mathbf{b}^{-1}) = \frac{1}{2}(\mathbf{I} - \mathbf{V}^{-2}). \quad (19)$$

Since a strain measure should be zero whenever  $\mathbf{U} = \mathbf{V} = \mathbf{I}$ , other strain tensors can be defined in elasticity. The following generalization for material strain tensors is possible [65]:

$$\begin{array}{ll} \frac{1}{m}(\mathbf{U}^m - \mathbf{I}) & m \neq 0 \\ \ln \mathbf{U} & m = 0 \end{array} \quad (20)$$

The case when  $m = 0$  is known as *Hencky strain* whereas when  $m = 1$  the tensor is called *Biot strain*; both measures have their uses in elasticity. The Green strain tensor, which corresponds to the case when  $m$  is equal to 2, is used in this research.

The deformation gradient  $\mathbf{F}$  (and its inverse) are used to move between Lagrangian and Eulerian descriptions when expressing quantities. Also, the volume and area after deformation can be related to the initial volume and area using  $\mathbf{F}$ . Denoting the current values with lower case and initial values with upper case letters, the following relations are given for the current volume  $v$  and area  $\mathbf{a}$ :

$$dv = J dV, \quad (21)$$

$$d\mathbf{a} = J \mathbf{F}^{-T} d\mathbf{A}, \quad (22)$$

where  $J$  denotes the determinant of  $\mathbf{F}$ . In solid mechanics, it is usually possible to follow particles, hence the Lagrangian description is convenient to use. However, Cauchy stress, by definition, is an Eulerian quantity, since Cauchy's theorem proving the existence of a second order tensor  $\boldsymbol{\sigma}$ , which is the Cauchy stress tensor, refers to a traction and area in the deformed configuration [54]. In the deformed configuration, we can relate the force acting on a differential area to the Cauchy stress tensor as

$$d\mathbf{h} = \boldsymbol{\sigma} d\mathbf{a}, \quad (23)$$

where  $d\mathbf{h}$  is the force acting on the differential area  $d\mathbf{a}$ . It is possible to shift the area vector  $d\mathbf{a}$  to its initial configuration by substituting Eq. (22) into Eq. (23):

$$d\mathbf{h} = J \boldsymbol{\sigma} \mathbf{F}^{-T} d\mathbf{A} = \mathbf{P} d\mathbf{A}, \quad (24)$$

where  $\mathbf{P}$  is the *first Piola-Kirchhoff* (or *nominal*) *stress tensor* defined as

$$\mathbf{P} = J \boldsymbol{\sigma} \mathbf{F}^{-T}. \quad (25)$$

Note that,  $\mathbf{P}$  is a mixed (or two-point) tensor that shifts the area element from its material configuration to its current configuration.

The force vector  $d\mathbf{h}$  can be related to the initial configuration  $d\mathbf{H}$  in a similar manner. Noting that

$$d\mathbf{h} = \mathbf{F} d\mathbf{H}. \quad (26)$$

Eq. (24) can be rearranged to give

$$d\mathbf{H} = J \mathbf{F}^{-1} \boldsymbol{\sigma} \mathbf{F}^{-T} d\mathbf{A} = \mathbf{S} d\mathbf{A}, \quad (27)$$

where  $\mathbf{S}$  is the *second Piola-Kirchhoff* (or *conjugate*) *stress tensor*, defined as

$$\mathbf{S} = J \mathbf{F}^{-1} \boldsymbol{\sigma} \mathbf{F}^{-T}. \quad (28)$$

Since  $\mathbf{S}$  operates in the initial configuration, it is a material tensor.

In the literature, both Piola-Kirchhoff stress tensors are usually derived using the principle of virtual work. Multiplying Eq. (4) by a virtual velocity, say  $\boldsymbol{\nu}$ , and integrating it over the problem domain yields

$$W = (\boldsymbol{\sigma} + \boldsymbol{\Pi}) \boldsymbol{\nu} = 0, \quad (29)$$

where  $W$  denotes the virtual power, which is a scalar quantity. Using the divergence theorem, Eq. (29) can be put into the following form:

$$\mathbf{n} \cdot \boldsymbol{\sigma} \mathbf{v} d + \boldsymbol{\sigma} : \mathbf{v} d + \Pi \mathbf{v} d = 0. \quad (30)$$

Note that the gradients and the integral domains are current quantities. The second term in this equation is the strain power and can be expressed as contractions of different pairs. The first and second Piola-Kirchhoff stress tensors can be defined, using this term and applying similar manipulation as in Eqs. (24) and (27), as

$$\boldsymbol{\sigma} : \mathbf{v} d = \mathbf{P} : \dot{\mathbf{F}} d_0 = \mathbf{S} : \dot{\mathbf{E}} d_0, \quad (31)$$

where  $\dot{\mathbf{F}} = \dot{\mathbf{v}}$  and  $\dot{\mathbf{E}}$  indicate the time derivatives of  $\mathbf{F}$  and  $\mathbf{E}$ , respectively.  $\mathbf{P}$  and  $\dot{\mathbf{F}}$ , and  $\mathbf{S}$  and  $\dot{\mathbf{E}}$  are said to be *conjugate pairs* since their contraction gives the same scalar quantity. It should be noted that the right two integrals are evaluated on the initial domain.

The two Piola-Kirchhoff stress tensors do not have a physical meaning. They are used to simplify problem formulations in elasticity and can be easily converted to a Cauchy stress tensor that has a physical meaning.

### 3.3 Constitutive Modeling and Hyperelasticity

The basic laws of motion, namely conservation of mass, momentum, angular momentum and energy, and second law of thermodynamics are valid for all types medium independent of their internal structure and constituents. The equations that reflect the effects of these structural differences on the mechanics of the medium are called constitutive equations. Since basic laws of motion create more unknowns than equations, constitutive equations are needed to make problems solvable.

The following axioms are fundamental in formulating constitutive equations of a medium [28, 31]:

- 1) **Axiom of causality:** Motion and temperature are self-evident observable phenomena. Once a set of independent variables is selected which are derived from motion and temperature, the remaining quantities are the “causes” or the dependent variables. This axiom is aimed to give guidance on how to pick the independent constitutive variables.

**2) Axiom of determinism:** The value that the constitutive equations take at a point  $\mathbf{X}$  of a body depends on the motion and temperature history of all the points in the body. This axiom basically excludes any effects due to the points outside the body or due to future events.

**3) Axiom of equipresence:** Initially, all constitutive equations should be assumed to depend on the same list of independent variables. Simplifications during modeling might cause some variables to be eliminated from constitutive equations, however, until this is the case we can not be prejudiced against any class of variables.

**4) Axiom of Objectivity (or Material Frame Indifference):** Constitutive equations should be form-independent with respect to rigid motions of the spatial reference frame. To understand this axiom, it is essential to know the objectivity concept. What is commonly referred to as ‘objectivity’ in the literature is actually Eulerian objectivity and can be defined as follows:

Given an orthogonal transformation  $\mathbf{Q}$  that rotates the current reference frame to a new one (denoted by ‘\*’), a scalar  $S$ , a vector  $\mathbf{v}$ , and a second order tensor  $\mathbf{T}$  are objective if they transform as

$$S^* = S \quad \mathbf{v}^* = \mathbf{Q}\mathbf{v} \quad \mathbf{T}^* = \mathbf{Q}^T\mathbf{T}\mathbf{Q}. \quad (32)$$

Cauchy stress  $\boldsymbol{\sigma}$ , along with other Eulerian quantities defined in the previous section, is objective. Constitutive equations describe the Cauchy stress tensor as a function of motion.

The axiom of objectivity requires that a transformation of a spatial point  $\mathbf{x}$  to a new one  $\mathbf{x}'$  using an orthogonal transform  $\mathbf{Q}(t)$  and a translation vector  $\mathbf{b}(t)$  in the form

$$\mathbf{x}' = \mathbf{Q}(t)\mathbf{x} + \mathbf{b}(t), \quad (33)$$

should properly induce the corresponding transformation in the Cauchy stress tensor, i.e.,

$$\boldsymbol{\sigma} = f(\mathbf{x}(t), \mathbf{X}) \quad \boldsymbol{\sigma}^* = f(\mathbf{Q}(t)\mathbf{x}(t) + \mathbf{b}(t), \mathbf{X}), \quad (34)$$

where  $f(\dots)$  denotes the constitutive equation relating motion to stress.

For completeness, we define also the Lagrangian objectivity here. Using the same notation as in Eq. (32), a scalar  $S$ , a vector  $\mathbf{v}$ , and a second order tensor  $\mathbf{T}$  are objective if they are invariant with respect to orthogonal transformation  $\mathbf{Q}$ , i.e.

$$S^* = S \quad \mathbf{v}^* = \mathbf{v} \quad \mathbf{T}^* = \mathbf{T}, \quad (35)$$

Lagrangian quantities such as  $\mathbf{C}$ ,  $\mathbf{U}$  and  $S$  are objective in Lagrangian sense but obviously not in a classical (Eulerian) sense. Still, such quantities are useful to establish constitutive equations, due to their invariance characteristics.

**5) Axiom of Material Invariance:** Constitutive equations should be form-independent with respect to orthogonal transformation of the material frame corresponding to the material symmetries existing in the medium. This axiom says that the constitutive equations should be consistent with various forms of isotropy that might exist in the materials.

The set of all orthogonal transformations that describe material symmetries is called the *symmetry group* of the material. Mathematically, given a deformation gradient  $\mathbf{F}$  and transformation  $\mathbf{K}$  from the symmetry group of the material, the constitutive response function  $f$  should fulfill

$$f(\mathbf{KF}, \mathbf{X}) = f(\mathbf{F}, \mathbf{X}). \quad (36)$$

**6) Axiom of Neighborhood (or Local Action):** The values of constitutive variables at distant material points from  $\mathbf{X}$  do not have a significant effect on the values of constitutive variables at  $\mathbf{X}$ . This principle is usually put into mathematical terms in the following way: If two given motions  $\mathbf{x}(t)$  and  $\bar{\mathbf{x}}(t)$  coincide in the neighborhood  $N(\mathbf{X})$  of a material point  $\mathbf{X}$ , then the constitutive function takes equal values at this point for both of the motions, i.e.,

$$W(\mathbf{x}(t), \mathbf{X}) = W(\bar{\mathbf{x}}(t), \mathbf{X}), \quad (37)$$

where  $W$  denotes the constitutive function of the medium.

**7) Axiom of Memory:** The values of constitutive variables at distant past time do not have a significant effect on the values of the constitutive functions at the current time. There is no unique way of putting this principle into mathematical terms. The axiom essentially says that events in the nearer past have a stronger effect on the material behavior.

**8) Axiom of Admissibility:** Constitutive equations should be consistent with conservation laws of continuum mechanics and the second law of thermodynamics.

The above axioms are used as guidelines to establishing constitutive equations. The above list should not be considered as unique. Depending on the material or situation some of these items might become irrelevant or take different mathematical forms.

The concept of an elastic material is almost intuitive to many scientists and engineers. Still, being familiar with the deformation gradient  $\mathbf{F}$  gives us the opportunity to define an elastic material more formally. A material is said to be *elastic* when stress and entropy density at a material point  $\mathbf{X}$  at time  $t$  depend only on the values of deformation gradient  $\mathbf{F}$ , temperature at that point and time, and are not related to thermo-mechanical history of the point. Our analyses are all isothermal such that temperature is not taken into consideration when writing the constitutive equations.

Hyperelasticity is a type of elasticity where the stress at any point can be derived from the deformation gradient and from an energy function. A suitable function can be defined using Eq. (31). The integrand of the last equality of Eq. (31) can be defined as stress power per unit (initial) volume, and is in general not an exact differential. When the integrand is an exact differential, then the material is said to be *hyperelastic* (or *Green elastic*) and we are allowed to write

$$\dot{\Psi} = \mathbf{S}^E : \dot{\mathbf{E}} = \frac{\partial \Psi}{\partial \mathbf{E}} : \dot{\mathbf{E}}, \quad (38)$$

where  $\Psi$  is the strain energy function which is equal to the Helmholtz free energy function multiplied with the initial density  $\rho_0$  for a hyperelastic material. The second Piola-Kirchhoff stress tensor is then expressed as

$$\mathbf{S}^E = \frac{\partial \Psi}{\partial \mathbf{E}} = 2 \frac{\partial \Psi}{\partial \mathbf{C}}. \quad (39)$$

where Eq. (17) is used, and the superscript ‘E’ is added to imply that the quantity originates from elastic deformation. Using Eq. (28) the Cauchy stress,  $\boldsymbol{\sigma}^E$ , can be expressed as

$$\boldsymbol{\sigma}^E = 2J^{-1} \mathbf{F} \frac{\partial \Psi}{\partial \mathbf{C}} \mathbf{F}^T, \quad (40)$$

where  $J$  is the determinant of  $\mathbf{F}$ .

Different hyperelastic laws have been used in engineering to model a wide variety of materials. Once a form for  $\psi$  is selected, the determination of the related coefficients is an experimental issue. Aside from certain conditions that arise from continuum mechanics principles, there are some other intuitive principles that a hyperelastic material has to fulfill. They are mentioned in detail elsewhere [59, 93]. These rules give guidelines about the direction of stretch and tension. (For example, if everything else is fixed, a material should elongate along direction of a positive traction.) These guidelines normally have a limited range of validity and should be used with caution.

Hyperelastic material laws are used often in biomechanics. In addition to articular cartilage, other soft tissues in the human body has been treated as hyperelastic, both in experimental studies, where the aim was to determine the material properties, and numerical studies, where their mechanical behavior is to be simulated. Recent examples include arteries [42, 74, 77], annulus fibrosis [48], brain [60, 71], heart [61], temporomandibular joint disc [19], buttocks [23], lung [51] and blood-perfused skeletal muscle [95]. Strain energy functions inspired from Fung's [34] exponential form have been popular in these studies. Since soft tissues generally owe their structural integrity to the presence of collagen fibers, exponential forms that are based on the mechanical behavior of those fibers seems to fit well with experimental data for many tissues.

Recently, the bimodular nature of cartilage, i.e. its different behavior in tension and compression has been taken into account. This is usually achieved by proposing a strain energy function that is continuously differentiable but only piecewise twice continuously differentiable at deformation states that reflect a transition from tension to compression [22]. Soltz *et al.* [79] proposed an orthotropic model that is valid for small deformation and tested it in confined and unconfined compression. Numerically, the different behavior in tension and compression constitutes another type of nonlinearity in the problem even if the material behaves piecewise linear.

The free energy function,  $\psi$ , a scalar quantity, should be invariant under rigid body transformation. Hence it is convenient to express  $\psi$  as a function of  $\mathbf{C}$  (or  $\mathbf{E}$ ) which itself is invariant under rigid body motion. For an isotropic tissue, in view of Eq. (39), the dependence on  $\mathbf{C}$  should be through its matrix invariants. In this research we use the following form proposed by Holmes [40] to model articular cartilage:

$$\psi = \frac{e^{\alpha_1(I_1-3) + \alpha_2(I_2-3)}}{I_3}. \quad (41)$$

Here  $I_1$ ,  $I_2$  and  $I_3$  denote the principal matrix invariants of  $\mathbf{C}$  and,  $\alpha_0$ ,  $\alpha_1$ ,  $\alpha_2$  and  $\alpha_3$  are material parameters. The strain energy function for the fluid phase is a constant independent of the deformation because of the inviscid assumption. At equilibrium (i.e. when  $I_1 = I_2 = 3$  and  $I_3 = 1$ ) there is no stress which, in view of Eq. (40), implies  $\alpha_0 = \alpha_1 + 2\alpha_2$ . Note also that as stretches go to 0 or  $\infty$ , i.e. in case of extreme compression or stretching,  $I_3$  approaches 0 or  $\infty$ , respectively, such that Eq. (41) gives an infinitely large energy. The derivation of  $\mathbf{S}^E$  corresponding to the above strain energy function is described in Appendix A.

Many soft tissues, including articular cartilage, are sometimes modeled as transversely isotropic. For a transversely isotropic solid,  $\mathbf{C}$  has five matrix invariants, the two extra ones originating from the preferred direction of the transverse isotropy [13].

Large deformation causes the tissue permeability to change. Beside hyperelasticity, this strain-dependent permeability phenomenon is also incorporated into the current work. For cartilage the following relation is proposed to express permeability as a function of  $I_3$ :

$$\kappa = \kappa_0 \frac{\phi_0^s \phi^s}{\phi_0^f \phi^f} e^{M(I_3 - 1)/2}, \quad (42)$$

where  $L$  and  $M$  are constants, and subscript ‘0’ refers to quantities in the undeformed configuration.

The nonlinear finite element formulation for the biphasic soft tissue with hyperelastic solid phase with strain-dependent permeability is derived in the coming chapter.

## Chapter 4

### Finite Element Formulation

#### 4.1 Introduction

In this chapter, the linear and nonlinear versions of velocity-pressure ( $v$ - $p$ ) finite element formulation (corresponding to linear elastic and hyperelastic materials, respectively) are described in detail. Related issues such as time integration techniques and solution methods for nonlinear equations are briefly reviewed. The displacement-pressure ( $u$ - $p$ ) form of the nonlinear formulation is introduced. The implementation of both linear and nonlinear versions in the SCOREC finite element framework is also discussed in this chapter.

#### 4.2 Velocity-Pressure Formulation

A formulation where solid velocity and pressure are the main variables have been derived and used for a number of biphasic (or poroelastic) problems both in civil engineering and biomechanics. Almeida [1] points out the computational advantage of the  $v$ - $p$  formulation over other types of formulations due to the relatively low number of degrees of freedom involved. Especially for 3-D problems, its advantage is substantial and hence we preferred to work with the  $v$ - $p$  formulation in our research. To solve the nonlinear problems on physiological geometries, a ( $u$ - $p$ ) formulation is also considered, and is described in Section 4.6.3.

Simon *et al.* [76] used a linear  $u$ - $w$  formulation ( $w$  here referring to the relative velocity) to analyze the intervertebral disk while Wu *et al.* [100] formulated a mixed  $u$ - $w$ - $p$  finite element method for the same problem. Oomens and coworkers [67] applied a 2-D nonlinear  $v$ - $p$  analysis to study skin under confined compression. A similar study has been performed on the heart left ventricle using an anisotropic quasi-linear viscoelastic law for the solid phase [47]. A  $u$ - $p$  method has also been used to study lung parenchyma under finite deformation, where the fluid phase corresponded to the air [51]. Articular cartilage has been studied with a  $u$ - $p$  formulation by Wayne *et al.* [98] in experimental configurations.

#### 4.3 Weak Form

In the  $v$ - $p$  approach, quantities related to the fluid phase velocity are eliminated in favor of pressure and fluid flux, and the momentum balance is expressed in terms of total

stress. To eliminate the fluid velocity, Eqs. (3) and (5) are first substituted into Eq. (4) to express the linear momentum equation of the fluid phase in terms of the pressure gradient,

$$\phi^f(\mathbf{v}^f - \mathbf{v}^s) = -\kappa p. \quad (43)$$

This expression is solved for  $\phi^f \mathbf{v}^f$  and substituted into the continuity equation, Eq. (1). Noting that  $\phi^s + \phi^f = 1$  for a saturated mixture gives,

$$\text{div}(\mathbf{v}^s - \kappa p) = 0. \quad (44)$$

Finally, the linear momentum balance for the solid phase and fluid phase, Eq. (4), are added to obtain,

$$\text{div}(\boldsymbol{\sigma}^E - p\mathbf{I}) = \mathbf{0}. \quad (45)$$

Equations (44) and (45) constitute the modified governing equations of the biphasic continuum used for the  $v$ - $p$  finite element formulation. The corresponding fluid flux boundary condition is expressed as,

$$\bar{Q} = \phi^f(\mathbf{v}^f - \mathbf{v}^s) \cdot \mathbf{n} = -\kappa p \cdot \mathbf{n} \quad \text{on } \mathcal{Q}, \quad (46)$$

where  $\bar{Q}$  is the prescribed fluid flux at the corresponding domain boundary. The remaining boundary conditions are prescribed displacement (or velocity),

$$\mathbf{u}^s = \bar{\mathbf{u}}^s \quad \text{on } \mathcal{u}, \quad (47)$$

prescribed pressure,

$$p = \bar{p} \quad \text{on } \mathcal{p}, \quad (48)$$

and prescribed total traction, corresponding to the sum of  $\boldsymbol{\sigma}^s$  and  $\boldsymbol{\sigma}^f$ ,

$$\boldsymbol{\sigma}^{Tot} \cdot \mathbf{n} = \bar{\mathbf{t}} \quad \text{on } \mathcal{t}. \quad (49)$$

Note that  $\mathcal{p}$  and  $\mathcal{Q}$  denote boundaries where Dirichlet and Neumann boundary conditions, respectively, are set for  $p$ . Similarly,  $\mathcal{u}$  and  $\mathcal{t}$  constitute the Dirichlet-Neumann boundary condition pair for  $\mathbf{u}^s$ . For a given quantity (either  $p$  or  $\mathbf{u}^s$ ) the Dirichlet and Neumann boundary conditions complement the boundary without overlapping (i.e., using set notation,  $\mathcal{u} \cap \mathcal{t} = \emptyset$  and  $\mathcal{u} \cup \mathcal{t} = \partial \Omega$ ). On the other hand, boundaries related to different quantities might coincide, totally or partially; for example, it is possible to specify the pressure and the total traction on the same part of the boundary such that solid phase traction takes a desired value.

Interelement continuity is required for both solid velocity and pressure in our formulation. In mathematical terms, they belong to the space of functions which are integrable, have integrable first derivatives, and satisfy the Dirichlet boundary conditions. Corresponding weighting functions have similar integrability, but satisfy the homogeneous form of the Dirichlet boundary conditions. We use a Taylor-Hood element that has quadratic and linear interpolations for solid velocity and pressure, respectively, because equal order interpolation does not satisfy the required stability condition for this mixed formulation at  $t = 0^+$  [64].

For the remainder of the finite element development, the superscript ‘s’ will be dropped from velocity and displacement terms since fluid velocity and displacement no longer exist as problem variables. In the weighted residual method, Eqs. (44), (45), (46) and (49) are multiplied by arbitrary weighting functions,  $\mathbf{w}$ ,  $q$ ,  $s$  and  $r$ , respectively, integrated over the appropriate domains and summed to give

$$\begin{aligned} & \{ \mathbf{w} \cdot [ \cdot (\boldsymbol{\sigma}^E - \mathbf{p}\mathbf{I}) ] + q [ \cdot (\mathbf{v} - \kappa \mathbf{p}) ] \} d \\ & + \int_V s \cdot (\bar{\mathbf{t}} - \boldsymbol{\sigma}^{Tot} \cdot \mathbf{n}) d + \int_V r (\bar{Q} + \kappa \mathbf{p} \cdot \mathbf{n}) d = 0 \end{aligned} \quad (50)$$

The order of differentiation in Eq. (50) is reduced by using theorems of integral calculus. Using the divergence theorem, the first term in Eq. (50) can be written as

$$\begin{aligned} \int_V \mathbf{w} \cdot ( \cdot \boldsymbol{\sigma}^E ) d &= \int_V \cdot (\boldsymbol{\sigma}^E \cdot \mathbf{w}) d - \int_V \mathbf{w} : \boldsymbol{\sigma}^E d \\ &= \int_V \mathbf{w} \cdot (\boldsymbol{\sigma}^E \cdot \mathbf{n}) d - \int_V \mathbf{w} : \boldsymbol{\sigma}^E d \end{aligned} \quad (51)$$

where ‘:’ indicates double contraction. To reduce the order of differentiation further, the term involving the Laplacian of the pressure is manipulated such that

$$\int_V q \cdot (\kappa \mathbf{p}) d = \int_V q (\kappa \mathbf{p}) \cdot \mathbf{n} d - \int_V (\kappa \mathbf{p}) \cdot \mathbf{q} d \quad (52)$$

Also, the term involving the pressure gradient can be written, for simplification and to maintain symmetry once the function spaces are chosen, as

$$\int_V \mathbf{w} \cdot \mathbf{p} d = \int_V \mathbf{p} \mathbf{w} \cdot \mathbf{n} d - \int_V \mathbf{p} \cdot \mathbf{w} d \quad (53)$$

Substituting Eqs. (51),(52) and(53) into Eq. (50) results in the following expression:

$$\begin{aligned}
& \int_{\tau} \mathbf{w} \cdot (\boldsymbol{\sigma}^E \cdot \mathbf{n}) d - \int_{\tau} \mathbf{w} : \boldsymbol{\sigma}^E d - \int_{\tau} p \mathbf{w} \cdot \mathbf{n} d + \int_{\tau} p \cdot \mathbf{w} d \\
& + \int_{\varrho} q \cdot \mathbf{v} d - \int_{\varrho} q(\kappa p) \cdot \mathbf{n} d + \int_{\varrho} (\kappa p) \cdot q d \quad . \quad (54) \\
& + \int_{\tau} \mathbf{s} \cdot \bar{\mathbf{t}} d - \int_{\tau} \mathbf{s} \cdot (\boldsymbol{\sigma}^{Tot} \cdot \mathbf{n}) d + \int_{\varrho} r \bar{Q} d + \int_{\varrho} r \kappa p \cdot \mathbf{n} d = 0
\end{aligned}$$

As commonly done in finite element analysis, we use the Galerkin approach, and thus set  $\mathbf{w} = \mathbf{s}$  and  $q = r$  to simplify the formulation. By doing so, the sixth and the last terms in Eq. (54) cancel each other. We also note from the definition of total traction that,

$$\int_{\tau} \mathbf{w} \cdot (\boldsymbol{\sigma}^{Tot} \cdot \mathbf{n}) d = \int_{\tau} \mathbf{w} \cdot (\boldsymbol{\sigma}^E \cdot \mathbf{n}) d - \int_{\tau} p \mathbf{w} \cdot \mathbf{n} d \quad , \quad (55)$$

which causes the first, third and ninth terms to vanish. With these simplifications the weak form becomes

$$\begin{aligned}
& \left\{ \int_{\tau} \mathbf{w} : \boldsymbol{\sigma}^E - \int_{\varrho} q \cdot \mathbf{v} - \int_{\tau} p \cdot \mathbf{w} - \int_{\varrho} \kappa (p \cdot q) \right\} d \\
& = \int_{\tau} \mathbf{w} \cdot \bar{\mathbf{t}} d + \int_{\varrho} q \bar{Q} d \quad (56)
\end{aligned}$$

The derivation thus far has been general and does not make any assumptions about the solid material law. As a result, Eq. (56) is valid for a wide variety of materials. In the coming sections, the above weak form will be processed separately for cases where the solid phase is a linear or nonlinear elastic material.

#### 4.4 Linear Formulation

For small deformation, the solid phase of the cartilage can be approximated with a linear elastic material, for which the constitutive law can be written as,

$$\boldsymbol{\sigma}^E = \mathbf{C} \boldsymbol{\varepsilon} \quad , \quad (57)$$

where  $\mathbf{C}$  is the fourth-order material property tensor and  $\boldsymbol{\varepsilon}$  is the small strain tensor defined as the symmetric part of the gradient of solid displacement,

$$\boldsymbol{\varepsilon} = \frac{1}{2} \left( \mathbf{u} + (\mathbf{u})^T \right) = {}^{sym} \mathbf{u} \quad . \quad (58)$$

Inserting these into the weak form, Eq. (56), gives

$$\begin{aligned}
\{ (\mathbf{w})^T : \mathbf{C} : \text{sym} \mathbf{u} - q \cdot \mathbf{v} - p \cdot \mathbf{w} - \kappa (p \cdot q) \} d \\
= \mathbf{w} \cdot \bar{\mathbf{t}} d + q \bar{Q} d
\end{aligned} \tag{59}$$

Solid velocity  $\mathbf{v}$  should not be viewed as an additional unknown in the problem, as it is the time derivative of the solid displacement  $\mathbf{u}$ . For now we keep both quantities in the formulation.

Next, the problem domain is subdivided into elements, and the primary unknowns, pressure, solid velocity and displacement, are interpolated with a finite-dimensional function space and degrees of freedom associated with each node. In matrix form, those quantities in element ‘ $e$ ’ are expressed as

$$\mathbf{v}_e = N_e^v \mathbf{v}_e^n \quad \mathbf{u}_e = N_e^u \mathbf{u}_e^n \quad p_e = N_e^p p_e^n, \tag{60}$$

where  $N_e^v$ ,  $N_e^p$  denote the matrices containing the shape functions of velocity and pressure, respectively. The column vectors  $\mathbf{v}_e^n$ ,  $\mathbf{u}_e^n$ , and  $p_e^n$  contain the degrees of freedom. The weighting functions are interpolated using the same shape functions, a characteristic of Galerkin formulations (or sometimes called Bubnov-Galerkin to distinguish it from Petrov-Galerkin where the trial and test spaces are different)

$$\mathbf{w}_e = N_e^v \mathbf{w}_e^n \quad q_e = N_e^p q_e^n. \tag{61}$$

The arbitrary nature of the weighting functions is guaranteed by the column vectors  $\mathbf{w}_e^n$  and  $q_e^n$ , that have arbitrary degrees of freedom.

The weak form can then be written as a sum of contributions from each element. At this point it is convenient to express strain as a column vector and the material property tensor as a matrix. It is also necessary to put gradient, symmetric gradient and divergence operators into matrix form. We therefore define the following operators:

$$L_{div} = \begin{bmatrix} \frac{\partial}{\partial x} & \frac{\partial}{\partial y} & \frac{\partial}{\partial z} \end{bmatrix} \quad L^{sca} = \begin{bmatrix} \frac{\partial}{\partial x} \\ \frac{\partial}{\partial y} \\ \frac{\partial}{\partial z} \end{bmatrix} \quad L^{sym} = \begin{bmatrix} \frac{\partial}{\partial x} & 0 & 0 \\ 0 & \frac{\partial}{\partial y} & 0 \\ 0 & 0 & \frac{\partial}{\partial z} \\ \frac{\partial}{\partial y} & \frac{\partial}{\partial x} & 0 \\ \frac{\partial}{\partial z} & 0 & \frac{\partial}{\partial x} \\ 0 & \frac{\partial}{\partial z} & \frac{\partial}{\partial y} \end{bmatrix} \tag{62}$$

Here  $L_{div}$ ,  $L^{sca}$  and  $L^{sym}$  denote the divergence, scalar gradient and symmetric vector gradient operators, respectively. After these manipulations Eq. (59) can be written as,

$$\begin{aligned}
& \sum_{e=1}^{nel} \left\{ \mathbf{w}_e^{nT} (L^{sym} \mathbf{N}_e^v)^T \mathbf{C} (L^{sym} \mathbf{N}_e^v) \mathbf{u}_e^n - \mathbf{q}_e^{nT} \mathbf{N}_e^p{}^T (L_{div} \mathbf{N}_e^v) \mathbf{v}_e^n \right. \\
& \left. - \mathbf{w}_e^{nT} (L_{div} \mathbf{N}_e^v)^T \mathbf{N}_e^p \mathbf{p}_e^n - \mathbf{q}_e^{nT} (L^{sca} \mathbf{N}_e^p)^T \kappa (L^{sca} \mathbf{N}_e^p) \mathbf{p}_e^n \right\} d \\
& = \sum_{e=1}^{nel} \mathbf{w}_e^{nT} \mathbf{N}_e^{vT} \mathbf{t} d + \sum_{\bar{Q}} \mathbf{q}_e^{nT} \mathbf{N}_e^{pT} \bar{Q} d
\end{aligned} \tag{63}$$

Here  $\mathcal{e}$ ,  $\mathcal{t}$ , and  $\bar{Q}$  refer to the element domain, and element boundaries where traction and flux, respectively, are prescribed. The symmetric material property tensor is converted into a  $6 \times 6$  symmetric matrix which is denoted (by change of font) as  $\mathbf{C}$ . It is important to note that in actual analysis we have one canonical element, one local coordinate system and one set of shape functions defined in this coordinate system. The calculation for each element is performed using these canonical coordinates along with the transformation matrix that maps canonical coordinates and quantities to global coordinates.

The vectors representing the degrees of freedom can be brought outside of the integrals since they are independent of the coordinates. Hence, the above equation can be written in the following compact form:

$$\begin{aligned}
& \sum_{e=1}^{nel} \begin{bmatrix} \mathbf{w}_e^{nT} & \mathbf{q}_e^{nT} \end{bmatrix} \begin{bmatrix} \mathbf{0} & -\mathbf{A}_{vp}^e & \mathbf{v}_e^n \\ -\mathbf{A}_{vp}^{eT} & -\mathbf{H}^e & \mathbf{p}_e^n \end{bmatrix} + \begin{bmatrix} \mathbf{K}^{se} & \mathbf{0} & \mathbf{u}_e^n \\ \mathbf{0} & \mathbf{0} & \mathbf{p}_e^n \end{bmatrix} , \\
& = \sum_{e=1}^{nel} \begin{bmatrix} \mathbf{w}_e^{nT} & \mathbf{q}_e^{nT} \end{bmatrix} \begin{bmatrix} \mathbf{F}_t^e \\ \mathbf{F}_Q^e \end{bmatrix} ,
\end{aligned} \tag{64}$$

where,

$$\mathbf{A}_{vp}^e = (L_{div} \mathbf{N}_e^v)^T \mathbf{N}_e^p d , \tag{65}$$

$$\mathbf{H}^e = (L^{sca} \mathbf{N}_e^p)^T \kappa (L^{sca} \mathbf{N}_e^p) d , \tag{66}$$

$$\mathbf{K}^{se} = (L^{sym} \mathbf{N}_e^v)^T \mathbf{C} (L^{sym} \mathbf{N}_e^v) d , \tag{67}$$

$$\mathbf{F}_t^e = \mathbf{N}_e^{vT} \mathbf{t} d , \tag{68}$$

$$\mathbf{F}_Q^e = \mathbf{N}_e^p \overline{\mathbf{Q}}^e d . \quad (69)$$

It is straightforward to assemble Eq. (64) into a global system where all vectors and matrices are used to build their assembled counterpart according to standard finite element assembly algorithms. The assembled matrices are defined by dropping the letter ‘e’ as a subscript or superscript. Since assembled  $\mathbf{w}$  and  $\mathbf{q}$  are arbitrary vectors, Eq. (64) can be satisfied only if,

$$\begin{pmatrix} \mathbf{0} & -\mathbf{A}_{vp} & \mathbf{v}^n & \mathbf{K}^s & \mathbf{0} & \mathbf{u}^n \\ -\mathbf{A}_{vp}^T & -\mathbf{H} & \mathbf{p}^n & \mathbf{0} & \mathbf{0} & \mathbf{0} \end{pmatrix} + \begin{pmatrix} \mathbf{0} & \mathbf{0} & \mathbf{0} & \mathbf{0} & \mathbf{0} & \mathbf{0} \\ \mathbf{0} & \mathbf{0} & \mathbf{0} & \mathbf{0} & \mathbf{0} & \mathbf{0} \end{pmatrix} = \begin{pmatrix} \mathbf{F}_t \\ \mathbf{F}_Q \end{pmatrix} , \quad (70)$$

where all vectors and matrices are written in global form.

Equation (70) forms a first order differential-algebraic system to be solved in time with a finite-difference method. There are alternative difference schemes that can be used to solve such a system. A Crank-Nicholson scheme will be used, thus solid displacement is given as,

$$\mathbf{u}_{k+1}^n = (\omega \mathbf{v}_{k+1}^n + (1-\omega) \mathbf{v}_k^n) \Delta t + \mathbf{u}_k^n, \quad (71)$$

where the subscript refers to the time-step number,  $\omega$  is a time-integration parameter and  $\Delta t$  is the size of the time-step. As we see, displacement is calculated from a weighted average of velocity at the next time-step ( $k+1$ ) and the current one ( $k$ ). For  $\omega > 0.5$ , this method is stable independent of the size of the time-step.

Substituting (71) into (70) and rearranging, results in,

$$\begin{pmatrix} \omega \Delta t \mathbf{K}^s & -\mathbf{A}_{vp} & \mathbf{v}_{k+1}^n \\ -\mathbf{A}_{vp}^T & -\mathbf{H} & \mathbf{p}_{k+1}^n \end{pmatrix} = \begin{pmatrix} \mathbf{F}_t - \mathbf{K}^s (\mathbf{u}_k^n + \mathbf{v}_k^n (1-\omega) \Delta t) \\ \mathbf{F}_Q \end{pmatrix} . \quad (72)$$

Equation (72) indicates that the system is solved for the first time step after the initial conditions of the problem are imposed on the right hand side. The solution at current time step ( $k$ ) is used to update the right hand side for the solution of the next time step ( $k+1$ ) Note that the coefficient matrix does not change in this linear formulation unless  $\Delta t$  or  $\omega$  are chosen to vary.

## 4.5 Computer Implementation

### 4.5.1 Object Oriented Programming

*Object-oriented programming* (OOP) is a programming paradigm aimed at easy extensibility and maintainability of large computer codes. An object-oriented simulation models an application as a collection of objects. Each defined object models a specific entity or event in an application problem and all objects work together to achieve the goal and the task of the overall system. Objects can be compared to variables in traditional programming languages but there is a significant difference. Unlike an object, a regular variable captures only the data structure aspect of an object, not its behavior. In OOP, each object is associated with certain data *and* functions [30].

Some programming languages are specifically designed for OOP, C++ being the one in most widespread use. In C++, the object is called a *class*. Each class has a collection of data that might include other class objects, and functions that perform tasks related to the class and generally make use of the class data to do that. It is possible to derive subtypes of objects that inherit the specified data and functions of the parent object, but also possesses their own data and functions. The data and functions in each object have different levels of accessibility from other objects including the parent and child objects.

With that structure, running a finite element analysis code can be as simple as invoking the “run” function of the “finite element analysis” class. This action then invokes other actions which themselves activate other functions and make use of other objects. The programmer can design a class structure that contain as many nested processes as necessary.

The finite element formulations developed in this research are implemented within *Trellis* [11], the object oriented finite element analysis framework of SCOREC, and used to solve the problems described in the following chapters. Figure 5 displays the symbols used to represent class objects, and indicates the derivation of a child class from a parent class and the ownership of one class by the other. These symbols are utilized in the class diagrams in the coming section.

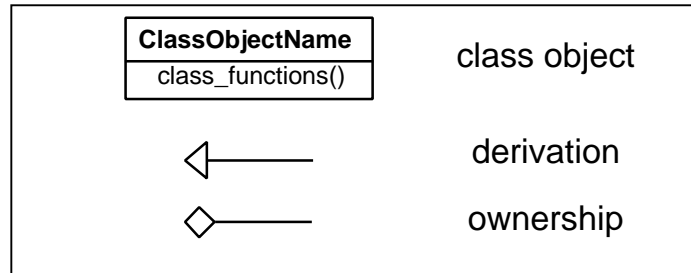


Figure 5: Symbols used in object oriented diagrams.

#### 4.5.2 Implementation of the Linear Analysis

*Trellis* is an object-oriented collection of software tools for general finite element analysis [11]. It is written in the C++ programming language. The main libraries of *Trellis* contain objects related to general finite element analysis, programming utilities, mesh and model handling. The general finite element library includes all objects corresponding to general and specific analyses, shape functions and mappings. Objects related to data representation and storage, such as lists, are included in the programming utilities library. The mesh library includes all mesh related objects such as elements, faces, vertices or usages. The model library not only includes model related objects but also has interfaces to different commercial solid modeler packages such as *Parasolid* used in the current work. Other software packages such as the *PETSc* matrix algebra package are also interfaced to *Trellis* in a convenient manner.

Our formulation is implemented as a separate library within this framework. For routine finite element operations such as numerical integration, assembly or linear system solving basic libraries of *Trellis* are utilized. A complete description of *Trellis* is beyond the scope of this work; only those major object hierarchies related to the current implementation are described here.

One major object is the analysis object which is a high level class called `FEAnalysis` for general finite element analysis from which different types of finite element analyses objects such as `ElasticityAnalysis` or `HeatTransferAnalysis` are derived. `FEAnalysis` also owns a class called

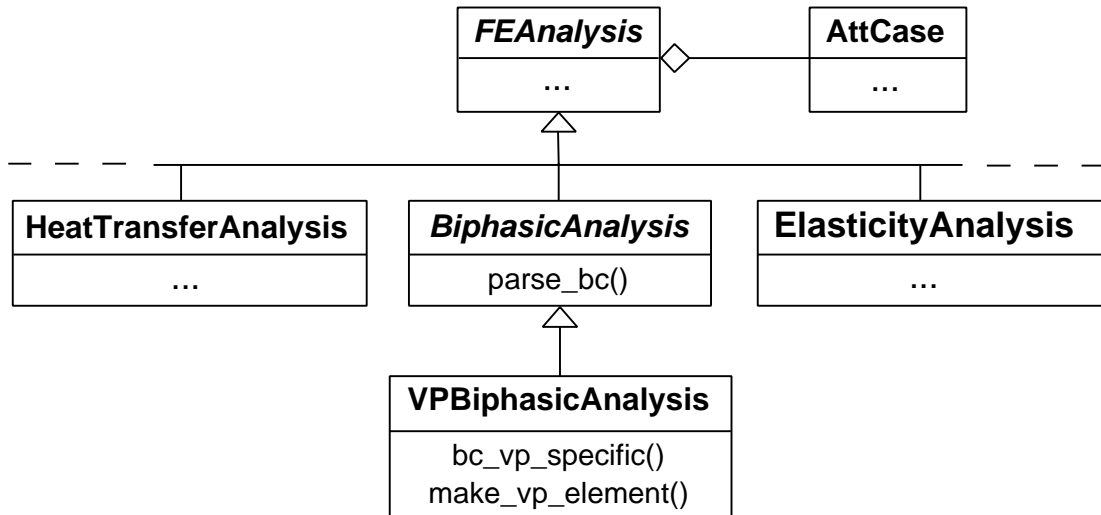


Figure 6: Analysis hierarchy of the implemented finite element code.

`AttCase` that handles the necessary attribute information for the problem under analysis (Fig. 6). The parent object performs some general tasks, such as handling the mesh and the model, while the child classes are assigned tasks specific to a certain analysis like taking the necessary steps to set up the stiffness matrix for the problem. We have a `BiphasicAnalysis` object which is derived from `FEAnalysis`. All the relevant data, such as fields and boundary conditions for a biphasic analysis are defined (but not implemented) in this class. This class parses the boundary conditions by invoking the necessary functions in the child classes. The `VPBiphasicAnalysis` class is derived from `BiphasicAnalysis` and implements the necessary functions defined there according to the  $v$ - $p$  formulation described in this chapter. It creates the element object and boundary condition objects of the  $v$ - $p$  formulation (note that the same physical boundary condition might have a different mathematical form in different finite element formulations). Other finite element formulations of the soft tissue problem will require different classes derived from `BiphasicAnalysis`.

Another important class is `StiffnessContributor` which is a parent class for many objects that contribute to the coefficient matrix of the final linear system, such as element matrices or essential boundary conditions. The `BiphasicElement3D` class that implements some element aspects that are common to different finite element formulation of the soft tissue problem is derived from this class. For example the solid stiffness term, Eq. (67), is known to be the same in all known formulations and hence can be created in this generic object (it can be always re-implemented in the child class when necessary). The functions that calculate element matrices specific to the  $v$ - $p$  formulation

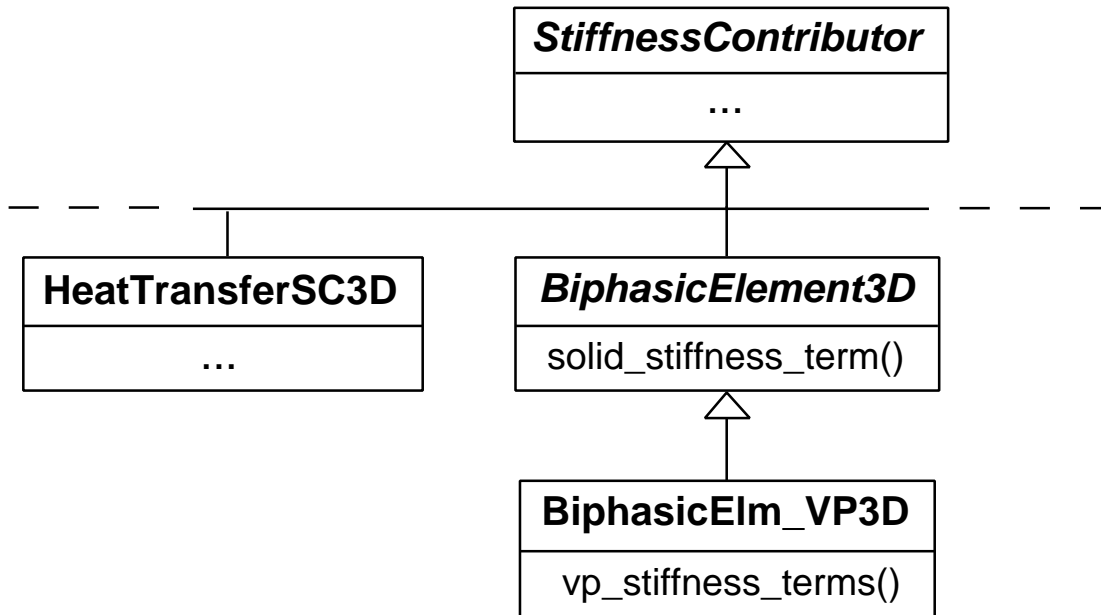


Figure 7: Element hierarchy of the implemented finite element code.

are members of `BiphasicElm_VP3D` class which is a child of `BiphasicElement3D` (Fig. 7).

`VPtrapezoidalTI` class handles the trapezoidal time integration and controls the time-stepping using velocity and displacement. It owns a class `VPTrapTIAssm` that processes and assembles the system contributors, namely element matrices and force vectors, according to the trapezoidal time integration rule. It also updates the system at each time step as prescribed by the  $v$ - $p$  formulation and trapezoidal rule (Fig. 8). Other integration rules will require that new classes be implemented.

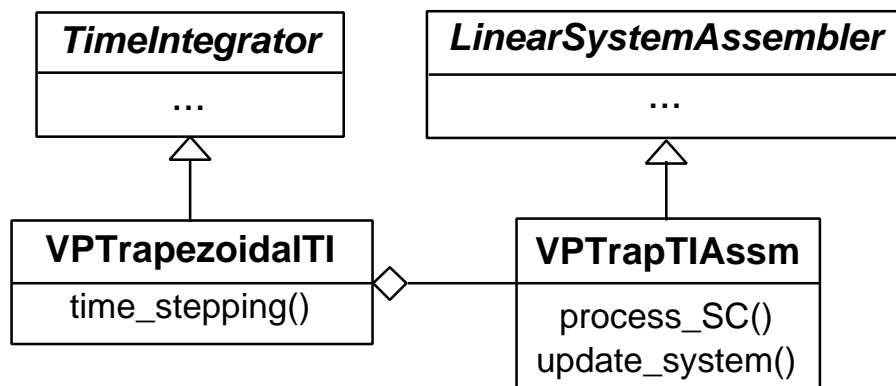


Figure 8: Time integrator and system assembler hierarchy of the implemented finite element code.

Another important class used in the implementation is `VPFaceTraction`, which is derived from `ForceContributor` class and calculates the force vector terms (i.e. contributes to the force vector of the final linear system).

The material property information in our analysis is maintained by the `BiphasicMaterial` class, which owns an elastic solid phase object (the `ElasMat3dDispForm` class) such as `LinearIsotropicElasticMaterial` or `TransverselyIsotropicElasticMaterial` as member data. The properties that are unique to a biphasic material, such as permeability or the volume fraction of the phases, are handled by `BiphasicMaterial`. The actions related to the solid phase, such as returning the stiffness matrix or calculating the stress, are functions in the solid phase classes. In that sense the `BiphasicMaterial` class provides access to the solid phase (Fig. 9).

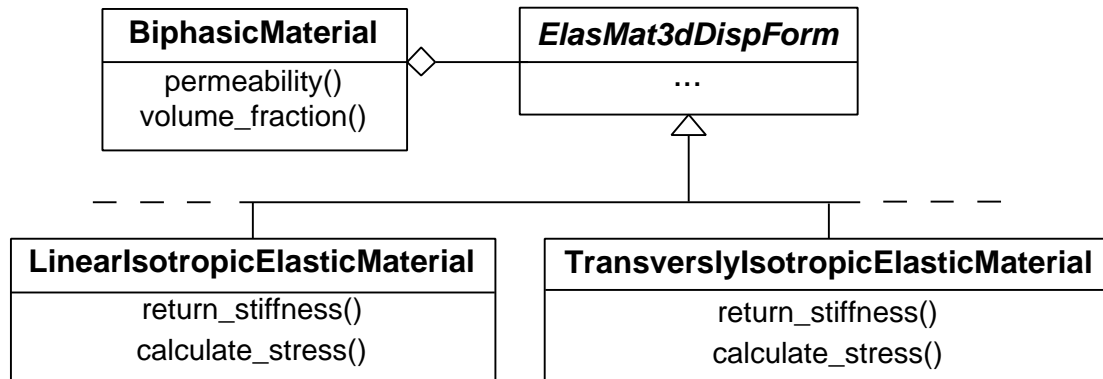


Figure 9: Material hierarchy of the implemented finite element code.

## 4.6 Nonlinear Formulation

In many physiological cases cartilage undergoes large deformations such that an infinitesimal strain analysis is not adequate to describe its *in vivo* mechanical behavior. In this section, the analysis described previously in this chapter is extended to take geometric and material nonlinearities into account. In this work, as is common in solid mechanics problems, a Lagrangian description is used to follow motion of the material points of the body.

As pointed out earlier, the weak form of our problem, Eq. (56), is derived in a general way such that it is valid for geometric and/or material nonlinearities. In nonlinear analysis, however, the problem domain and boundary are no longer fixed. They are

likely to change shape and size with deformation and the integrals need to be evaluated accordingly. Keeping the deformed integration domains in Eq. (56) results to the so-called *updated Lagrangian* formulation where the problem domain needs to be “updated” as motion occurs. An alternative to the updated Lagrangian formulation is the *total Lagrangian* formulation where all quantities are “pushed back” to the initial configuration, i.e. expressed in a material coordinate system [10].

In the finite element method, interpolation functions for each element are formed using the coordinates of the nodes in the element. Hence, the difference between spatial and initial derivative quantities is dependent on whether deformed or initial nodal coordinates are used in those interpolations. Depending on the structure of the computer program used, one way can be easier than the other. A mixed approach where some quantities are expressed in spatial configuration and others in the initial configuration is also possible [1]. In this thesis the total Lagrangian approach is used. One reason for that was that the resulting analysis was implemented in an object-oriented framework. An updated Lagrangian approach would necessitate that nodal coordinates be updated every time step, and potentially every iteration, depending on the nonlinear solver chosen. Although it is possible to update the mesh when necessary, this operation complicates the computer implementation and undermines object-oriented paradigm.

A total Lagrangian form of the problem can be obtained when Eq. (56) is rewritten such that its differentiation operations and integral domains are expressed with respect to the initial configuration using  $\mathbf{F}$  and Eq. (21). In that case, after substituting Eq. (40), (56) takes the following form:

$$\int_{\Omega_0} \left\{ \text{tr} \left[ 2 \mathbf{e}_0 \mathbf{w}^T \mathbf{F} \frac{\partial}{\partial \mathbf{C}} \right] - q(\mathbf{F}^{-T} : \mathbf{e}_0 \mathbf{v}) J - p(\mathbf{F}^{-T} : \mathbf{e}_0 \mathbf{w}) J - \kappa(\mathbf{F}^{-T} : \mathbf{e}_0 p) \cdot (\mathbf{F}^{-T} : \mathbf{e}_0 q) J \right\} d\Omega_0 = \int_{\Gamma_0} \mathbf{w} \cdot \bar{\mathbf{t}}_0 J d\Omega_0 + \int_{\Omega_0} q \bar{Q} J d\Omega_0 \quad (73)$$

Here,  $\mathbf{e}_0$  denotes the gradient operator with respect to the initial configuration and is related to  $\mathbf{e}$  through components of  $\mathbf{F}^{-1}$ . The ratio of the current area to the initial area,  $J$ , can be found by taking the dot product of Eq. (22) with itself to give

$$J = J \sqrt{\mathbf{n}_0^T \mathbf{C}^{-1} \mathbf{n}_0}, \quad (74)$$

where  $\mathbf{n}_0$  is the reference surface normal. It should be noted that the prescribed traction  $\bar{\mathbf{t}}_0$  is expressed in the initial configuration. The first term in Eq. (73) is the solid phase nonlinearity and will be denoted by  $G^s$ , i.e:

$$G^s = \text{tr}[(\mathbf{0}\mathbf{w})^T \mathbf{F} \mathbf{S}^E] d_0. \quad (75)$$

$G^s$  is the dominant nonlinear term in Eq. (73) representing the material nonlinearity in the problem. In the remaining terms,  $\mathbf{F}$  and  $J$ , which are functions of the motion are multiplied in various combinations creating geometric nonlinearities. These terms take into account the changing shape and size of the problem domain when evaluating derivatives and integrating.

#### 4.6.1 Linearization

A nonlinear equation such as Eq. (73) is solved through an iterative technique where consecutive contribution are made to an initial guess at each iteration until convergence occurs. In general, given a system of nonlinear equations  $\mathbf{r}(\mathbf{u})$

$$\mathbf{r}(\mathbf{u}) = \mathbf{0}, \quad (76)$$

to be solved for  $\mathbf{u}$ , the corresponding Newton-Raphson procedure creates at each iteration a linear system like

$$\left. \frac{\mathbf{r}(\mathbf{u})}{\mathbf{u}} \right|_{\tilde{\mathbf{u}}} \delta \mathbf{u} = D\mathbf{r}(\tilde{\mathbf{u}})[\delta \mathbf{u}] = \delta \mathbf{r} = -\mathbf{r}(\tilde{\mathbf{u}}), \quad (77)$$

where  $\tilde{\mathbf{u}}$  denotes the current state of the solution variables and  $\delta \mathbf{u}$  is the variation from the current state. In practice, in a Newton-Raphson iteration scheme  $\tilde{\mathbf{u}}$  is the solution estimated from the previous iteration and  $\delta \mathbf{u}$  is the correction proposed to it. In the rest of this chapter, the notation  $D\mathbf{T}(\tilde{\mathbf{u}})[\delta \mathbf{u}]$ , or  $\delta \mathbf{T}$  in short, will denote the change in the tensor  $\mathbf{T}$  at the current deformation state  $\tilde{\mathbf{u}}$  along the direction  $\delta \mathbf{u}$  (i.e. its directional derivative).

Applying the linearization as demonstrated in Eq. (77) to all terms in (73) is a fairly straightforward procedure and results in the following expression for the fully linearized form of our nonlinear system:

$$\begin{aligned}
& \{ \delta G^s - q(\delta \mathbf{F}^{-T} : \tilde{\mathbf{v}}) \tilde{J} - q(\tilde{\mathbf{F}}^{-T} : \mathbf{0}(\delta \mathbf{v})) \tilde{J} - q(\tilde{\mathbf{F}}^{-T} : \tilde{\mathbf{v}}) \delta J \\
& \quad - \delta p(\tilde{\mathbf{F}}^{-T} : \mathbf{0} \mathbf{w}) \tilde{J} - \tilde{p}(\delta \mathbf{F}^{-T} : \mathbf{0} \mathbf{w}) \tilde{J} - \tilde{p}(\tilde{\mathbf{F}}^{-T} : \mathbf{0} \mathbf{w}) \delta J \\
& \quad - \kappa(\delta \mathbf{F}^{-T} : \tilde{\mathbf{p}}) \cdot (\tilde{\mathbf{F}}^{-T} : \mathbf{0} q) \tilde{J} - \kappa(\tilde{\mathbf{F}}^{-T} : \mathbf{0}(\delta p)) \cdot (\tilde{\mathbf{F}}^{-T} : \mathbf{0} q) \tilde{J} \\
& \quad - \kappa(\tilde{\mathbf{F}}^{-T} : \tilde{\mathbf{p}}) \cdot (\delta \mathbf{F}^{-T} : \mathbf{0} q) \tilde{J} - \kappa(\tilde{\mathbf{F}}^{-T} : \tilde{\mathbf{p}}) \cdot (\tilde{\mathbf{F}}^{-T} : \mathbf{0} q) \delta J \} d \mathbf{0} \\
& = - \{ \text{tr} [ 2(\mathbf{0} \mathbf{w})^T \tilde{\mathbf{F}} \frac{\partial}{\partial \mathbf{C}} ] - q(\tilde{\mathbf{F}}^{-T} : \tilde{\mathbf{v}}) \tilde{J} - \tilde{p}(\tilde{\mathbf{F}}^{-T} : \mathbf{0} \mathbf{w}) \tilde{J} \\
& \quad - \kappa(\tilde{\mathbf{F}}^{-T} : \tilde{\mathbf{p}}) \cdot (\tilde{\mathbf{F}}^{-T} : \mathbf{0} q) \tilde{J} \} d \mathbf{0} + \mathbf{w} \cdot \dot{\mathbf{t}}_0 \tilde{J} d \mathbf{0} + q \bar{Q} \tilde{J} d \mathbf{0}
\end{aligned} \tag{78}$$

where

$$\delta G^s = (\text{tr} [ 2(\mathbf{0} \mathbf{w})^T \delta \mathbf{F} \mathbf{S}^E ] + \text{tr} [ 2(\mathbf{0} \mathbf{w})^T \tilde{\mathbf{F}} \delta \mathbf{S}^E ]) d \mathbf{0}. \tag{79}$$

In Eq. (78), the  $\sim$  overbar indicates that the quantity is evaluated at the current deformation state, i.e. at  $\tilde{\mathbf{u}}$ . Recall that  $\mathbf{F}$  and  $J$  are also functions of the deformation and, unlike the partial linearization approach used by Almeida [2], they are linearized as well<sup>1</sup>. On the other hand, the deformation-dependent permeability  $\kappa$  is not linearized. Note that the chain rule is utilized when linearizing terms that have more than one deformation-dependent parameter. Equation (79) is the variation in solid phase nonlinearity,  $\delta G^s$ , and represents the linearized stiffness. The other terms originate from the  $J$  and  $\mathbf{F}$  terms, hence they are related with the geometric nonlinearity in the problem.

In general, a linear approximation to a deformation-dependent tensor  $\mathbf{T}$  at the neighborhood of a given displacement  $\tilde{\mathbf{u}}$  and along a specified incremental displacement  $\delta \mathbf{u}$  can be obtained by expanding it in a Taylor series and ignoring quadratic and higher order terms:

$$\mathbf{T}(\tilde{\mathbf{u}} + \delta \mathbf{u}) \approx \mathbf{T}(\tilde{\mathbf{u}}) + \delta \mathbf{T} = \mathbf{T}(\tilde{\mathbf{u}}) + DT(\tilde{\mathbf{u}})[\delta \mathbf{u}], \tag{80}$$

where  $DT(\tilde{\mathbf{u}})[\delta \mathbf{u}]$ , the change in  $\mathbf{T}$  at  $\tilde{\mathbf{u}}$  in the direction of  $\delta \mathbf{u}$ , is given as

$$DT(\tilde{\mathbf{u}})[\delta \mathbf{u}] = \left. \frac{d}{d\varepsilon} \right|_{\varepsilon=0} \mathbf{T}(\tilde{\mathbf{u}} + \varepsilon \delta \mathbf{u}). \tag{81}$$

Using Eq. (81), the variation in  $\mathbf{F}$ ,  $\mathbf{C}$ ,  $\mathbf{E}$  and  $\mathbf{S}^E$  can be expressed as:

---

<sup>1</sup> Note that  $J$  is also a function of deformation but its linearization is skipped for simplicity.

$$DF(\tilde{\mathbf{u}})[\delta\mathbf{u}] = (\delta\mathbf{u})\mathbf{F} = {}_0(\delta\mathbf{u}) = \delta\mathbf{F}, \quad (82)$$

$$DC(\tilde{\mathbf{u}})[\delta\mathbf{u}] = \tilde{\mathbf{F}}^T {}_0(\delta\mathbf{u}) + ({}_0(\delta\mathbf{u}))^T \tilde{\mathbf{F}} = \delta\mathbf{C}, \quad (83)$$

$$DE(\tilde{\mathbf{u}})[\delta\mathbf{u}] = \frac{1}{2}\delta\mathbf{C} = \delta\mathbf{E}, \quad (84)$$

$$DS^E(\tilde{\mathbf{u}})[\delta\mathbf{u}] = \frac{\mathbf{S}}{\mathbf{C}} \Big|_{\tilde{\mathbf{u}}} DC(\tilde{\mathbf{u}})[\delta\mathbf{u}] = \frac{1}{2} \tilde{\mathbf{C}} : \delta\mathbf{C} = \tilde{\mathbf{C}} : \delta\mathbf{E} = \delta\mathbf{S}^E, \quad (85)$$

where quantities with  $\sim$  are evaluated at  $\tilde{\mathbf{u}}$ . Note that the chain rule is utilized in (85).  $\mathbf{C}$  is the fourth-order elasticity tensor corresponding to the modulus at the given deformation stage expressed as

$$\mathbf{C} = 2 \frac{\mathbf{S}^E}{\mathbf{C}} = \frac{\mathbf{S}^E}{\mathbf{E}} = 4 \frac{\partial^2}{\partial \mathbf{C} \mathbf{C}}, \quad (86)$$

where Eq. (39) is made use of. Substituting Eqs. (82) and (85) into (79) gives the following form for  $\delta G^s$

$$\begin{aligned} \delta G^s = & \frac{1}{2} \left( ({}_0\mathbf{w})^T \tilde{\mathbf{F}} \right) : \tilde{\mathbf{C}} : \left( \tilde{\mathbf{F}}^T {}_0(\delta\mathbf{u}) + ({}_0(\delta\mathbf{u}))^T \tilde{\mathbf{F}} \right) \\ & + tr \left( ({}_0\mathbf{w})^T {}_0(\delta\mathbf{u}) \tilde{\mathbf{S}}^E \right) \Big| d_0, \end{aligned} \quad (87)$$

where  $\tilde{G}_e^s$  is Eq. (75) evaluated at  $\tilde{\mathbf{u}}$  and equal to

$$\tilde{G}_e^s = tr \left[ ({}_0\mathbf{w})^T \tilde{\mathbf{F}} \tilde{\mathbf{S}}^E \right] d_0. \quad (88)$$

Considering the fact that  $\mathbf{C}$  is a symmetric tensor, (87) simplifies to

$$\delta G^s = \left\{ \left( ({}_0\mathbf{w}_e)^T \tilde{\mathbf{F}} \right)^{sym} : \tilde{\mathbf{C}} : \left( \tilde{\mathbf{F}}^T {}_0(\delta\mathbf{u}) \right)^{sym} + tr \left( ({}_0\mathbf{w})^T {}_0(\delta\mathbf{u}) \tilde{\mathbf{S}}^E \right) \right\} d_0. \quad (89)$$

At this point, it is clear that in the linearized form, Eq. (89), weighting and shape functions multiply only known quantities, i.e. those indicated with  $\sim$ .

To derive the remaining terms in (78) the linearized forms of  $\mathbf{F}^{-1}$  and  $J$  are needed. They are given as:

$$D\mathbf{F}^{-1}(\tilde{\mathbf{u}})[\delta\mathbf{u}] = -\tilde{\mathbf{F}}^{-1} {}_0(\delta\mathbf{u})\tilde{\mathbf{F}}^{-1} = \delta\mathbf{F}^{-1}, \quad (90)$$

$$DJ(\tilde{\mathbf{u}})[\delta\mathbf{u}] = \tilde{J} tr({}_0\delta\mathbf{u}) = \tilde{J}(\tilde{\mathbf{F}}^{-T} : {}_0(\delta\mathbf{u})) = \delta J. \quad (91)$$

Substituting the linearized forms (89),(90),(91) into Eq. (78) gives the following linearized weak form:

$$\begin{aligned}
& \int_0 \left\{ \left( ( \mathbf{w} )^T \tilde{\mathbf{F}} \right)^{sym} : \tilde{\mathbf{C}} : \left( \tilde{\mathbf{F}}^T \mathbf{0} (\delta \mathbf{u}) \right)^{sym} + tr \left( ( \mathbf{w} )^T \mathbf{0} (\delta \mathbf{u}) \tilde{\mathbf{S}}^E \right) + q \left( \tilde{\mathbf{F}}^{-1} \mathbf{0} (\delta \mathbf{u}) \tilde{\mathbf{F}}^{-1} : \mathbf{0} \tilde{\mathbf{v}} \right) \tilde{\mathbf{J}} \right. \\
& - q \left( \tilde{\mathbf{F}}^{-T} : \mathbf{0} (\delta \mathbf{v}) \right) \tilde{\mathbf{J}} - q \left( \tilde{\mathbf{F}}^{-T} : \mathbf{0} \tilde{\mathbf{v}} \right) \tilde{\mathbf{J}} \left( \tilde{\mathbf{F}}^{-T} : \mathbf{0} (\delta \mathbf{u}) \right) - \delta p \left( \tilde{\mathbf{F}}^{-T} : \mathbf{0} \mathbf{w} \right) \tilde{\mathbf{J}} \\
& + \tilde{p} \left( \tilde{\mathbf{F}}^{-1} \mathbf{0} (\delta \mathbf{u}) \tilde{\mathbf{F}}^{-1} : \mathbf{0} \mathbf{w} \right) \tilde{\mathbf{J}} - \tilde{p} \left( \tilde{\mathbf{F}}^{-T} : \mathbf{0} \mathbf{w} \right) \tilde{\mathbf{J}} \left( \tilde{\mathbf{F}}^{-T} : \mathbf{0} (\delta \mathbf{u}) \right) \\
& + \kappa \left( \tilde{\mathbf{F}}^{-1} \mathbf{0} (\delta \mathbf{u}) \tilde{\mathbf{F}}^{-1} \mathbf{0} \tilde{p} \right) \cdot \left( \tilde{\mathbf{F}}^{-T} \mathbf{0} q \right) \tilde{\mathbf{J}} - \kappa \left( \tilde{\mathbf{F}}^{-T} \mathbf{0} (\delta p) \right) \cdot \left( \tilde{\mathbf{F}}^{-T} \mathbf{0} q \right) \tilde{\mathbf{J}} \\
& + \kappa \left( \tilde{\mathbf{F}}^{-T} \mathbf{0} \tilde{p} \right) \cdot \left( \tilde{\mathbf{F}}^{-1} \mathbf{0} (\delta \mathbf{u}) \tilde{\mathbf{F}}^{-1} \mathbf{0} q \right) \tilde{\mathbf{J}} - \kappa \left( \tilde{\mathbf{F}}^{-T} \mathbf{0} \tilde{p} \right) \cdot \left( \tilde{\mathbf{F}}^{-T} \mathbf{0} q \right) \tilde{\mathbf{J}} \left( \tilde{\mathbf{F}}^{-T} : \mathbf{0} (\delta \mathbf{u}) \right) \} d_0 \\
& = - \int_0 \left\{ tr \left[ ( \mathbf{w} )^T \tilde{\mathbf{F}} \tilde{\mathbf{S}} \right] - q \left( \tilde{\mathbf{F}}^{-T} : \mathbf{0} \tilde{\mathbf{v}} \right) \tilde{\mathbf{J}} - \tilde{p} \left( \tilde{\mathbf{F}}^{-T} : \mathbf{0} \mathbf{w} \right) \tilde{\mathbf{J}} \right. \\
& \left. - \kappa \left( \tilde{\mathbf{F}}^{-T} \mathbf{0} \tilde{p} \right) \cdot \left( \tilde{\mathbf{F}}^{-T} \mathbf{0} q \right) \tilde{\mathbf{J}} \right\} d_0 + \int_0 \mathbf{w} \cdot \mathbf{i}_0 \tilde{\mathbf{J}} d_0 + \int_0 q \bar{Q} \tilde{\mathbf{J}} d_0
\end{aligned} \tag{92}$$

Equation (92) can be written as a summation of contributions from each element. Every term involves a problem unknown, either  $\mathbf{v}$  (or  $\mathbf{u}$ ) or  $p$ , and one weighting function, either  $\mathbf{w}$  or  $q$ , and it is fairly straightforward to find which degrees of freedom they are related to and determine their position in the final assembled system. The element submatrices originating from these terms are relatively complex and it is more convenient to define them in a triple product with the corresponding element degree of freedom vector of the problem unknowns and of the weighting functions. The submatrices  $\mathbf{K}_L^e, \mathbf{K}_G^e, \mathbf{A}_1^e, \mathbf{A}_{vp}^e, \mathbf{A}_2^e, \mathbf{A}_3^e, \mathbf{A}_4^e, \mathbf{H}_1^e, \mathbf{H}^e, \mathbf{H}_2^e$  and  $\mathbf{H}_3^e$  are defined as follows:

$$\mathbf{w}_e^{nT} \mathbf{K}_L^e \delta \mathbf{u}_e^n = \int_0 \left( ( \mathbf{w} )^T \tilde{\mathbf{F}} \right)^{sym} : \tilde{\mathbf{C}} : \left( \tilde{\mathbf{F}}^T \mathbf{0} (\delta \mathbf{u}) \right)^{sym} d_0, \tag{93}$$

$$\mathbf{w}_e^{nT} \mathbf{K}_G^e \delta \mathbf{u}_e^n = \int_0 tr \left( ( \mathbf{w} )^T \mathbf{0} (\delta \mathbf{u}) \tilde{\mathbf{S}}^E \right) d_0, \tag{94}$$

$$\mathbf{q}_e^{nT} \mathbf{A}_1^e \delta \mathbf{u}_e^n = \int_0 q \left( \tilde{\mathbf{F}}^{-1} \mathbf{0} (\delta \mathbf{u}) \tilde{\mathbf{F}}^{-1} : \mathbf{0} \tilde{\mathbf{v}} \right) \tilde{\mathbf{J}} d_0, \tag{95}$$

$$\mathbf{q}_e^{nT} \mathbf{A}_{vp}^e \delta \mathbf{v}_e^n = \int_0 q \left( \tilde{\mathbf{F}}^{-T} : \mathbf{0} (\delta \mathbf{v}) \right) \tilde{\mathbf{J}} d_0, \tag{96}$$

$$\mathbf{q}_e^{nT} \mathbf{A}_2^e \delta \mathbf{u}_e^n = \int_0 q \left( \tilde{\mathbf{F}}^{-T} : \mathbf{0} \tilde{\mathbf{v}} \right) \tilde{\mathbf{J}} \left( \tilde{\mathbf{F}}^{-T} : \mathbf{0} (\delta \mathbf{u}) \right) d_0, \tag{97}$$

$$\mathbf{w}_e^{nT} \mathbf{A}_3^e \delta \mathbf{u}_e^n = \underset{0}{\tilde{\mathbf{p}}(\tilde{\mathbf{F}}^{-1}(\delta \mathbf{u}) \tilde{\mathbf{F}}^{-1}: \mathbf{w}) \tilde{\mathbf{J}} d}_0, \quad (98)$$

$$\mathbf{w}_e^{nT} \mathbf{A}_4^e \delta \mathbf{u}_e^n = \underset{0}{\tilde{\mathbf{p}}(\tilde{\mathbf{F}}^{-T}: \mathbf{w}) \tilde{\mathbf{J}}(\tilde{\mathbf{F}}^{-T}: \delta \mathbf{u}) d}_0, \quad (99)$$

$$\mathbf{q}_e^{nT} \mathbf{H}_1^e \delta \mathbf{u}_e^n = \underset{0}{\kappa(\tilde{\mathbf{F}}^{-1}(\delta \mathbf{u}) \tilde{\mathbf{F}}^{-1} \tilde{\mathbf{p}}) \cdot (\tilde{\mathbf{F}}^{-T} \mathbf{q}) \tilde{\mathbf{J}} d}_0, \quad (100)$$

$$\mathbf{q}_e^{nT} \mathbf{H}^e \delta \mathbf{p}_e^n = \underset{0}{\kappa(\tilde{\mathbf{F}}^{-T}(\delta \mathbf{p}_e)) \cdot (\tilde{\mathbf{F}}^{-T} \mathbf{q}_e) \tilde{\mathbf{J}} d}_0, \quad (101)$$

$$\mathbf{q}_e^{nT} \mathbf{H}_2^e \delta \mathbf{u}_e^n = \underset{0}{\kappa(\tilde{\mathbf{F}}^{-T} \tilde{\mathbf{p}}) \cdot (\tilde{\mathbf{F}}^{-1}(\delta \mathbf{u}) \tilde{\mathbf{F}}^{-1} \mathbf{q}) \tilde{\mathbf{J}} d}_0, \quad (102)$$

$$\mathbf{q}_e^{nT} \mathbf{H}_3^e \delta \mathbf{u}_e^n = \underset{0}{\kappa(\tilde{\mathbf{F}}^{-T} \tilde{\mathbf{p}}) \cdot (\tilde{\mathbf{F}}^{-T} \mathbf{q}) \tilde{\mathbf{J}}(\tilde{\mathbf{F}}^{-T}: \delta \mathbf{u}) d}_0. \quad (103)$$

The  $\mathbf{K}_L^e$  and  $\mathbf{K}_G^e$  element matrices are often encountered in nonlinear elasticity and called the *large deformation stiffness matrix* and *geometric stiffness matrix*, respectively.

Substituting Eqs. (93) through (103) in the weak form, (92), gives the following linear first order system:

$$\begin{aligned} & \underset{e=1}{nel} \begin{bmatrix} \mathbf{w}_e^{nT} & \mathbf{q}_e^{nT} \end{bmatrix} \begin{bmatrix} \mathbf{0} & -\mathbf{A}_{vp}^e \delta \mathbf{v}_e^n \\ -\mathbf{A}_{vp}^{eT} & -\mathbf{H}^e \delta \mathbf{p}_e^n \end{bmatrix} + \begin{bmatrix} \mathbf{M}^e & \mathbf{0} \\ \mathbf{D}^e & \mathbf{0} \end{bmatrix} \delta \mathbf{u}_e^n \\ & = \underset{e=1}{nel} \begin{bmatrix} \mathbf{w}_e^{nT} & \mathbf{q}_e^{nT} \end{bmatrix} \begin{bmatrix} \mathbf{F}_t^e & -\mathbf{K}^{se} \tilde{\mathbf{u}}_e^n \\ \mathbf{F}_Q^e & \mathbf{0} \end{bmatrix} + \begin{bmatrix} \mathbf{A}_{vp}^e \tilde{\mathbf{p}}_e^n \\ \mathbf{A}_{vp}^{eT} \tilde{\mathbf{v}}_e^n + \mathbf{H}^e \tilde{\mathbf{p}}_e^n \end{bmatrix} \end{aligned} \quad (104)$$

where

$$\mathbf{M}^e = \mathbf{K}_L^e + \mathbf{K}_G^e + \mathbf{A}_3^e - \mathbf{A}_4^e, \quad (105)$$

$$\mathbf{D}^e = \mathbf{A}_1^e - \mathbf{A}_2^e + \mathbf{H}_1^e + \mathbf{H}_2^e - \mathbf{H}_3^e, \quad (106)$$

$$\mathbf{K}^{se} = \mathbf{K}_L^e + \mathbf{K}_G^e. \quad (107)$$

As the next step all the known quantities are moved to the right hand side and assembly is performed such that all matrices and vectors are replaced with their global counter parts. Since the weighting functions are arbitrary, Eq. (104) constitutes a solvable linear system that is expressed as:

$$\begin{bmatrix} \mathbf{0} & -\mathbf{A}_{vp} & \delta \mathbf{v}^n \\ -\mathbf{A}_{vp}^T & -\mathbf{H} & \delta \mathbf{p}^n \end{bmatrix} + \begin{bmatrix} \mathbf{M} & \mathbf{0} & \delta \mathbf{u}^n \\ \mathbf{D} & \mathbf{0} & \mathbf{0} \end{bmatrix} = \begin{bmatrix} \mathbf{F}_t \\ \mathbf{F}_Q \end{bmatrix} - \begin{bmatrix} \mathbf{K}^s \tilde{\mathbf{u}}^n \\ \mathbf{0} \end{bmatrix} + \begin{bmatrix} \mathbf{A}_{vp} \tilde{\mathbf{p}}^n \\ \mathbf{A}_{vp}^T \tilde{\mathbf{v}}^{sn} + \mathbf{B} \tilde{\mathbf{p}}^n \end{bmatrix}. \quad (108)$$

Equation (108) is a first order differential-algebraic system due to the presence of velocity  $\mathbf{v}$  and displacement  $\mathbf{u}$  as unknowns. It can be solved for the unknown increments  $\delta \mathbf{v}$ ,  $\delta \mathbf{p}$  and  $\delta \mathbf{u}$  in order to update the current solution estimates  $\tilde{\mathbf{v}}$ ,  $\tilde{\mathbf{p}}$ , and  $\tilde{\mathbf{u}}$ . The right hand side of Eq. (108) is the problem residual and should slowly vanish as convergence occurs through the iterative process.

#### 4.6.2 Partial Linearization

When solving Eq. (76), any procedure that causes successive reductions in the residual at each iteration is an acceptable scheme. In other words, there is no unique ‘‘convergence path’’ leading to the solution. This fact is utilized by calculating an approximate tangent matrix (left hand side of Eq. (77)) rather than an exact one. In biphasic tissue problems, it is common to approximate the tangent matrix by taking the  $G^s$  term as the only nonlinearity present and ignoring the geometric nonlinearities [2, 67, 98]. The same approach, when applied to Eq. (73) causes the matrices  $\mathbf{A}_1^e, \mathbf{A}_2^e, \mathbf{A}_3^e, \mathbf{A}_4^e, \mathbf{H}_1^e, \mathbf{H}_2^e$  and  $\mathbf{H}_3^e$  to vanish, simplifying Eq. (104) to

$$\begin{aligned} & \begin{bmatrix} \overset{nel}{\mathbf{w}_e^{nT}} & \overset{nel}{\mathbf{q}_e^{nT}} \end{bmatrix} \begin{bmatrix} \mathbf{0} & -\mathbf{A}_{vp}^e & \tilde{\mathbf{v}}_e^n \\ -\mathbf{A}_{vp}^{eT} & -\mathbf{H}^e & \tilde{\mathbf{p}}_e^n \end{bmatrix} + \begin{bmatrix} \mathbf{K}^{se} & \mathbf{0} & \delta \mathbf{u}_e^n \\ \mathbf{0} & \mathbf{0} & \mathbf{0} \end{bmatrix} \\ & = \begin{bmatrix} \overset{nel}{\mathbf{w}_e^{nT}} & \overset{nel}{\mathbf{q}_e^{nT}} \end{bmatrix} \begin{bmatrix} \mathbf{F}_t^e \\ \mathbf{F}_Q^e \end{bmatrix} - \begin{bmatrix} \mathbf{K}^{se} \tilde{\mathbf{u}}_e^n \\ \mathbf{0} \end{bmatrix} + \begin{bmatrix} \mathbf{A}_{vp}^e \tilde{\mathbf{p}}_e^n \\ \mathbf{A}_{vp}^{eT} \tilde{\mathbf{v}}_e^n + \mathbf{H}^e \tilde{\mathbf{p}}_e^n \end{bmatrix} \end{aligned} \quad (109)$$

The partially linearized form given in Eq. (109) is encountered often, so it is proper to show the corresponding element matrices in operator notation as done in the linear formulation. First, we define the following operators:

$$\begin{aligned} \overline{X} & & L_0^{sca} & \begin{bmatrix} \mathbf{0} & \mathbf{0} \\ \mathbf{0} & L_0^{sca} \\ \mathbf{0} & \mathbf{0} & L_0^{sca} \end{bmatrix} & \mathbf{0} \\ L_0^{sca} = \overline{Y} & & L_0^{div} & = \begin{bmatrix} \mathbf{0} & L_0^{sca} & \mathbf{0} \\ \mathbf{0} & \mathbf{0} & L_0^{sca} \end{bmatrix} & \mathbf{0} = \mathbf{0} \\ \overline{Z} & & & & \mathbf{0} \end{aligned} \quad (110)$$

Using the above linear operators, element matrices and vectors in Eq. (109) are given as:

$$\mathbf{A}_{vp}^e = \begin{pmatrix} \mathbf{F}_{INV} & L_0^{div} & \mathbf{N}_e^v \end{pmatrix}^T \mathbf{N}_e^p \mathbf{J} d_0, \quad (111)$$

$$\mathbf{H}^e = \underset{0}{\mathbf{F}^T L_0^{sca} \mathbf{N}_e^p} \kappa \underset{0}{\mathbf{F}^T L_0^{sca} \mathbf{N}_e^p} J d_0, \quad (112)$$

$$\mathbf{F}_t^e = \underset{0_t}{\mathbf{N}_e^v \cdot \tilde{\mathbf{t}}_0} J d_0, \quad (113)$$

$$\mathbf{F}_Q^e = \underset{0_Q}{\mathbf{N}_e^p \bar{\mathbf{Q}}} J d_0. \quad (114)$$

The matrix  $\mathbf{F}_{INV}$  is composed of the entries of  $\mathbf{F}^{-1}$  and defined in the Appendix B. Similarly,  $\mathbf{K}_L^e$  and  $\mathbf{K}_G^e$ , defined in Eqs. (93) and (94), can be rewritten separate from the multiplying degree of freedom vectors using the same operators:

$$\mathbf{K}_L^e = \underset{0}{(\mathbf{F}_L L_0^{div} \mathbf{N}_e^v)^T} \tilde{\mathbf{C}} (\mathbf{F}_L L_0^{div} \mathbf{N}_e^v) d_0, \quad (115)$$

$$\mathbf{K}_G^e = \underset{0}{(L_0^{div} \mathbf{N}_e^v)^T} \mathbf{S}_G^E (L_0^{div} \mathbf{N}_e^v) d_0. \quad (116)$$

In the above equations,  $\tilde{\mathbf{C}}$ , as in the linear analysis, is the matrix representing the fourth-order tensor  $\mathbf{C}$ .  $\mathbf{F}_L$  is a matrix composed of the entries of  $\mathbf{F}$  and are given in Appendix B.  $\mathbf{S}_G^E$  is defined as

$$\mathbf{S}_G^E = \begin{bmatrix} \mathbf{S}^E & \mathbf{0} & \mathbf{0} \\ \mathbf{0} & \mathbf{S}^E & \mathbf{0} \\ \mathbf{0} & \mathbf{0} & \mathbf{S}^E \end{bmatrix}. \quad (117)$$

After assembly, the corresponding global system becomes:

$$\begin{bmatrix} \mathbf{0} & -\mathbf{A}_{vp} & \delta \mathbf{v}^n \\ -\mathbf{A}_{vp}^T & -\mathbf{H} & \delta \mathbf{p}^n \end{bmatrix} + \begin{bmatrix} \mathbf{K}^s & \mathbf{0} & \delta \mathbf{u}^n \\ \mathbf{0} & \mathbf{0} & \mathbf{0} \end{bmatrix} = \begin{bmatrix} \mathbf{F}_t \\ \mathbf{F}_Q \\ \mathbf{0} \end{bmatrix} - \begin{bmatrix} \mathbf{K}^s \tilde{\mathbf{u}}^n \\ \mathbf{0} \\ \mathbf{0} \end{bmatrix} + \begin{bmatrix} \mathbf{A}_{vp} \tilde{\mathbf{p}}^n \\ \mathbf{A}_{vp}^T \tilde{\mathbf{v}}^{sn} + \mathbf{B} \tilde{\mathbf{p}}^n \end{bmatrix}. \quad (118)$$

Note that the right hand side of the above equation is still equivalent to the residual. Unlike the fully linearized form, Eq. (104), the above system is symmetric and requires that fewer terms be computed; this makes it computationally desirable. On the other hand, depending on the problem at hand, this form might take a higher number of iterations to converge due to inexactness of the tangent matrix.

Equations (108) and (118) representing, respectively, fully linearized and minimally linearized forms of the weak form, and are two extremes in complexity when solving the nonlinear soft tissue problem. It is possible to choose an intermediate method by selectively linearizing terms other than  $G^s$ . The nonlinear penetration problem is a

challenging numerical problem and thus different intermediate linearizations were attempted to increase numerical efficiency. One efficient way is to linearize the  $F$  terms while ignoring the nonlinearity associated with  $J$ . In that case, the final system has the following simplified forms for  $M$  and  $D$ .

$$M^e = K_L^e + K_G^e + A_3^e, \quad (119)$$

$$D^e = A_1^e + H_1^e + H_2^e. \quad (120)$$

The final linear equation system can be written in a simple notation as:

$$Y\delta v + K\delta u = f, \quad (121)$$

where

$$Y = \begin{matrix} \mathbf{0} & -A_{vp} \\ -A_{vp}^T & -H \end{matrix} \quad K = \begin{matrix} M & \mathbf{0} \\ D & \mathbf{0} \end{matrix} \quad \delta v = \begin{matrix} \delta v^n \\ \delta p^n \end{matrix} \quad \delta u = \begin{matrix} \delta u^n \\ \mathbf{0} \end{matrix} \quad (122)$$

$$f = \begin{matrix} F_t \\ F_Q \end{matrix} - \begin{matrix} K^s \tilde{u}^n \\ \mathbf{0} \end{matrix} + \begin{matrix} A_{vp} \tilde{p}^n \\ A_{vp}^T \tilde{v}^n + B \tilde{p}^n \end{matrix}$$

#### 4.6.3 Solution of the Nonlinear System

As in the linear analysis, the relation between velocity and displacement is established using the Crank-Nicholson rule according to Eq. (71). Before going into the details of this scheme it is worthwhile to briefly describe other methods to solve differential algebraic systems.

It is possible to treat methods to solve differential algebraic systems or ordinary differential equations, in general, in two categories: one-step and multi-step methods. Each group includes explicit and implicit methods. Using ordinary differential equation notation, a first order system can be expressed as:

$$\dot{y} = f(y) \quad y(0) = y_0. \quad (123)$$

For the above system, explicit one-step, explicit multi-step, implicit one-step and implicit multi-step methods are given, respectively, as:

$$\begin{aligned} y_{k+1} &= P(y_k) \\ y_{k+1} &= P(y_k, y_{k-1}, \dots, y_{k-l}) \\ y_{k+1} &= P(y_{k+1}, y_k) \\ y_{k+1} &= P(y_{k+1}, y_k, \dots, y_{k-l}) \end{aligned} \quad (124)$$

where  $P$  indicates a function describing the numerical procedure

Explicit one-step methods are not used since they are known to be unstable. Multi-step methods, both implicit and explicit, require evaluation of the stiffness matrix at more than one past time steps. This will require storing of the solution at as many previous time steps as the order of the method prescribes. Furthermore, the method can be applied only after this number of time steps has been taken with another method (usually a one-step method) that gives the “initial condition” for the multi-step method. A multi-step method is relatively complex but can lead to increased accuracy. The efficiency of such a scheme from a computational point of view poses an important research question; however, it is beyond the scope of this thesis.

To solve our differential algebraic system, an implicit one-step method is the simplest option providing reasonable accuracy. As a result, a Crank-Nicholson rule was chosen, where the integration parameter  $\omega$  is modified according to the nature of the problem at hand (i.e. considering the type of boundary conditions, and geometry of the problem domain) to ensure stability.

It is possible to use a higher-order implicit time integration method for time stepping such as an implicit Runge-Kutta method [17, 37]. In this method the parameters required for time stepping are unknown and need be determined as part of the solution process. This approach was not studied.

In Eq. (121), the problem unknowns are the increments of the problem variables, unlike in linear analysis where the unknowns are the variables themselves. At each time step the system should be repeatedly solved until convergence occurs. Then the solution is updated to form an initial guess for the next time step and the iteration is repeated until convergence is again achieved. The variations in the solution variables,  $\delta \mathbf{v}$  and  $\delta \mathbf{u}$ , are defined with respect to the time integration scheme as:

$$\begin{aligned}\delta \mathbf{v}_{k+1}^{(i)} &= \mathbf{v}_{k+1}^{(i)} - \mathbf{v}_{k+1}^{(i-1)} \\ \delta \mathbf{u}_{k+1}^{(i)} &= \mathbf{u}_{k+1}^{(i)} - \mathbf{u}_{k+1}^{(i-1)}\end{aligned}\tag{125}$$

where the superscript denotes the iteration number and the subscript, as in the linear analysis, indicates the time step. Using (71) and noting that the variation of  $\mathbf{u}_n$  and  $\mathbf{v}_n$ , the converged solutions from the previous time step, is zero, gives the relation between  $\delta \mathbf{u}$  and  $\delta \mathbf{v}$  as

$$\delta \mathbf{u}_{k+1}^{(i)} = \omega \ t \delta \mathbf{v}_{k+1}^{(i)}.\tag{126}$$

Substituting Eq. (126) into Eq. (121) and rearranging gives

$$(\mathbf{Y}_{k+1}^{(i-1)} + \omega \ t \mathbf{K}_{k+1}^{(i-1)}) \delta \mathbf{v}_{k+1}^{(i)} = \mathbf{f}_{k+1}^{(i-1)}, \quad (127)$$

where subscripts and superscripts have been added to the matrices to indicate the time step and iteration number, respectively, of the deformation state at which they are formed.

In a full Newton-Raphson method, Eq. (127) is solved and the solution is updated using

$$\begin{aligned} \mathbf{v}_{k+1}^{(i)} &= \mathbf{v}_{k+1}^{(i-1)} + \delta \mathbf{v}_{k+1}^{(i)} \\ \mathbf{u}_{k+1}^{(i)} &= \mathbf{u}_{k+1}^{(i-1)} + \delta \mathbf{u}_{k+1}^{(i)} = \mathbf{u}_{k+1}^{(i-1)} + \omega \ t \delta \mathbf{v}_{k+1}^{(i)} \end{aligned} \quad (128)$$

The right-hand side and left-hand side of Eq. (127) are updated by reevaluating  $\mathbf{Y}$ ,  $\mathbf{K}$  and  $\mathbf{f}$  at the new approximation to give the new system of equations. This procedure is repeated until convergence occurs. Convergence is checked by observing a suitable norm of  $\mathbf{f}$  which should decrease since it indicates the magnitude of the residual of the problem.

In an effort to increase the numerical efficiency in the nonlinear penetration problem, a  $u$ - $p$  formulation has also been studied. That requires  $\delta \mathbf{u}^n$  to be retained in the problem. In this case, using Eq. (126),  $\delta \mathbf{v}^n$  is eliminated, and  $\mathbf{u}$  and  $p$  (rather than  $\mathbf{v}$  and  $p$ ) become the main problem variables. It is easy to show that this closely-related formulation gives the following final system of equations:

$$(\mathbf{Y}_{k+1}^{(i-1)} + \mathbf{K}_{k+1}^{(i-1)}) \delta \mathbf{u}_{k+1}^{(i)} = \mathbf{f}_{k+1}^{(i-1)}, \quad (129)$$

where

$$\mathbf{Y}_{k+1}^{(i-1)} = \begin{bmatrix} \mathbf{0} & -\mathbf{A}_{vp}^{(i-1)} \\ -\frac{1}{\omega \ t} \mathbf{A}_{vp}^T & -\mathbf{H}_{k+1} \end{bmatrix} \quad \delta \mathbf{u}_{k+1}^{(i-1)} = \begin{bmatrix} \delta \mathbf{u}^n \\ \delta p^n \end{bmatrix} \quad (130)$$

In the above equation, the indices attached to the brackets indicate the time step and iteration at which the corresponding matrix and vector are evaluated. The  $\mathbf{K}$  and  $\mathbf{f}$  terms have the same form as in the  $v$ - $p$  formulation. Note the vector  $\delta \mathbf{u}$  contains degrees of freedom for both main problem variables,  $\mathbf{u}$  and  $p$ .

A full Newton-Raphson method requires the full linear system to be updated and solved at every iteration. This is computationally expensive and thus more efficient approaches are taken. In quasi-Newton methods, the tangent-stiffness matrix (or its inverse) is approximated without performing a linearization and updated whenever necessary at each iteration. The various quasi-Newton algorithms, such as Secant,

Broyden or Broyden-Fletcher-Goldfarb-Shanno (BFGS) methods, differ only by the choice of the matrix updating formula [49].

In the modified Newton method, only the right hand side of the system, namely the problem residual  $\mathbf{f}$ , is updated after every iteration. In this approach, Eq. (127) becomes

$$(\mathbf{Y}_{k+1}^{(0)} + \omega \ t\mathbf{K}_{k+1}^{(0)})\delta\mathbf{v}_{k+1}^{(i)} = \mathbf{f}_{k+1}^{(i-1)}. \quad (131)$$

Updating  $\mathbf{f}$  insures that the residual is evaluated at every iteration. As long as the residual gradually decreases and vanishes at the end of iterations, the analyst is free to choose if or when to update the left hand side of Eq.(131). As mentioned earlier in this chapter, there is no unique “path” to a converged solution in an iterative technique. With respect to Eq. (127), any updating procedure that will reduce the norm of  $\mathbf{f}$  properly will lead eventually to a converged solution. In this work, the modified Newton scheme is adopted; the numerical solution procedure is outlined on Table 1.

*Table 1: The numerical procedure for the nonlinear problem*

**Iteration at timestep n+1:**

- 1) If it is the first iteration within that time step, namely  $i = 0$ , obtain the estimates for  $\mathbf{v}$  and  $\mathbf{u}$  vector from the converged values of the previous time step :

$$\mathbf{v}_{n+1}^{(0)} = \mathbf{v}_n \quad \mathbf{u}_{n+1}^{(0)} = \mathbf{u}_n + \ t\mathbf{v}_n$$

- 2) Do the following until  $|\delta\mathbf{v}|$  is sufficiently small indicating convergence

- a) Solve the system to find the increment

$$(\mathbf{Y}_{n+1}^{(0)} + \omega \ t\mathbf{K}_{n+1}^{(0)})\delta\mathbf{v}_{n+1}^{(i)} = \mathbf{f}_{n+1}^{(i-1)}$$

- b) If necessary do a line search to find  $\beta$ , otherwise set  $\beta = 1.0$

$$\mathbf{v}_{n+1}^{(i)} = \mathbf{v}_{n+1}^{(i-1)} + \beta \delta\mathbf{v}_{n+1}^{(i)} \quad \mathbf{u}_{n+1}^{(i)} = \mathbf{u}_{n+1}^{(i-1)} + \omega \ t\delta\mathbf{v}_{n+1}^{(i)}$$

- c) Update the right hand side only, or potentially the whole system depending on the convergence behavior. Update the iterate counter to  $i+1$

- 3) Go to the next time step

#### 4.6.4 Line Search

The performance of a solution procedure depends not only on the finite element formulation used but also on the type of problem (i.e. geometry of the problem domain, boundary conditions etc.) to be solved. In many cases, the Newton iteration does not converge when strong nonlinearities are present in the problem. Such is the case for the example problems presented in Chapter 7. As an additional precaution to insure convergence, a line search algorithm was incorporated with the modified Newton solver.

The line search technique is often utilized in unconstrained optimization and can be used with a wide range of iterative solution methods [21]. In line search, instead of updating the approximation to the solution at each iteration by the full correcting increment, the correcting increment is multiplied by a scaling factor  $\beta$ . The scaling factor is determined such that the scaled increment gives a better approximation to the solution than the full increment. The usual strategy is to define an objective function  $(\beta)$  and choose  $\beta$  in such a way that this function fulfills a specified condition. It is possible to select a function that vanishes when  $\beta$  is optimal. In other words, the condition that the line search should fulfill is

$$(\mathbf{v}^i + \beta\delta\mathbf{v}^i) = 0. \quad (132)$$

This approach is computationally expensive since has to be evaluated several times until Eq. (132) is satisfied [49]. What is usually done in practice is to set a condition on  $(\beta)$  such that it is monotonically and sufficiently reduced from one iteration to the next. This can be expressed as

$$(\mathbf{v}^i + \beta\delta\mathbf{v}^i) < \eta (\mathbf{v}^i), \quad (133)$$

where  $0 < \eta < 1.0$  is a scalar that is problem-dependent and chosen heuristically. Several objective functions have been proposed in the literature to determine the scaling factor [32]. In our research, as our objective function we picked the magnitude of the residual and tried to fulfill

$$|\mathcal{f}^{i+1}| < \eta |\mathcal{f}^i|, \quad (134)$$

where the bars denote the magnitude of the vector.

In our implementaton, if the modified Newton iteration fulfills (134), the line search procedure is skipped. Otherwise,  $\beta$  is reduced starting from a specified value,  $\beta_0$ , with a specified increment  $\Delta\beta$ . If reducing  $\beta$  increases the magnitude of the residual, then

$\beta$  is increased with the same increment. The solution estimates are updated using the optimal  $\beta$  accordingly as

$$\begin{aligned}\mathbf{v}_{k+1}^{(i+1)} &= \mathbf{v}_{k+1}^{(i)} + \beta \delta \mathbf{v}_{k+1}^{(i)} \\ \mathbf{u}_{k+1}^{(i+1)} &= \mathbf{u}_{k+1}^{(i)} + \beta \delta \mathbf{u}_{k+1}^{(i)}\end{aligned}\tag{135}$$

The residual  $\mathbf{f}$  is reevaluated with the above estimates. This procedure is repeated until Eq. (134) is satisfied. If none of the  $\beta$  values within the specified range fulfills this condition, a full-Newton update is performed by reevaluating  $\mathbf{Y}$ ,  $\mathbf{K}$  and  $\mathbf{f}$ , and the system is solved again. In our tests, this procedure has proven to be effective for a wide variety of problem configurations. However, the “correct”  $\beta_0$  and  $\Delta\beta$  differ from one problem to the other and their choice is critical to the efficiency of the algorithm. For example, a  $\beta_0$  that is too low might lead to excessive full-Newton updates, or a  $\Delta\beta$  too small might necessitate excessive residual evaluations, either of which reduces the computational efficiency. On the other hand, some computational inefficiency might be risked to ensure convergence.

## 4.7 Computer Implementation of the Nonlinear Analysis

The general structure of *Trellis* has been described earlier. The general capabilities for implementing a nonlinear finite element analysis exist in *Trellis* and have been used for elasticity problems. However, the time-dependent nature of our problem required some general finite element objects to be programmed beyond those specific to nonlinear biphasic analysis.

The first object necessary to implement the nonlinear biphasic problem is a corresponding analysis class which is called `NonlinVPBiphasicAnalysis` and is derived from `VPBiphasicAnalysis`. The `NonlinVPBiphasicAnalysis` class specializes the function of `VPBiphasicAnalysis` that invokes the calculation of the element matrix object. Also, the traction boundary condition, which has a different form in nonlinear analysis, is calculated by invoking a different function (Fig. 10). The element matrix object for the nonlinear analysis is called `BiphasicElm_NonlinVP3D`, and is a child of `BiphasicElm_VP3D` class. The `BiphasicElm_NonlinVP3D` class re-implements the functions that calculate the element matrices since they are mathematically different in nonlinear analysis (Fig. 11).

Similarly, the force vector, which is different in nonlinear analysis, is calculated using a new class, called `VPFaceTractionLD`, that takes large deformation into account.

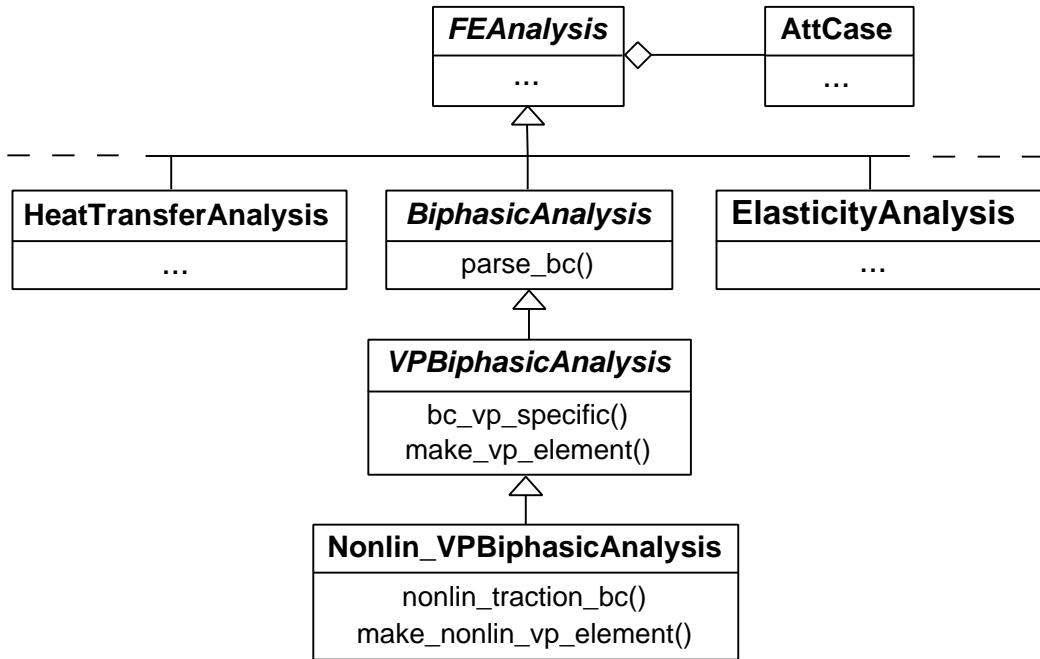


Figure 10: Nonlinear analysis object in the analysis hierarchy.

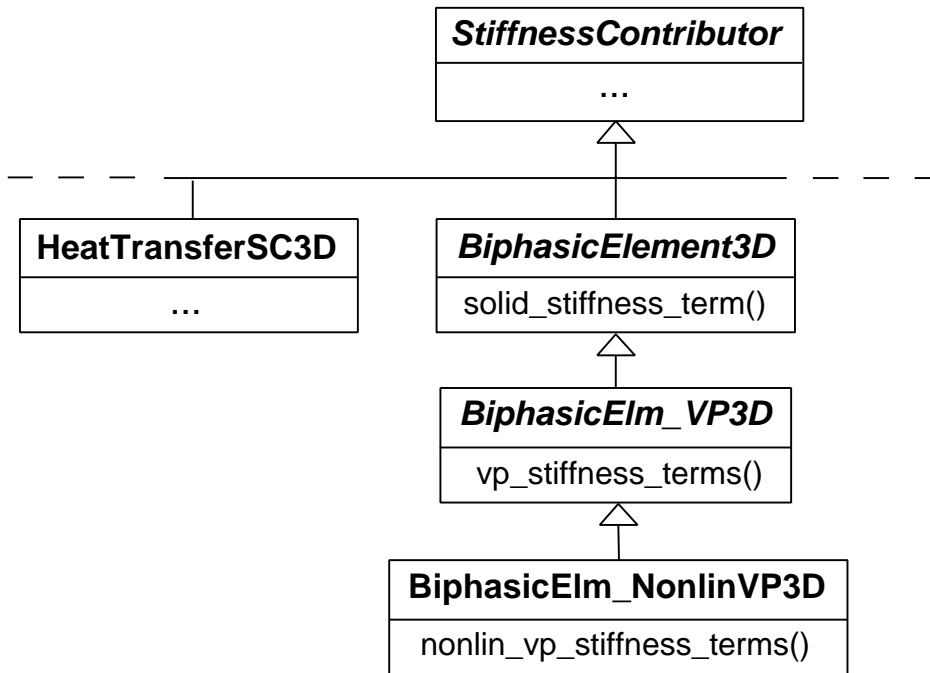


Figure 11: Nonlinear biphasic stiffness object in the stiffness contributor hierarchy.

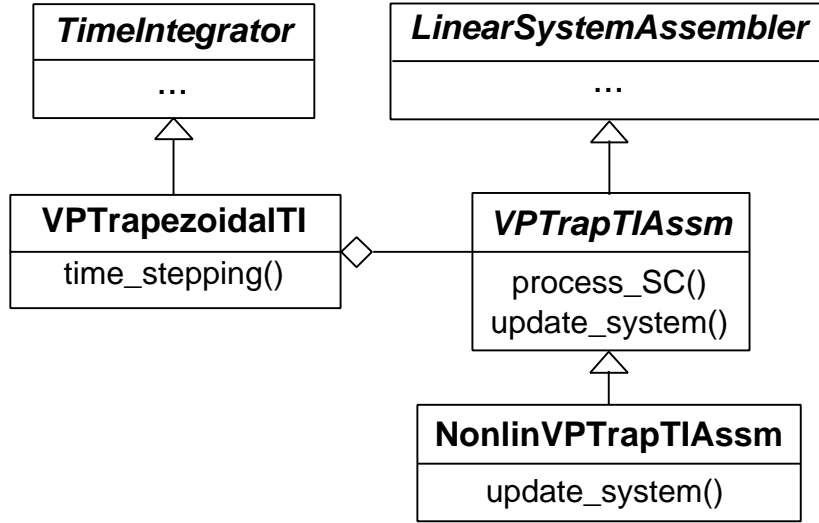


Figure 12: Nonlinear assembler object in the assembler hierarchy.

In nonlinear analysis, the same trapezoidal rule gives a different form for the final assembly of the element matrices, compared to the linear analysis. This requires the implementation of a new assembler object, named `NonlinVPTrapTIAssm`, which is derived from `VPTrapTIAssm`. (Fig. 12).

Each hyperelastic law that can potentially be used in cartilage research should be a separate class derived from a common parent. The law prescribed by Eq. (41) is implemented under the name `IsotropicHyperelasMaterial` (Fig. 13). `BiphasicElm_NonlinVP3D` class and other stiffness contributor classes interface to the material properties of the solid phase through specific classes that abstract the operations. For an isotropic linear elastic material the abstraction consists of evaluation of stress and returning the two independent material properties. For a hyperelastic material like `IsotropicHyperelasMaterial`, the same calls will return the tangent stiffness matrix to the element class and evaluate the stress for a given displacement field and material point. The material classes also know whether the requested material properties vary spatially.

Permeability and volume fraction are properties that are not specific to a solid phase and thus they are not handled by the solid phase class. In the linear analysis, `BiphasicMaterial` returns them when necessary. In the case of strain-dependent permeability (i.e. nonlinear analysis), `BiphasicMaterial` evaluates the current permeability and volume fraction using the deformation gradients calculated from the displacement field. These types of abstractions allow the computer code flexibility

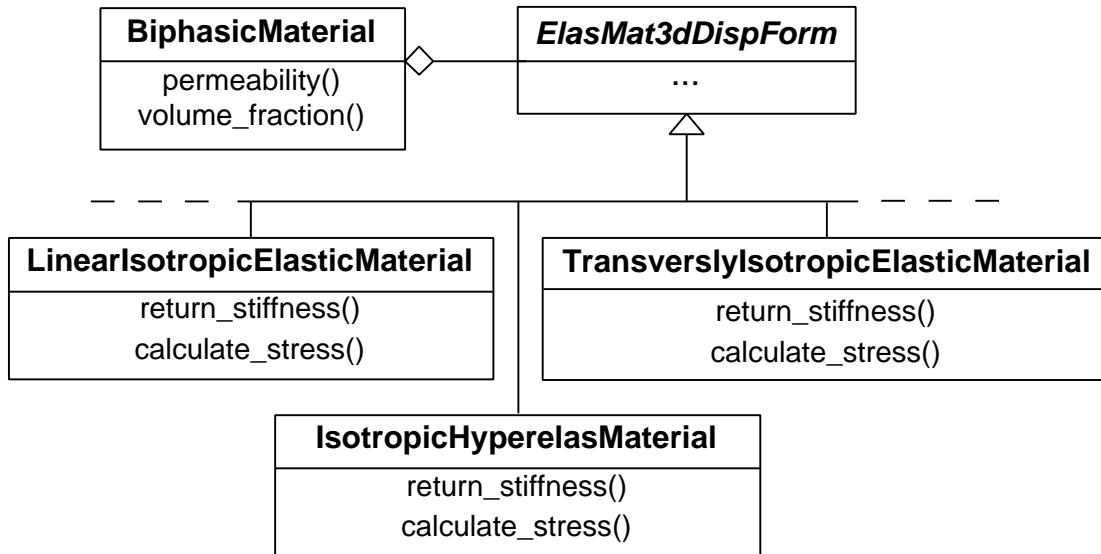


Figure 13: Nonlinear biphasic stiffness object in the stiffness contributor hierarchy.

characteristic of OOP. With respect to the above example, the program source does not require modification when different material classes are used. As common in *Trellis*, the correct material property class is created automatically if a corresponding keyword is encountered among the problem attributes.

The conventional full Newton-Raphson (`Newton` class) method is present in *Trellis*. As described earlier, for a time-dependent problem where consecutive linear systems need to be solved, full Newton-Raphson iteration is numerically inefficient. Hence, the modified Newton (`ModifiedNewton` class) method was implemented in *Trellis* as a part of this research. It is derived from the same parent class, called `SystemSolver`, as the `Newton` class. The time integration is performed using the `VPTrapezoidalTI` class. This object invokes the chosen nonlinear solver and performs a full Newton update to proceed to the next time step once convergence is achieved within the current time step.

In a total Lagrangian approach, element integrals are evaluated in the undeformed domain. The deformation is accounted for by adjusting the derivative terms using  $\mathbf{F}$ , resulting in the complex integrands presented in this chapter. Stand-alone C++ functions to compute these complex integrands were also written as part of the programming effort.

# Chapter 5

## Penetration Method

### 5.1 Introduction

The mechanical behavior of diarthrodial joints is dominated by contact, as forces are transmitted across the joint through the soft tissue layers. However, analysis of 3-D multi-phase contact is complicated and computationally demanding. In an effort to reduce the computational cost, a penetration-based method to approximate soft tissue contact mechanics has been developed. This “penetration method” reduces the intrinsically nonlinear and coupled problem of two biphasic tissues in contact over an unknown area to two uncoupled problems each with prescribed traction distributions over a pre-calculated (and therefore known) contact area (Fig. 14). This replaces the intrinsic nonlinearity of contact analysis with a geometry-dependent preprocessing step. This chapter describes how experimental kinematic data is used to derive the traction boundary conditions.

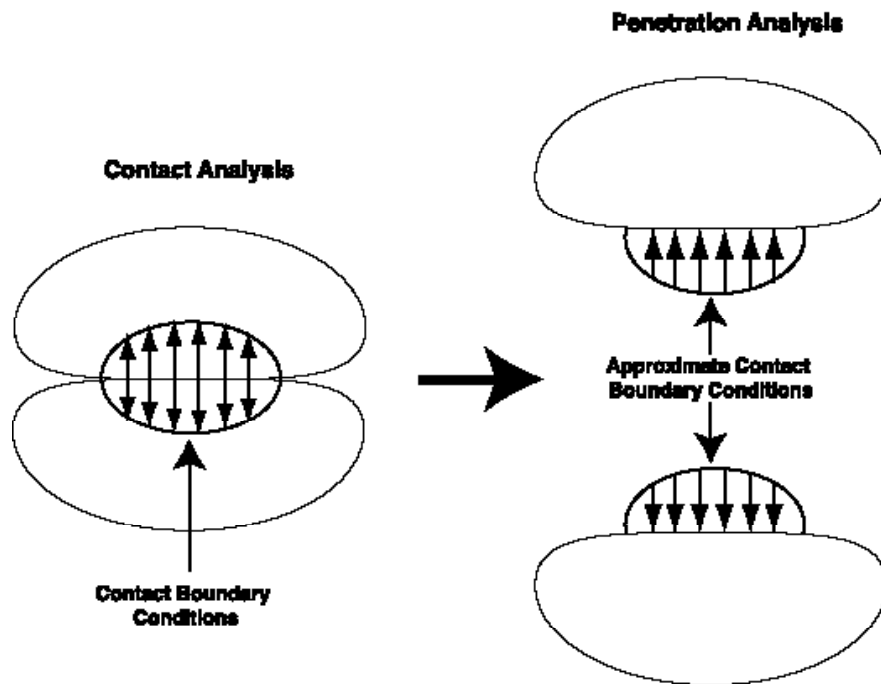


Figure 14: Graphical depiction of the idea behind penetration method

The penetration method requires the following input data: (i) joint kinematics, and the resultant force producing those kinematics, at one or more physiological positions;

(ii) geometry of the tissue layers in an undeformed state; and (iii) material parameters for the biphasic soft tissue. We use this data and the governing equations in a series of four steps to obtain the approximate traction distribution: (1) the geometric models are queried to determine the geometric overlap, or penetration, between the undeformed tissues; (2) this vector penetration field is split between the two contacting layers; (3) the vector is scaled to represent a traction; and (4) the traction is divided between the solid and fluid phases of each tissue.

## **5.2 Experimental Kinematics Data**

The input data to be used in the penetration method originates from *in vivo* or *in vitro* joint experiments. Compared to cartilage, subchondral bone has a relatively high modulus and is considered in this work as a rigid body. With this assumption a convenient way of observing the joint kinematics is to track the motion of the subchondral bone underlying the articular cartilage layers.

Different visualization techniques can be utilized to observe the motion of a diarthrodial joint, stereophotogrammetry (SPG) and MRI being two of them. Although they are not a direct part of this research, SPG and MRI procedures to obtain kinematic data are relevant to the performance of the method and briefly described here for completeness.

### **5.2.1 Visualization Techniques**

SPG is a destructive visualization technique that is recruited as an *in vitro* experimental tool for joint research. In this method the kinematics of the intact cadaveric joint is carefully observed during an imposed motion by recording the motion of the bones. Afterwards the joint is disarticulated and the bones in the joint are separated, retaining the overlaying cartilage layers. After the cartilage layers are relaxed a grid of light is reflected on them. Their surface image is taken with two cameras simultaneously whose relative positions are known. This “stereo visualization” allows the 3-D surface geometry of the cartilage to be captured [80].

Next, the cartilage layers are chemically removed to expose the surface of the subchondral bone. The 3-D surface geometry of the subchondral bone (which is also the geometry of the bottom face of the cartilage) is recoded in the same manner. This step concludes the experimental part of the joint kinematics analysis.

As the next step, the contacting and bone surfaces of the cartilage that are obtained from SPG are exported to solid modeling software and the “gap” between these

surfaces is numerically filled to give a 3-D solid model of the cartilage layers. The experimental kinematics data, recorded when the joint was intact, can now be used together with the 3-D cartilage geometry to simulate and visualize the motion of the cartilage layers in the diarthrodial joint.

The SPG method has a relatively high accuracy, but possesses two drawbacks; it is destructive (can be applied only *in vitro*), and it is not a real time visualization tool. Also, if the tissue surface geometry is complex (or example, highly curved) the camera may not be able to capture a complete picture of the tissue. In spite of these drawbacks, SPG has proven to be a powerful research tool [7, 81].

MRI is a well-known diagnostic tool widely used in health sciences. It can also be used for experimental purposes to visualize tissue geometry [29]. In MRI, the deformation of the tissue can be observed directly. An important advantage of MRI is that it is also possible to capture the different stages of the cartilage deformation *in vivo*, something not possible with SPG. Although MRI is not as accurate as some other methods and it is hard to distinguish the cartilage-bone border with this method, it is being improved through on-going research.

### 5.2.2 Interpolation through Discrete Kinematics Data

As mentioned earlier, joint kinematics is observed by following the motion of the bones, which are assumed to be rigid. The motion of the bone is recorded at discrete points, and an interpolation through these discrete points produces a smooth motion in 3-D space. The discrete motion data is made of a set of coordinates which defines the change in the position of a specified point on the bone, and rotation matrices that give the change in the orientation of a line segment in the bone with respect to this point.

Interpolating through a set of *rotation matrices* (or orientations) can be done by parametrizing the rotations (e.g. using Euler angles) by choosing a local coordinate system and applying a spline algorithm to these rotation parameters. There are more complex mathematical methods that can be used if the interpolation is required to satisfy a constraint or if it is to be independent of the choice of the local coordinates. For our purposes the former approach is adequate.

The discrete data is converted to a smooth motion so that the transformation can be evaluated at any time during a given motion. With respect to a reference coordinate system the transformation information can be described as a matrix  $\mathbf{T}$  that depends on time through the rotation parameters,  $\theta_1, \theta_2$ , and  $\theta_3$ , and the translation vector  $\mathbf{l}$ , i.e.

$$\mathbf{T} = \mathbf{T}(\theta_1(t), \theta_2(t), \theta_3(t), \mathbf{I}(t)). \quad (136)$$

For example, if an arm elevation motion of the glenohumeral joint of the shoulder is given, the corresponding rotation parameters and the translation vector can be evaluated at a desired time and the relative position of the contacting cartilage layers can be determined.

### 5.3 Biphasic Contact Boundary Conditions and Load Sharing

For purposes of deriving the penetration method, an indicial notation will be employed. The boundary conditions between two contacting biphasic bodies, denoted with superscripts  $A$  and  $B$ , have been derived using conservation equations, including a discontinuity in the volume fractions across the contact interface and possible friction [45]. Assuming both phases to be incompressible, the contact boundary conditions in their frictionless form are given as [5],

$$v_i^{sA} n_i^A + v_i^{sB} n_i^B = 0, \quad (137)$$

$$\left( \phi^{fA} v_i^{fA} + \phi^{sA} v_i^{sA} \right) n_i^A + \left( \phi^{fB} v_i^{fB} + \phi^{sB} v_i^{sB} \right) n_i^B = 0, \quad (138)$$

$$p^A - p^B = 0, \quad (139)$$

$$\sigma_{ij}^{EA} n_i^A n_j^A - \sigma_{ij}^{EB} n_i^B n_j^B = 0, \quad (140)$$

with  $n_i$  indicating the components of the unit normal on the contact surface. Physically, Eqs. (137),(138),(139) and (140) represent two kinematic conditions and two kinetic boundary conditions. Equation (137) indicates the continuity of the normal component of the solid phase velocity. This condition is necessary to maintain the contact of the tissues. The fluid mass passing from one tissue layer to the other across the contact must be conserved, which is dictated by Eq. (138). That equation is often interpreted as the continuity of a phase averaged mixture velocity. Equations (139) and (140) are derived from energy and mass balance equations. Equation (139) implies there cannot be a jump in the pressure over the contact area. Equation (140) requires the continuity of normal elastic traction. Adding Eqs. (139) and (140) provides a useful continuity condition on the total traction;

$$\sigma_{ij}^{TotA} n_i^A n_j^A - \sigma_{ij}^{TotB} n_i^B n_j^B = 0, \quad (141)$$

In biphasic contact the total load is shared by the fluid and solid phases. We can equivalently say that the total traction is shared by the normal elastic traction and pressure, since, considering Eq. (7),

$$\sigma_{ij}^{Tot} n_i n_j = -p + \sigma_{ij}^E n_i n_j. \quad (142)$$

Equation (142) indicates that in a frictionless contact only two of the three traction-related quantities, namely pressure, and normal components of elastic traction and total traction, are independent. Knowing two quantities enables the computation of the third and characterization of the load sharing at the contact. The penetration method is aimed at determining the normal components of elastic and total traction using the kinetic continuity conditions (Eqs. (139) and (140)), and computing pressure using Eq. (142). In the  $v$ - $p$  (or  $u$ - $p$ ) finite element formulation described in Chapter 4, the computed normal component of the total traction will reflect itself in a natural boundary condition (the first term at the right hand side of Eq. (56)), and pressure will be an essential boundary condition. That way the load sharing information that is consistent with kinetic contact continuity conditions will be imposed as boundary conditions on the appropriate faces of the models.

It is convenient to characterize the load sharing with one scalar quantity. Before going into the derivation, we define a load sharing parameter,  $\phi^s = \phi^* - 1$  that is defined as the ratio of the normal component of the elastic traction to the normal component of the total traction.

$$\phi^* = \frac{\sigma_{ij}^s n_i n_j}{\sigma_{ij}^{Tot} n_i n_j}. \quad (143)$$

The normal components of solid and fluid traction can be written in terms of  $\phi^*$  as

$$t_i^s n_i = \sigma_{ij}^s n_i n_j = \phi^* \sigma_{ij}^{Tot} n_i n_j, \quad (144)$$

$$t_i^f n_i = \sigma_{ij}^f n_i n_j = (1 - \phi^*) \sigma_{ij}^{Tot} n_i n_j. \quad (145)$$

From Eq. (142), pressure can be written as

$$p = \sigma_{ij}^E n_i n_j - \sigma_{ij}^{Tot} n_i n_j. \quad (146)$$

Substituting Eq. (146) into Eq. (2), the normal component of the solid traction can be written in the following form:

$$\sigma_{ij}^s n_i n_j = \phi^f \sigma_{ij}^E n_i n_j + \phi^s \sigma_{ij}^{Tot} n_i n_j. \quad (147)$$

Equation (143) can be rewritten using (147) as

$$\phi^* = \phi^s + \phi^f \frac{\sigma_{ij}^E n_i n_j}{\sigma_{ij}^{Tot} n_i n_j}, \quad (148)$$

According to Eq. (148), a  $\phi^*$  value of 1 indicates that the load is fully supported by the solid phase, and a value of  $\phi^s$  that the load is only supported by the pressure, in which case elastic traction is zero and only a fraction of pressure equal to  $\phi^s$  is carried by the solid phase (Eq. (2)).

The kinematic contact boundary conditions are not enforced directly. First, it is mathematically not possible to prescribe a Dirichlet and a Neumann boundary condition on a boundary for the same variable in a parabolic problem such as ours. Theoretically, it might be possible to develop an approximate method where contact of soft tissue layers is simulated by prescribing  $\mathbf{v}$  (instead of traction) and  $p$  on the contact surface. This approach looks unnatural since contact is more like a “creep” type of phenomenon dictated by the transfer of tractions across contact interface. Also, the accuracy of stress and strain is more significant for our purposes compared to displacement since these quantities are closely related with the mechanical performance of the cartilage.

#### 5.4 Derivation of the Approximate Boundary Conditions

In this section, we will approximate total traction and elastic traction making use of the experimental data to characterize contact. The mathematical part of the penetration method requires the joint kinematics and the geometry of the undeformed cartilage tissues as input data from visualization techniques. As the first step the tissue geometries are imported into a solid modeling package, creating mathematical representations of the tissues. Given a smooth joint motion and the corresponding kinematics data, the transformation information can be determined from Eq. (136) at any instant during the joint motion. The solid modeler has the capability to apply the transformation to the computer model of the cartilage tissue. Using kinematic data corresponding to the time point under consideration, and modeler operations, the undeformed cartilage models are positioned in a physiological orientation. In this position, the *in vivo* soft tissues are in contact and deformed. However, the undeformed solid models, when placed at the same position as the actual deformed tissues, will interpenetrate resulting to an overlap. This overlap that we refer to as “penetration” is quantitatively and qualitatively related to the total deformation that the cartilage layers experience in the intact joint.

We assume that the penetration can be treated as the actual deformation the tissues experience if it is quantified properly. Clearly, the penetration should be quantified as a vector field at discrete points that we will call “support points”. The solid modeler is utilized to determine the magnitude and direction of the vector at each support point as follows. The penetration that typically occurs between two tissues  $A$  and  $B$  as result of the above-mentioned modeling operation is graphically depicted in Fig. 15. Assume that the derivation is being made for tissue  $A$ , and that tissue  $B$  will analyzed in a separate step. A grid of support points is laid on the contact surface of  $A$ . We assume that, at each contact point, the tissue deforms perpendicular to the contact surface. Hence, the total penetration vector,  $\mathbf{g}^{Tot}$ , is measured in a direction normal to the contact surface at each support point. The local thickness of tissue  $A$  and tissue  $B$ ,  $h^A$  and  $h^B$ , respectively, are also measured along this normal direction. It is important to note that  $\mathbf{g}^{Tot}$  at each support point varies in time as tissue  $B$  moves relative to tissue  $A$ . Local thickness values, on the other hand stays constant throughout the motion.

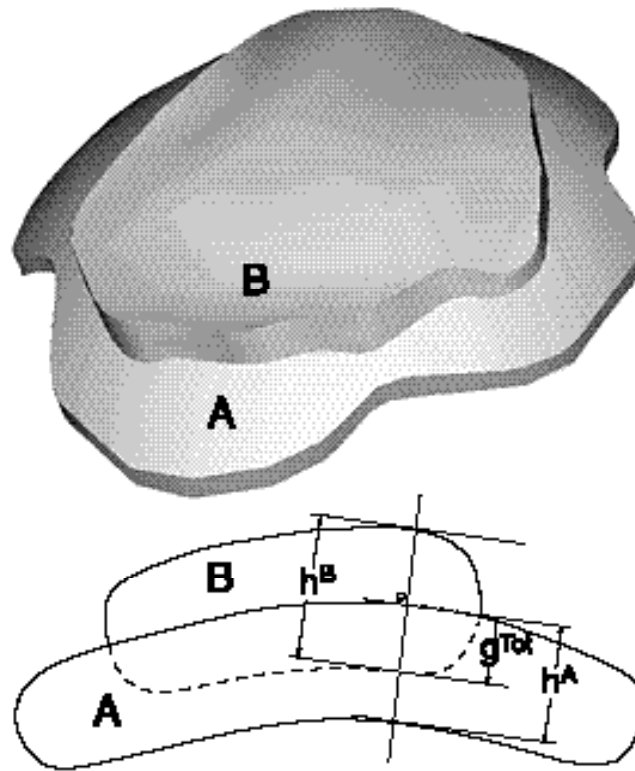


*Figure 15: Picture of overlapping cartilage models as obtained from the solid modeler (top). Definitions of geometric parameters in overlapped models(bottom).*

The fraction of  $\mathbf{g}^{Tot}$  experienced by tissue  $A$  should be determined to proceed with the analysis. For convenience, consider an orthogonal tangent-normal coordinate system defined on the loaded face of each layer, and denote the normal and tangential components of a vector with subscripts ‘ $n$ ’, ‘ $t_1$ ’ and ‘ $t_2$ ,’ respectively. By construction, the only non-zero component of  $\mathbf{g}^{Tot}$  is the normal component,  $g_n^{Tot}$ . Let  $0 \leq \eta \leq 1$  be the part of the total penetration that is associated with tissue  $A$ . In that case, the displacements of layers  $A$  and  $B$ , denoted by  $\mathbf{g}^A$  and  $\mathbf{g}^B$  respectively, are given by:

$$\mathbf{u}_n^A = \mathbf{g}_n^A = \eta \mathbf{g}_n^{Tot}, \quad (149)$$

$$\mathbf{u}_n^B = \mathbf{g}_n^B = (1 - \eta) \mathbf{g}_n^{Tot}, \quad (150)$$

$$\mathbf{u}_n^A + \mathbf{u}_n^B = \mathbf{u}_n^{Tot} = \mathbf{g}_n^{Tot}. \quad (151)$$

The parameter  $\eta$  will be evaluated from the continuity of elastic traction on the contact surface, Eq. (140). Note that  $\mathbf{g}^A$  and  $\mathbf{g}^B$  are by definition parallel to  $\mathbf{g}^{Tot}$  and only their normal components are non-zero<sup>2</sup>. In biphasic contact, for constant  $\phi^s$ , the variation of the pressure is relatively uniform through the thickness, a fact observed both in numerical [25] and semi-analytical [50] studies. Also, the first order term in an asymptotic solution for pressure in biphasic contact is not dependent on depth [6]. Thus, in view of Eq. (45), it is reasonable to assume that the normal component of the elastic strain is also relatively uniform through the thickness and can be approximated as

$$\epsilon_{nn}^{E^A} = \frac{\delta h^A}{h^A} = \frac{g_n^A}{h^A}, \quad (152)$$

where  $\delta h^A$  denotes the change in the local thickness of tissue due to deformation (Fig. 15).

There are no tangential components in the penetration vector. Although model curvature, or a gradient in the penetration vector with position, could cause in-plane strains, we show in the Appendix C that strains caused by these effects are negligibly small for *in vivo* joint geometries. Hence, we disregard any existing tangential strain. Also, for frictionless contact, the shear stresses on the contact surfaces are negligible.

---

<sup>2</sup> A vector that is normal to tissue  $A$  is, in general, not exactly normal to tissue  $B$ . However, for physiological geometries the error made through this assumption is negligibly small.

These assumptions are summarized as

$$\boldsymbol{\varepsilon}_{t_1 t_1}^E = \boldsymbol{\varepsilon}_{t_2 t_2}^E = \boldsymbol{\varepsilon}_{t_1 t_2}^E = 0 \quad \boldsymbol{\sigma}_{n_1}^E = \boldsymbol{\sigma}_{n_2}^E = \boldsymbol{\sigma}_{t_1 t_2}^E = 0. \quad (153)$$

The stress-strain law for a linear elastic material is expressed in indicial notation as

$$\sigma_{ij}^E = C_{ijkl} \varepsilon_{kl}^s. \quad (154)$$

Representing the solid phase of cartilage as transversely isotropic with the material axis normal to the tissue surface [20],[27], Eq. (154) can be expressed in matrix form as:

$$\begin{pmatrix} \sigma_{nn}^E \\ \sigma_{t_1 t_1}^E \\ \sigma_{t_2 t_2}^E \\ \sigma_{t_1 t_2}^E \\ \sigma_{n_1}^E \\ \sigma_{n_2}^E \end{pmatrix} = \begin{pmatrix} C_{11} & C_{12} & C_{13} & 0 & 0 & 0 \\ C_{12} & C_{22} & C_{23} & 0 & 0 & 0 \\ C_{13} & C_{23} & C_{33} & 0 & 0 & 0 \\ 0 & 0 & 0 & C_{44} & 0 & 0 \\ 0 & 0 & 0 & 0 & C_{55} & 0 \\ 0 & 0 & 0 & 0 & 0 & C_{66} \end{pmatrix} \begin{pmatrix} \varepsilon_{nn}^E \\ \varepsilon_{t_1 t_1}^E \\ \varepsilon_{t_2 t_2}^E \\ \varepsilon_{t_1 t_2}^E \\ \varepsilon_{n_1}^E \\ \varepsilon_{n_2}^E \end{pmatrix}, \quad (155)$$

where the terms in  $C_{ij}$  are related to five material parameters and the predominant material direction. Making use of Eqs. (149),(152)(153) and (155), the first term in Eq. (140) can be written as

$$\sigma_{ij}^{E^A} n_i n_j = C_{ijkl}^A \varepsilon_{kl}^{E^A} n_i n_j \quad C_{11}^A \varepsilon_{nn}^{E^A} = C_{11}^A \frac{g_n^A}{h^A} = C_{11}^A \frac{\eta g_n^{Tot}}{h^A}. \quad (156)$$

The same calculations are performed for tissue  $B$  in a similar manner, using Eq. (150), and yield the following expression for the second term in Eq. (140):

$$\sigma_{ij}^{E^B} n_i n_j = C_{ijkl}^B \varepsilon_{kl}^{E^B} n_i n_j \quad C_{11}^B \varepsilon_{nn}^{E^B} = C_{11}^B \frac{g_n^B}{h^B} = C_{11}^B \frac{(1 - \eta) g_n^{Tot}}{h^B}. \quad (157)$$

Substituting Eqs. (156),(157) into Eq. (140) and solving for  $\eta$  gives

$$\eta = \frac{1}{1 + \frac{C_{11}^A h^B}{C_{11}^B h^A}}, \quad (158)$$

which indicates that the penetration is shared between the layers on the basis of the local modulus and thickness of the contacting tissues (both of which may vary *in vivo*). Because of the variation in thickness values, each support point has an  $\eta$  value that varies

over the contact surface. Once  $\eta$  is known, the normal component of the elastic traction,  $\sigma_{ij}^{E^A} n_i n_j$ , can also be calculated at each support point using Eq. (156).

Note that for an isotropic solid phase,

$$C_{11} = H_A = (2\mu^s + \lambda^s), \quad (159)$$

where  $H_A$  is the aggregate modulus and  $\mu^s$  and  $\lambda^s$  are the Lamé parameters of the solid phase. In transversely isotropic models of cartilage, the axis perpendicular to the plane of isotropy is generally aligned along the surface normal due to the structure of the cartilage (See Chapter 1). Hence the material property matrix in Eq. (155) will preserve its sparsity and the above derivation is applicable also to transversely isotropic cartilage model.

Having obtained  $\sigma_{ij}^{E^A} n_i n_j$  the next step is to calculate the normal component of total traction acting on a tissue layer.

Total normal traction is made of elastic traction and pressure. The elastic traction part is directly related with the deformation of the solid phase. Pressure might seem unrelated to the deformation at the first instance. However, at any instant during the deformation the pressure distribution in the contact interface should be related to the distribution of the deformation. In other words, if the normal strain in the contact interface has a, say, parabolic distribution, the pressure distribution should be also reasonable close to a parabola. In fact, axisymmetric biphasic contact finite element studies confirm this observation, and we assume that the distribution of the normal component of the total traction over the contact area is linearly proportional to the normal component of the elastic strain. The relation between these quantities can be expressed using vectorial and indicial notation, respectively, as

$$\mathbf{t}^{Tot} = \gamma^A \frac{\mathbf{g}^A}{h^A}, \quad (160)$$

$$\sigma_{ij}^{Tot} n_i n_j = \gamma^A \frac{g_n^A}{h^A} = \gamma^A \epsilon_{nn}^{E^A}, \quad (161)$$

where  $\mathbf{t}^{Tot}$  is the vector of total traction and  $\gamma^A$  is a proportionality constant. Equation (160) requires that the total traction vector be parallel to the penetration vector, and therefore normal to the contact surface, consistent with the assumption of frictionless contact. It should be noted that in this approach even though  $\mathbf{t}^{Tot}$  and  $\mathbf{g}^A$  may vary over the contact surface  $\gamma^A$  does not.

We assumed  $\sigma_{ij}^{E^A} n_i n_j$  to be proportional  $\epsilon_{nm}^{E^A}$  in Eq. (156). Equation (161) implies a similar proportionality between  $\sigma_{ij}^{Tot} n_i n_j$  and  $\epsilon_{nm}^{E^A}$ . In the view of Eq. (142), this implicitly means that pressure is also proportional to  $\epsilon_{nm}^{E^A}$  at the contact surface, i.e.

$$p \quad \epsilon_{nm}^A = \frac{g_i^A}{h^A}. \quad (162)$$

The total force acting on a joint can be determined either through *in vivo* and *in vitro* experiment, or through a computer model involving the joint geometry, the geometry of the related connective tissues, such as muscles, tendons and ligaments, and their anatomical insertion sites. Then, for a given joint orientation the total force acting on the joint can be calculated using the force-displacement diagrams of the connecting tissues.

In this study the total force acting on the joint,  $\mathbf{F}$  (not to be confused with the deformation gradient  $\mathbf{F}$  of the previous chapters), is assumed to be known. It is obvious that the total traction when integrated over the contact interface should be equal to  $\mathbf{F}$ . Thus, for any component of the resultant force  $\mathbf{F}$  applied on the joint, we can write

$$t_i^{Tot} d^c = \gamma^A \frac{g_i^A}{h^A} d^c = F_i. \quad (163)$$

Note that in this calculation, to be able to perform the integration we use a fixed coordinate system, such as the cartesian coordinate system, rather than the tangent-normal coordinate system that varies locally. Note that all components of  $\mathbf{t}^{Tot}$  and  $\mathbf{g}$ 's are nonzero, in general, when expressed in a cartesian coordinate system. We calculate  $\gamma^A$  by requiring that the magnitude of the resultant force produced by the total traction be equal to the force applied to the joint kinetics,  $|\mathbf{F}|$ . This gives

$$|\mathbf{F}|^2 = \sum_{i=1}^3 F_i^2 = \sum_{i=1}^3 \gamma^A \frac{g_i^A}{h^A} d^c. \quad (164)$$

Considering  $\gamma^A$  is constant, the above equation can be solved for it to give

$$\gamma^A = \frac{|\mathbf{F}|}{\sqrt{\sum_{i=1}^3 \frac{\eta g_i^{Tot}}{h^A} d^c}}. \quad (165)$$

In the above derivation only the magnitude of  $\mathbf{F}$  is used, although experimental or numerical procedures might provide both the magnitude and the direction of the resulting

force. In our approach, the direction of the force is determined by the integral in Eq. (163). If the method is close enough to the actual joint kinematics it should produce a force direction that is also close to reality.

After finding  $\gamma^A$ , the total traction distribution can be calculated from Eq. (160). Knowing normal elastic traction and total traction reveals us how the total load is split between the phases. Substituting expressions for the elastic traction, Eq. (156), and the total traction, Eq. (161), into Eq. (148) gives the following expression for  $\phi^*$ :

$$\phi^* = \phi^s + \phi^f \frac{C_{11}^A}{\gamma^A} . \quad (166)$$

Equation (166) indicates that the penetration approach gives a constant load partitioning factor  $\phi^*$  over the contact interface for a homogeneous material. This is expected because both  $\sigma_{ij}^{E^A} n_i n_j$  and  $\sigma_{ij}^{Tot} n_i n_j$  are assumed to be linearly related to the  $\epsilon_{mn}^{E^A}$  such that the  $\epsilon_{mn}^{E^A}$  term in the numerator and denominator cancel out. If a different relationship (say quadratic) had been assumed for one of these quantities,  $\phi^*$  would have locally depended on the  $\epsilon_{mn}^{E^A}$  and been non-constant.

## 5.5 Extension to Hyperelastic Solid Phase

The approach taken for a nonlinear biphasic analysis is similar to the linear penetration derivation described in the previous section. Equation (148), which defines  $\phi^*$ , is general and does not make any assumption about the solid material law.

The deformation in a cartilage layer is within linear limits at small times. At longer times, as the fluid phase starts to move, the traction carried by the solid phase increases and the cartilage layers deform beyond linear limits. The mechanism involved in large deformation of cartilage is not any different than the one we observed in small deformation. As pointed out earlier, the stress through the cartilage thickness does not have large variations and the fluid phase movement occurs mostly laterally, leading gradually to a large deformation in the tissue at large times. Hence, it is reasonable to assume that the cartilage, even at large deformations, does not possess large gradients through the thickness. With that assumption it is possible to define the stretch using the experimentally determined quantities as

$$\lambda^A = 1 - \frac{g^A}{h^A} = 1 - \frac{\eta g^{Tot}}{h^A} , \quad (167)$$

where  $\lambda^A$  indicates the stretch experienced by tissue  $A$  and the remaining quantities are as defined in the linear penetration analysis. This stretch is oriented normal to the contact surface and the tangential stretches are neglected. Similarly,  $\lambda^B$ , the stretch experienced by the tissue  $B$  is given by

$$\lambda^B = 1 - \frac{g^B}{h^B} = 1 - \frac{(1-\eta)g^{Tot}}{h^B}. \quad (168)$$

Since the biphasic contact conditions, Eqs. (137) through (140), are valid for large deformation, we can still make use of the continuity of the elastic traction, Eq. (140), when splitting the penetration between layers  $A$  and  $B$ . This time, however, the relation between elastic stress and the penetration is nonlinear. Let  $f_{ET}^A$  and  $f_{ET}^B$  denote the nonlinear functions that relate the stretch along the surface normal to the normal elastic traction., i.e.:

$$\sigma_{ij}^{E^A} n_i^A n_j^A = f_{ET}^A(\lambda^A) \quad \sigma_{ij}^{E^B} n_i^B n_j^B = f_{ET}^B(\lambda^B). \quad (169)$$

With that notation, Eq. (140) is expressed as

$$f_{ET}^A(\lambda^A) = f_{ET}^B(\lambda^B). \quad (170)$$

This can be written as one nonlinear algebraic equation

$$f_{ET}^A(\lambda^A) - f_{ET}^B(\lambda^B) = F(\eta) = 0, \quad (171)$$

which needs to be solved for  $\eta$  numerically. Once  $\eta$  is known, in view of Eqs. (167) and (168),  $\lambda^A$  and  $\lambda^B$  can be calculated using the available geometric and penetration information, and normal component of the elastic traction can found for both tissue layers using  $f_{ET}^A$  and  $f_{ET}^B$ .

To calculate the total traction distribution we again assume a distributional relation between the total traction and the deformation at each contact point. Suppose that a linear relationship is observed between the total traction and a function of stretch, say,  $f_D^A$ . Mathematically this is expressed as

$$\mathbf{t}^{Tot} = \gamma^A f_D^A(\lambda^A), \quad (172)$$

or

$$\mathbf{t}^{Tot} = \gamma^A f_D^A(\lambda^A). \quad (173)$$

where  $\gamma^A$  is the proportionality constant. In a hyperelastic material, a change in the total traction should cause a disproportional change in stretch, hence  $f_D^A$  is in general a nonlinear function.

A vectorial equation analogous to Eq. (160) can be written as

$$\mathbf{t}^{Tot} = \gamma^A f_D^A(\lambda^A) \mathbf{n}, \quad (174)$$

recalling that the total traction is assumed to be parallel to the surface normal  $\mathbf{n}$ . Equation (174) is integrated to obtain a relationship with the total force  $\mathbf{F}$ .

$$t_i^{Tot} d^c = \gamma^A f_D^A(\lambda^A) n_i d^c = F_i. \quad (175)$$

As in the linear penetration analysis, using the magnitude of the resultant force known from experiment and Eq. (175),  $\gamma^A$  is found to be

$$\gamma^A = \frac{|\mathbf{F}|}{\sqrt{\sum_{i=1}^3 f_D^A(\lambda^A) n_i d^c}}. \quad (176)$$

Finally, from Eq. (148) the following expression for  $\phi^*$  can be derived using Eqs. (170) and (173).

$$\phi^* = \phi^s + \phi^f \frac{f_{ET}^A(\lambda^A)}{\gamma^A f_D^A(\lambda^A)}. \quad (177)$$

The function  $f_{ET}^A$  is determined uniquely from the hyperelastic law. On the other hand,  $f_D^A$  can be chosen in different ways based on observation, such that it expresses the relation between the total load and the deformation as precisely as possible.

As an example we can apply the above derivation to the hyperelastic material described by the Eq. (41). For this material, the relation between stretch and the elastic stress in a uniaxial deformation is given by (dropping the superscript  $A$ , for convenience)

$$\sigma_{nn}^E = \frac{1}{2} H_M \frac{\lambda^2 - 1}{\lambda^{2\beta+1}} e^{\beta(\lambda^2-1)}, \quad (178)$$

where  $H_M = 4 \mu_0 (\mu_1 + \mu_2)$  and  $\beta = \mu_1 + 2 \mu_2$ .  $H_M$  denotes the initial modulus of the material (i.e. at zero deformation). For demonstrational purposes, we define  $f_D$  as

$$f_D(\lambda) = \frac{\lambda^2 - 1}{2\lambda^{2\beta+1}} e^{\beta(\lambda^2-1)}. \quad (179)$$

This expression, in view of Eq. (178), is a quantification of the deformation. As pointed out before other choices based on numerical, analytical or experimental experience are possible.

Substituting Eqs. (178) and (179) into (177) gives the following simplification for  $\phi^*$

$$\phi^* = \phi^s + \phi^f \frac{H_M}{\gamma^A} . \quad (180)$$

Other choices for  $f_D$  might render the term in the bracket deformation dependent. In any case,  $\phi^f$  and  $\phi^s$  in Eq. (180) refer to current values under finite deformation and are functions of deformation, hence  $\phi^*$ , unlike in linear penetration analysis, is deformation-dependent.  $\phi^f$  and  $\phi^s$  can be approximated, again considering a unidirectional deformation and using Eq. (21), as

$$\phi^s = \frac{\phi_0^s}{\lambda} , \quad (181)$$

$$\phi^f = 1 - \frac{\phi_0^s}{\lambda} = \phi_0^f + \phi_0^s \left(1 - \frac{1}{\lambda}\right) , \quad (182)$$

where the subscript '0' indicates the undeformed values of the phase fractions. With that approximation  $\phi^*$  becomes

$$\phi^* = \frac{\phi_0^s}{\lambda} + \left( \phi_0^f + \phi_0^s \left(1 - \frac{1}{\lambda}\right) \right) \frac{H_M}{\gamma^A} . \quad (183)$$

For consistency, Eq. (183) should reduce to Eq. (166) as the deformation becomes infinitesimal. This can be easily shown to be the case.

### 5.5.1 Application and Computer Implementation

As previously noted, the penetration analysis described above is applied separately as a preprocessing step to both tissues in contact. In other words, the calculations above are repeated to obtain the contact boundary conditions for tissue *B*. To be consistent, the method should return a set of boundary conditions that satisfy Eqs. (139) and (140).

In the  $v$ - $p$  formulation of the biphasic tissue problem, the pressure and total traction boundary conditions are applied to enforce this load partitioning. Unlike true contact analysis, which requires nonlinear interaction between the two layers to resolve

the unknown area of contact, the inter-layer dependency of this penetration-based contact analysis occurs in the preprocessing stage. As a result, after preprocessing, the layers can be analyzed independent of each other.

The finite element formulation applies a finite difference scheme for time interpolation that is described in detail in Chapter 4. For a given motion, a set of contact boundary conditions are derived for each discrete time point and applied at the corresponding time step to simulate the relative movement of the contacting layers. The solid modeler package that is utilized in the penetration calculations is *Parasolid* which is interfaced to *Trellis*, the SCOREC finite element framework. The procedure described above is accomplished by using finite element libraries in *Trellis*, including the interface to *Parasolid*, in combination with stand-alone programming. An object-oriented computer code is designed and implemented to accomplish this preprocessing. Many *Parasolid* commands are invoked explicitly in the preprocessing software, while some are accessed through the *Trellis* interface in the computer code.

Finite element shape functions and mesh are used to perform certain calculations required by the penetration method. The penetration field (and thus the approximated deformation field) is expressed in terms of the finite element shape functions, and the integrals in Eq. (144) are evaluated numerically. The computer code creates as many files as there are time steps in the analysis. They contain the total traction information expressed on a grid of support points on the contact surface. In the finite element method, traction boundary conditions are applied at Gauss points of the mesh faces located in the contact surface. In general, these points do not coincide with the support points. Therefore, to determine the traction value at a non-support point, a simple bilinear interpolation is performed on the parametric coordinate system using the traction values at the neighboring support points.

# Chapter 6

## Linear Examples

### 6.1 Introduction

The penetration method is validated in this chapter using a canonical geometry that is an idealization of a physiological joint contact problem. The kinematic input data for this penetration example are obtained from a biphasic axisymmetric contact code [25] and treated as if they originated from visualization data for a joint experiment. Following validation, the method is demonstrated on physiological shoulder geometries.

### 6.2 Canonical Examples

The penetration method has been validated for the short-time response of two canonical problems whose geometry and properties resemble the glenohumeral joint in the shoulder. The definitions of problem geometry and geometric parameters are shown in Fig. 16; Table 2 gives the values used in this study. The lower and upper tissue layers in each case are referred to as  $A$  and  $B$  respectively. The radii of curvature of the articular and bone surfaces are referred to as  $R_{Ac}$  and  $R_{Ab}$ , respectively, for the lower layer, and  $R_{Bc}$  and  $R_{Bb}$  for the upper layer. The thickness of layers  $A$  and  $B$  at the axis of rotation are  $t_B$  and  $t_A$ . For case CT the thickness is constant through the layer, and for case VT the thickness varies with radial position. Layers of rigid, impermeable bone support the cartilage layers; the lower bone supporting structure is fixed and an axially directed force is applied to the upper tissue layer through the bone. Note that the bone is not modeled explicitly, but rather used to transmit boundary conditions and load. The first geometric model consists of two tissues having the same thickness, but different radii of curvature; in the second model, tissue  $A$  is 50% thicker than tissue  $B$ . Note that tissue thickness varies with position from the axis of rotation. We quantify the congruency of contact as follows:

$$\frac{1}{R_{Bc}} - \frac{1}{R_{Ac}} = \frac{1}{\text{congruency}}$$

The first example (CT) is more congruent than the second (VT).

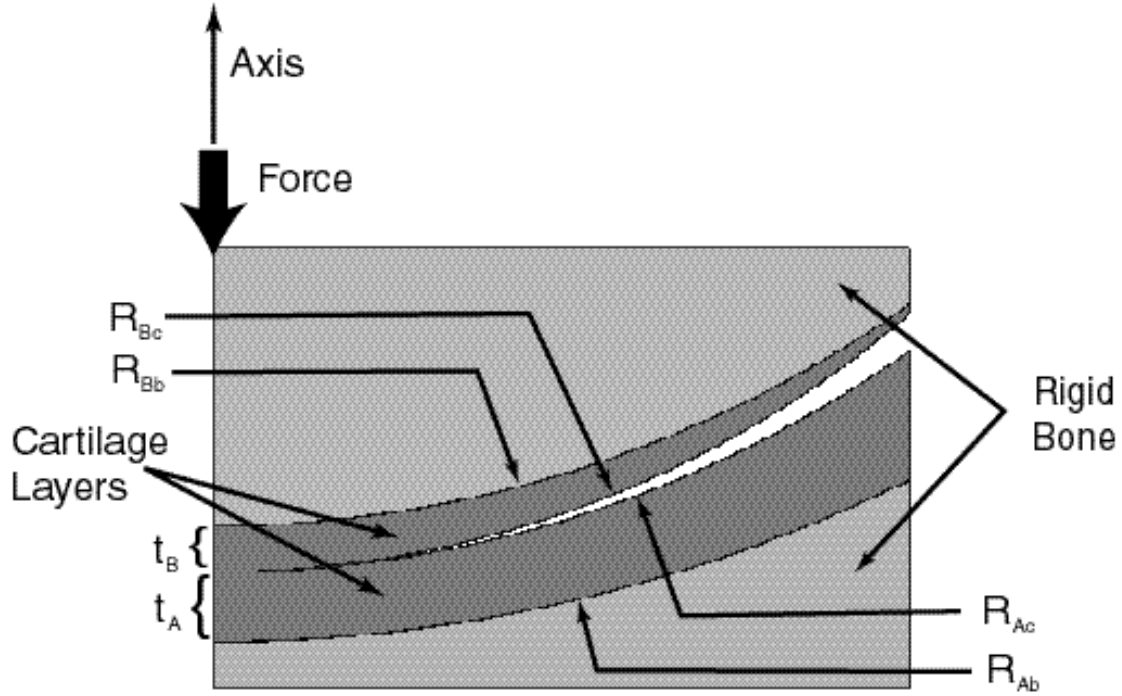


Figure 16: Problem definition and geometry for the 2-D biphasic contact and 3-D penetration-based analyses. Cartilage layers (dark gray) are attached to rigid bone (light gray). A force is applied along the axis of symmetry. The centerline thickness of layer A and layer B, and radii of curvature are defined.

Table 2: The values of geometrical parameters defined in Figure 2 for cases CT and VT.

Case	$R_{Ac}$ (mm)	$R_{Ab}$ (mm)	$R_{Bc}$ (mm)	$R_{Bb}$ (mm)	$t_A$ (mm)	$t_B$ (mm)	congruency (mm)
CT	26	26	25	25	1.0	1.0	650
VT	26	34	23	26	1.5	1.0	200

The canonical cases are run with two different sets of material properties to test the penetration method in this situation. The case where both layers have the same material properties is referred as CP. In this case, both tissues have a solid phase Young's modulus,  $E$ , of 556 kPa, solid phase Poisson's ratio,  $\nu$ , of 0.05, permeability,  $k$ , of  $1.7 \times 10^{-15} \text{ m}^4/\text{Ns}$  and solid content,  $\phi^s$ , of 0.25. To understand the influence of variable material properties on the preprocessing calculations, the same problems were also run

with Young's modulus halved in layer *B*. In this second case, referred to as VP, the material properties of tissue *A* are the same as in Case CP, but the tissue *B* has a Young's modulus of 278 kPa, half of the value of tissue *A*. A force of 75 N is applied to the rigid bone of the upper layer over a linear 1.0 sec. ramp, then held constant for an additional 1.0 sec. Simulations were carried out for the full 2.0 sec. time period.

Each configuration is first analyzed using the 2-D axisymmetric biphasic contact finite element [26], serving in this validation as the "experimental" data for the penetration-based method, from which the displacement of the upper rigid body at  $t = 2.0$ s is computed. This computed displacement value is then applied within the solid modeler to the upper layer of the 3-D solid model, allowing it to rigidly penetrate the lower layer of the model. Preprocessing starts by quantifying this penetration. After obtaining the total traction and elastic traction, as described earlier, the corresponding 3-D analysis is run using a time step of  $t = 0.1$  s. Results obtained at  $t = 1.0$  sec. are compared with those obtained from the 2-D biphasic contact analysis.

### 6.2.1 Results for Case CT

Case CT constitutes a highly congruent geometry, and the radii of curvature for the contacting tissues are close to those of a human shoulder joint. In addition to validating the penetration method by comparison to a 2-D axisymmetric biphasic contact analysis, case CT is used to demonstrate the self-consistency of the penetration method, in terms of the satisfaction of the contact boundary conditions, and the validity of the assumptions used in deriving the penetration method.

Figures 17 and 18 compare the pressure and normal elastic traction distribution on the contacting faces of tissues *A* and *B* for cases CP and VP, respectively. Note that on these faces, pressure and normal elastic traction are boundary conditions originating from the penetration analysis. The pressure and normal elastic traction have similar distributions on the contacting tissues, indicating that the penetration method produces boundary conditions that are consistent with the kinetic contact continuity requirements, Eqs. (139) and (140).

The kinematic contact conditions, Eqs (137) and (138), are not directly enforced by the penetration method. Rather, the displacement and velocity results in the zone of contact are computed by the independent 3-D biphasic analyses. It is therefore important to determine if the deformation of the tissues is consistent with contact.

In the full biphasic contact analysis, layers *A* and *B* are in contact only along at the center ( $r=0$ ) before the load is applied. Away from this point, there is a gap between

the layer geometries that becomes larger with increasing radial distance. In contact, the displacements of layers *A* and *B* should match exactly at the axial contact point. Farther from that point, the tissue layers first deform without contacting each other, closing the local gap, and then start to deform together. The axial displacement results in the contact region of tissues *A* and *B*, obtained from the penetration-based 3-D biphasic analysis appear to support this behavior. The axial displacement results shown in Fig. (19) for case CP indicate a relatively close match between the axial displacement values close to the axis. The small deviation between the curves at this point indicates that layer *A* is displaced slightly more than layer *B* leaving a small gap. Considering the approximate nature of the method, this error is found to be reasonably small. Away from the initial contact point, the compressive displacement of layer *A* decreases, reaching positive displacement values eventually. This corresponds to the ‘bulging’ of the tissue commonly observed in biphasic materials. Layer *B* bulges less since it is convex rather than concave. Still, around  $r = 5$  mm, layer *B* experiences minimal displacement. That means that the model gap at this point is closed mostly by the upward bulging of layer *A*. For case VP, as shown in Fig. (20), the displacement mismatch tends to become larger if one of the tissues is significantly more compliant than the other. However, the displacement behavior of individual layers is the same; bulging is still more prominent on layer *A*.

In general, it is observed that the velocity, being the derivative of displacement, tends to fluctuate more than the displacement. Figure (21) shows the normal velocity distribution of layers *A* and *B* for case CP originating from a more refined penetration analysis where the change in the contact area during ramp phase has been taken into account. While this pushes the velocity values towards more meaningful numbers, the mismatch between the results for layers *A* and *B* seems to be still high for this quantity. The error close to the edge of the contact is generally large because, unlike contact analysis, there is no ‘opposing tissue’ in the penetration analysis that constrains the velocity. Similar to what is observed for displacement, the error for velocity is larger for case VP (Fig. (22)).

Figures (23) and (24) compare the magnitude of the elastic traction on layers *A* and *B* for cases CP and VP, respectively, with the corresponding shear stress components in the planes parallel to the axis. In frictionless contact, all shear stress components should vanish at the contact interface. The penetration-based analysis gives shear stress values that are much smaller than the elastic traction, indicating that the applied loading is a close approximation to frictionless contact.

In general, it can be said that the penetration method satisfies the kinetic contact continuity requirements well. The kinematic conditions are not directly enforced and the performance of the penetration-based analysis in satisfying those is mixed. While the displacement shows a reasonable consistency with contact, the error in the velocity seems to be higher. For our purposes, the kinetic consistency of the method is more important since stress-like quantities are of greater importance to evaluate the mechanical performance of the articular cartilage.

The next set of figures compares the results of the penetration-based 3-D biphasic analysis directly with those originating from the 2-D axisymmetric contact analysis. Figures 25 and 26 show the total traction distribution on tissue *A* for case CP, and on tissue *B* for case VP. Total traction also originates from the penetration analysis and it is seen that the peak value is overestimated significantly using the penetration method compared with the corresponding results of the contact analysis. In contact, part of the contact area forms due to a bulging effect. In the penetration method, this effect cannot be fully captured due to the nature of the method (i.e. the fact that we are dealing with undeformed models). As a result, the penetration method, in general, underestimates the contact area. The same force when distributed to a smaller contact area gives rise to a higher total traction value, something we consistently observed in the canonical examples.

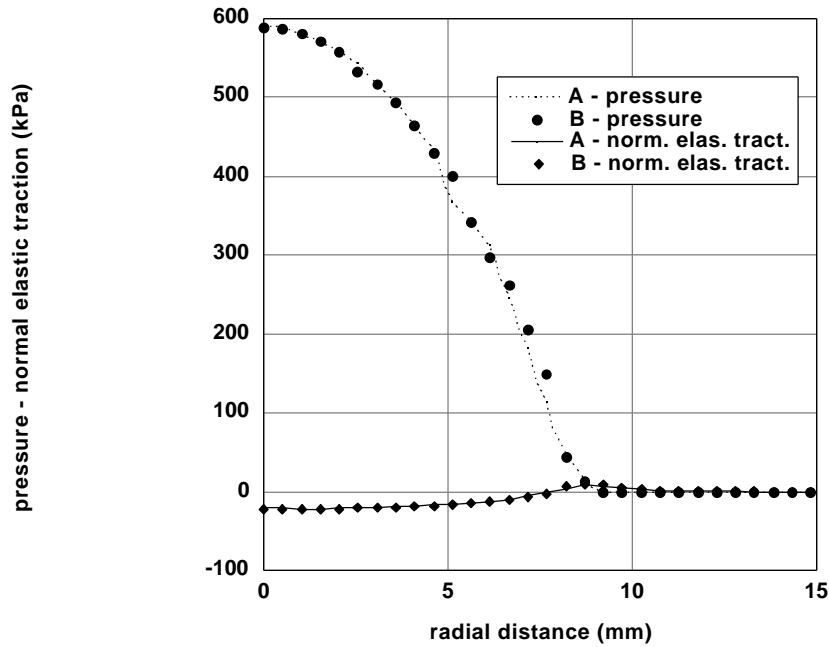


Figure 17: Case CT-CP, comparison of pressure and normal elastic traction distribution on layers A and B,  $t = 1$  sec.

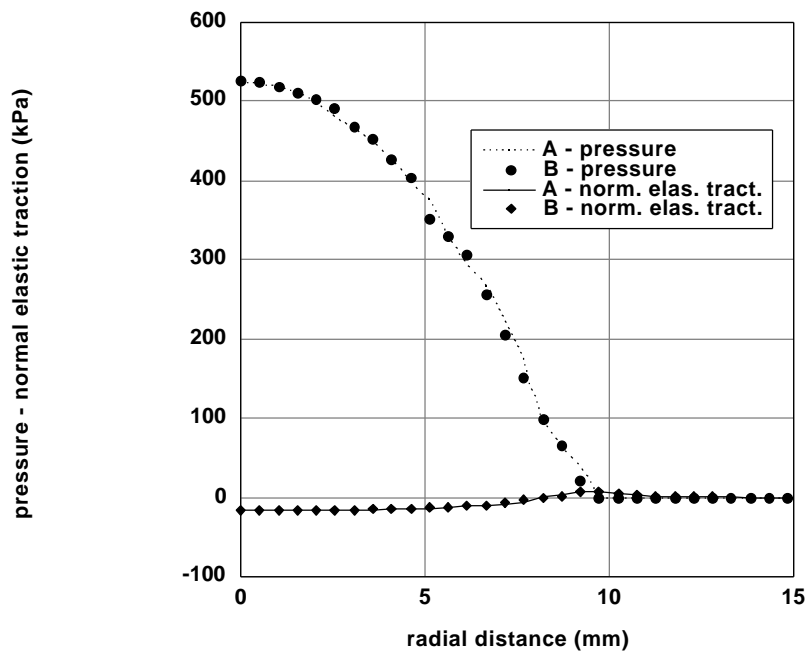


Figure 18: Case CT-VP, comparison of pressure and normal elastic traction distribution on layers A and B,  $t = 1$  sec.

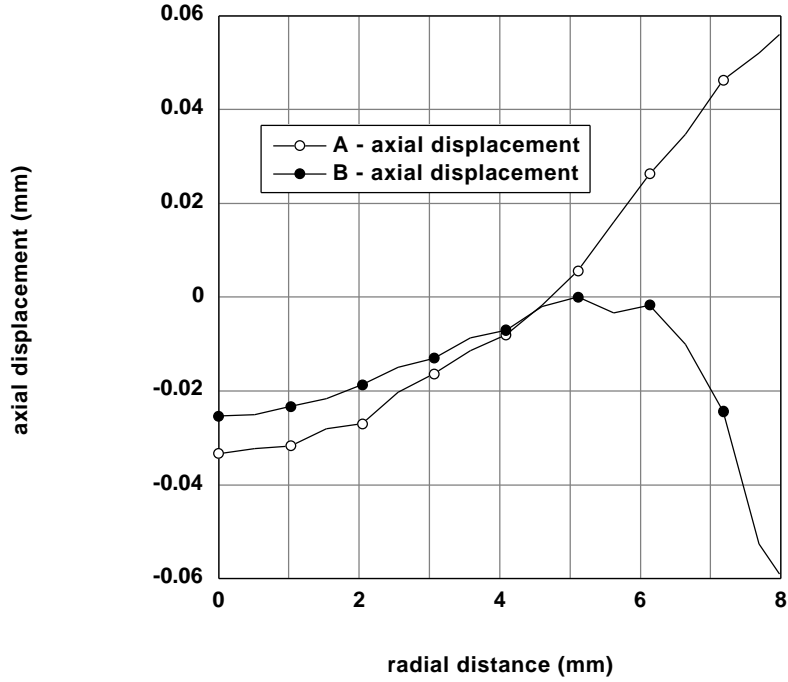


Figure 19: Case CT-CP, the axial displacement at the contact interface of layers A and B,  $t = 1$  sec.

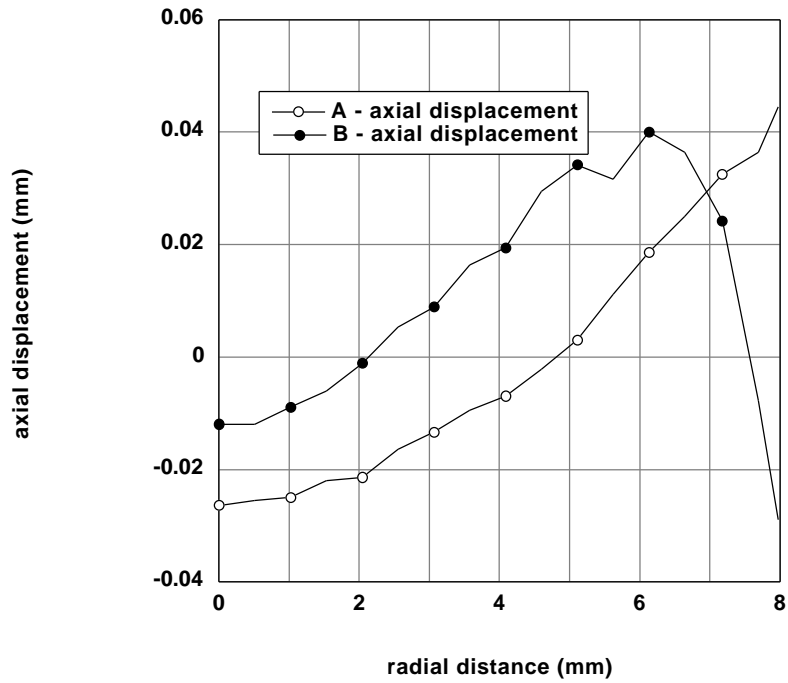


Figure 20: Case CT-VP, the axial displacement at the contact interface of layers A and B,  $t = 1$  sec.

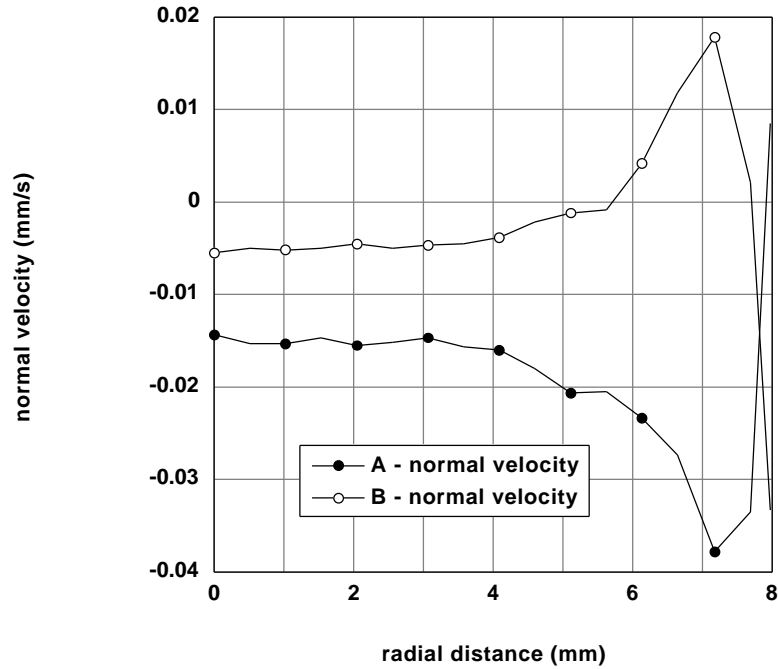


Figure 21: Case CT-CP, the normal velocity at the contact interface of layers A and B,  $t = 1$  sec.

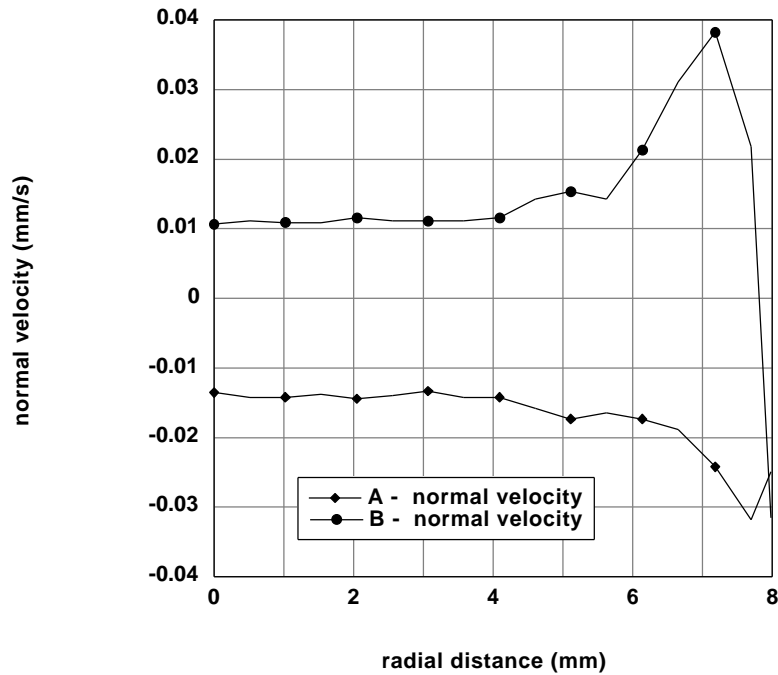


Figure 22: Case CT-VP, the normal velocity at the contact interface of layers A and B,  $t = 1$  sec.

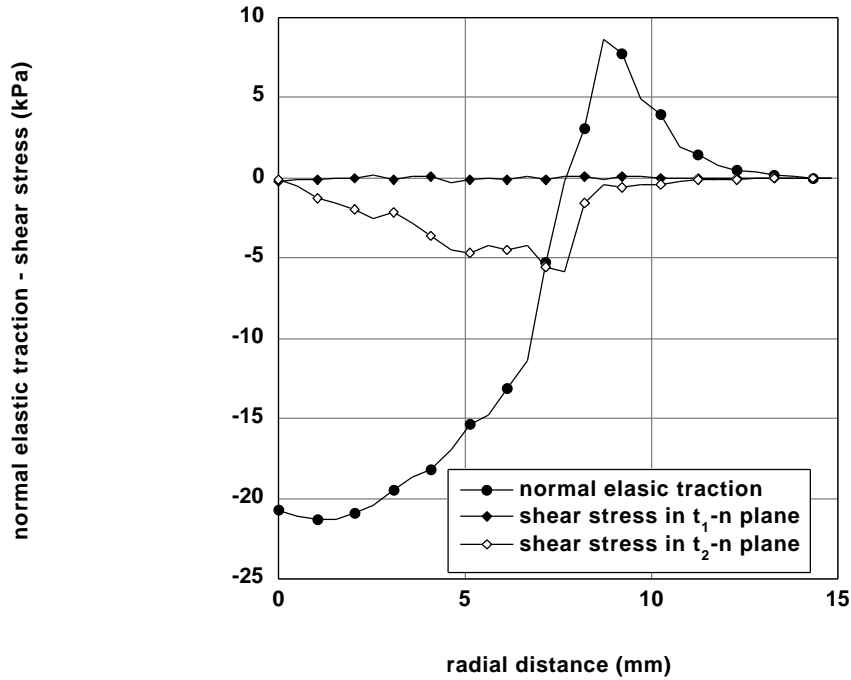


Figure 23: Case CT-CP, tissue A, comparison of the normal elastic traction with the shear stress components in the planes along the normal direction,  $t = 1$  sec.

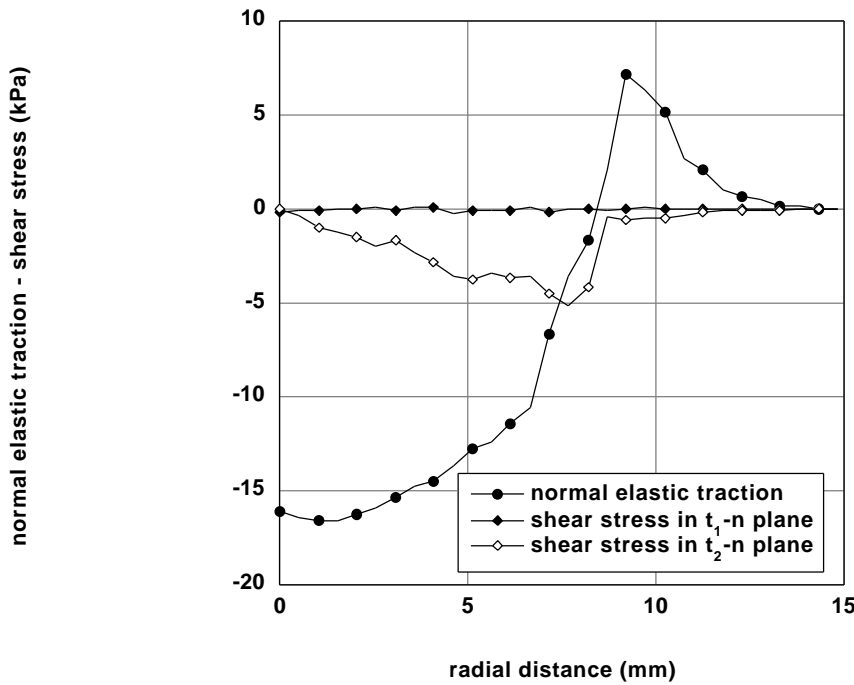


Figure 24: Case CT-VP, tissue B, comparison of the normal elastic traction with the shear stress components in the planes along the normal direction,  $t = 1$  sec.

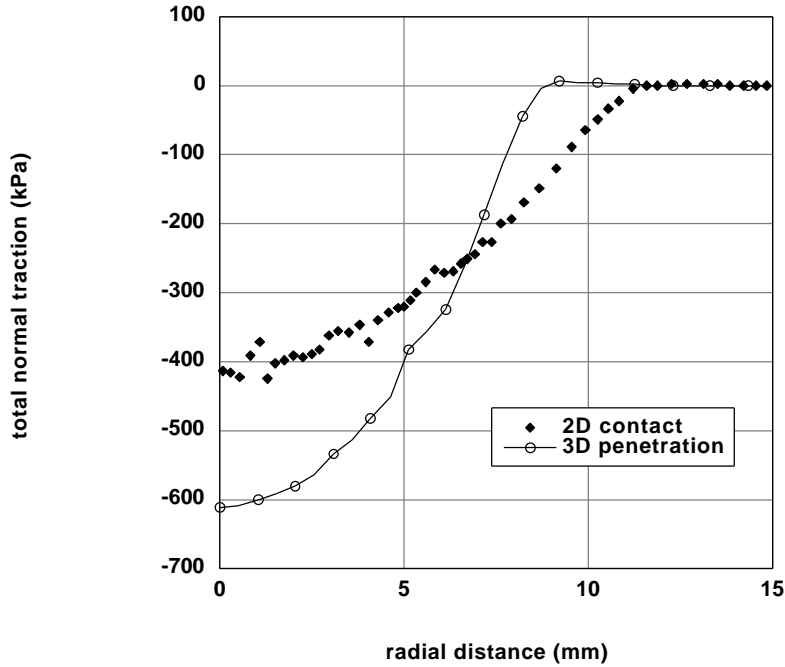


Figure 25: Case CT-CP, tissue A, total normal traction distribution from 3D penetration compared with 2D contact finite element analysis result,  $t = 1$  sec.

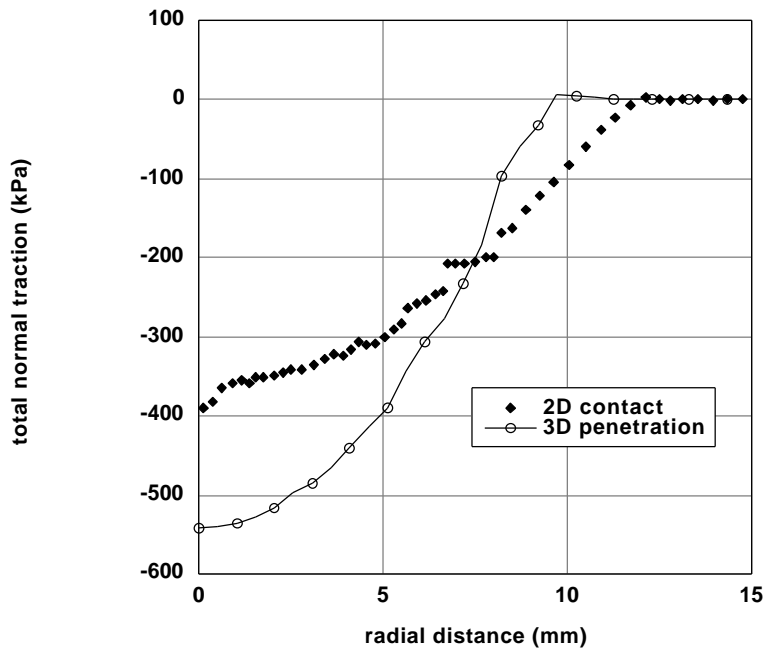


Figure 26: Case CT-VP, tissue B, total normal traction distribution from 3D penetration compared with 2D contact finite element analysis result,  $t = 1$  sec.

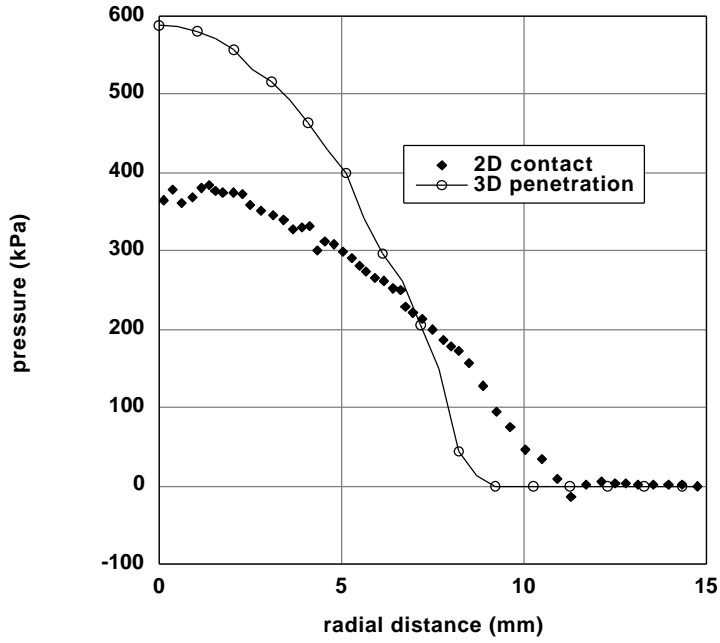


Figure 27: Case CT-CP, tissue B, pressure distribution from 3D penetration compared with 2D contact finite element analysis result,  $t = 1$  sec.

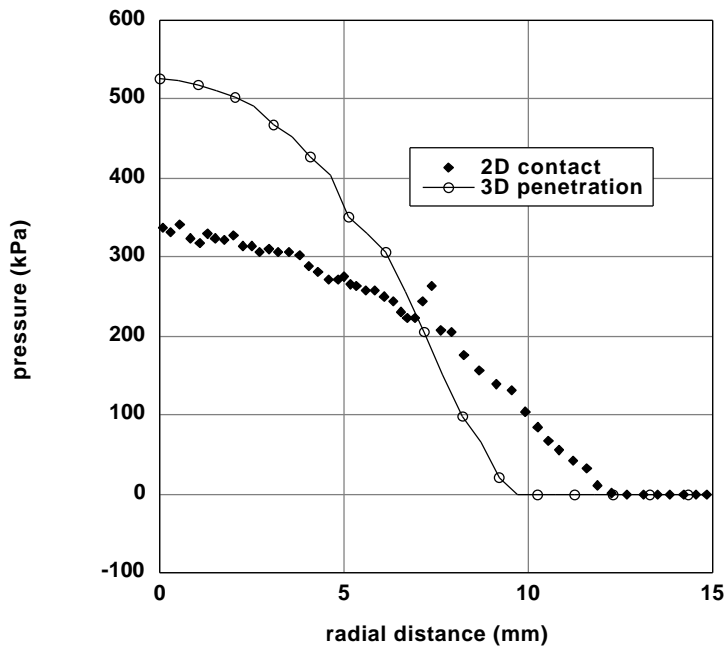


Figure 28: Case CT-VP, tissue B, pressure distribution from 3D penetration compared with 2D contact finite element analysis result,  $t = 1$  sec.

A similar trend is observed in the contact pressure values. Figures 27 and 28 display typical pressure results where it is clear that the penetration method overestimates the pressure on the contact interface.

Normal elastic traction distribution, particularly the peak values, on layers *A* and *B* for cases CP and VP compare well with values obtained from axisymmetric contact analysis, as depicted on Figures 29 through 32. Note that the elastic traction, in general, is much smaller compared to the total traction in magnitude; hence the contact analysis result for this quantity looks scattered. Recall that in the penetration analysis, the normal elastic stress is assumed to be relatively uniform through the thickness and calculated accordingly from penetration, tissue thickness and the modulus (See Eq.(156)). The results confirm that this assumption is reasonably close to reality for this particular geometry. The effect of the underestimated contact radius is again visible as we approach the edge of the contact region.

Figures 33-36 show the axial displacement results on tissues *A* and *B* for cases CP and VP. In this figure, the displacement values are expressed relative to the rigid bone underlying layer *A* in each case to facilitate comparison with the contact analysis. In the finite element analysis, axial displacement is a calculated quantity and not a prescribed one. Recall that, the axial translation of the rigid bone underlying layer *B* obtained from the contact analysis provided the input data to derive the tractions in the penetration preprocessing. As seen the penetration-based finite element analysis returns displacement values close to those that are initially used in the penetration method, implying the consistency of the penetration approach as a whole. Another feature that is captured qualitatively is the positive displacements at the edge of contact.

Normal velocity on layers *A* and *B* for case CP, as shown in Fig. 37, deviate from each other in both approaches which is consistent with what is observed in Figs. 21-22. The sudden change close to the edge of contact is qualitatively captured by the penetration method. For case VP, the contact analysis results start to become scattered hence a comparison for that case is not shown here. Case VP appears to constitute a more difficult numerical problem for the contact analysis.

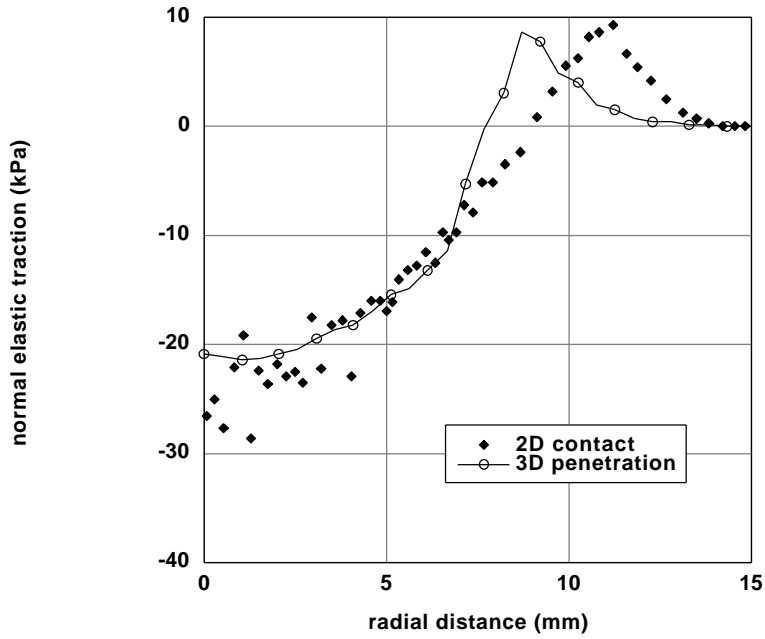


Figure 29: Case CT-CP, tissue A, normal elastic traction distribution from 3D penetration compared with 2D contact finite element analysis result,  $t = 1$  sec.

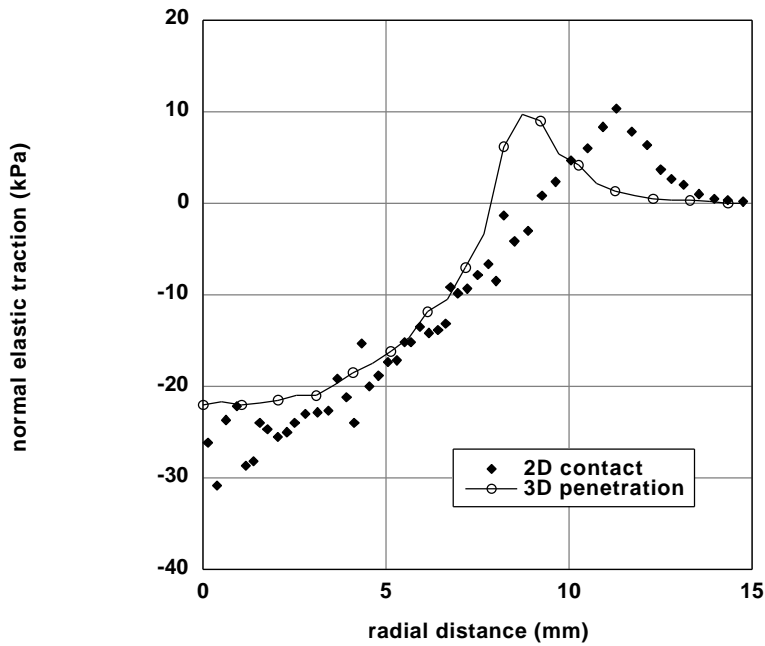


Figure 30: CT-CP, tissue B, normal elastic traction distribution from 3D penetration compared with 2D contact finite element analysis result,  $t = 1$  sec.

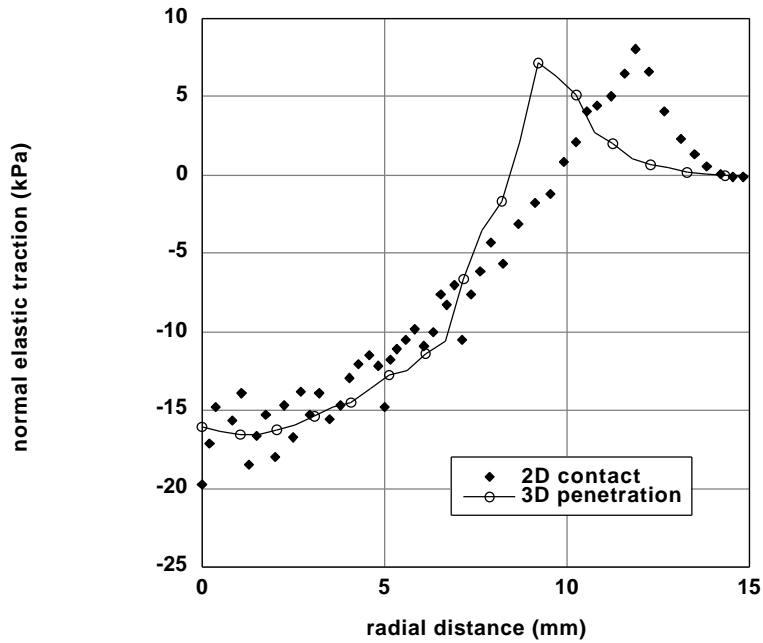


Figure 31: Case CT-VP, tissue A, normal elastic traction distribution from 3D penetration compared with 2D contact finite element analysis result,  $t = 1$  sec.

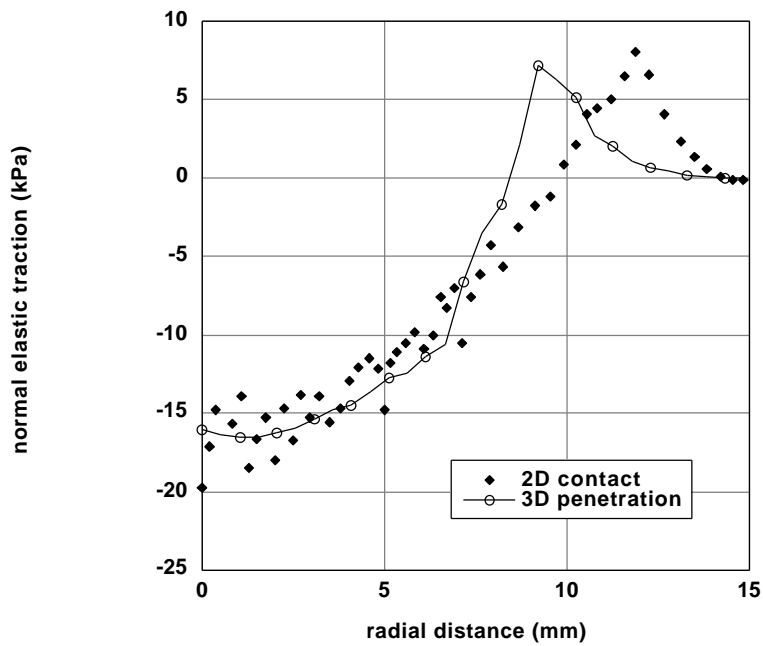


Figure 32: Case CT-VP, tissue B, normal elastic traction distribution from 3D penetration compared with 2D contact finite element analysis result,  $t = 1$  sec.

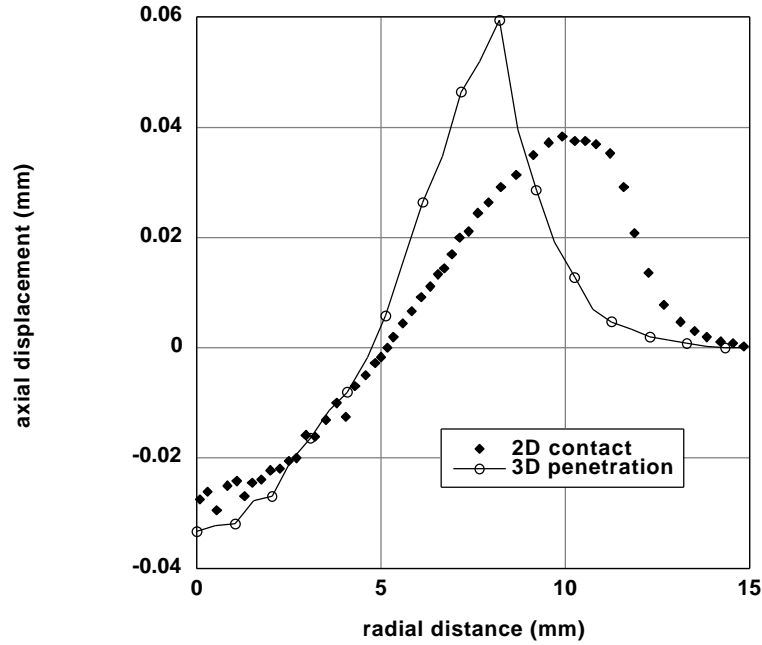


Figure 33: Case CT-CP, tissue A, axial displacement from 3D penetration compared with 2D contact finite element analysis result,  $t = 1$  sec.

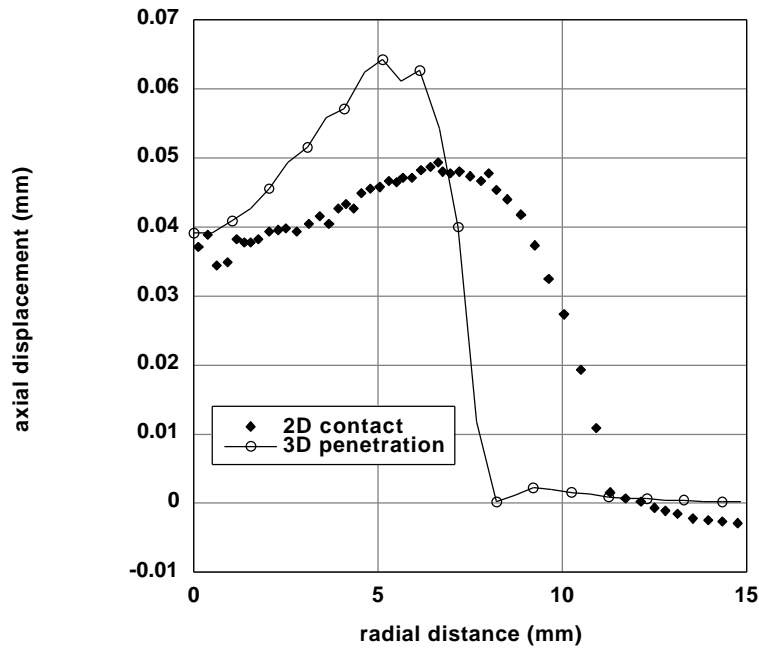


Figure 34: Case CT-CP, tissue B, axial displacement from 3D penetration compared with 2D contact finite element analysis result,  $t = 1$  sec.

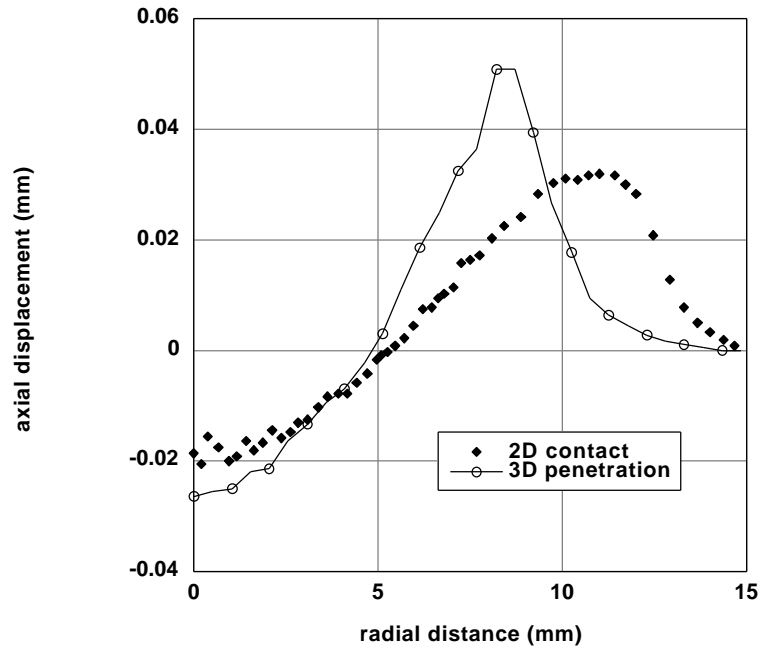


Figure 35: Case CT-VP, tissue A, axial displacement from 3D penetration compared with 2D contact finite element analysis result,  $t = 1$  sec.

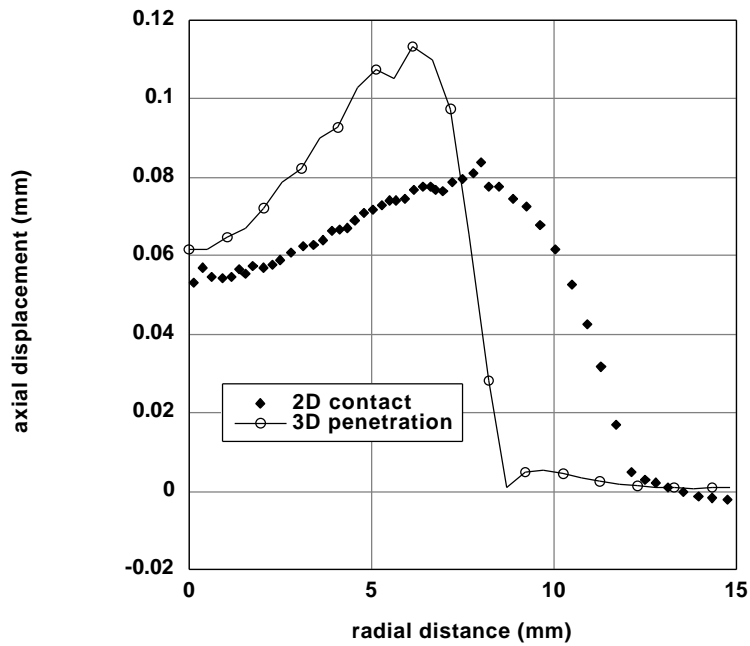


Figure 36: Case CT-VP, tissue B, axial displacement from 3D penetration compared with 2D contact finite element analysis result,  $t = 1$  sec.

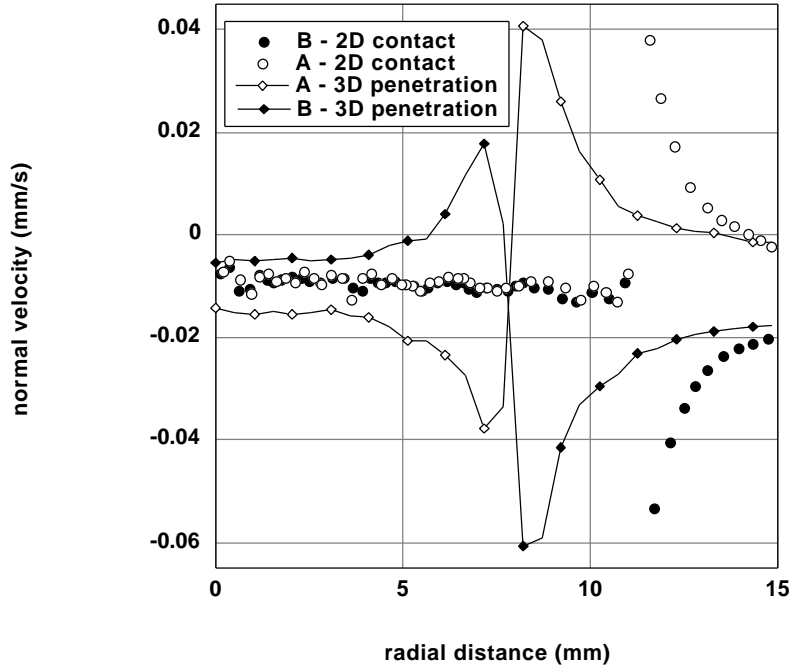


Figure 37: Case CT-CP, normal velocity from 3D penetration compared with 2D contact finite element analysis result,  $t = 1$  sec.

### 6.2.2 Results for Case VT

Case VT constitutes a pair of contacting layers with nonuniform thickness values and a lower congruency. Along the axis of rotation, the thickness of tissue A is 50% larger than tissue B. While the non-uniformity in thickness resembles actual joints, such as the glenohumeral joint, the low congruency is physiologically atypical. Our main purpose is to evaluate the performance of the penetration method on a more complex geometry.

Comparing the distribution of pressure and normal elastic traction on the contacting layers reveals that the method still satisfies the kinetic contact continuity requirements (Figs. 38 and 39), despite a small deviation in the normal elastic traction distribution. Total normal traction (Figs. 40 and 41) and pressure (Figs. 42 and 43) deviate less from axisymmetric contact analysis compared to the same comparisons for Case CT. This is expected since in a less congruent geometry the error in predicting the contact radius due to the bulging effect is smaller.

Considering the normal elastic traction, the accuracy of the results seems to differ from layer A to layer B. While the distribution for tissue B for both CP (Fig. 45) and VP

(Fig. 47) compares reasonably well with the contact finite element results, there seems to be significant deviation for tissue *A* (Figs. 44 and 46).

Interestingly, in the axial displacements we observe the opposite trend. The axial value (at  $r = 0$ ) is relatively close to the contact solution for tissue *A* for both sets of material properties (Figs. 48 and 50) while the deviation is significant for tissue *B* (Figs. 49 and 51).

### 6.2.3 Evaluation of the Penetration Analysis Results

It can be concluded that for Case VT our assumptions to derive the penetration method are less valid compared to Case CT. The assumption that the normal strain does not vary much through the thickness starts to lose its validity. This is more true for layer *A*, considering the large deviation in normal elastic traction despite the relatively good match in axial displacement that we observe in this tissue.

The accuracy of normal elastic traction in Case CT is significant and encouraging. It is well known that pressure (or any isotropic stress state, in general) does not contribute to the failure of solid materials. With respect to cartilage mechanics, the elastic stress, rather than the solid stress is the quantity that needs to be addressed when correlating loading to the tissue damage. The overestimated pressure on the contact interface is not a significant drawback as long as the normal elastic traction is approximated reasonably well.

It should be kept in mind that the results displayed in this chapter target merely a comparison between penetration method and contact finite element analysis. The 2-D axisymmetric contact analysis that we utilized is still a numerical approximation and should not be treated like an “analytical solution”. In fact, especially for the case VT, the contact finite element analysis gives results that are more scattered. Moreover, pair-wise comparison of Figs. 44 and 45, and Figs. 46 and 47, reveals that it also deviates from the kinetic contact continuity requirements, as does the corresponding penetration-based finite element analysis. Remember that the continuity requirements are well-satisfied on case CT by both penetration and contact finite element approaches. Clearly, case VT constitutes a problem harder to handle numerically.

The 2-D axisymmetric finite element code employed in this work is based on a penalty formulation, which is the simplest possible approach for contact finite element formulation. Penalty finite element methods do not introduce any additional field to the problem in order to satisfy the contact constraints. Their drawback is the presence of a highly problem-dependent penalty parameter and the associated lack of robustness. A

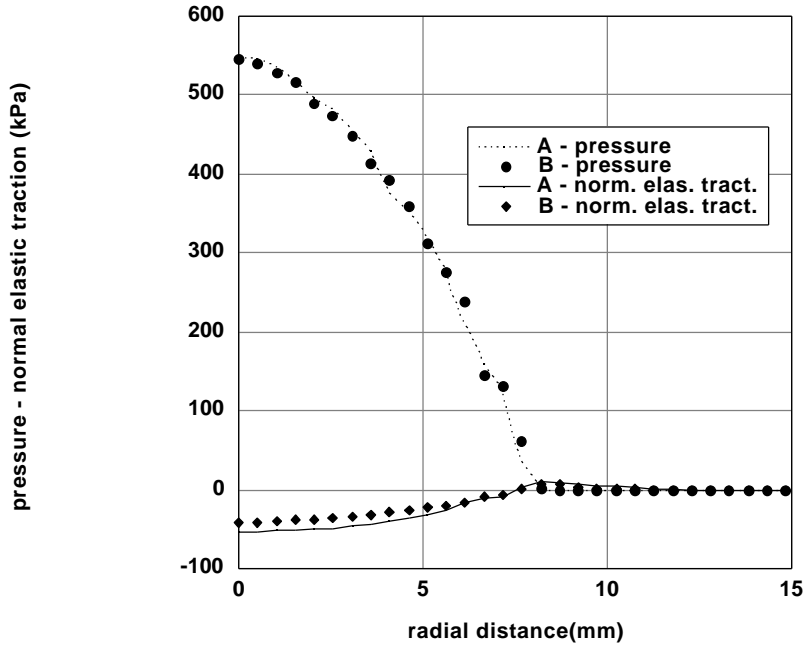


Figure 38: Case VT-CP, comparison of pressure and normal elastic traction distribution on layers A and B,  $t = 1$  sec.

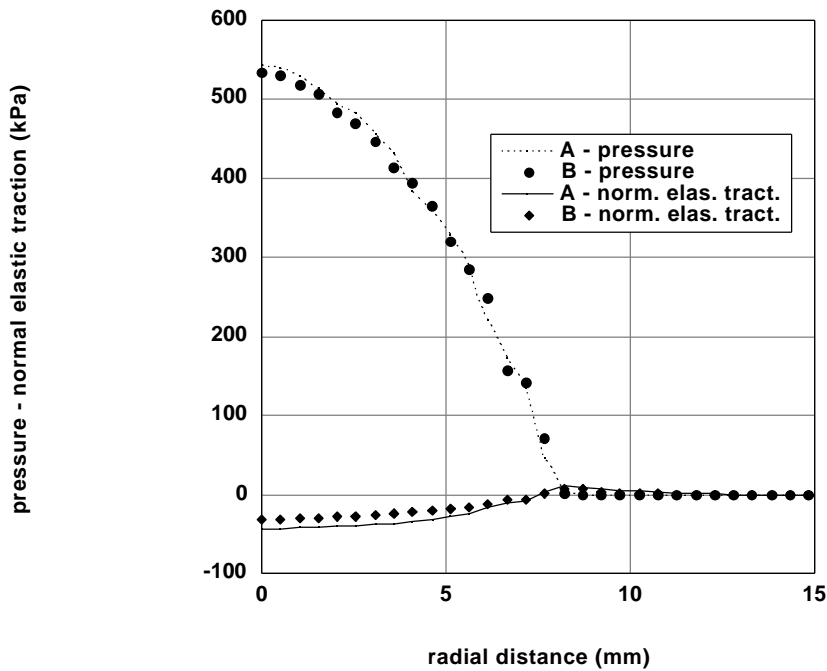


Figure 39: Case VT-VP, comparison of pressure and normal elastic traction distribution on layers A and B,  $t = 1$  sec.

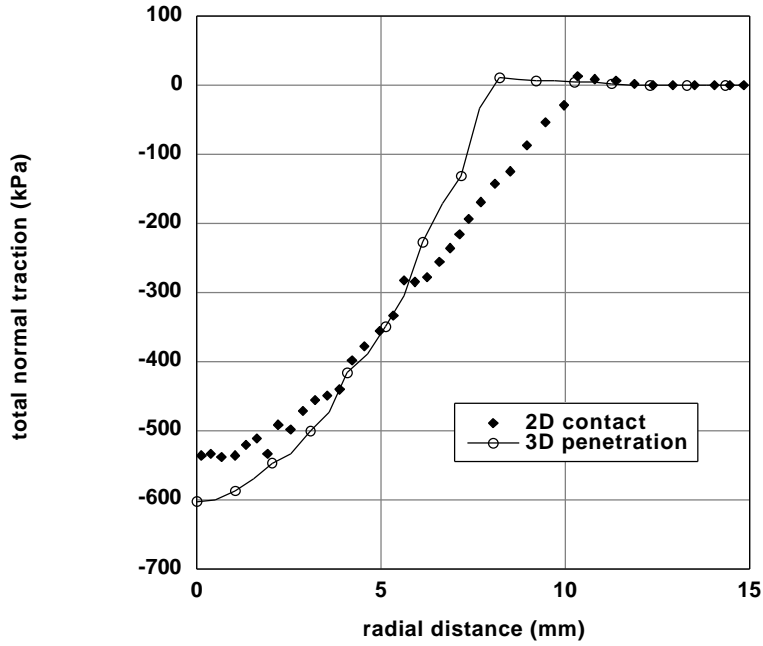


Figure 40: Case VT-CP, tissue A, total normal traction distribution from 3D penetration compared with 2D contact finite element analysis result,  $t = 1$  sec.

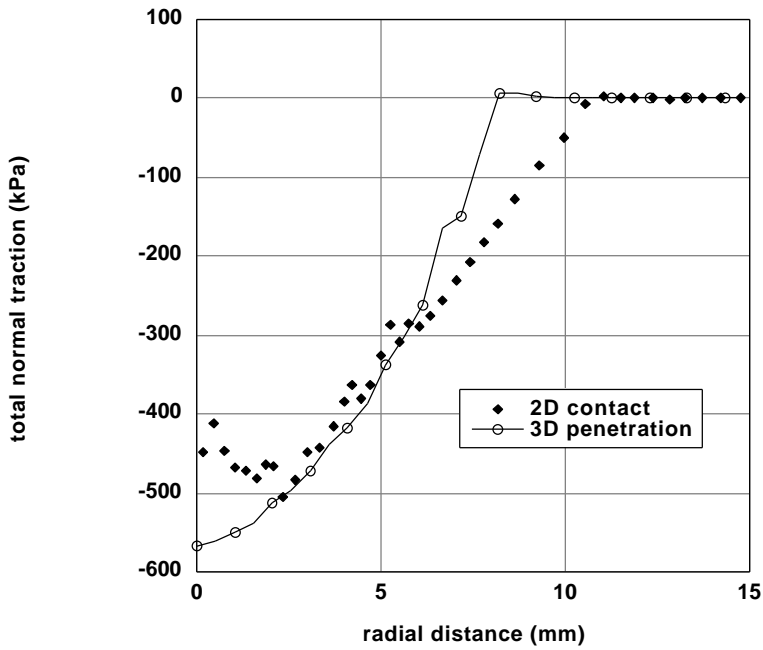


Figure 41: Case VT-VP, tissue B, total normal traction distribution from 3D penetration compared with 2D contact finite element analysis result,  $t = 1$  sec.

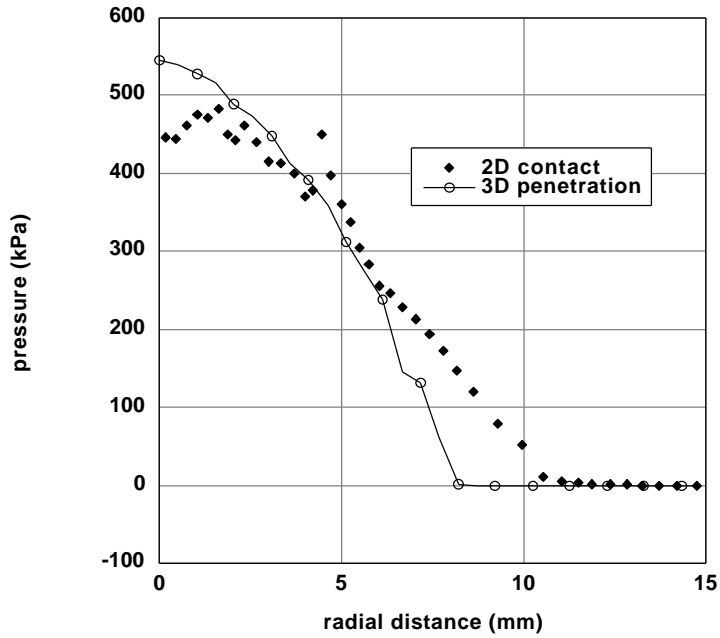


Figure 42: Case VT-CP, tissue B, pressure distribution from 3D penetration compared with 2D contact finite element analysis result,  $t = 1$  sec.

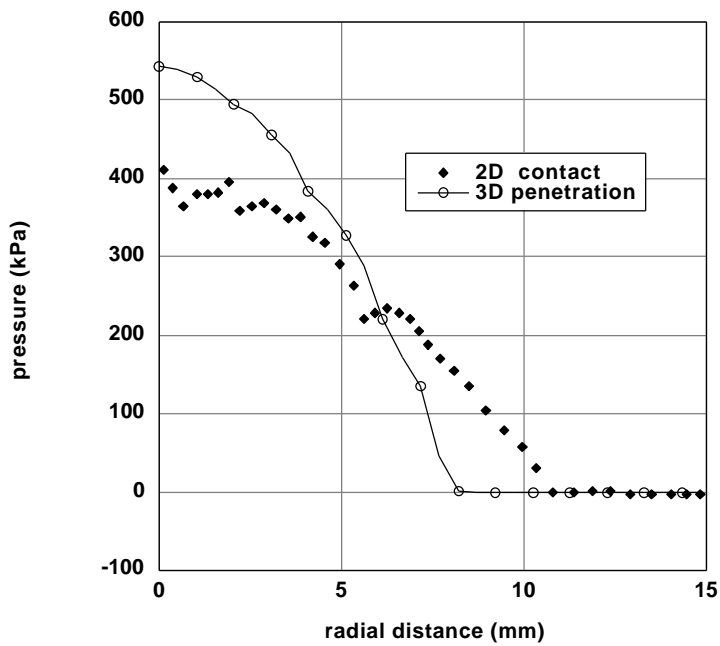


Figure 43: Case VT-VP, tissue A, pressure distribution from 3D penetration compared with 2D contact finite element analysis result,  $t = 1$  sec.

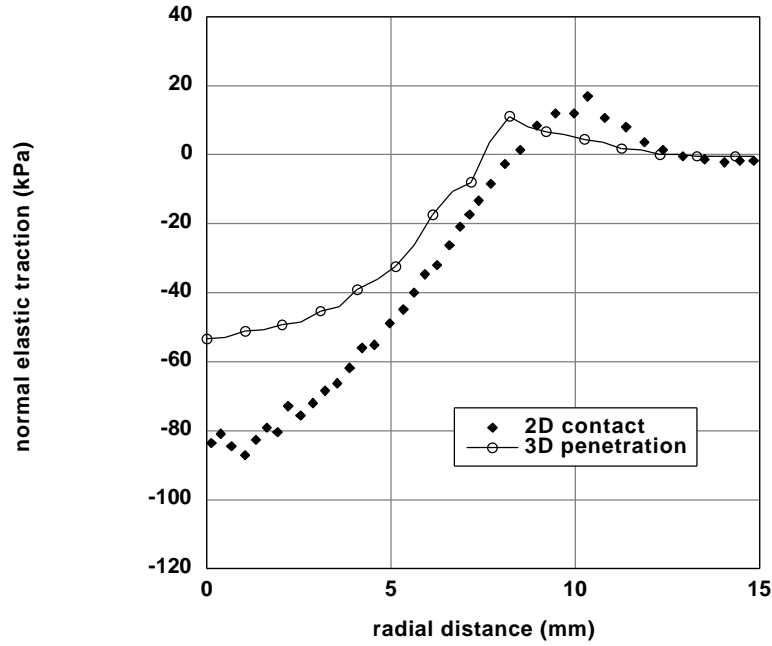


Figure 44: Case VT-CP, tissue A, normal elastic traction distribution from 3D penetration compared with 2D contact finite element analysis result,  $t = 1$  sec.

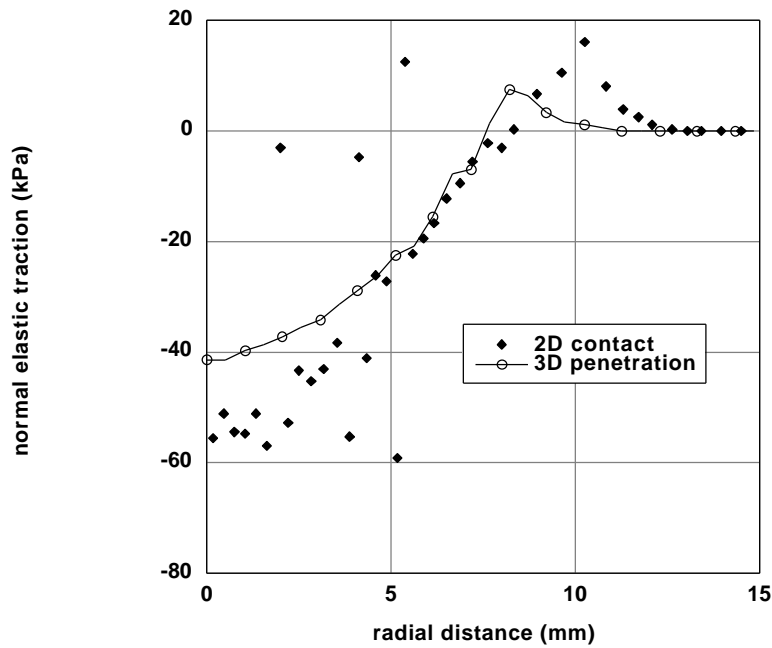


Figure 45: Case VT-CP, tissue B, normal elastic traction distribution from 3D penetration compared with 2D contact finite element analysis result,  $t = 1$  sec.

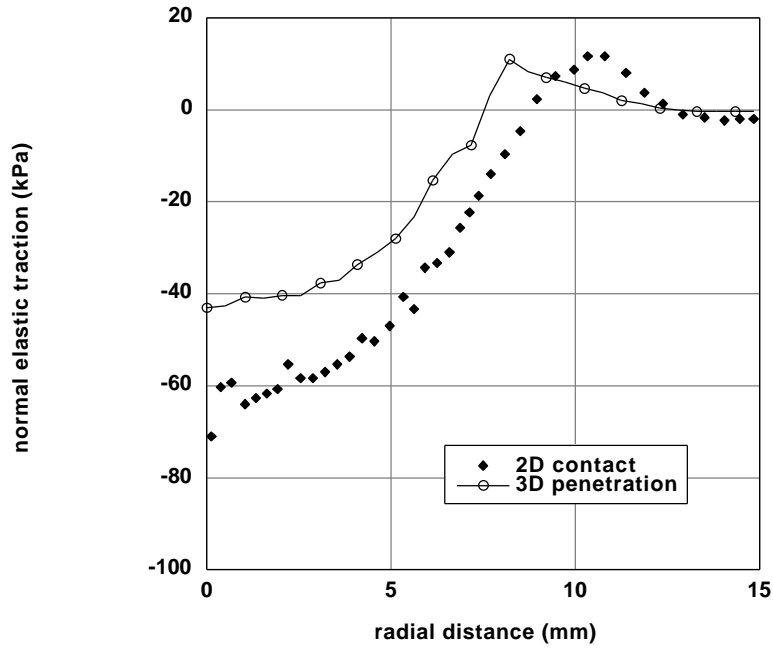


Figure 46: Case VT-VP, tissue A, normal elastic traction distribution from 3D penetration compared with 2D contact finite element analysis result,  $t = 1$  sec.

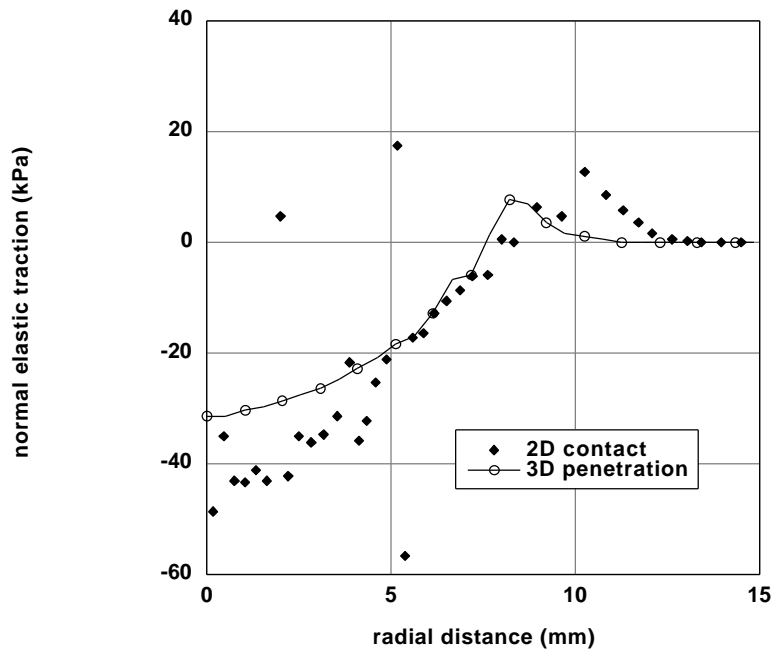


Figure 47: Case VT-VP, tissue B, normal elastic traction distribution from 3D penetration compared with 2D contact finite element analysis result,  $t = 1$  sec.

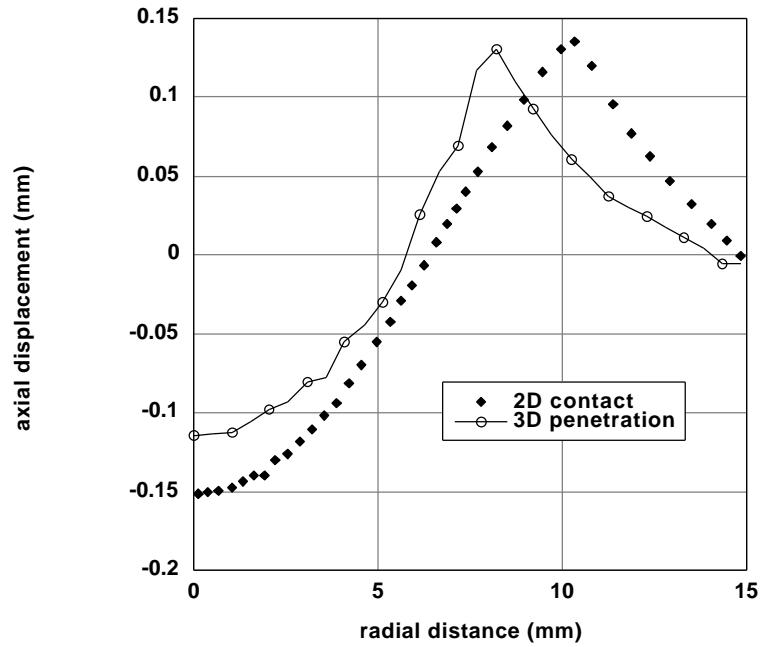


Figure 48: Case VT-CP, tissue A, axial displacement from 3D penetration compared with 2D contact finite element analysis result,  $t = 1$  sec.

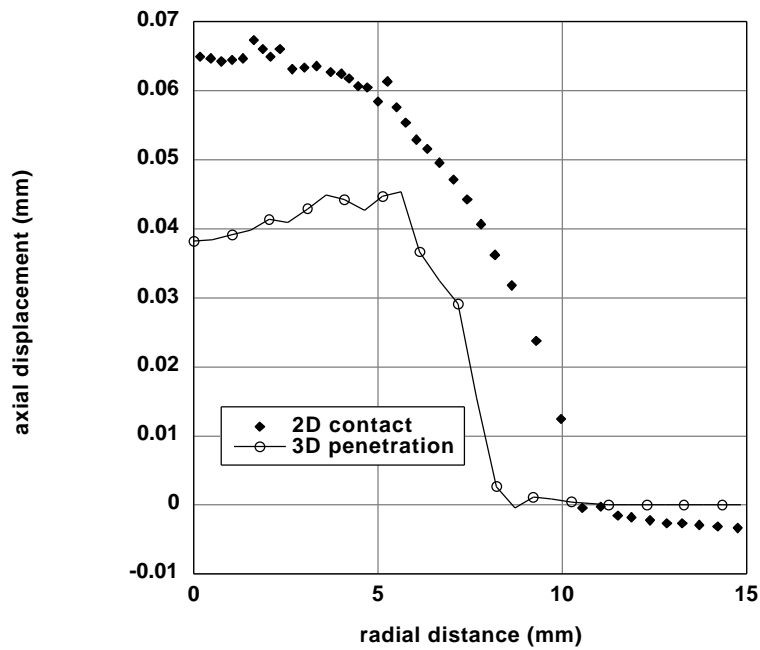


Figure 49: Case VT-CP, tissue B, axial displacement from 3D penetration compared with 2D contact finite element analysis result,  $t = 1$  sec.

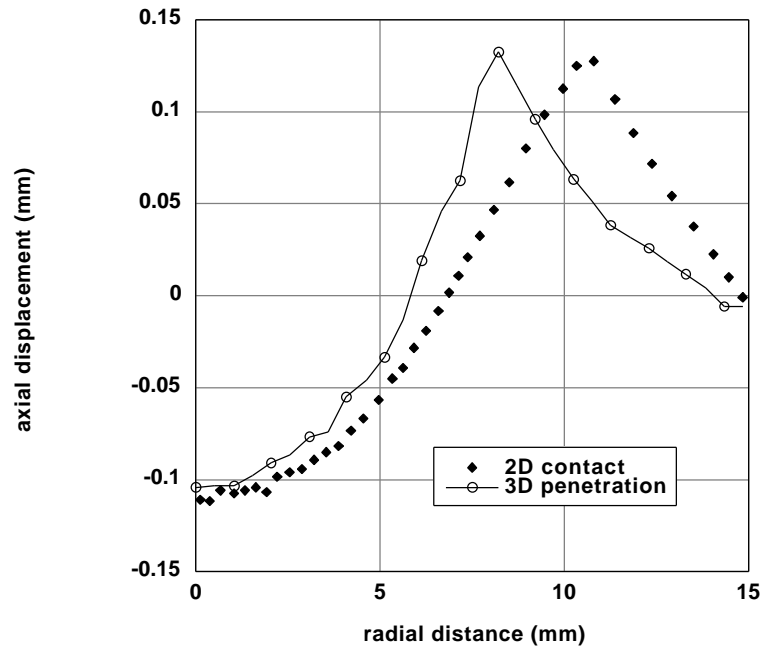


Figure 50: Case VT-VP, tissue A, axial displacement from 3D penetration compared with 2D contact finite element analysis result,  $t = 1$  sec.

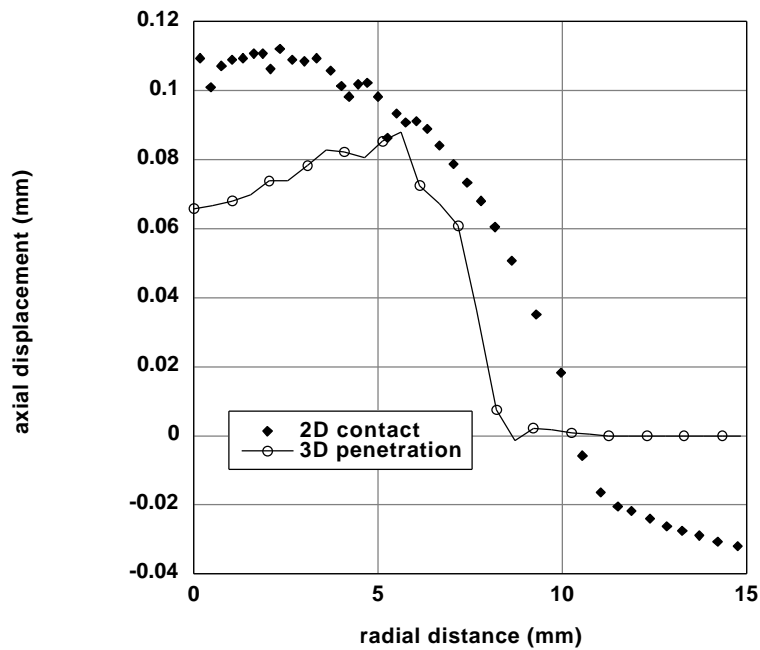


Figure 51: Case VT-VP, tissue B, axial displacement from 3D penetration compared with 2D contact finite element analysis result,  $t = 1$  sec.

more sophisticated approach would be to use (as often done in finite element analysis) Lagrange multipliers to satisfy the continuity constraint. The higher accuracy and improved robustness of this approach comes with a price of higher computational resources necessary, since additional unknowns are introduced to the problem that need to be solved for. Hence, a proper 3-D contact finite element analysis can be computationally overwhelming. From that point of view, penetration method looks like a reasonable alternative that requires significantly less computational power and provides a reasonable accuracy and robustness.

### **6.3 Glenohumeral Analysis**

In this section, penetration method is demonstrated on a physiological example, namely the glenohumeral joint (GHJ) contact of the shoulder. The anatomy of the shoulder joint with contacting glenoid and humerus cartilages highlighted is shown in Fig. (52).

The geometry for humeral head and glenoid cartilage have been determined through SPG from cadaver shoulder joints in the Orthopaedic Research Laboratory at Columbia University. The tissue kinematics and the total force on the joint obtained for different elevation angles of the humerus provides the raw data for the penetration method. The magnitude of the force depends on the elevation angle and varied between 50-185 N in this study. Both tissue layers have material parameters typical for human joint [40]; namely, Young's modulus,  $E$ , of 407 kPa, solid phase Poisson's ratio,  $\nu$ , of 0.05, solid content,  $\phi^s$  of 0.25, permeability,  $\kappa$ , of  $1.2 \times 10^{-14}$  m<sup>4</sup>/Ns. The SPG method cannot produce deformation information in physiological time ranges such as a second, and the data obtained for our simulation likely corresponds to deformation that took place over several minutes in the laboratory (although we are not certain of the exact time). Still, the corresponding motion will be treated as if occurring in physiological time. The simulated motion considered for this demonstration corresponds to an arm elevation from 40° to 60° occurring in 15 sec. With a time step of 1 sec., the traction distribution at 40° was first applied in a ramp of 5 sec., then the elevation angle was changed by 2° at each time step and the traction distribution and pressure (which are, in general, different both

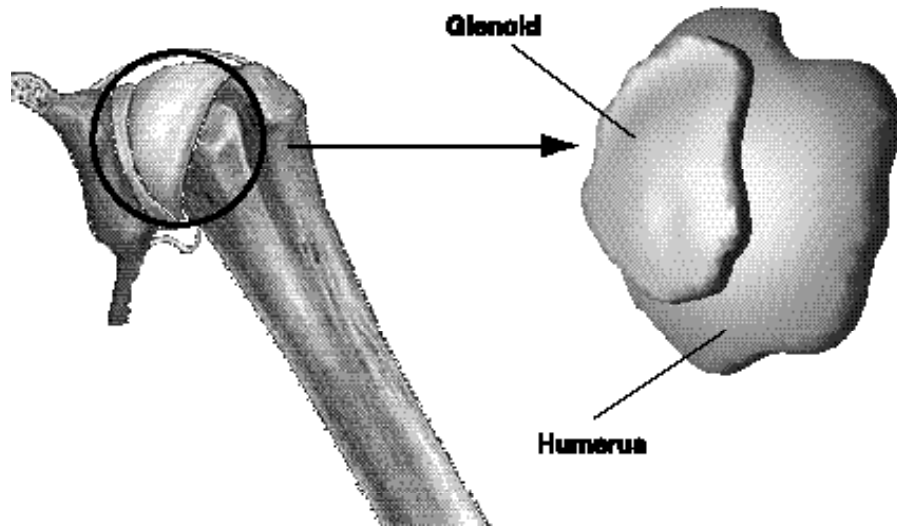


Figure 52: Shoulder geometry with glenoid and humerus cartilages.

in magnitude and position at different elevation angles) corresponding to that angle was applied.

While it is numerically possible to apply a larger angle change in the linear analysis, the time stepping parameters (and elevation angle changes) were picked in order to facilitate comparison with the equivalent nonlinear example presented in the next chapter. An angle change of  $2^\circ$  per time step, which is sufficiently small for the convergence of the nonlinear analysis, was used. As mentioned in Chapter 5, SPG cannot always capture the whole geometry and may therefore produce artificial edges in the models (note the unnaturally sharp edges occurring in the SPG models shown at the right hand side picture of Fig. (52)). In addition to handling an “incomplete” geometric model, it is also difficult to assign a suitable boundary condition to these artificial edges. Our experience shows that high loads applied close to the edge may give unrealistic results. Hence, in order to minimize the effects of these model artifacts, the motion was started at  $40^\circ$  elevation angle, when the imprint on the humerus is away from its edge. On the other hand, being the smaller of the tissues, the loading of the edges in the glenoid cannot be avoided. The tissue that extends from the cartilage like a meniscus and contributes to the stability and load distribution is called *glenoid labrum* [18]. Due to its absence in the geometric model of the joint, the effect of the edge loading is particularly severe when analyzing the glenoid cartilage. In the analyses that follow, the side face of the glenoid model is made impermeable to fluid flux to account partially for the missing labrum.

### 6.3.1 Approximate Contact Boundary Conditions

First it is checked if the penetration methods produce contact boundary conditions in agreement with kinetic contact continuity conditions, Eqs (139) and (141). Figure (53) shows the distribution of the magnitude of the total traction and the pressure on the contacting tissue layers as given by the penetration method at an arm elevation angle of  $40^\circ$  degrees. The distribution patterns of both quantities match perfectly on the contacting tissue layers. The magnitude of the quantities are slightly higher on the glenoid.

When a comparison is done at  $60^\circ$  elevation angle a similar trend is observed (Fig. (54)), although the difference in the magnitude of these boundary condition type of quantities are smaller compared to a  $40^\circ$  elevation.

Numerical experience shows that the number of the grid points at which penetration is calculated, the fineness of the mesh over which the numerical integration of penetration (Eq. (1)) is performed can cause a deviation in the magnitude and distribution of total traction and pressure. With the finer grid and finer mesh, the difference in the distribution pattern can be completely eliminated; however, some deviation in the magnitude is unavoidable since the integral is evaluated over slightly different contact areas. Recall that the penetration procedure is performed on the original undeformed models. The difference in the curvature of the contacting faces of these models will give different contact areas (See Fig. 15), which will affect the outcome of the penetration integration. For this particular model pair, the glenoid peak traction was in general about 10% higher than the humeral head, which is reasonable. For congruent geometries such as diarthrodial joints a high deviation is not likely to appear.

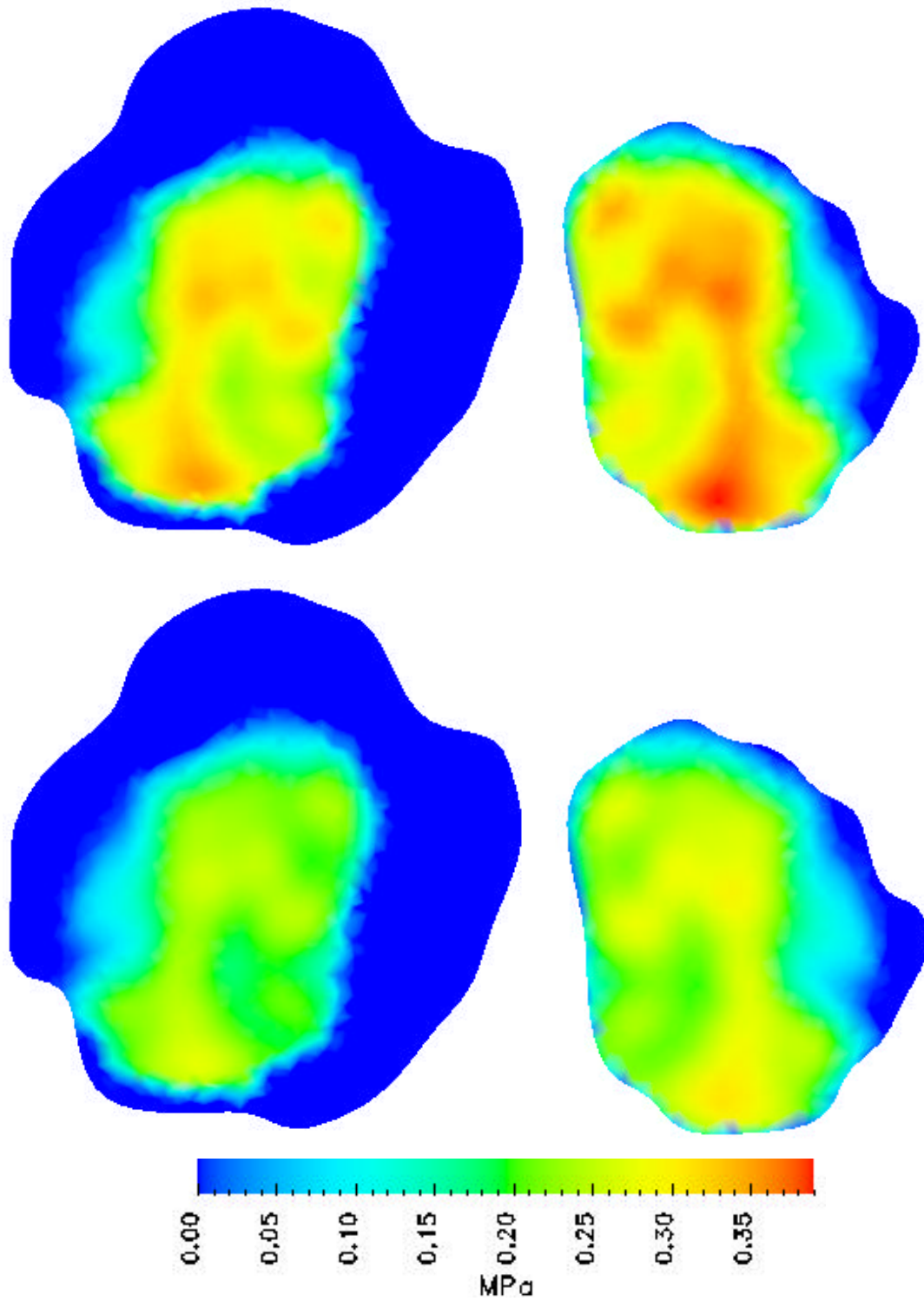


Figure 53: Comparison of magnitude of the total traction (upper) and pressure (lower) on the contact faces of humeral head (left) and glenoid (right) cartilages at an arm elevation angle of 40°.

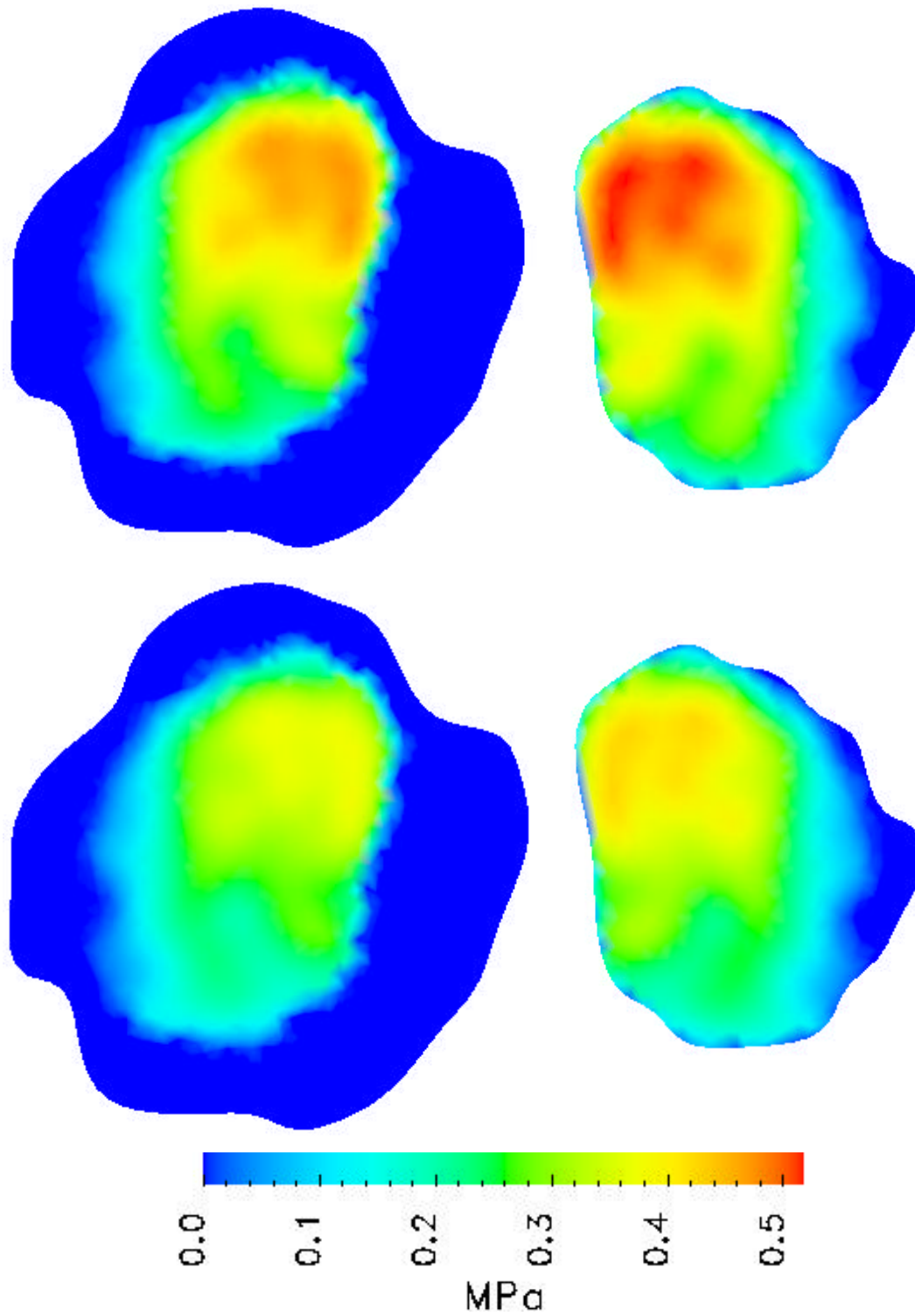


Figure 54: Comparison of magnitude of the total traction (upper) and pressure(lower) on the contact faces of humeral head (left) and glenoid (right) cartilages at an arm elevation angle of  $60^\circ$ .

### 6.3.2 Humerus Results

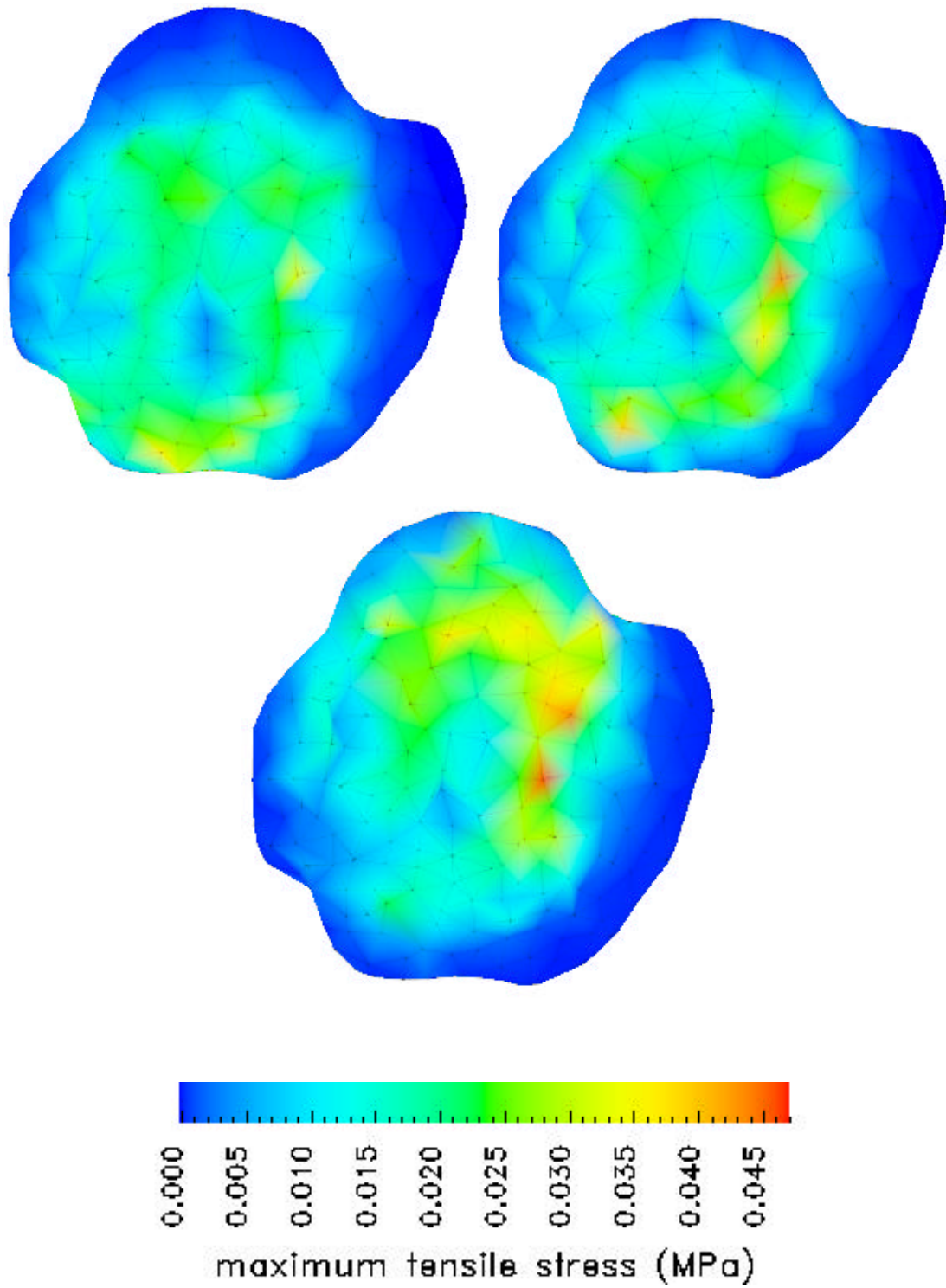
For the humeral analysis, a mesh that has six layers of elements through the thickness of the tissue is used. Numerical observation shows that further through-thickness refinement does not affect the solution significantly. In total, the mesh is made of 14819 tetrahedral elements and 30450 nodes. Stress-like quantities are of major interest since they are related to the tissue performance. They are displayed at three different times,  $t = 5, 10,$  and  $15$  sec. during the motion, corresponding to elevation angles of  $40^\circ, 50^\circ$  and  $60^\circ$  degrees respectively.

Figure 55 shows both a change in the distribution pattern and the magnitude of the maximum tensile stress on the contacting face. The imprint of the glenoid edges is clearly visible as high stress areas. It is noted that the stress pattern moves from the inferior (lower) towards the superior (upper) side of the humerus and the stress increases as the elevation angle changes. In this range, the force acting on the joint typically increases as the elevation angle grows; so, part of the increase in the stress with increasing angle can be attributed to this phenomenon.

An advantage of numerical simulation is that it enables researchers to gain insight about quantities that are difficult, if not impossible, to measure experimentally such as stresses at the cartilage bone interface. Figures 56-59 display stress results at the bone interface of the humerus.

The incongruent loading pattern, typical for diarthrodial joints, is clearly visible in maximum tensile stress distribution at the bone interface, as depicted in Fig. 56. While there is a circular high stress region, the center seems to experience relatively low tensile stresses. The increase in the stress at higher arm elevation is again visible. Note also that the tensile stresses at bone interface is significantly larger compared to the contacting face of the tissue. Considering the distribution at  $60^\circ$  we observe a highly localized high stress point.

The maximum compressive stress (Fig. 57) and the maximum shear stress (Fig. 58) at the bone interface follow a trend similar to maximum tensile stress in terms of the shape and the evolution of the pattern, and the location of areas of high stress. Another important observation is that the stress magnitude is close to the maximum tensile stress for both quantities.



*Figure 55: Maximum tensile stress distribution on the contacting face of the humerus at arm elevations of 40° (top left), 50° (top right) and 60° (bottom).*

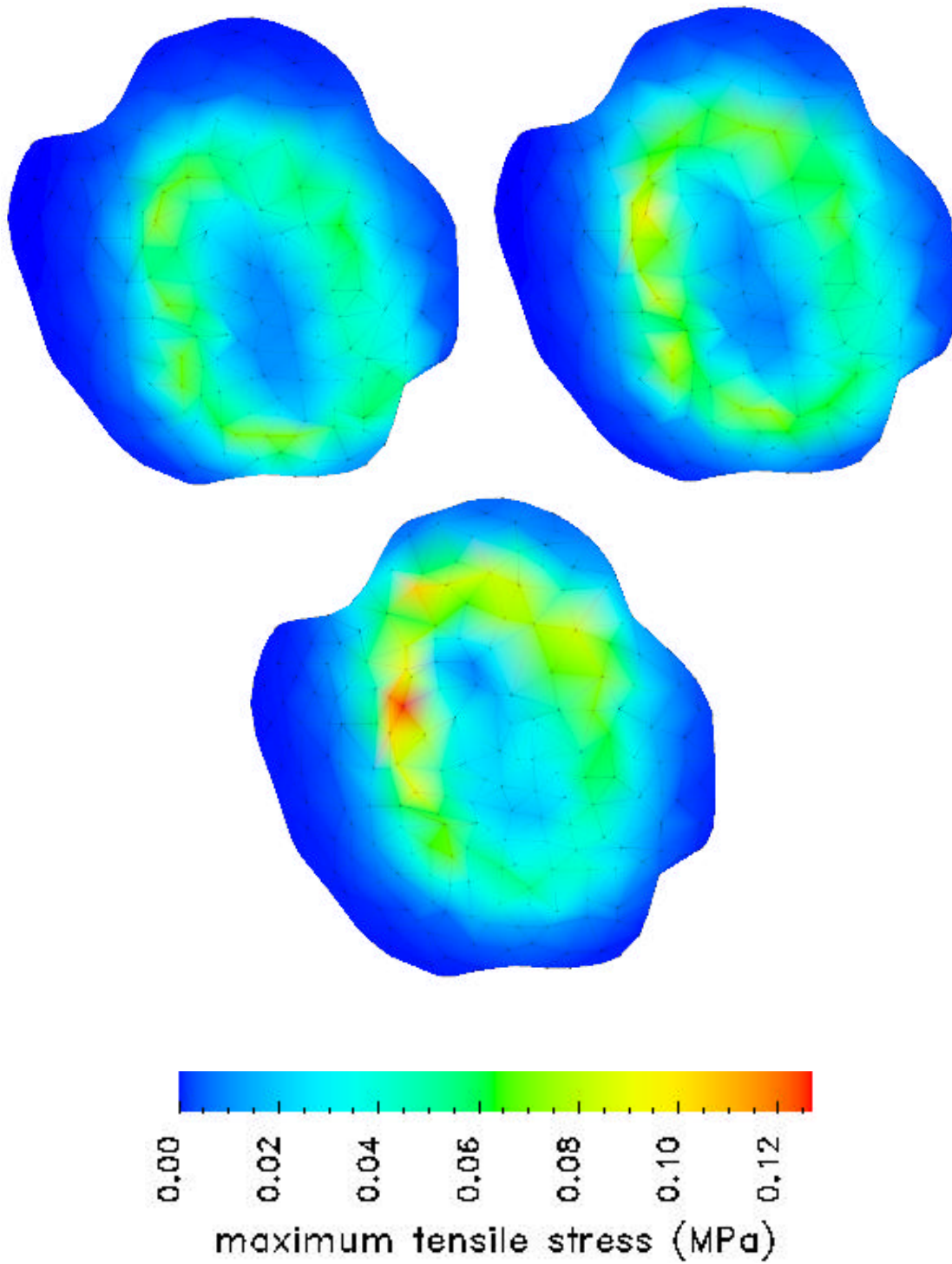


*Figure 56: Maximum tensile stress distribution on the bone interface of the humerus at arm elevations of 40° (top left), 50° (top right) and 60° (bottom).*

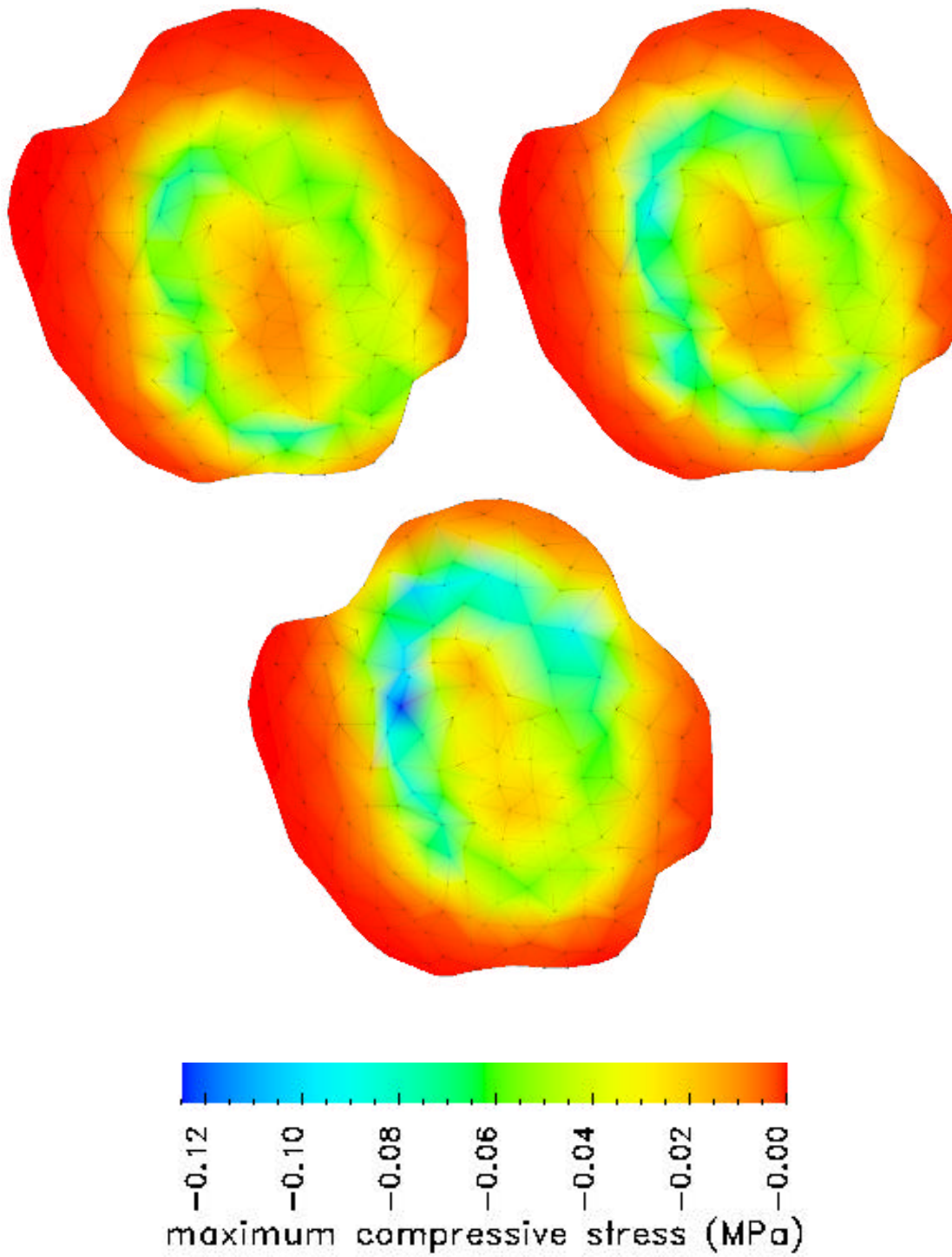


*Figure 57: Maximum compressive stress distribution on the bone interface of the humerus at arm elevations of 40° (top left), 50° (top right) and 60° (bottom).*

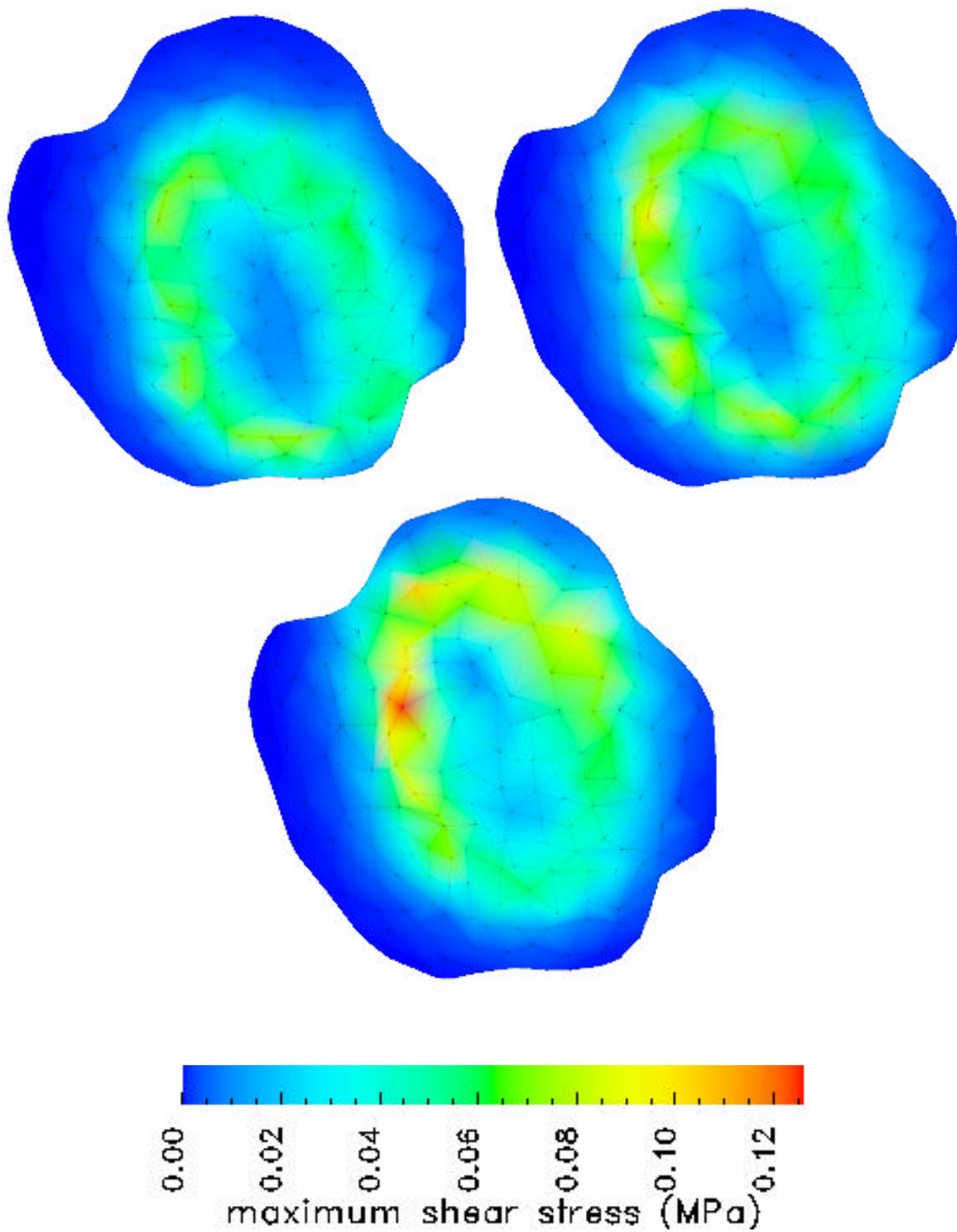


*Figure 58: Maximum shear stress distribution on the bone interface of the humerus at arm elevations of 40° (top left), 50° (top right) and 60° (bottom).*

### **6.3.3 The Glenoid Results**

The glenoid, in general, experiences stresses that are quantitatively and qualitatively different than we observe in the humerus. Due to the modeling constraints mentioned in Section 6.3, it is more difficult to draw firm conclusions on the glenoid results.

The mesh for the glenoid model has eight layers of elements through the thickness (note that the glenoid is thicker than the humerus). The number of elements and nodes are 11781 and 24116, respectively.

Considering the physiology of the shoulder joint, the glenoid, being the smaller of the contacting tissue layers, should not experience drastic pattern changes; this is confirmed by the maximum tensile stress distribution on the contacting face of the glenoid, Fig. 59. The stresses are higher at the edges and lower in the center as expected from the incongruity of this joint. General stress levels increase as the angle increases (although, due to the scale of the figure, it is not immediately obvious). As the elevation angle changes, the high stress area seems to shift from the inferior part to the superior part.

Similar observations can be made when looking at Figs. 60-62. The tensile, compressive and shear stress pattern on the bone interface follow the same trend as the maximum tensile stress at the contacting face. While the anterior (front, left hand side in Fig. 59, right hand side in Figs. (60-62) edge seems to undergo relatively high stresses, the stress level at the posterior (back) edge is much lower. The magnitudes of maximum tensile, compressive and shear stresses at the bone interface is not as close to each other as they are on the humerus. Also, there is not a clear difference in the level of stress that the contacting face and bone interface experience, unlike what was observed on the humerus.

### **6.3.4 Evaluation of the Glenohumeral Analysis Results**

Comparison of the total traction and pressure on the contacting faces of the humerus and glenoid shows that linear penetration method satisfies the kinetic contact continuity requirements reasonably well.

The results on the humerus confirm what we know about the mechanics of the diarthrodial joints. For this particular joint model, the average radius of the curvature of the contacting face of the glenoid is larger than that of the humeral contact face. This incongruity reflects itself on the stress results as a circular high stress region and a low stress center.

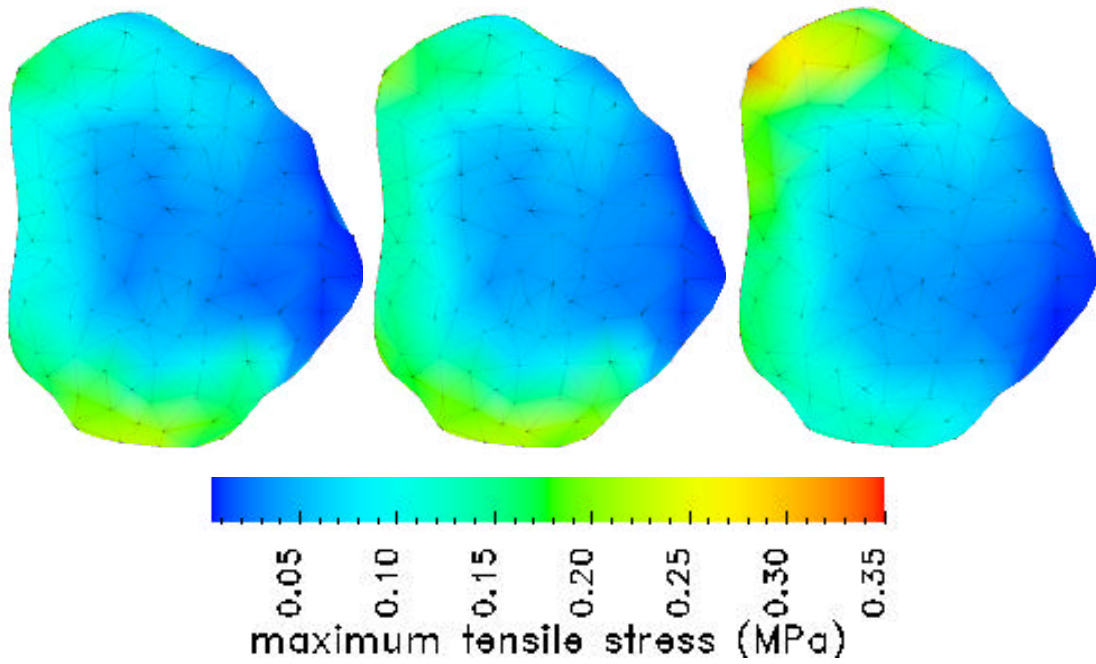


Figure 59: Maximum tensile stress distribution on the contacting face of the glenoid at arm elevations of 40° (left), 50° (center) and 60° (right).

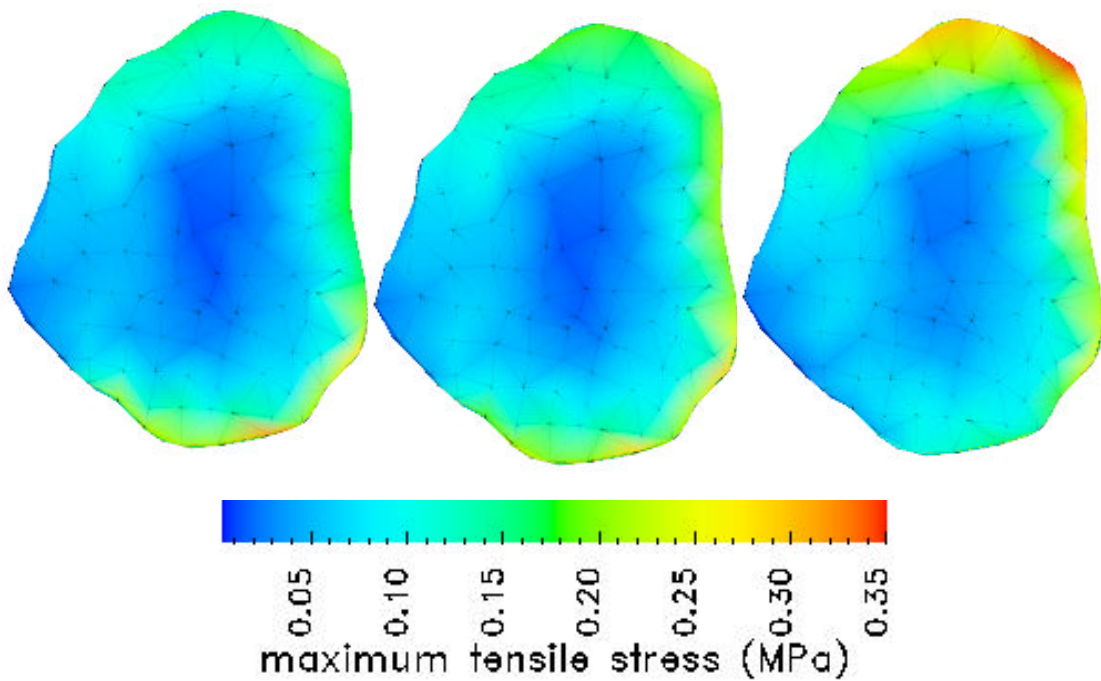


Figure 60: Maximum tensile stress distribution on the bone interface of the glenoid at arm elevations of 40° (left), 50° (center) and 60° (right).

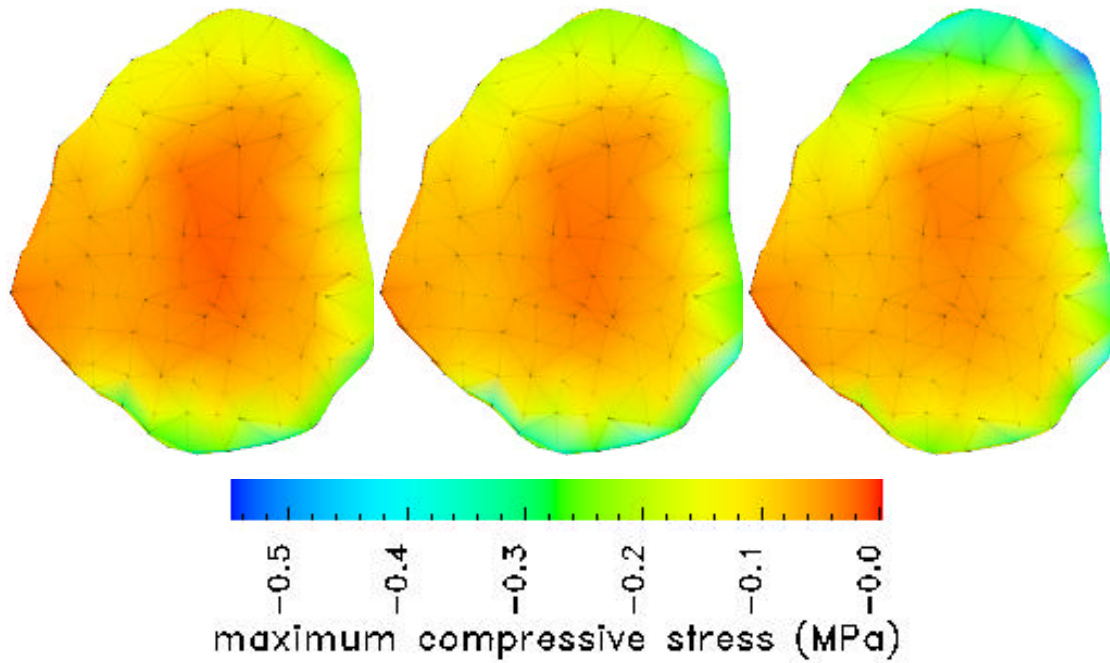


Figure 61: Maximum compressive stress distribution on the bone interface of the glenoid at arm elevations of 40° (left), 50° (center) and 60° (right).

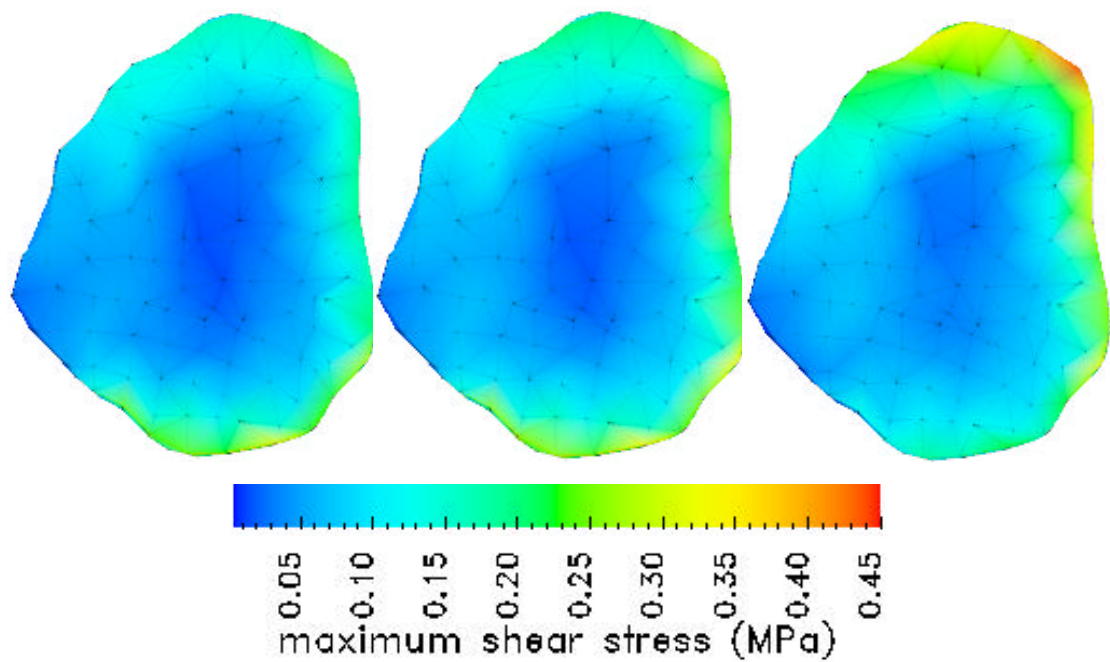


Figure 62: Maximum shear stress distribution on the bone interface of the glenoid at arm elevations of 40° (left), 50° (center) and 60° (right).

The short-time asymptotic solution for the contact of linear biphasic tissues gives equal peak values for the maximum tensile, compressive, and shear stresses in the tissues. It is encouraging to see that the stress results for the humerus is in agreement with the trend of the asymptotic solution.

In the glenoid tissue, high stresses seem to concentrate at the edges. While this makes sense physiologically part of this effect can be attributed to defects of the geometric glenoid model obtained through SPG. On both faces, the area of peak stress shifts from inferior to anterior to the superior edge as the elevation angle increases. The posterior edge does not encounter large stresses, in general.

In the next chapter, it will be seen if and how these observations change in the case of tissue layers of hyperelastic material with strain dependent permeability.

# Chapter 7

## Nonlinear Examples

### 7.1 Introduction

In this chapter we will first check the correctness of the developed nonlinear code, then demonstrate the ability of the nonlinear penetration analysis to satisfy the kinetic contact continuity conditions on a glenohumeral joint model. It is not possible to test the nonlinear penetration method the way we tested the linear one in the previous chapter since a nonlinear biphasic contact code is yet to be developed. A nonlinear penetration-based finite element analysis will be performed on the same physiological model used in the linear analysis and the effects of nonlinearity on trends in the results will be observed.

### 7.2 Confined Compression Examples

Confined compression experiment as depicted by Fig. 1 is a 1-D problem. A plug of tissue is tightly fit into a chamber and compressed with a highly-permeable, porous indenter giving rise to a uniaxial motion of the tissue and the interstitial fluid. From an analytical point of view, confined compression represents an easy problem. However, numerically, it is a challenging problem due to the existence of steep gradients near the loaded surface, and has therefore been widely used to test the performance of finite element codes developed for studies in soft tissue mechanics.

The force-controlled confined compression experiment is called the *creep* experiment whereas the displacement controlled one is referred as the *stress relaxation* experiment. In this section we compare the results of the nonlinear biphasic finite element code developed with a converged finite difference solution. While the finite element analyses are run on a 3-D geometry the finite difference solutions are 1-D. Comparisons are made for both creep and stress relaxation problems.

#### 7.2.1 Creep

In the confined compression creep (CC-CR) problem, a traction that will result to an equilibrium stretch of 0.6 is applied as a 5 sec. ramp and held steady. The time step and integration parameter are  $\Delta t = 0.5$  sec. and  $\omega = 0.6$ , respectively. The material properties, typical for soft tissues [40], are selected as  $\sigma_0 = 0.0921$  MPa,  $\nu_1 = 0.9887$ ,  $\nu_2 = 0.058158$ ,  $\phi_0^s = 0.2$  and  $\kappa_0 = 0.00247$  mm<sup>4</sup>/Ns.

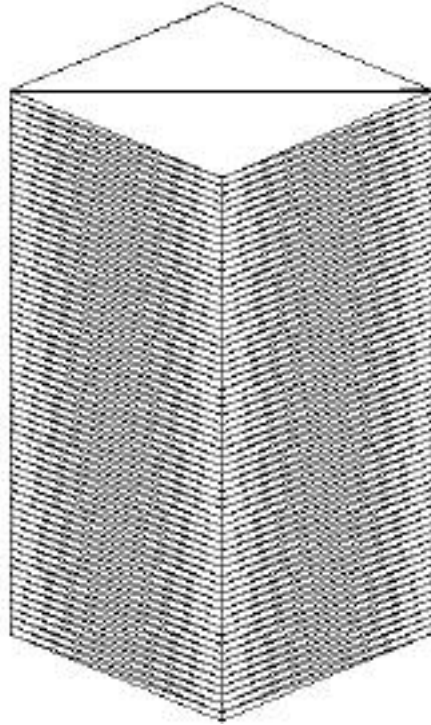


*Figure 63: The finite element mesh used in confined compression problems*

The finite element mesh used in the analysis is shown in Fig. 63. The height of the geometry is 1 mm and there are 64 layers of elements of equal thickness through the height such that there are a total of 384 elements and 1026 nodes.

Figures 64-66 compare the finite element (indicated as FE in the figure captions) results for pressure, axial displacement and axial stress with converged finite difference (indicated as FD in the figure captions) results at various time points. The axial stress differs slightly from the finite difference solution at  $t = 10$  sec. Otherwise, the agreement seem to be perfect for all quantities at all times. Numerically, the difference is generally less than 1 % although the finite difference mesh is much finer than the finite element mesh.

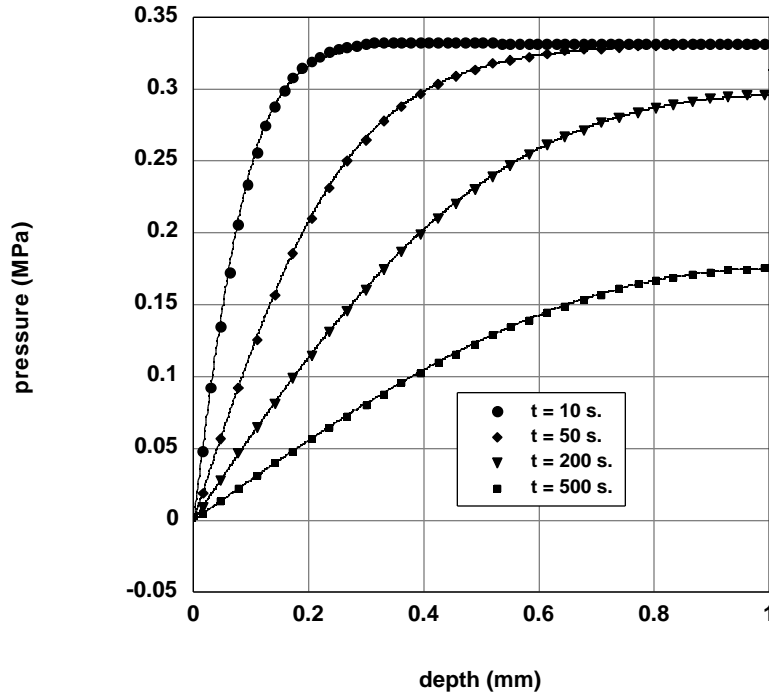


Figure 64: Pressure as function of depth at various time point in CC-CR. Solid lines indicate converged FD results while symbols are FE results.

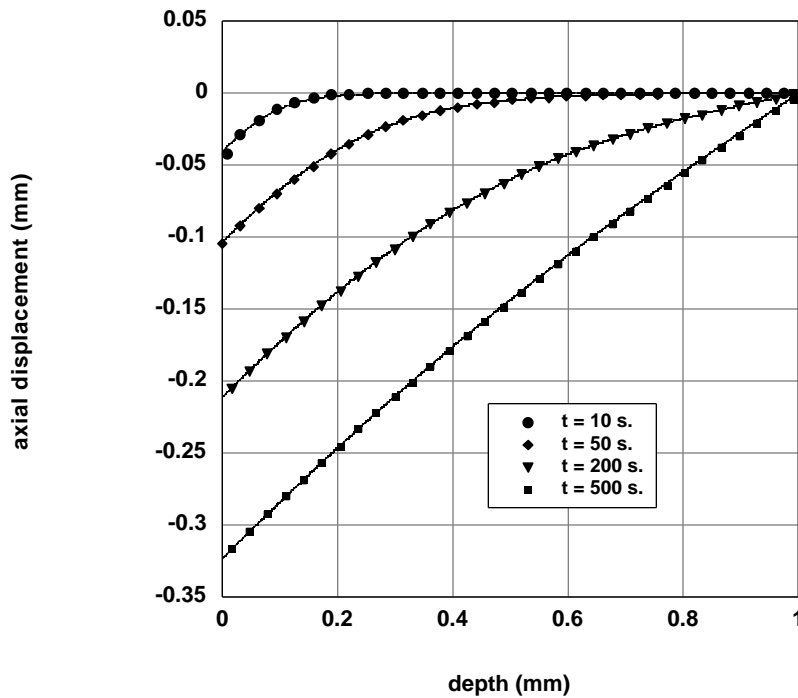


Figure 65: Axial displacement as function of depth at various time point in CC-CR. Solid lines indicate converged FD results while symbols are FE results.

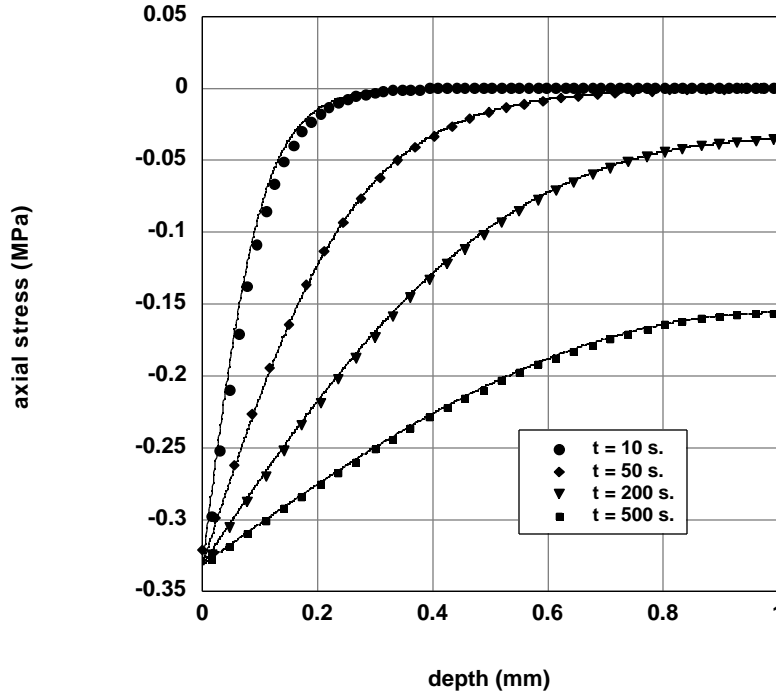


Figure 66: Axial stress as function of depth at various time point in CC-CR. Solid lines indicate converged FD results while symbols are FE results.

### 7.2.2 Stress Relaxation

In the confined compression stress relaxation (CC-SR) example, a displacement corresponding to an equilibrium stretch of 0.9 is applied as a ramp of 50 sec. and then held steady. The time step and integration parameter are  $\Delta t = 1.0$  sec. and  $\omega = 0.6$ , respectively. This loading produced stresses close to the maximum value observed in the creep problem, and thus the nonlinearity was sufficiently strong for the appropriate testing of the code. The geometry, material properties and the finite element mesh used are the same as in the creep problem.

Figures 67-69 compare the finite element results for pressure, axial displacement and axial stress at various time points. In the stress relaxation problem, there is typically a rapid decay at the point when the ramp reaches its maximum point where numerical errors are likelier to occur. Figure 67 shows that there is a slight deviation in pressure from the finite difference solution at deeper zones of the tissue at  $t = 50$  sec. Otherwise, the agreement with the finite difference solution is perfect for this quantity. (Note the rapid decay in pressure from  $t = 50$  sec. to  $t = 60$  sec.)

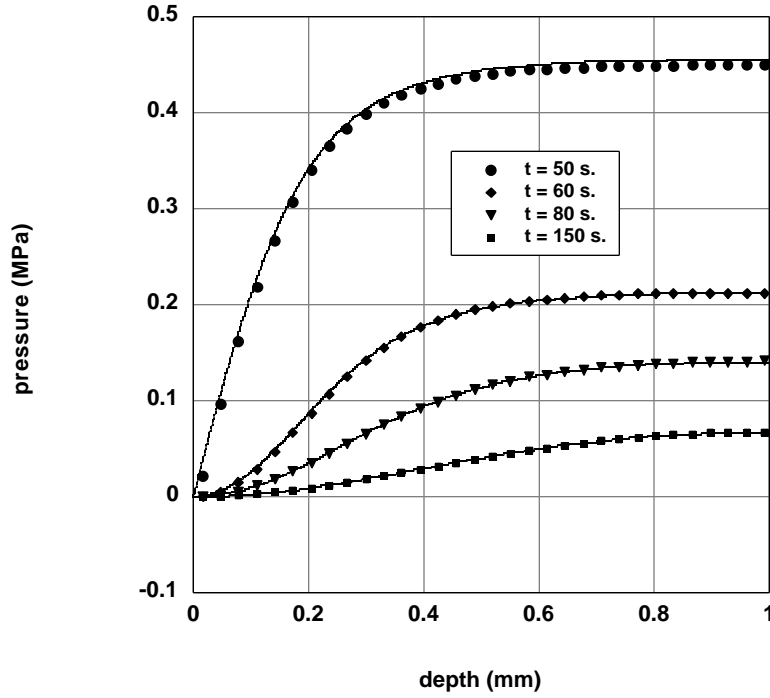


Figure 67: Pressure as function of depth at various time point in CC-SR. Solid lines indicate converged FD results while symbols are FE results.

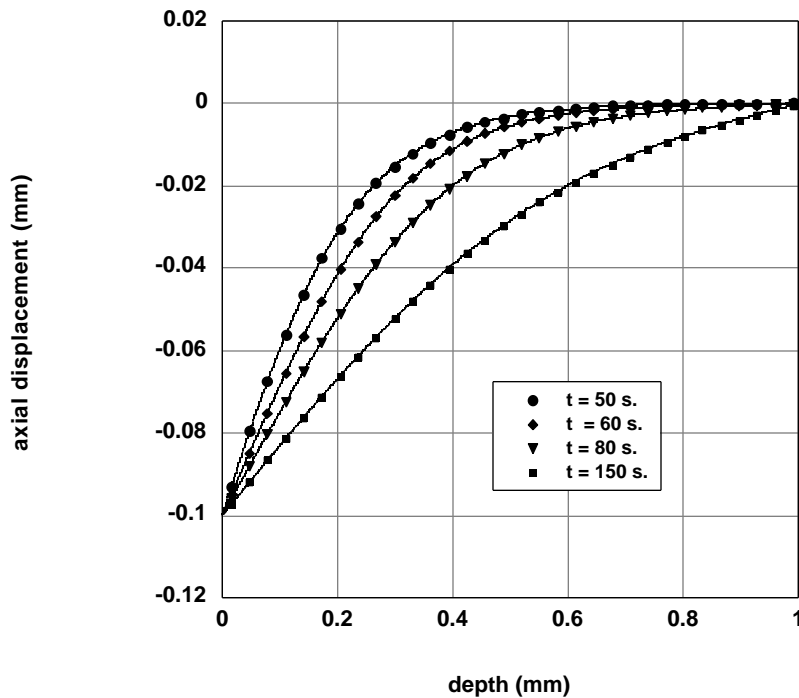


Figure 68: Axial displacement as function of depth at various time point in CC-SR. Solid lines indicate converged FD results while symbols are FE results.

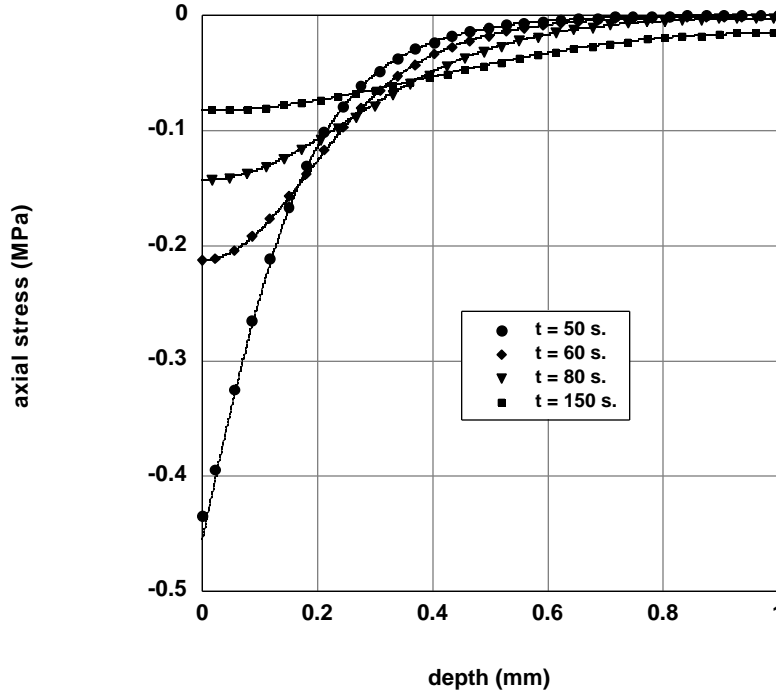


Figure 69: Axial stress as function of depth at various time point in CC-SR. Solid lines indicate converged FD results while symbols are FE results.

Figures 68 and 69 show that axial displacement and axial stress agree perfectly with converged finite difference solution at all times.

### 7.2.3 Evaluation of the Confined Compression Analysis Results

The confined compression results presented in this section demonstrate that the nonlinear code is correct and, though 3-D, has a comparable accuracy to a 1-D finite difference scheme. It is known that the solution in a linear creep problem might oscillate and that a time integration factor  $\omega > 0.5$  is necessary for the oscillations to die out. Compared to the creep problem, the linear stress relaxation problem where an essential (rather than a natural) boundary condition is prescribed on the top face of the tissue constitutes a numerically simpler problem.

The situation is reversed in the nonlinear analysis. The nonlinear stress relaxation problem is numerically challenging due to its sensitivity to the time step, element size and the magnitude of the applied displacement. A relatively fast application of the prescribed displacement in the presence of a fine mesh might cause some elements to deform to “negative volumes” during the first Newton iteration making the code fail. This phenomenon is observed both in the finite difference code and the nonlinear finite element code used. On the other hand, the nonlinear creep problem could be run with

relatively large applied tractions and the Newton iteration converges even on coarser meshes.

In general, the modified-Newton solver with line search provided stabilization in both problems against variations in the time step, load level and mesh. Hence, convergence was achieved for a broad spectrum of problem parameters.

### **7.3 Glenohumeral Analysis**

The glenohumeral analysis of the previous chapter is repeated in this section for the demonstration of the nonlinear penetration-based finite element method on a physiological geometry. The experimental data obtained through SPG and utilized in the previous chapter provides this time the input to the nonlinear penetration procedure as described in Section 5.3. The resulting total traction and pressure boundary conditions are applied to the biphasic tissue with a hyperelastic solid phase. The motion simulated is the same arm elevation motion as in the linear penetration-based analysis described in Section 6.3.

The hyperelastic material properties of the solid phase are  $\sigma_0 = 0.0921$  MPa,  $\nu_1 = 0.9887$ ,  $\nu_2 = 0.058158$ , with initial permeability,  $\kappa_0$  of  $0.012 \text{ mm}^4/\text{Ns}$  and initial solid content,  $\phi_0^s$ , of 0.25. Note that at infinitesimal deformation these properties are equivalent to those used in the linear glenohumeral analysis such that a quantitative comparison between linear and nonlinear approaches can be made.

#### **7.3.1 Approximate Contact Boundary Conditions**

Figures 70 and 71 compare the total traction and pressure boundary conditions at arm elevations of  $40^\circ$  and  $60^\circ$ , respectively, on the contacting faces of the humerus and glenoid as calculated through nonlinear penetration method. As in the linear penetration approach, the resulting boundary conditions have identical distribution patterns and satisfy the contact kinetic contact continuity requirements reasonably well. The deviation in peak values between humerus and glenoid is smaller than in the linear penetration approach.

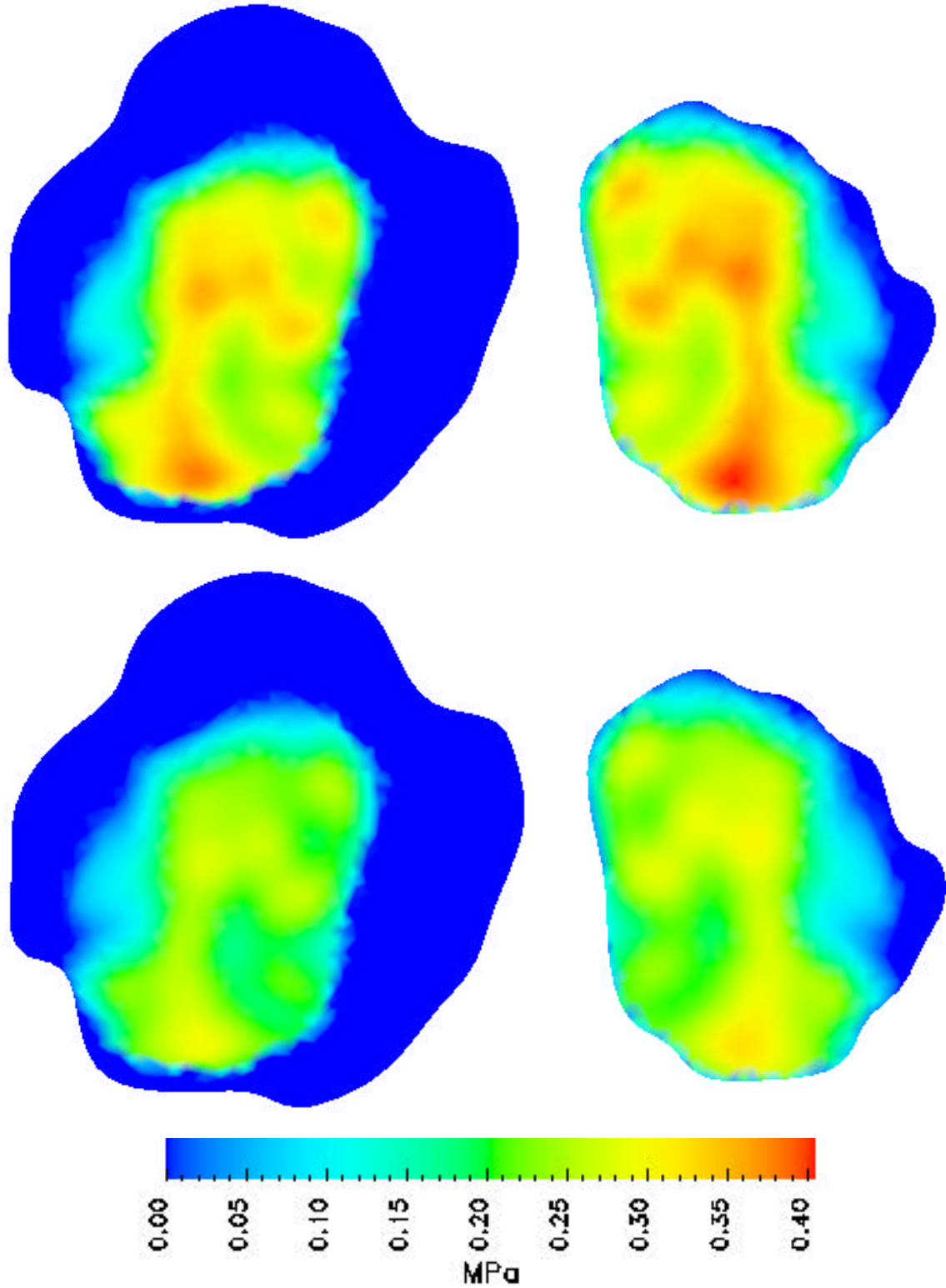


*Figure 70: Comparison of magnitude of the total traction (upper) and pressure(lower) on the contact faces of humeral head (left) and glenoid (right) cartilages at an arm elevation angle of 40° originating from nonlinear penetration procedure.*

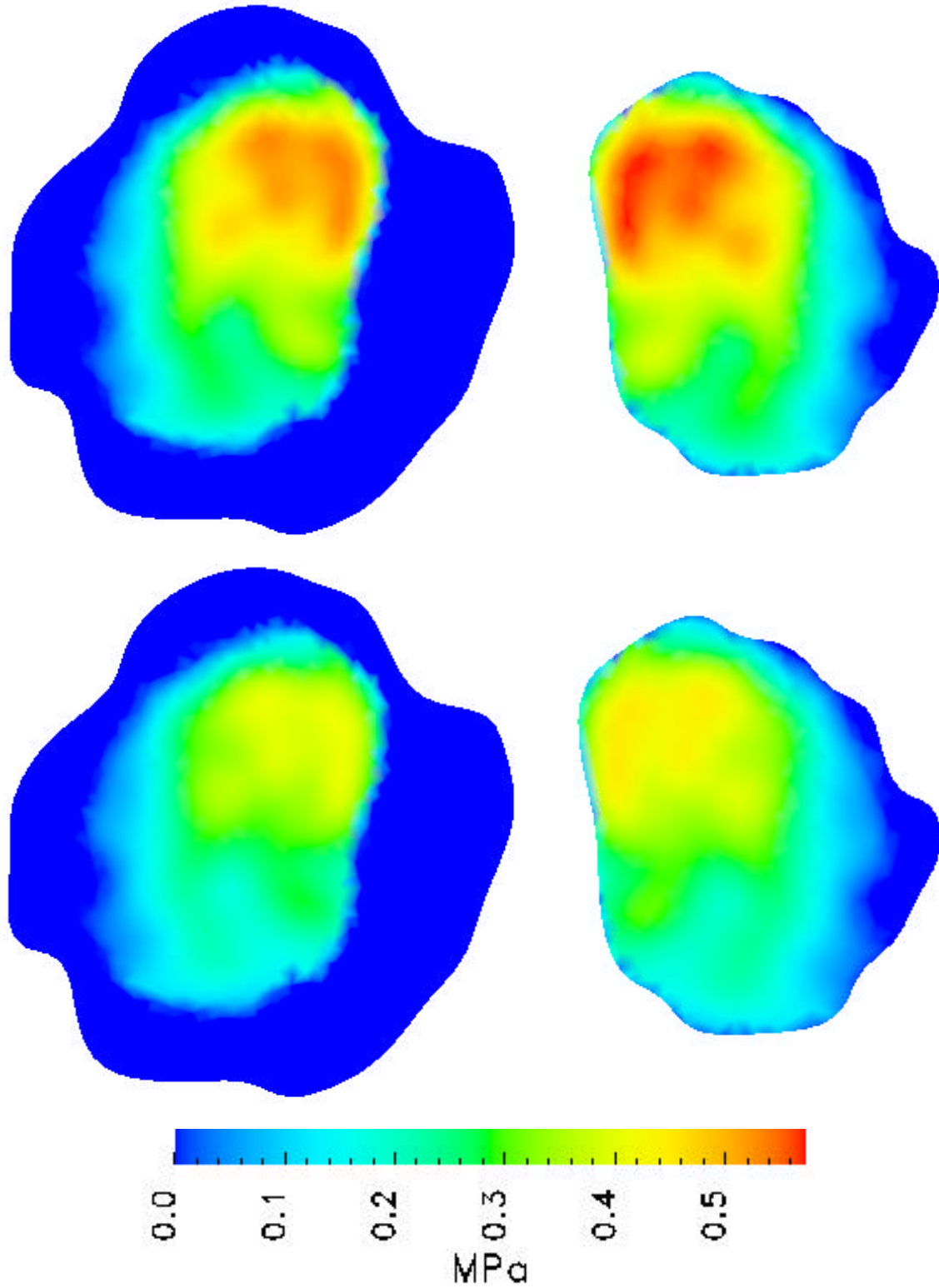


*Figure 71: Comparison of magnitude of the total traction (upper) and pressure(lower) on the contact faces of humeral head (left) and glenoid (right) cartilages at an arm elevation angle of 60° originating from nonlinear penetration procedure.*

### **7.3.2 Humerus Results**

To analyze the humerus under finite deformation, the same mesh used in the linear analysis is utilized here. Various stress quantities are displayed on the contacting face and the bone interface of the humerus at elevation angles of 40°, 50° and 60° in Figures 72-75.

Figure 72 shows the maximum tensile stress on the contacting face. The distribution is relatively uniform and the circular loading pattern observed in the linear analysis is no longer present; however, high stress spots, although smaller, still shifts from the inferior region to the superior one with increasing elevation angle. The peak value experienced is more than twice as large compared to the linear analysis (Compare Fig. 72 with Fig. 55).

The circular loading pattern observed in the linear analysis is also encountered in the nonlinear analysis when looking at the results for the maximum tensile, compressive and shear stresses at the bone interface (Figs. 73-75). Their distribution and evolution with changing arm elevation is almost identical to the linear analysis and the same qualitative conclusions can be drawn.

Despite the presence of qualitative similarities with the results originating from the linear analysis, the nonlinear analysis seems to cause major differences quantitatively. In particular, the nonlinear approach predicts higher tensile stresses (compare Figs. 73 and 56) and lower compressive stresses (compare Figs. 74 and 57) at the bone interface. The peak values for the maximum shear stress are comparable to the linear analysis.

### **7.3.3 Glenoid Results**

In the previous chapter it was noted that the high stress values occurring at the edges of the glenoid tissue are partially attributed to model defects originating from the limitations of the SPG technique and the absence of the glenoid labrum in the mechanical analysis. Factors that cause poor results in a linear analysis can have more severe effects in a nonlinear analysis since they can compromise convergence.

It is observed that a nonlinear analysis on the available glenoid geometry could be run only by constraining the displacement on the side face and making that face permeable to fluid flow. Still, at higher arm elevations, when the tractions are higher the code fails to convergence. Thus, the stress results are presented at angles of 40° and 50°, only.

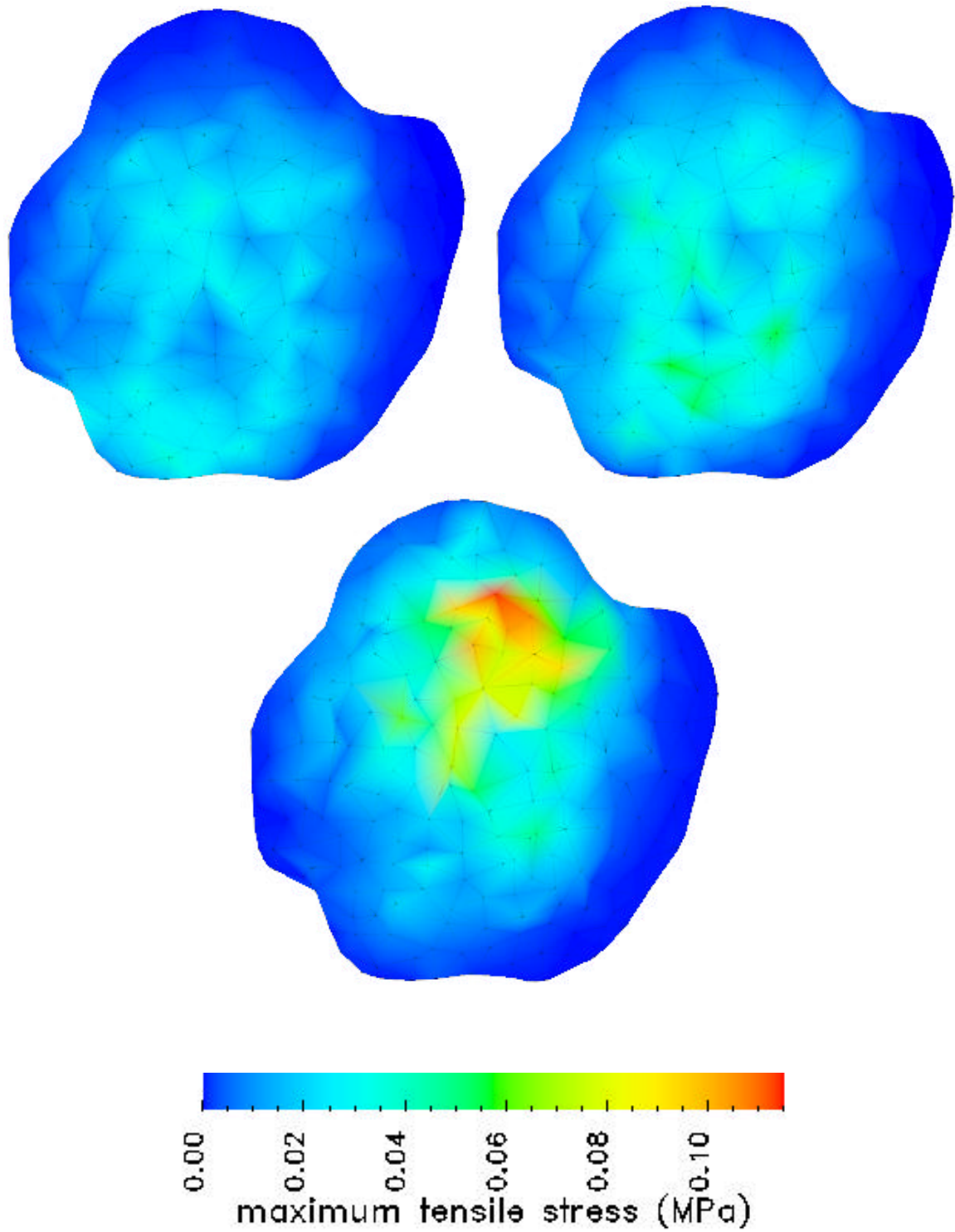


*Figure 72: Maximum tensile stress distribution on the contacting face of the humerus at arm elevations of 40° (top left), 50° (top right) and 60° (bottom) degrees.*

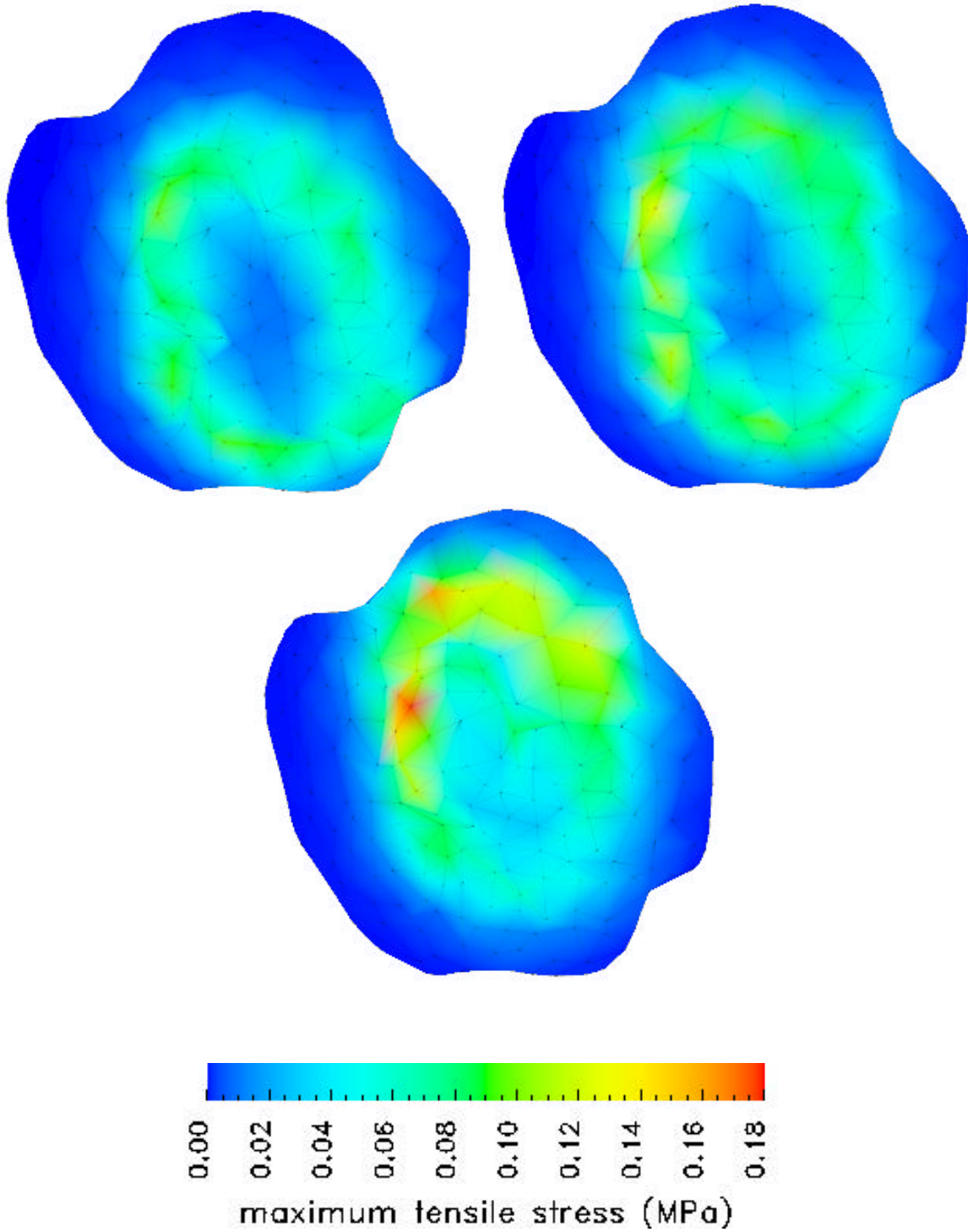


*Figure 73: Maximum tensile stress distribution on the bone interface of the humerus at arm elevations of 40° (top left), 50° (top right) and 60° (bottom) degrees.*

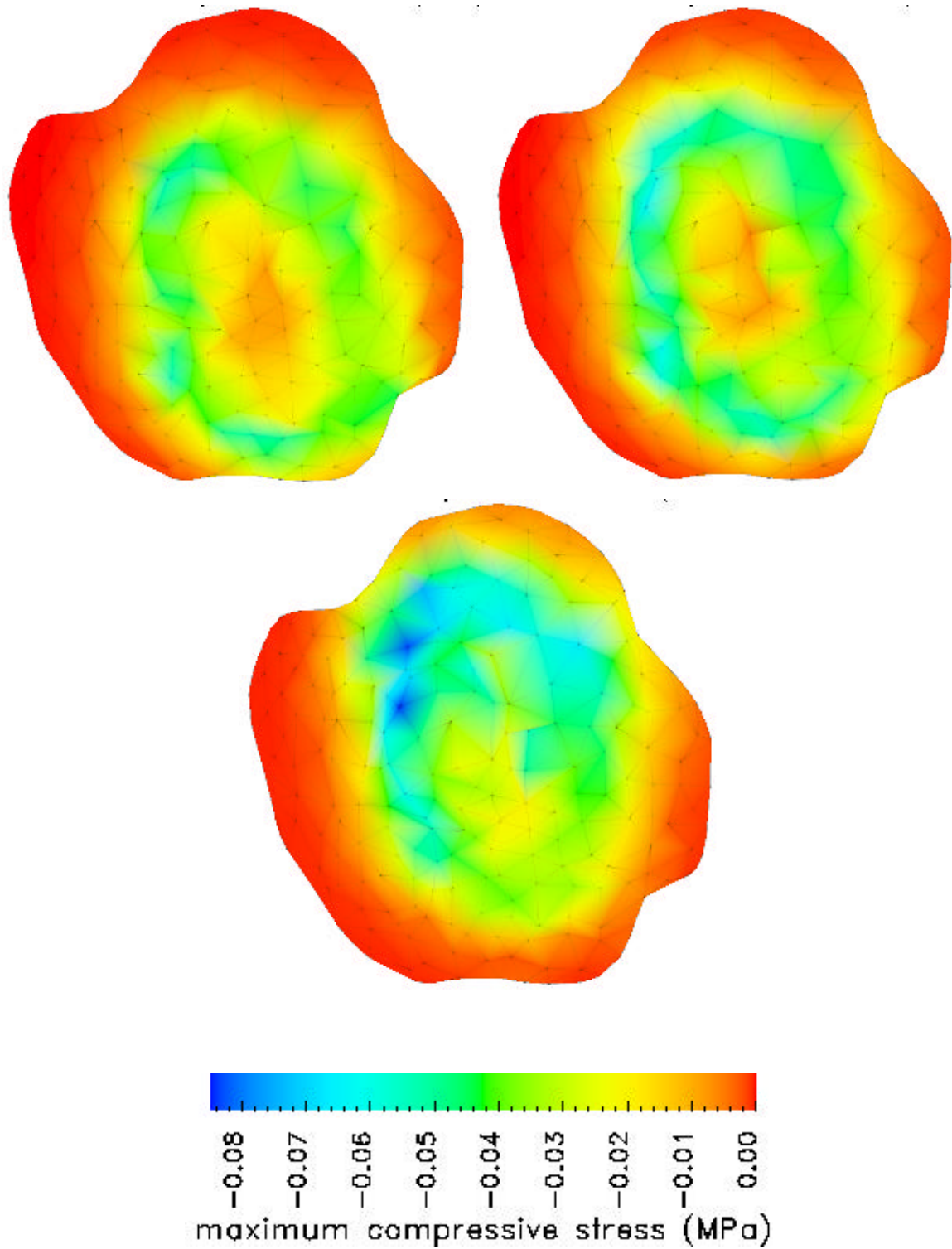


*Figure 74: Maximum compressive stress distribution on the bone interface of the humerus at arm elevations of 40° (top left), 50° (top right) and 60° (bottom) degrees.*

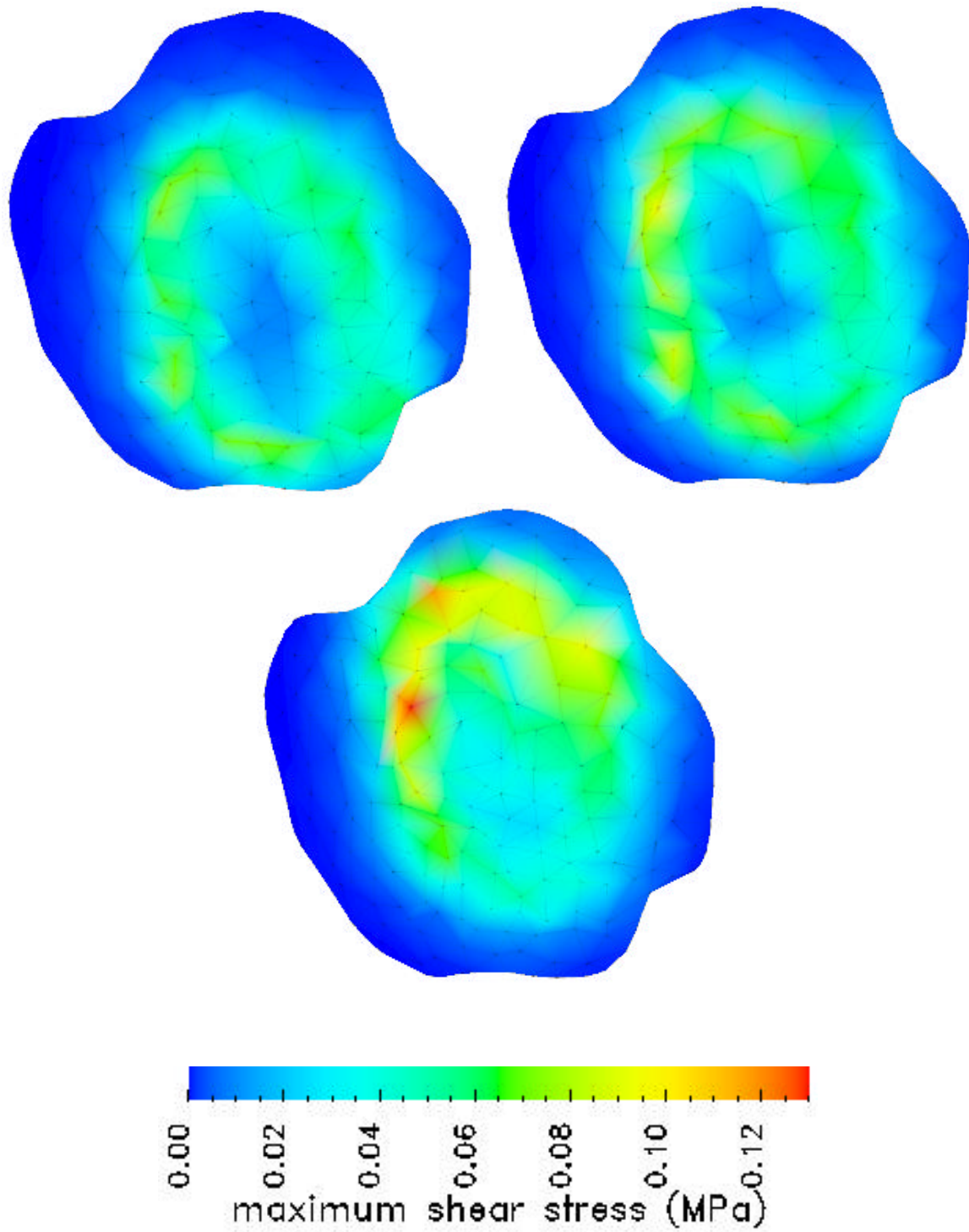


*Figure 75: Maximum shear stress distribution on the bone interface of the humerus at arm elevations of 40° (top left), 50° (top right) and 60° (bottom) degrees.*

The maximum tensile stress on the contacting face is displayed in Fig. 76. The circular stress pattern originating from the nonlinear analysis has disappeared on the glenoid as it does on the humerus. High stress region move from the inferior to the superior side with increasing arm elevation. Considering the central part only, the stress magnitude is larger than in the linear analysis. Closer to the edges, a comparison turns out to be inconclusive.

Unlike what is observed on the humerus, maximum tensile, compressive and shear stress at the bone interface of the glenoid does not display the circular incongruity pattern of the joint (Figs. 77-79). Instead, the stresses are more uniformly distributed.

Due to the vast difference in the picture scales, a visual comparison with the results of the linear analysis is hard to make; however, a numerical comparison reveals the following information:

At the central part, maximum tensile stress, in general, is slightly higher than in the linear analysis. On the other hand, the maximum compressive stress is clearly lower than the values obtained in the linear analysis, following a similar trend to humerus. The maximum shear stress values encountered on the glenoid is comparable to those observed in the linear analysis.

#### **7.3.4 Evaluation of the Glenohumeral Analysis Results**

The results presented in the previous three sections indicate that nonlinear finite element analysis of the contacting biphasic tissue layers can give qualitatively and quantitatively different results than the linear analysis. The nature of the hyperelastic solid phase and its the strain-dependent permeability is main factor behind this effect. Hence, the nonlinearities due to large deformation and strain-dependent permeability of the solid phase should be accounted for when appropriate for accurate finite element analysis of the contacting tissues. The derived total traction and pressure boundary conditions have higher peak values compared to the linear penetration analysis which is the other factor inducing the difference between linear and nonlinear approaches.

Considering, the relatively large time scale of SPG measurements, the actual tissues must have been under large deformation when their kinematics were measured. The boundary conditions derived through nonlinear penetration analysis satisfy the kinetic contact continuity requirements better than the linear analysis, which seems to confirm the presence of nonlinear effects in the tissue. Although not explicitly displayed here, the humerus results also indicate the appropriateness of the uniform through-thickness pressure assumption made in the penetration derivation.

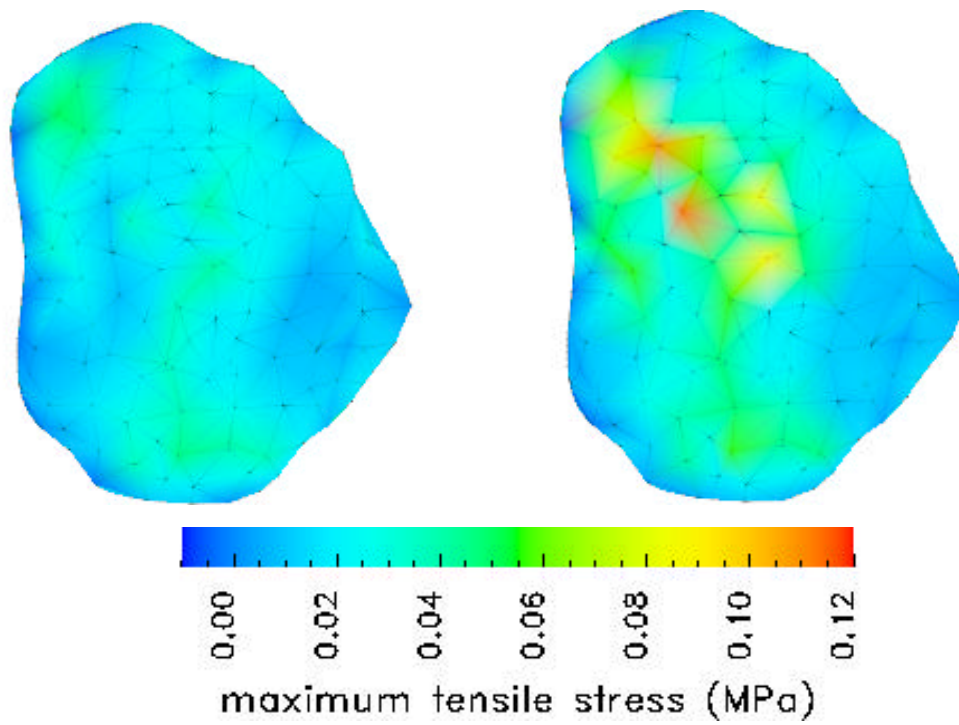


Figure 76: Maximum tensile stress distribution on the contacting face of the glenoid at arm elevations of 40° (left) and 50° (right).

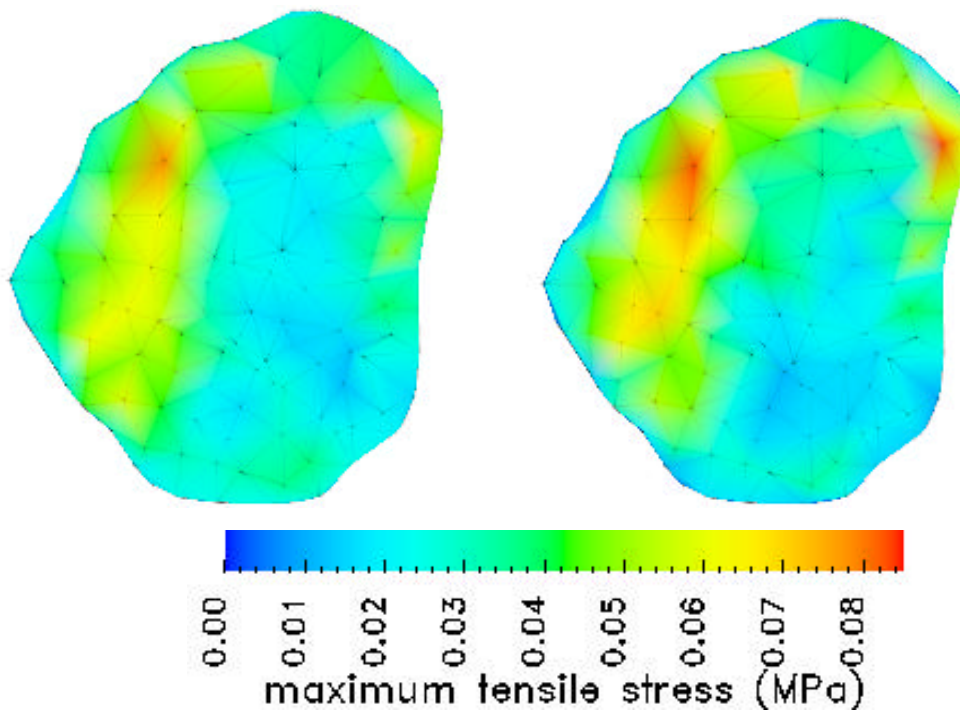


Figure 77: Maximum tensile stress distribution on the bone interface of the glenoid at arm elevations of 40° (left) and 50° (right).

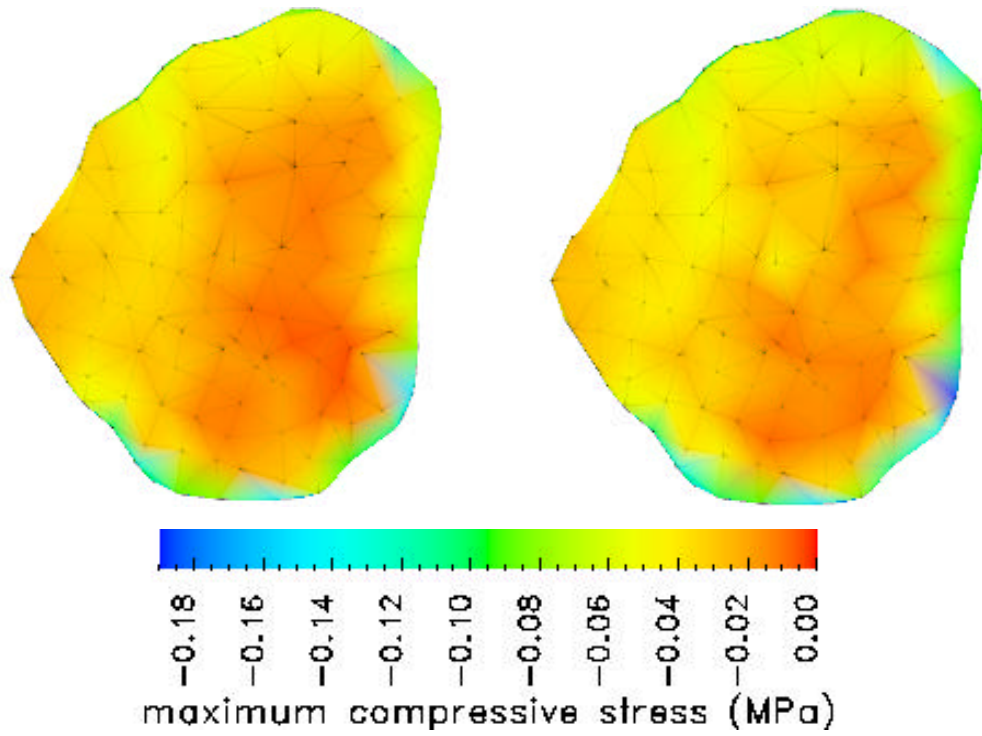


Figure 78: Maximum compressive stress distribution on the bone interface of the glenoid at arm elevations of 40° (left) and 50° (right).

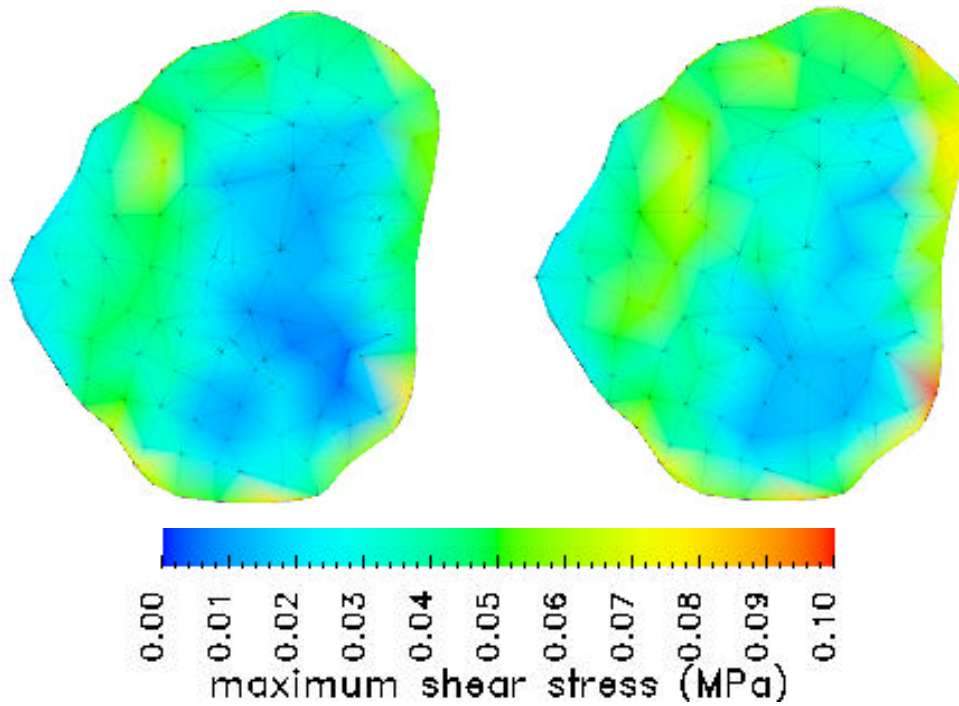


Figure 79: Maximum shear stress distribution on the bone interface of the glenoid at arm elevations of 40° (left) and 50° (right).

Since there is no independent nonlinear finite element contact program or analytical solution for nonlinear contact available, the nonlinear penetration procedure cannot be verified as done for the linear penetration procedure. However, the results presented in this chapter are thought to be consistent and plausible.

## Chapter 8

### Summary, Conclusions and Future Research

#### 8.1 Summary and Conclusions

The ability to predict the response of biphasic soft tissues in contact is fundamental to the understanding of diarthrodial joint biomechanics, and it represents a challenging computational mechanic problem. From a mechanics point of view, it requires a representative continuum theory, associated constitutive models, measured materials properties, geometry, kinematic and kinetic conditions, all of which must be validated against experimental and physiological data. The present research represents the initial attempt to analyze soft tissue contact under *in vivo* conditions, using physiological geometry and loading, taking into account large deformation and strain-dependent permeability of the biphasic tissue layers. An approximate method to simulate the time-dependent deformation of contacting biphasic cartilage layers during *in vivo* diarthrodial joint motion was developed and implemented. In order to address complex physiological joints, the research addressed three major components:

- Derivation and validation of a penetration-based approximation for 3-D contact of linear and nonlinear biphasic tissue layers based on the biphasic governing equations and biphasic contact conditions.
- Evaluation of alternate linearizations of the nonlinear biphasic problem discretized using a velocity-pressure or displacement-pressure finite element formulation, together with alternate line search strategies that provide robust solutions to problems with realistic physiological tissue geometry and material properties.
- Implementation and testing of these methods within the Trellis analysis framework in order to allow more systematic analysis of physiological problems.

The penetration method is a preprocessing technique that uses kinematic data that may originate from various experimental visualization techniques as input. The quantities that must be measured and provided as input for our analysis are: the undeformed geometry and material properties of the contacting tissue layers; the kinematics of the hard tissues to which the tissue layers are attached; and the force vector(s) associated

with the motion. In our examples, this data was provided through an experimental study at the Orthopedic Research Laboratory at Columbia University. This data is then imported, and a geometric model of the tissues layers is constructed using commercial modeling software. Assuming the hard tissues are rigid, the kinematic data can be used to position tissue layers physiologically. Since the tissue geometry is the undeformed geometry, the physiological positions will produce tissue overlap, or penetration, whose distribution can be characterized by the solid modeling software.

The penetration method uses the time-dependent penetration distributions, tissue geometry and material properties, and total force vector to calculate approximate contact traction boundary conditions (as a function of time for articulating joints) for each of the contacting tissues. Since this is a preprocessing step, the 3-D linear or nonlinear biphasic analyses can then be performed independently on each of the layers. By this method, the intrinsic nonlinearity of contact is avoided.

The applied tractions in the contact region for each layer were derived based on the linear or nonlinear biphasic governing equations, and the contact boundary conditions for biphasic tissues. Using these equations, and assumptions that are supported by numerical observation or independent studies, the distribution of traction, and the split between the solid and fluid phases (i.e., total traction and pressure), were derived as a function of the penetration distribution, point-wise tissue depth and material properties, and load vector. The derivation was done for both linear and nonlinear hyperelastic biphasic materials, and it applies to any time during the joint articulation. These approximate contact boundary conditions were used in conjunction with linear  $v$ - $p$  and nonlinear  $v$ - $p$  and  $u$ - $p$  finite element methods to analyze tissue layers in contact.

Several canonical axisymmetric problems (with varying geometry, congruity and material properties), with geometry and properties representative of a human glenohumeral joint, was used to validate the penetration-based linear  $v$ - $p$  finite element method. The validation consisted of two steps; first, the 3-D penetration-based biphasic solutions were checked for self-consistency. In this the step the contact boundary conditions and assumptions used in the derivation of the method were examined; second, the 3-D penetration-based solutions were compared with a 2-D axisymmetric biphasic contact analysis to assess the accuracy of the method.

In the self-consistency phase of validation, the results demonstrate approximate satisfaction of the contact boundary conditions. They further demonstrated that the assumptions made in the derivation were appropriate: strain components neglected in the

derivation were found to be either small or of no consequence; and the through-thickness distribution of the normal strain and pressure were relatively uniform,

The comparisons with a 2-D axisymmetric contact finite element analysis for the same canonical geometry showed that the penetration-based finite element method produces relatively accurate results for elastic stress and displacement, and that accuracy improved as joint congruity increased. The results for elastic stress were particularly encouraging since this quantity is thought by a number of researches to be particularly relevant to tissue performance.

Based on these results, it is concluded that the penetration method is a reasonable first order approximation to full biphasic contact analysis. The main drawback of the penetration method was that it underestimated the contact area, and as a result, overestimated the total stress and pressure, in general. Also the accuracy of the method dropped close to the edge of the contact area, however, this is not of great concern since stress quantities tend to be lower at that part of the geometry and the maximum values experienced by the tissue are not affected by this error. It is clear that the method is computationally less complex than full contact analysis, and therefore requires less computational resources, however a full study of the method's accuracy for arbitrary 3-D problems will have to await the development of 3-D biphasic contact methods.

The penetration method has been used to analyze the glenohumeral joint (GHJ) of the human shoulder, with experimental data provided by the Orthopedic Research Laboratory at Columbia University, both for linear elastic and for hyperelastic solid phases. For a moving joint, penetration method produces natural (traction) and essential (pressure) boundary conditions that are both time and space-dependent to be applied on a relatively complex geometry of a thin tissue layer. The results showed that the kinetic contact continuity conditions in more complex physiological models could be satisfied by the penetration method. The linear penetration-based analyses were completed successfully. However, whereas it was found that the nonlinear analysis with hyperelastic solid phase and strain dependent permeability was robust for canonical geometries, the analysis was found to converge slowly and in some cases fail to converge, when used for the GHJ analyses. This lack of robustness, believed related to the thinness of the tissues, necessitated studies to improve the nonlinear analysis.

First, a line search algorithm was developed to update the solution estimate in an optimal manner in the iterative scheme. The accuracy of the nonlinear code and the performance of the line search algorithm was first evaluated by comparing the analysis

results with those obtained from a previously confirmed finite difference solution of the canonical, but numerically challenging, confined compression problem. Convergence occurred for a wide range of material properties, applied loads and different levels of mesh fineness. The line search was found to be crucial for convergence of any problem where the load levels were moderate or high.

To handle the time and space-varying boundary conditions on physiological models, additional steps were taken to improve the numerical performance of the iterative modified Newton scheme. In addition to the dominant nonlinear elasticity term, other nonlinearities in the weak form were selectively linearized and different combinations of linearization tested. Both  $v-p$  and  $u-p$  versions of finite element method were run using those modified Newton approaches. A  $u-p$  approach where the deformation gradient terms were linearized along with the nonlinear elasticity term, and the nonlinearities due to presence of the Jacobian term ignored, performed particularly well for the problem at hand.

Both linear and nonlinear glenohumeral joint analysis demonstrated the usefulness of the numerical approaches in predicting quantities that are experimentally hard to determine. The linear analysis predicted the maximum tensile, compressive and shear stresses to be of the same order at the cartilage-bone interface. This observation was in agreement with the available analytical solutions derived on canonical biphasic contact configurations. It was observed that linear and nonlinear penetration-based finite element analyses result to different values for various key stress quantities. The nonlinear analysis predicted lower compressive and higher tensile stresses at the bone interface compared to the linear analysis. That indicates tissue nonlinearity should be taken into account when appropriate in such analyses.

Linear and nonlinear versions of the finite element methods and the penetration method as a preprocessing technique have been implemented into the object-oriented analysis framework, *Trellis*, of the Scientific Computation Research Center at Rensselaer Polytechnic Institute using C++ programming language. The object oriented environment provided flexibility and extendability to the codes. The implementation of the penetration method was performed in such a way that the necessary boundary condition information as input to finite element analysis is created automatically for a given joint motion and the corresponding kinematic data. The implemented procedure can analyze any joint as long as the provided visualization data is compatible with the solid modelers available in *Trellis*. That enables the systematic treatment of physiological problems.

## 8.2 Future Research

The work described in this thesis can be considered as necessary first steps toward realistic numerical simulation of articular cartilage contact. There are numerous possibilities exist to improve the current approach. As the current work constitutes a methodology combining experimental methods with numerical approaches, improvements in both will naturally lead to more accurate and reliable results.

The SPG technique cannot always capture the complete geometry, as has been the case for the shoulder models analyzed. The method creates artificial edges in the models and it is difficult to justify the application of any boundary condition on those. Also, high tractions acting close to these edges might cause the analysis to return unrealistically high stresses. Improved experimental techniques are likely to result in better models and more accurate kinematic data that will eliminate such problems. From that point of view, the MRI technique has good potential to be used along with penetration-based finite element.

Other relevant experimental work that will benefit the current research are better measurement (and/or estimation) of material properties of the cartilage layers and the force acting on the joint. It should be noted that lack of accuracy in those quantities can produce numerical problems in the simulation procedure.

Improvements can be achieved in the numerical procedures as well. The performance of the iterative solution procedure for nonlinear problems is found to be relatively sensitive to entities of the problem physics such as material parameters and problem geometry, as well as those of problem numerical aspects such as mesh refinement and time step. Designing a proper problem-specific solver will not only provide robustness with respect to those entities but also improve the numerical performance in terms of CPU time required to run the analysis.

Another numerical entity that deserves further exploration is the time integration scheme. Particularly in the nonlinear problem, an improved time integration scheme (such as a multi-step method) can enhance the numerical performance by enabling the usage of larger time steps and providing better initial estimates at each time step.

The penetration method presented in this thesis is considered as an introductory method to simulate the mechanical behavior of biphasic cartilage layers under *in vivo* conditions. In addition to improving the numerical procedure applied, it is possible to refine the modeling process. The natural next step is to implement full 3-D biphasic contact finite element formulations for both linear and nonlinear biphasic materials. As implied in the relevant chapters of the current thesis, the implementation of a nonlinear

biphasic contact finite element method is a challenging task given the current computer resources available. Hence, improvements in the numerical procedure, such as designing more efficient solvers, or using more sophisticated computing paradigms, such as parallel-processor programming, should go hand in hand with the implementation of the problem physics as a numerical procedure.

Advanced material models constitute a broad area to explore within a numerical framework. The intrinsic viscoelasticity of the solid phase, or the triphasic and quadriphasic theories of cartilage are already used within finite element method in canonical problems. Their implementation within a 3-D contact framework still needs to be accomplished. The extension of these material models to large deformation and their numerical implementation will open new insights for biomedical researchers and, ultimately, clinicians.

## Bibliography

1. Almeida, E.S., *Finite Element Formulations for Biological Soft Hydrated Tissues Under Finite Deformation*, PhD thesis, Rensselaer Polytechnic Institute, 1995
2. Almeida, E.S. and Spilker, R.L., Mixed and penalty finite element models for the nonlinear behavior of biphasic soft tissues in finite deformation: Part I - Alternate formulations, *Comp. Meth. in Biomech. and Biomed. Engng.*, **1**: 25-46., 1997
3. An, K., Chao, E.Y.S., and Kaufman, K.R., Analysis of muscle and joint loads, in *Basic Orthopaedic Biomechanics*, V.C. Mow and W.C. Hayes eds., Lippincott-Raven, Philadelphia, pp. 1-37, 1997
4. Armstrong, C.G., Lai, W.M., and Mow, V.C., An analysis of the unconfined compression of articular cartilage., *J. Biomech. Engng.*, **106**: 165-173., 1984
5. Ateshian, G.A., A theoretical model for boundary friction in articular cartilage, *Annals Biomed. Engng.*, **22,Suppl 1**: 63., 1994
6. Ateshian, G.A., Lai, W.M., Zhu, W.B., and Mow, V.C., An asymptotic solution for the contact of two biphasic cartilage layers, *J. Biomech.*, **27**: 1347-1360., 1994
7. Ateshian, G.A., Soslowky, L.J., and Mow, V.C., Quantitation of articular surface topography and cartilage thickness in knee joints using stereophotogrammetry, *J. Biomech.*, **24**: 761-776., 1991
8. Ateshian, G.A. and Wang, H., A theoretical solution for the frictionless rolling contact of cylindrical biphasic articular cartilage layers, *J. Biomech.*, **28**: 1341-1355., 1995
9. Athanasiou, K.A., Rosenwasser, M.P., Buckwalter, J.A., Malinin, T.I., and Mow, V.C., Interspecies comparisons of *in situ* intrinsic mechanical properties of distal femoral cartilage, *J. Orthop. Res.*, **9**: 330- 340., 1991
10. Bathe, K.J., *Finite Element Procedures in Engineering Analysis*, Prentice-Hall, Englewood Cliffs, NJ, 1982
11. Beall, M.W. and Shephard, M.S., An object-oriented framework for reliable numerical simulations, *Engng. Comp.*, **15**: 61-72., 1999
12. Biot, M.A., General theory of three-dimensional consolidation, *J. Appl. Physics*, **12**: 155-164., 1941

13. Bonet, J. and Burton, A.J., A simple orthotropic, transversely isotropic hyperelastic constitutive equation for large strain computations, *Comp. Meth. Appl. Mech. Engng.*, **162**: 151-164., 1998
14. Bonet, J. and Wood, R.D., *Nonlinear continuum mechanics for finite element analysis*, Cambridge University Press, Cambridge, 1997
15. Bowen, R.M., Theory of mixtures, in *Continuum Physics*, A.C. Eringen ed. Academic Press, New York, 3, pp. 1-127, 1976
16. Bowen, R.M., Incompressible porous media models by use of the theory of mixtures, *Int. J. Engng. Science*, **18**: 1129-1148., 1980
17. Butcher, J.C., Implicit Runge-Kutta processes, *Math. Comput.*, **18**: 50-64., 1964
18. Carey, J., Small, C.F., and Pichora, D.R., In situ compressive properties of the glenoid labrum, *Journal of Biomedical Materials Research*, **51**: 711-716., 2000
19. Chen, J., Akyuz, U., Xu, L., and Pidaparti, R.M.V., Stress analysis of the human temporomandibular joint, *Med. Eng. Phys.*, **20**: 565-572., 1998
20. Cohen, B., Gardner, T.R., and Ateshian, G.A., The influence of transverse isotropy on cartilage indentation behavior -- A study of the human humeral head, in *Transactions of the 39th Annual Meeting of the Orthopaedic Research Society*, ORS, Park Ridge, IL, 18, pp. 185, 1993
21. Crisfield, M.A., *Non-linear Finite Element Analysis of Solids and Structures: Essentials*, John Wiley and Sons, 1991
22. Curnier, A., He, Q., and Zysset, P., Conewise linear elastic material, *J. Elast.*, **37**: 1-38., 1995
23. Dabnichki, P.A., Crocombe, A.D., and Hughes, S.C., Deformation and stress analysis of supported buttock contact, *Proc. Instn Mech. Engrs*, **208**: 9-17., 1994
24. de Boer, R., Highlights in the historical development of the porous media theory: Toward a consistent macroscopic theory, *Appl. Mech. Rev.*, **49**: 201-262., 1996
25. Donzelli, P.S., *A Mixed-Penalty Contact Finite Element Formulation for Biphasic Soft Tissues*, Ph.D. thesis, Rensselaer Polytechnic Institute, 1995
26. Donzelli, P.S. and Spilker, R.L., A contact finite element formulation for biological soft hydrated tissues, *Comp. Meth. Appl. Mech. Engng.*, **153**: 63-79., 1998

27. Donzelli, P.S., Spilker, R.L., Ateshian, G.A., and Mow, V.C., Contact analysis of biphasic transversely isotropic cartilage layers and correlations with tissue failure, *J. Biomech.*, **32**: 1037-1047., 1999
28. Drozdov, A.D., *Finite Elasticity and Viscoelasticity*, World Scientific, 1996
29. Eckstein, F., Adam, C., Sittek, H., Becker, C., Milz, S., Schulte, E., Reiser, M., and Putz, S., Non-invasive determination of cartilage thickness throughout joint surfaces using magnetic resonance imaging, *J. Biomech.*, **30**: 285-289., 1997
30. Ege, R., *Object-Oriented Programming with C++*, Academic Press, 1994
31. Eringen, A.C., *Mechanics of Continua*, John Wiley & Sons, inc., 1967
32. Esche, S.K., Kinzel, G.L., and Altan, T., Issues in convergence improvement for non-linear finite element programs, *Int. J. Num. Meth. in Engng.*, **40**: 4577-4594., 1997
33. Frijns, A.J.H., Huyghe, J.M., and Janssen, J.D., A validation of the quadriphasic mixture theory for intervertebral disc tissue, *Int. J. Engng. Science*, **35**: 1419-1429., 1997
34. Fung, Y.C., *Biomechanics: Mechanical Properties of Living Tissues.*, Springer-Verlag, New York, NY, 1993
35. Goldsmith, A.A.J. and Clift, S.E., Investigation into the biphasic properties of a hydrogel for use in a cushion form replacement joint, *J. Biomech. Engng.*, **120**: 362-369., 1998
36. Guilak, F., Ratcliffe, A., and Mow, V.C., Chondrocyte deformation and local tissue strain in articular cartilage: A confocal microscopy study, *J. Orthop. Res.*, **13**: 410-421., 1995
37. Hairer, E. and Wanner, G., *Solving Ordinary Differential Equations 2: Stiff and Differential Algebraic Problems*, Springer Verlag, Berlin, 1991
38. Hale, J.E., Rudert, M.J., and Brown, T.D., Indentation assessment of biphasic mechanical property deficits in size-dependent osteochondral defect repair, *J. Biomech.*, **26**: 1319-1325., 1993
39. Hasler, E.M., Herzog, W., Wu, J.Z., Muller, W., and Wyss, U., Articular cartilage biomechanics: theoretical models, material properties, and biosynthetic response, *Critical Reviews in Biomedical Engineering*, **27**: 415-488., 1999

40. Holmes, M. and Mow, V., The nonlinear characteristics of soft gels and hydrated connective tissues in ultrafiltration, *J. Biomech.*, **23**: 1145-1156., 1990
41. Holmes, M.H., Lai, W.M., and Mow, V.C., Singular perturbation analysis of the nonlinear, flow-dependent compressive stress relaxation behavior of articular cartilage, *J. Biomech. Engng.*, **107**: 206-218., 1985
42. Holzapfel, G.A. and Weizsacker, H.W., Biomechanical behavior of the arterial wall and its numerical characterization, *Computers in Biology and Medicine*, **28**: 377-392., 1998
43. Hon, Y.C., Lu, M.W., Xue, W.M., and Zhou, X., A new formulation and computation of the triphasic model for mechano-electrochemical mixtures, *Computational Mechanics*, **24**: 155-165., 1999
44. Hon, Y.C., Lu, M.W., Xue, W.M., and Zhu, Y.M., Multiquadratic method for the numerical solution of a biphasic mixture model, *Applied Mathematics and Computation*, **88**: 153-175., 1997
45. Hou, J.S., Holmes, M.H., Lai, W.M., and Mow, V.C., Boundary conditions at the cartilage-synovial fluid interface for joint lubrication and theoretical verifications, *J. Biomech. Engng.*, **111**: 78-87., 1989
46. Huang, C.Y., Mow, V.C., and Ateshian, G.A., The role of flow-independent viscoelasticity in the biphasic tensile and compressive responses of articular cartilage, *J. Biomech. Engng.*, **123**: 410-417., 2001
47. Huyghe, J.M., Van Campen, D.H., Arts, T., and Heethaar, R., A two-phase finite element model of the diastolic left ventricle, *J. Biomech.*, **24**: 527-538., 1991
48. Iatridis, J.C., Setton, L.A., Foster, R.J., Rawlins, B.A., Weidenbaum, M., and Mow, V.C., Degeneration affects the anisotropic and nonlinear behaviors of human anulus fibrosus in compression, *J. Biomech.*, **31**: 535-544., 1998
49. Kardestuncer, H., *The Finite Element Handbook*, McGraw Hill, 1987
50. Kelkar, R. and Ateshian, G.A., Contact creep of biphasic cartilage layers, *J. Biomech. Engng.*, **66**: 137-145., 1999
51. Kowalczyk, P., Mechanical model of lung parenchyma as a two-phase porous medium, *Transport in Porous Media*, **11**: 281-295., 1993

52. Lai, W.M., Hou, J.S., and Mow, V.C., A triphasic theory for the swelling and deformational behaviors of articular cartilage, *J. Biomech. Engng.*, **113**: 245-258., 1991
53. Lai, W.M. and Mow, V.C., Drag-induced compression of articular cartilage during a permeation experiment, *Biorheol.*, **17**: 111-123., 1980
54. Lai, W.M., Rubin, D., and Krempl, E., *Introduction to Continuum Mechanics*, Pergamon Press, Oxford, England, 1993
55. Levenston, M.E., Frank, E.H., and Grodzinsky, A.J., Variationally derived 3-field finite element formulations for quasistatic poroelastic analysis of hydrated biological tissues, *Comp. Meth. Appl. Mech. Engng.*, **156**: 231-246., 1998
56. Mak, A.F., The apparent viscoelastic behavior of articular cartilage-The contributions from the intrinsic matrix viscoelasticity and interstitial fluid flows, *J. Biomech. Engng.*, **108**: 123-130., 1986
57. Mak, A.F., Lai, W.M., and Mow, V.C., Biphasic indentation of articular cartilage: Part I, theoretical analysis, *J. Biomech.*, **20**: 703-714., 1987
58. Mankin, H.J., Mow, V.C., Buckwalter, J.A., Iannotti, J.P., and Ratcliffe, A., Articular cartilage structure, composition, and function, in *Orthopaedic Basic Science: Biology and Biomechanics of the Musculoskeletal System*, American Academy of Orthopaedic Surgeons, 2000
59. Marsden, J.E. and Hughes, T.J.R., *Mathematical Foundations of Elasticity*, Prentice-Hall, New Jersey, 1983
60. Mendis, K.K., Stalnaker, R.L., and Advani, S.H., A constitutive relationship for large deformation finite element modeling of brain tissue, *J. Biomech. Engng.*, **117**: 279-285., 1995
61. Moulton, M.J., Creswell, L.L., Actis, R.L., Myers, K.W., Vannier, M.W., Szabo, B.A., and Pasque, M.K., An inverse approach to determining myocardial material properties, *J. Biomech.*, **28**: 935-948., 1995
62. Mow, V.C., Holmes, M.H., and Lai, W.M., Fluid transport and mechanical properties of articular cartilage: A review, *J. Biomech.*, **17**: 377-394., 1984
63. Mow, V.C., Kuei, S.C., Lai, W.M., and Armstrong, C.G., Biphasic creep and stress relaxation of articular cartilage in compression: theory and experiments, *J. Biomech. Engng.*, **102**: 73-84., 1980

64. Murad, M.A. and Loula, A.F.D., On stability and convergence of finite element approximations of Biot's consolidation problem, *Int. J. Num. Meth. in Engng.*, **37**: 645-667., 1994
65. Ogden, R.W., *Nonlinear elastic deformation*, Ellis Horwood, New York, 1984
66. Oka, F., Validity and limits of the effective stress concept in geomechanics, *Mechanics of Cohesive-Frictional Materials*, **1**: 219-234., 1996
67. Oomens, C.W.J., Van Campen, D.H., and Grootenboer, H.J., A mixture approach to the mechanics of skin, *J. Biomech.*, **20**: 877-885., 1987
68. Op den Camp, O.M.G.C., Oomens, C.W., Veldpaus, F.E., and Janssen, J.D., An efficient algorithm to estimate material parameters of biphasic mixtures, *Int. J. Num. Meth. in Engng.*, **45**: 1315-1331., 1999
69. Pian, T.H.H., Hybrid models, in *Numerical and Computer Methods in Structural Mechanics*, S.J. Fenves, *et al.* eds., Academic Press, New York, 1973
70. Poole, A.R., Rizkalla, G., Reiner, A., Ionescu, M., and Bogoch, E., Changes in the extra-cellular matrix of articular cartilage in human osteoarthritis, in *Trends in Research and Treatment of Joint Diseases*, K. Hirohata, K. Mizuno, and T. Matsubara eds., Springer Verlag, Tokyo, 1992
71. Sahay, K.B., Mehrotra, R., Sachdeva, U., and Banerji, A.K., Elastomechanical characterization of brain tissues, *J. Biomech.*, **25**: 319-326., 1992
72. Schinagl, R.M., Ting, M.K., Price, J.H., and Sah, R.L., Video microscopy to quantitate the inhomogeneous equilibrium strain within articular cartilage during confined compression, *Annals Biomed. Engng.*, **24**: 500-512., 1996
73. Schreppers, G.J.M.A., Sauren, A.A.H.J., and Huson, A., A numerical model of the load transmission in the tibio-femoral contact area, *Journal of Engineering in Medicine*, **204**: 53-59., 1990
74. Simon, B.R., Kaufmann, M.V., McAfee, M.A., and Baldwin, A.L., Porohyperelastic finite element analysis of large arteries using ABAQUS, *J. Biomech. Engng.*, **120**: 296-298., 1998
75. Simon, B.R., Kaufmann, M.V., McAfee, M.A., Baldwin, A.L., and Wilson, L.M., Identification and determination of material properties for porohyperelastic analysis of large arteries, *J. Biomech. Engng.*, **120**: 188-194., 1998

76. Simon, B.R., Wu, J.S.S., Carlton, M.W., France, E.P., Evans, J.H., and Kazarian, L.E., Structural models for human spinal motion segments based on a poroelastic view of the intervertebral disk., *J. Biomech. Engng.*, **107**: 327-335., 1985
77. Singh, S.I. and Devi, S., A study of radial motion of arteries in vivo, *J. Biomech.*, **23**: 1087-1091., 1990
78. Snijders, H., Huyghe, J.M., and Janssen, J.D., Triphasic finite element model for swelling porous media, *Int. J. Num. Meth. Fluids*, **20**: 1039-1046., 1995
79. Soltz, M.A. and Ateshian, G.A., A conewise linear elasticity mixture model for the analysis of tension-compression nonlinearity in articular cartilage, *J. Biomech. Engng.*, **122**: 576-586., 2000
80. Soslowky, L.J., Ateshian, G.A., and Mow, V.C., Stereophotogrammetric determination of joint anatomy and contact areas, in *Biomechanics of Diarthrodial Joints*, V.C. Mow, T.A. Ratcliffe, and S. L-Y.Woo eds., Springer-Verlag, II, pp. 243-268, 1990
81. Soslowky, L.J., Flatow, E.L., Bigliani, L.U., and Mow, V.C., Articular geometry of the glenohumeral joint, *Clin. Orthop.*, **285**: 181-190., 1992
82. Spilker, R.L. and Maxian, T.A., A mixed-penalty finite element formulation of the linear biphasic theory for soft tissues, *Int. J. Num. Meth. in Engng.*, **30**: 1063-1082., 1990
83. Suh, J.-K. and Spilker, R.L., Indentation analysis of biphasic articular cartilage: Nonlinear phenomena under finite deformation, *J. Biomech. Engng.*, **116**: 1-9., 1994
84. Suh, J.-K., Spilker, R.L., and Holmes, M.H., A penalty finite element analysis for nonlinear mechanics of biphasic hydrated soft tissue under large deformation, *Int. J. Num. Meth. in Engng.*, **32**: 1411-1439., 1991
85. Suh, J.K. and Bai, S., Finite element formulation of biphasic poroviscoelastic model for articular cartilage, *J. Biomech. Engng.*, **120**: 195-201., 1998
86. Suh, J.K. and DiSilvestro, M.R., Biphasic poroviscoelastic behavior of hydrated biological soft tissue, *J. Appl. Mech.*, **66**: 528-535., 1999
87. Sun, D.N., Gu, W.Y., Guo, X.E., Lai, W.M., and Mow, V.C., A mixed finite element formulation of triphasic mechano-electrochemical theory for charged, hydrated biological soft tissues, *Int. J. Num. Meth. in Engng.*, **45**: 1375-1402., 1999

88. Tabolt, S., *Determination of the Material Parameters of the Linear Biphasic Equations Using Finite Element and Response Surface Methods*, MS thesis, Rensselaer Polytechnic Institute, 1995
89. Terzaghi, K., Principle of soil mechanics, *Engng. News Rec.*, 1925
90. Tissakht, M. and Ahmed, A.M., Parametric study using different elastic and poroelastic axisymmetric models of the femur-meniscus-tibia unit, in *Advances in Bionengineering, Winter Annual Meeting of ASME*, M.W. Bidez ed. ASME, New York, BED-22, pp. 241-244, 1992
91. Tissakht, M., Marchand, F., and Ahmed, A.M., Non-linear finite element analysis of the knee menisci: a composite fiber-reinforced model, in *Transactions, 37th Orthopaedic Research Society Meeting*, 16, pp. 294, 1991
92. Töyräs, J., Lyyra-Laitinen, T., Niinimäki, M., Lindgren, R., Nieminen, M.T., Kiviranta, I., and Jurvelin, J.S., Estimation of the Young's modulus of articular cartilage using an arthroscopic indentation instrument and ultrasonic measurement of tissue thickness, *J. Biomech.*, **34**: 251-256., 2001
93. Truesdell, C. and Noll, W., *The Non-linear Field Theories of Mechanics*, Springer-Verlag, Berlin, 1992
94. Truesdell, C. and Toupin, R.A., The classical field theories, in *Handbuck der physik*, S. Flügge ed. Springer-Verlag, 3/1, 1960
95. Vankan, W.J., Huyghe, J.M., Janssen, J.D., Huson, A., Hacking, W.J., and Schreiner, W., Finite element analysis of blood flow through biological tissue, *Int. J. Engng. Science*, **35**: 375-385., 1997
96. Vermilyea, M.E. and Spilker, R.L., A hybrid finite element formulation of the linear biphasic equations for soft hydrated tissues, *Int. J. Num. Meth. in Engng.*, **33**: 567-594., 1992
97. Vermilyea, M.E. and Spilker, R.L., Hybrid and mixed-penalty finite elements for 3D analysis of soft hydrated tissue, *Int. J. Num. Meth. in Engng.*, **36**: 4223-4243., 1993
98. Wayne, J.S., Woo, S.L.-Y., and Kwan, M.K., Application of the u-P finite element method to the study of articular cartilage, *J. Biomech. Engng.*, **113**: 397-403., 1991
99. Whitaker, S., Flow in porous media III: Deformable media, *Transport in Porous Media*, **1**: 127-154., 1986

100. Wu, J.S.S. and Chen, J.H., Clarification of the mechanical behaviour of spinal motion segments through a three-dimensional poroelastic mixed finite element model, *Med. Eng. Phys.*, **18**: 215-224., 1996
101. Wu, J.Z., Herzog, W., and Epstein, M., An improved solution for the contact of two biphasic cartilage layers, *J. Biomech.*, **30**: 371-375., 1997
102. Wu, J.Z., Herzog, W., and Ronsky, J., Modeling axi-symmetrical joint contact with biphasic cartilage layers - an asymptotic solution, *J. Biomech.*, **29**: 1263-1282., 1996
103. Yu, H. and Stone, J.S., Viscoelastic Finite Element Contact Analysis of Articular Joints, in *Proceedings of the 1998 Bioengineering Conference*, A.P. Yoganathan ed. ASME, BED-39, pp. 217-218, 1998

## Appendix A

### Derivation of the Tangent Stiffness for the Hyperelastic Material Law

The hyperelastic law, introduced in Chapter 3,

$$= \frac{e^{-1(I_1-3) - 2(I_2-3)}}{I_3}, \quad (\text{A.1})$$

is differentiated with respect to  $\mathbf{C}$  in Chapter 4 to linearize the nonlinear elasticity term in the weak form. The differentiation is performed through the principal invariant  $I_1$ ,  $I_2$  and  $I_3$  of  $\mathbf{C}$ , which are expressed as

$$I_1 = \text{tr } \mathbf{C} \quad I_2 = \frac{1}{2} [(\text{tr } \mathbf{C})^2 - \text{tr } \mathbf{C}^2] \quad I_3 = \det \mathbf{C}, \quad (\text{A.2})$$

and by utilizing the chain rule. Thus, the first derivative is given as

$$\frac{\partial}{\partial \mathbf{C}} = \frac{\partial I_1}{\partial \mathbf{C}} + \frac{\partial I_2}{\partial \mathbf{C}} + \frac{\partial I_3}{\partial \mathbf{C}}. \quad (\text{A.3})$$

Equation (A.3) is differentiated again to find the second derivative:

$$\begin{aligned} \frac{\partial^2}{\partial \mathbf{C} \partial \mathbf{C}} = & \frac{\partial^2 I_1}{\partial \mathbf{C}^2} + \frac{\partial^2 I_2}{\partial \mathbf{C}^2} + \frac{\partial^2 I_3}{\partial \mathbf{C}^2} \frac{\partial I_1}{\partial \mathbf{C}} + \frac{\partial^2 I_1}{\partial \mathbf{C}^2} \\ & + \frac{\partial^2 I_1}{\partial \mathbf{C}^2} \frac{\partial I_1}{\partial \mathbf{C}} + \frac{\partial^2 I_2}{\partial \mathbf{C}^2} \frac{\partial I_2}{\partial \mathbf{C}} + \frac{\partial^2 I_3}{\partial \mathbf{C}^2} \frac{\partial I_3}{\partial \mathbf{C}} + \frac{\partial^2 I_2}{\partial \mathbf{C}^2} \\ & + \frac{\partial^2 I_3}{\partial \mathbf{C}^2} \frac{\partial I_1}{\partial \mathbf{C}} + \frac{\partial^2 I_3}{\partial \mathbf{C}^2} \frac{\partial I_2}{\partial \mathbf{C}} + \frac{\partial^2 I_3}{\partial \mathbf{C}^2} \frac{\partial I_3}{\partial \mathbf{C}} + \frac{\partial^2 I_3}{\partial \mathbf{C}^2} \end{aligned} \quad (\text{A.4})$$

It is not hard to derive the following expressions for derivatives of the invariants [14]

$$\begin{aligned} \frac{\partial I_1}{\partial \mathbf{C}} &= \mathbf{I} & \frac{\partial^2 I_1}{\partial \mathbf{C}^2} &= \mathbf{0} \\ \frac{\partial I_2}{\partial \mathbf{C}} &= I_1 \mathbf{I} - \mathbf{C} & \frac{\partial^2 I_2}{\partial \mathbf{C}^2} &= (\mathbf{I} \quad \mathbf{I} - \mathbf{I}) \\ \frac{\partial I_3}{\partial \mathbf{C}} &= I_3 \mathbf{C}^{-1} & \frac{\partial^2 I_3}{\partial \mathbf{C}^2} &= I_3 (\mathbf{C}^{-1} \quad \mathbf{C}^{-1} + \mathbf{I}_{\mathbf{C}^{-1}}) \end{aligned} \quad (\text{A.5})$$

where  $\mathbf{I}$  and  $\mathbf{0}$  are second-order unity and zero tensors, respectively.  $\mathbf{I}$  and  $\mathbf{I}_{C^{-1}}$  are fourth-order tensor and their components are given in the indicial notation as

$$I_{ijkl} = \frac{1}{2} (\delta_{ik} \delta_{jl} + \delta_{il} \delta_{jk}), \quad (\text{A.6})$$

$$[I_{C^{-1}}]_{ijkl} = -\frac{1}{2} (C_{ik}^{-1} C_{jl}^{-1} + C_{il}^{-1} C_{jk}^{-1}). \quad (\text{A.7})$$

Denoting the partial derivative of  $\psi$  with respect to  $I_m$ ,  $m=1,2,3$ , as  $\alpha_m$ , the first and second partial derivatives of  $\psi$  with respect to the invariants can be written as

$$\begin{aligned} \alpha_{,1} &= \alpha_1 & \alpha_{,2} &= \alpha_2 & \alpha_{,3} &= -\frac{\beta}{I_3} \\ \alpha_{,11} &= \alpha_1^2 & \alpha_{,22} &= \alpha_2^2 & \alpha_{,33} &= \frac{\beta^2 + \beta}{I_3^2} \\ \alpha_{,12} &= \alpha_1 \alpha_2 & \alpha_{,13} &= -\frac{\alpha_1 \beta}{I_3} & \alpha_{,23} &= -\frac{\alpha_2 \beta}{I_3} \end{aligned} \quad (\text{A.8})$$

Using Eqs. (A.5) and (A.8), Eq. (A.3) becomes

$$\frac{\partial \psi}{\partial \mathbf{C}} = [(\alpha_1 + I_1 \alpha_2) \mathbf{I} - \alpha_2 \mathbf{C} - \beta \mathbf{C}^{-1}] \quad (\text{A.9})$$

The above expression is used in order to calculate the second Piola-Kirchoff stress tensor,  $\mathbf{S}^E$ . Similarly, Eq. (A.4) becomes

$$\begin{aligned} \frac{\partial^2 \psi}{\partial \mathbf{C} \partial \mathbf{C}} &= \alpha_1^2 \mathbf{I} + \alpha_1 \alpha_2 (\mathbf{I}_1 \mathbf{I} - \mathbf{C}) - \frac{\alpha_1 \beta}{I_3} \mathbf{I}_3 \mathbf{C}^{-1} - \mathbf{I} \\ &+ \alpha_1 \alpha_2 \mathbf{I} + \alpha_2^2 (\mathbf{I}_1 \mathbf{I} - \mathbf{C}) - \frac{\alpha_2 \beta}{I_3} \mathbf{I}_3 \mathbf{C}^{-1} - (\mathbf{I}_1 \mathbf{I} - \mathbf{C}) + \alpha_2 (\mathbf{I} - \mathbf{I} - \mathbf{I}) \\ &+ -\frac{\alpha_1 \beta}{I_3} \mathbf{I} - \frac{\alpha_2 \beta}{I_3} (\mathbf{I}_1 \mathbf{I} - \mathbf{C}) + \frac{\beta^2 + \beta}{I_3^2} \mathbf{I}_3 \mathbf{C}^{-1} - (\mathbf{I}_3 \mathbf{C}^{-1}) - \beta (\mathbf{C}^{-1} - \mathbf{C}^{-1} + \mathbf{I}_{C^{-1}}) \end{aligned} \quad (\text{A.10})$$

Rearranging Eq. (A.10) gives the following compact form for the tangent stiffness:

$$\begin{aligned}
\frac{\partial^2}{\partial \mathbf{C} \partial \mathbf{C}} = & \left[ (\alpha_2 + \alpha_1^2 + 2I_1\alpha_1\alpha_2 + I_1^2\alpha_2^2)(\mathbf{I} - \mathbf{I}) - (\alpha_1\alpha_2 + I_1\alpha_2^2)(\mathbf{I} - \mathbf{C} + \mathbf{C} - \mathbf{I}) \right. \\
& - \alpha_1\beta + \alpha_2\beta \frac{I_1}{I_3} (\mathbf{I} - \mathbf{C}^{-1} + \mathbf{C}^{-1} - \mathbf{I}) + \alpha_2^2(\mathbf{C} - \mathbf{C}) + \alpha_2\beta(\mathbf{C} - \mathbf{C}^{-1} + \mathbf{C}^{-1} - \mathbf{C}) \quad (\text{A.11}) \\
& \left. + \beta^2(\mathbf{C}^{-1} - \mathbf{C}^{-1}) - \alpha_2\mathbf{I} - \beta\mathbf{I}_{\mathbf{C}^{-1}} \right]
\end{aligned}$$

which is the expression used to calculate the tangent stiffness,  $\mathbf{C}$ .

## Appendix B

### Element Matrices of Nonlinear $v$ - $p$ Formulation

The following matrices are made of the entries of  $F$  tensor and its inverse, and are used in the nonlinear  $v$ - $p$  formulation.

$$\mathbf{F}_{INV} = \begin{bmatrix} F_{11}^{-1} & F_{21}^{-1} & F_{31}^{-1} & F_{12}^{-1} & F_{22}^{-1} & F_{32}^{-1} & F_{13}^{-1} & F_{23}^{-1} & F_{33}^{-1} \end{bmatrix} \quad (\text{B.1})$$

$$\mathbf{F}_L = \begin{bmatrix} F_{11} & 0 & 0 & F_{21} & 0 & 0 & F_{31} & 0 & 0 \\ F_{12} & 0 & 0 & F_{22} & 0 & 0 & F_{32} & 0 & 0 \\ F_{13} & 0 & 0 & F_{13} & 0 & 0 & F_{33} & 0 & 0 \\ F_{12} & F_{11} & 0 & F_{22} & F_{21} & 0 & F_{32} & F_{31} & 0 \\ F_{13} & 0 & F_{11} & F_{13} & 0 & F_{21} & F_{33} & 0 & F_{31} \\ 0 & F_{13} & F_{12} & 0 & F_{13} & F_{22} & 0 & F_{33} & F_{32} \end{bmatrix} \quad (\text{B.2})$$

Note that these matrices are defined for a specific order of degrees of freedom given in the unknown vectors.

## Appendix C

### Justification for Disregarding the Tissue Curvature Effect in Penetration Analysis

Typical tissue layers in the musculoskeletal system have curved faces. Assigning a displacement at each point that is normal to the surface, as done in the penetration method, will cause a corresponding tangential displacement. Here we demonstrate that the associated tangential strains are small compared to the normal strain and can be neglected in the elastic traction calculation in the pre-processing step. In the case of a flat surface the analysis is similar.

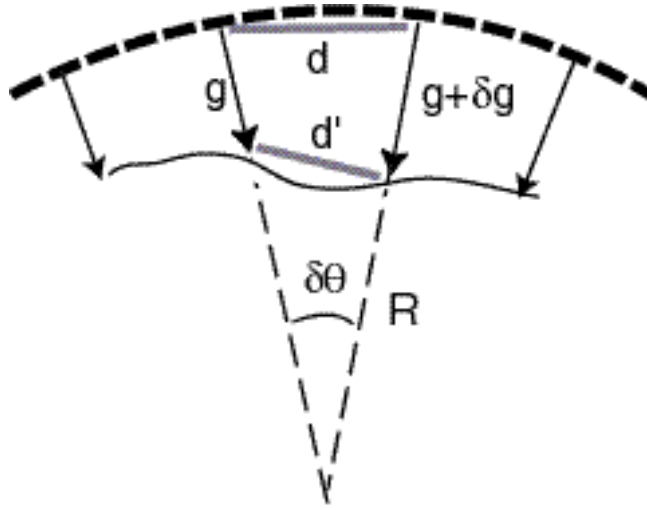


*Figure C.1: The penetration distribution assigned to a curved surface where  $g$  denotes the varying penetration field and  $R$  is the radius of curvature. Line segment of length  $d$  takes the length  $d'$  after penetration is applied.*

Consider a distribution of penetration vectors that is normal to a surface of curvature  $R$ , Fig. C1. For simplicity let  $R$  be constant. Considering a small angle, denoted as  $\delta\theta$ , a line segment of length  $d$  takes the length  $d'$  after the penetration field  $g$  deforms the surface. It is clear that  $d = R\delta\theta$  and the cosine law gives

$$d'^2 = (R - g)^2 + (R - g - \delta g)^2 - 2(R - g)(R - g - \delta g)\cos(\delta\theta) \quad (C.1)$$

For a small angle  $\delta\theta$ ,

$$1 - \cos(\delta\theta) \approx \frac{(\delta\theta)^2}{2} \quad (C.2)$$

Using this equation and neglecting higher order term, Eq. (C.1) can be rearranged to the following form:

$$d' = R\delta\theta \sqrt{\left(1 - \frac{g}{R}\right)^2 - \left(1 - \frac{g}{R}\right)\delta g + \frac{1}{R^2}\left(\frac{\delta g}{\delta\theta}\right)^2} \quad (C.3)$$

The tangential strain corresponding to this length change is

$$\varepsilon = \frac{d' - d}{d} \quad (C.4)$$

Substituting Eq. (C.3) into Eq. (C.4) and arranging terms gives

$$\varepsilon = \frac{R\delta\theta \sqrt{\left(1 - \frac{g}{R}\right)^2 - \left(1 - \frac{g}{R}\right)\delta g + \frac{1}{R^2}\left(\frac{\delta g}{\delta\theta}\right)^2} - R\delta\theta}{R\delta\theta} \quad (C.5)$$

The second term in the square root is of lower order and is neglected. The third term in the square root indicates (the square of) the change of penetration value per unit distance covered on the curved surface. For a paraboloidal penetration distribution with maximum value  $g_{max}$  over a circle of radius  $R_o$ , the maximum value that this quantity can take will be equal to  $2g_{max}/R_o$ . In our example problems,  $g_{max}$  and  $R_o$  are O(0.1mm) and O(10mm), respectively, so that this term is O(0.0001mm) and can be neglected compared to the first term, which is O(1). With these considerations, Eq. (C.5) simplifies to

$$\varepsilon = -\frac{g}{R} \quad (C.6)$$

Recall that in the analysis the magnitude of the normal strain is given as

$$\varepsilon_n = \frac{g}{h} \quad (C.7)$$

where  $h$  is the local thickness of the tissue. As a result we can say

$$\frac{\varepsilon}{\varepsilon_n} = O\left(\frac{h}{R}\right) \quad (C.8)$$

For a typical glenoid cartilage this quantity is around O(0.1). For a typical humeral head cartilage and for our example geometries it is even smaller.

The result for a flat surface can be derived from Eq (C.5) by letting  $R \rightarrow \infty$ . In this case, the term  $\delta g$  becomes significant while other terms vanish. Again, using a paraboloidal distribution it can be shown that

$$\frac{\varepsilon}{\varepsilon_n} = O\left(\frac{hg_{\max}}{R_0^2}\right) \quad (\text{C.9})$$

which is  $O(0.001)$  for our example problems. For physiological problems the ratio can have a higher order but is still negligible. The contribution of these in-plane strains to normal elastic traction on the surface is further diminished since they multiply smaller material coefficients (off-diagonal) in the stress-strain relation for typical isotropic and transversely isotropic soft tissue.